Spectroscopy of Neutron-Rich Nuclei via Inclusive Breakup Reactions

Doctoral Dissertation
by
Nobuyuki Kobayashi

Department of Physics,
Graduate School of Science and Engineering,
Tokyo Institute of Technology
O-okayama 2-12-1, Meguro, Tokyo 152-8551,Japan

February, 2013

Abstract

The one-neutron removal cross sections of the very neutron-rich near dripline nuclei ^{19,20}C, ^{29,31}Ne, ^{33,35,37}Mg, and ^{39,41}Si and the two-neutron removal cross sections of ^{20,22}C have been measured at around 240 MeV/nucleon at the RI-Beam Factory (RIBF) at RIKEN. The main goal of the thesis is to establish a new method using Coulomb and nuclear breakup reactions to probe the particle structures. The nuclei are investigated first by inclusive Coulomb breakup through their low-energy E1 strengths. Then, using the different sensitivities of the response to Coulomb and nuclear breakup, the single-particle configurations of the nuclei under study were deduced. The results provide evidence for the existence of halos in ^{22}C, ^{31}Ne, and ^{37}Mg. The nuclei studied here lie near the conventional magic numbers $N = 20$ and 28. The results presented here demonstrate in a number of cases significant changes in shell structure in the vicinity of the neutron dripline, and which correspond to deformation and the formation, in particular, of halos in ^{31}Ne and ^{37}Mg.

Contents

Chapter 1

Introduction

One of the goals of nuclear physics is to understand the various aspects of atomic nuclei based on simple microscopic rules. A nucleus is a finite many-body quantum system, where the behaviour of an ensemble of nucleons decides whole properties, such as shape, spin-parity, mass (separation energy), and magicity of the nucleus. The microscopic study of the structure of nuclei started with the shell model incorporating spin-orbit coupling as first introduced by Mayer [1] and Jensen [2]. This approach succeeded in explaining the magic numbers in stable nuclei. Hence, the basis for nuclear shell structure was established in terms of independent-particle motion in a self-consistent mean field. Since then the shell model has been used as one of basic theoretical frameworks to understand nuclear structure.

On the other hand, the development of high-energy heavy-ion accelerators has provided for the discovery of exotic phenomena in neutron-rich nuclei, such as the appearance of halo nuclei, and the "island of inversion", the melting of shell gaps and the disappearance of the conventional magic numbers and the appearance of new magic numbers. Halo nuclei appear in the vicinity of the neutron dripline, where nuclei are loosely bound. In halo nuclei, one- or two-valence neutrons with low-ℓ angular momentum, which makes no or small centrifugal barrier, are extended spatially over distances far from central potential. The size of the archetypal halo nucleus ^{11}Li is as large as that of ^{208}Pb.

The first halo nucleus ^{11}Li was found by a measurement of the total reaction reaction cross section at 800 MeV/u at Lawlence Berkley laboratory (LBL) in 1985 [3]. The deduced interaction nuclear radius R_I of 3.27(24) fm was about 20 % larger than that of the systematical value of 1.18 $A^{1/3}$ fm, A represents a number of nucleons, for ordinary nuclei as shown in Fig. 1.1. Furthermore, the momentum distribution of ^{9}Li fragment was found to be significantly narrower than that of ordinary nuclei [4, 5] as shown in Fig 1.2. The momentum distribution of ^{9}Li reflects the valence neutron orbital in ^{11}Li. According to the Heisenberg uncertainty principle, the narrow momentum distribution corresponds to the spatially broad neutron distribution. Therefore, the results confirmed the picture of a two-neutron halo.

Halos have also been investigated by utilizing Coulomb breakup. Halo nuclei were found to have strong $E1$ (electric dipole) transition probabilities at low excitation energies which is contrary to the ordinary nuclei where $E1$ strength is exhausted by the Giant Dipole Resonance (GDR) at the excitation energy $E_x \sim 80A^{1/3}$ MeV. For instance, Figure 1.3 shows $E1$ strength distribution of ^{11}Be [6], where a strong enhancement of $E1$ strength was observed just above the neutron threshold energy ($E_x = S_{1n}$). The enhancement is called soft $E1$ excitation and is an unique property of halo nuclei. Nakamura *et al.* [7] applied the Coulomb breakup to the spectroscopy of ^{19}C, where its structure had been controversial. This experiment could determine the single-particle configuration and separation energy of ^{19}C, which demonstrated that ^{19}C is another case of a halo nucleus. Namely, the Coulomb breakup reaction becomes a good spectroscopic tool for halo nuclei.

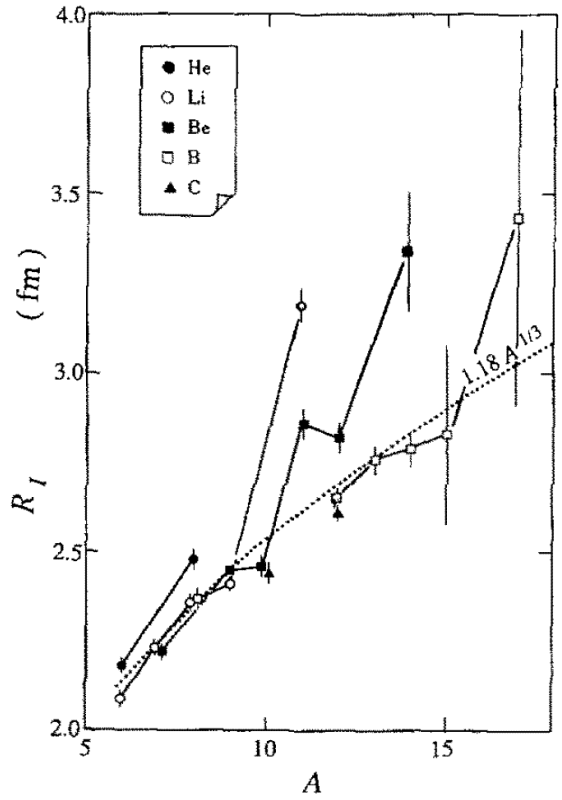

Figure 1.1: Systematics of interaction nuclear radius R_I as a function of mass number A. Doted line shows the systematical value of 1.18 $A^{1/3}$ for ordinary nuclei. In ^{11}Li, ^{11,14}Be, and ^{17}B, large radii were measured.

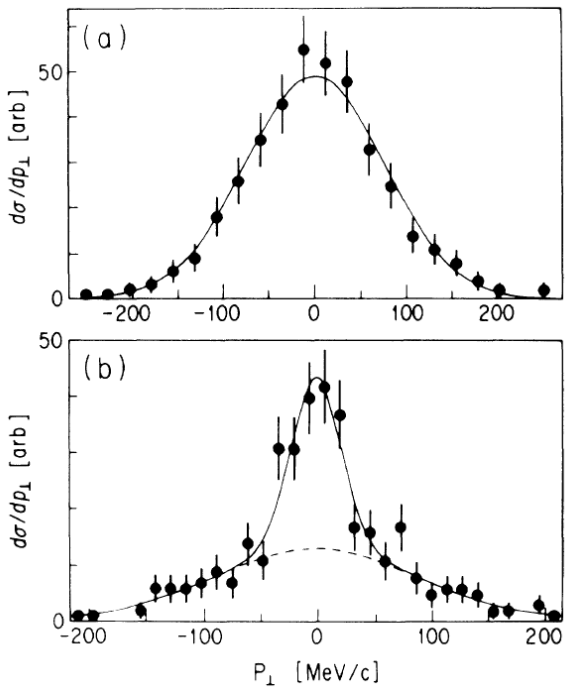

Figure 1.2: Transverse-momentum distributions of (a) ^{6}He fragments from reaction ^{8}He + C and (a) ^{9}Li fragments from reaction ^{9}Li + C. The solid lines are fitted Gaussian distributions.

Although halo nuclei have such interesting features, only several halo nuclei have been found in very light neutron-rich nuclei up to $A \approx 20$ as shown in Fig. 1.4, except for the newly-found $1n$ halo nucleus ^{31}Ne [8] (Chapter 5). We thus raise the question: can we observe halos in heavier nuclei? How and in what form can halo states appear in heavier nuclei? Therefore, finding new halo states in the heavier region is desired.

Another attractive feature in modern nuclear physics is the drastic modification of the shell structure when neutron number to proton number ratio is changed. Shell evolution in island of inversion is such a typical case which is not described by the conventional shell model. In the region around neutron-rich Ne, Na, and Mg isotopes as shown in Fig. 1.5 [10], the melting of $N = 20$ shell gap and mixing of single-particle orbitals occurs. The characteristic experimental results were obtained by γ spectroscopy of ^{32}Mg. Although the neutron number of ^{32}Mg is 20, which is the conventional magic number in ordinary nuclei, the first 2^+ excitation energy $E_x(2_1^+)$ was found to be significantly low ($E_x(2_1^+) = 885$ keV) [11]. Furthermore, $B(E2; 0^+_{\text{g.s.}} \rightarrow 2^+)$ of ^{32}Mg was found to be anomalously large ($B(E2; 0^+_{\text{g.s.}} \rightarrow 2^+) = 454(78)$ e^{2}fm^4) [12]. These anomalous values were interpreted as a result of the sd and pf shell mixing, and the large deformation of ^{32}Mg was concluded. From these experiments, disappearing of $N = 20$ magicity and large deformation were established for the nuclei around the island of inversion. The appearance of island of inversion is interpreted as a result of the shell evolution of neutron-rich region. However, the mechanism is not understood well, and hence further spectroscopic studies to investigate the configurations of the nuclei are needed.

More recently, a shell-evolution driven halo nucleus ^{31}Ne was found by the inclusive Coulomb breakup [7], which is one of the results discussed in this thesis (Chapter 5). This experiment suggested that this nucleus has a halo structure and pointed to the dominance of a loosely bound valence neutron in a p- or s-orbital; these features can be attributed to a change in the conventional shell order. In other words, it is formed due to the "melting" of the $N = 20$ and 28 shell gaps. However, spectroscopic data for neutron-rich nuclei around $N = 20$ and 28 are still very scarce, and hence the mechanism of shell evolution is not well understood. Neutron halo nuclei heavier than ^{31}Ne are not at all known at present.

The present thesis aims at investigating quantitatively the single-particle structure of neutron-rich C, Ne, Mg, and Si isotopes in the vicinity of the neutron drip line and of the conventional neutron magic numbers $N = 20$ and 28. The search for new halo states is also aimed through such investigations. For these purposes, two different probes are utilized: Coulomb and nuclear reactions at energies around 240 MeV/nucleon. The Coulomb breakup is sensitive to spatial distribution of a loosely bound valence neutron with low-ℓ angular orbital, hence the reaction is especially sensitive to halo structures. Nuclear breakup is sensitive to the single-particle configuration of the valence neutron. The combined analysis of the two results are used for the first time, and is proven to be a new and powerful spectroscopic tool as, in particular, it may be used with very weak beams of nuclei very far from stability. In this context, a series of experiments were performed at the new-generation RI beam facility, RI Beam Factory (RIBF) at RIKEN.

This thesis is organized as follows. Chapter 2 describes characteristic features of Coulomb and nuclear breakup reactions and includes a list of the separation energies of interest. Chapter 3 describes the experiment, i.e., the measured reaction channels, primary- and secondary-beam properties, production and reaction targets, and detector setups. In Chapters 5, 6, and 7, the experimental results are discussed. Chapter 5 describes the results for ^{31}Ne, which was studied as one of the "Day One" campaign experiments at the Zero Degree Spectrometer (ZDS) at RIBF in 2008. Chapter 6 describes the results for ^{29}Ne, ^{33,35,37}Mg, and ^{41}Si, which were studied as one of the "Day Three" campaign experiments at the ZDS in 2010. Chapter 6 describes the "Day One" results for ^{19,20,22}C. Finally, the summary and conclusions of this thesis are presented in Chapter 8.

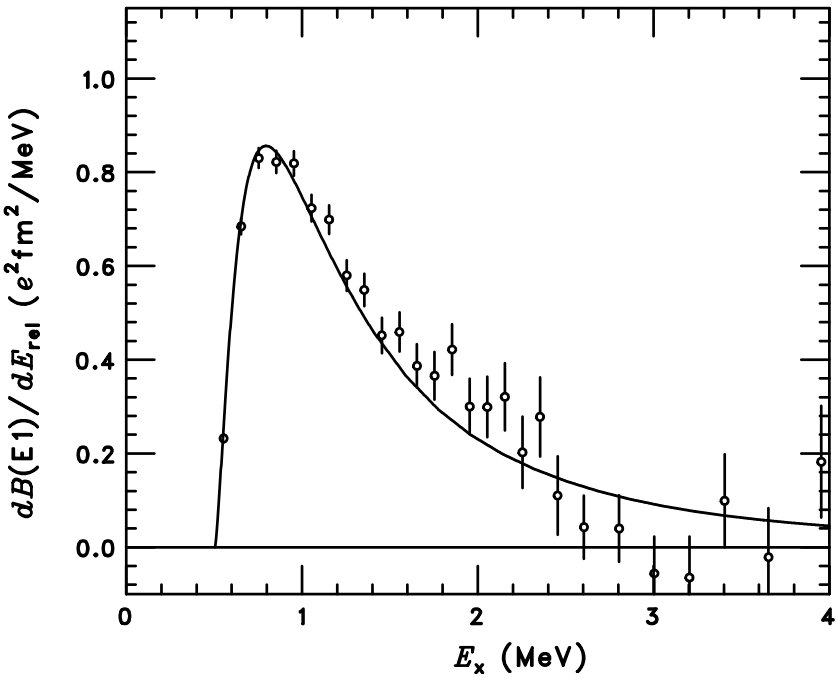

Figure 1.3: $E1$ strength distribution for ^{11}Be taken from Ref. [6] as a function of E_x, obtained from the angle-selected Coulomb breakup data on a Pb target ($\theta < 1.3$ degrees). The solid curve is the result of a calculation assuming direct breakup.

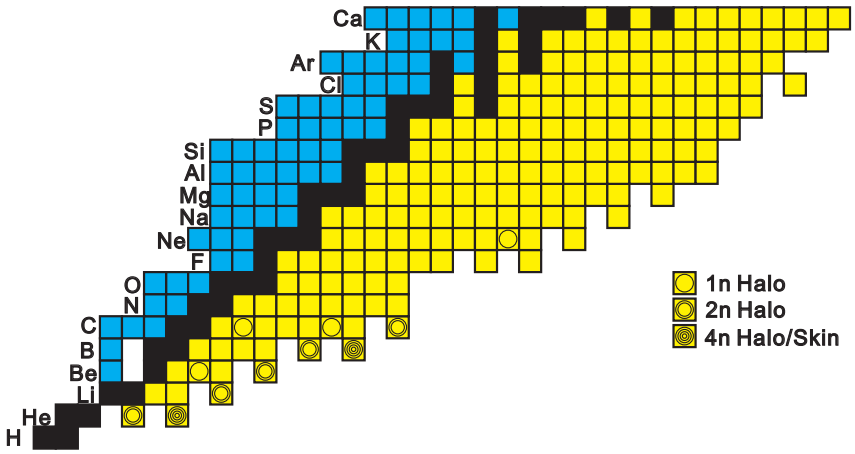

Figure 1.4: Nuclear chart up to $Z = 20$ (Ca) taken from Ref. [6], whose drip-lines are based on the known particle-bound nuclei. The known neutron halo nuclei are indicated. Evidence for halo structures in ^{22}C and ^{31}Ne have recently been obtained experimentally [8, 9].

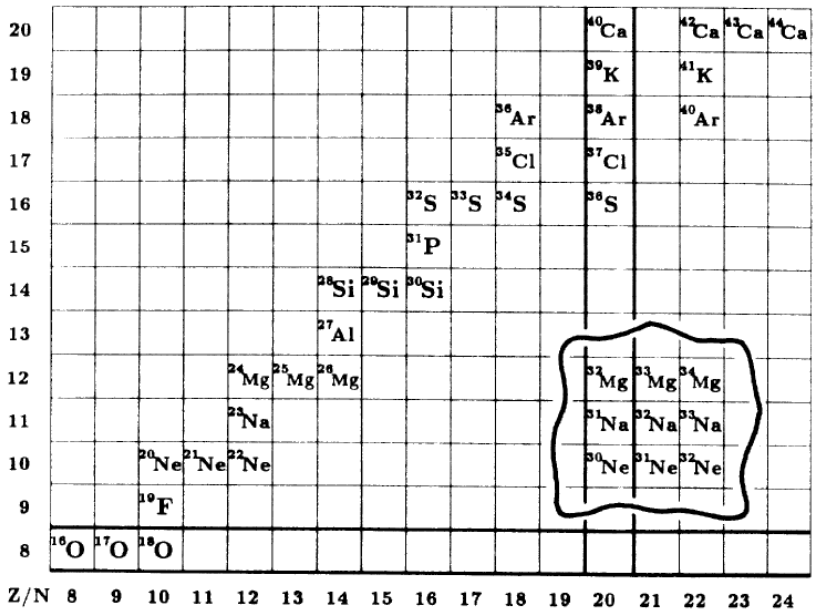

Figure 1.5: Section of the chart of the nuclides highlighting the "island of inversion" centered on ^{32}Na (Figure taken from Ref. [10]). The conventional magic numbers $Z = 8$ and $N = 20$ are emphasized with thick lines. Apart from the "island," only stable nuclei are shown.

Chapter 2

Experimental Considerations

This Chapter describes the experimental methods used in our study: inclusive Coulomb and nuclear breakup. In the past two decades, halo nuclei have been investigated well by the exclusive Coulomb breakup measurement. On the other hand, nuclear breakup reactions are used to study the single particle configurations of valence neutrons. In the following sections, their characteristic feature are described. It should be noted that, in the exclusive measurement, all the fragments, which are emitted after breakup reaction, have to be measured at the same time. On the other hand, inclusive measurement needs to measure only the core fragment. After the general description of Coulomb breakup, Secs. 2.1.2 and 2.1.3 describe the exclusive and inclusive Coulomb breakup measurement, respectively. Section 2.2 describes the features of the nuclear breakup reaction, theory of nuclear breakup reaction, and momentum distribution of a fragment nucleus after nuclear breakup reaction. Additionally, Section 2.3 shows a list of separation energies concerning the subject of this thesis.

2.1 Coulomb Breakup Reaction

2.1.1 General Description

Coulomb breakup reactions have become a powerful spectroscopic tool to explore the structure of halo nuclei far from stability. The halo nuclei have characteristic feature of enhanced low-energy E1 strengths , so-called soft $E1$ excitation, which is investigated by exclusive Coulomb breakup measurements. In the present experiment, based on a signal of the soft $E1$ strength, halo structure is investigated by using inclusive Coulomb breakup measurement. In Sec. 2.1.2 and Sec. 2.1.3, Details about the exclusive and inclusive Coulomb breakup reaction are described, respectively.

2.1.2 Exclusive Coulomb Breakup Method

The soft $E1$ excitation of halo nuclei has been investigated by using the exclusive Coulomb breakup method. When a projectile at speeds of several tens percent of the speed of light passes near a high Z target (e.g., lead target), the projectile is excited from ground state to dipole ($E1$) state by electric field made by the target (Fig. 2.1). The lines of electric force is Lorentz-contracted in the projectile direction, causing the strong electrical filed in the rest frame of the projectile.

The $E1$ excitation by the electrical field is considered to occur by absorption of a virtual photon (Fig. 2.1). Thus, the cross section of the $E1$ excitation is obtained from the product of the number of virtual photon and $E1$ transition probability. This is called equivalent photon

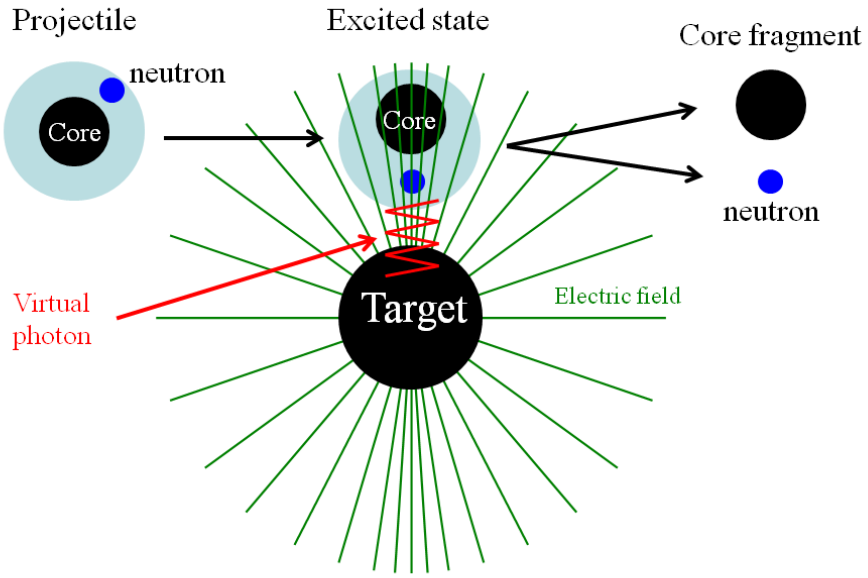

Figure 2.1: Schematic figure of Coulomb breakup reaction is shown. The lines of electric force is Lorentz-contracted in the projectile direction, causing the strong electrical filed in the rest frame of the projectile. The Coulomb excitation is considered to occur by absorption of virtual photon.

method:

$$\frac{d\sigma(E1)}{dE_x} = \frac{16\pi^3}{9\hbar c} N_{E1}(E_x) \frac{dB(E1)}{dE_x}, \tag{2.1}$$

where $d\sigma(E1)/dE_x$ represents the cross section of the $E1$ excitation as a function of excitation energy E_x of the projectile nucleus, N_{E1} represents the virtual photon number as a function of E_x, and $dB(E1)/dE_x$ represents $E1$ transition probability as a function of E_x.

$dB(E1)/dE_x$, called also $E1$ strength distribution, reflects the response to a $E1$ photon with the energy of E_x. Thus, the intrinsic property of nuclear structure of projectile nucleus can be deduced from $dB(E1)/dE_x$. In ordinary nuclei, these has an excitation mode at $E_x \approx 10-20$ MeV called Giant Dipole Resonance (GDR). On the other hand, halo nuclei has strong low-lying $E1$ excited state just above the neutron threshold. This is called soft $E1$ excitation. Figure 1.3 shows a typical $dB(E1)/dE_x$ spectrum for established halo nucleus ^{11}Be. This property has been investigated by Coulomb breakup method. From the results, the $E1$ strength distribution was found to be well-described by direct breakup model:

$$\frac{dB(E1)}{dE_x} = \sum_{n\ell j J^\pi} C^2S(J^\pi, n\ell j) \sum_{\ell_f j_f} |\langle \psi_{\ell_f j_f} | \hat{T}^{(E1)} | \phi_{n\ell j} \rangle|^2, \tag{2.2}$$

where $C^2S(J^\pi, n\ell j)$ denotes the spectroscopic factor for $^{30}\mathrm{Ne}(J^\pi) \otimes \phi_{n\ell j}$, and the $E1$ operator $\hat{T}^{(E1)}$ involves r, the relative distance between the core and valence neutron. The wave function $\psi_{\ell_f j_f}$ represents the neutron scattering state in the exit channel. The core is considered to be a spectator in the reaction. As the matrix element is related to the Fourier transformation of $r\phi(r)$, $B(E1)$ is enhances at low E_x for a halo system [7,13–15]. Furthermore, $dB(E1)/dE_x$ can extract quantitative information of $C^2S(J^\pi, n\ell j)$ and $\phi_{n\ell j}$, which represent intrinsic structural property of halo nucleus.

From an experimental point of view, the Coulomb breakup cross section $\sigma(E1)$ and excitation energy E_x of projectile should be measured to extract the energy differential Coulomb breakup cross section $d\sigma(E1)/dE_x$. The cross section $\sigma(E1)$ is obtained by counting projectiles and fragments produced by Coulomb breakup reaction. The excitation energy E_x is obtained from invariant mass method. In the method, E_x is extracted in the following manner. E_x can be defined by the equation:

$$E_x = M_{\rm inv} - M_{\rm proj}, \tag{2.3}$$

where, $M_{\rm inv}$ represents invariant mass of the excited state of the projectile, and $M_{\rm proj}$ the rest mass of the projectile. The invariant mass $M_{\rm inv}$ is described as Eq. (2.4):

$$M_{\rm inv} = \sqrt{(\sum_i E_i)^2 - (\sum_i \boldsymbol{P}_i)^2} = E_{\rm rel} + \sum_i M_i, \tag{2.4}$$

where E_i, $\boldsymbol{P}_i$, M_i, and $E_{\rm rel}$ represent total energy, momentum, rest mass of the each emitted particle i, and relative energy, respectively. By substituting Eq. (2.4) into Eq. (2.6), the following equation is obtained:

$$E_x = E_{\rm rel} + (\sum_i M_i - M_{\rm proj}) = E_{\rm rel} + S, \tag{2.5}$$

where S represents separation energy. In order to extract E_x with high resolution, the relative energy is experimentally obtained from the momentum vectors $\boldsymbol{P}_i$ of the emitted particles. Is is noted that the relative energy is interpreted as sum of kinetic energies $K_i^{\rm CM}$ of the emitted particles in the center-of-mass system:

$$E_{\rm rel} = \sum_i (E_i^{\rm CM} - M_i) = \sum_i K_i^{\rm CM}. \tag{2.6}$$

In Coulomb breakup reactions of neutron halo nuclei, the valence neutrons are emitted. As it is difficult to achieve high efficiency of neutron detection, a relatively large beam intensity is needed with respect to the inclusive measurement as is described in Sec. 2.1.3.

2.1.3 Inclusive Coulomb Breakup Method

In inclusive Coulomb breakup measurement, the core fragment emitted by the reaction is detected, and the neutron is not detected. Hence, both the energy differential cross section $d\sigma(E1)/dE_x$ and $E1$ strength distribution $dB(E1)/dE_x$ are not obtained. Instead, integrated cross section $\sigma(E1)$ is obtained:

$$\sigma(E1) = \int_{S_{1n}}^{\infty} \frac{16\pi^3}{9\hbar c} N_{E1}(E_x) \frac{dB(E1)}{dE_x} dE_x, \tag{2.7}$$

where, S_{1n} represents one-neutron separation energy, which represents also neutron threshold. Owing to soft $E1$ excitation, halo nuclei have large Coulomb breakup cross sections $\sigma(E1)$. The top panel of Fig. 2.2 shows a schematic view of the $E1$ strength distribution $dB(E1)/dE_x$. For ordinary nuclei, an excitation mode is observed at $E_x \approx 10 - 20$ MeV, which is called Giant Dipole Resonance (GDR). For halo nuclei, the soft $E1$ excitation can be seen at low energy just above the neutron threshold. On the other hand, the bottom Fig. 2.2 shows the E1 virtual photon number $N_{E1}(E_x)$. Hence the number is large at low energy, a product of $N_{E1}(E_x)$ and $dB(E1)/dE_x$ becomes large. By the way, $\sigma(E1)$ is described as an integral of $N_{E1}(E_x) \times dB(E1)/dE_x$ (Eq. 2.7). Thus, $\sigma(E1)$ of halo nucleus becomes large, although $\sigma(E1)$ of ordinary nucleus becomes small. Therefore, the signature of halo structure can be obtained from large inclusive Coulomb breakup cross section $\sigma(E1)$.

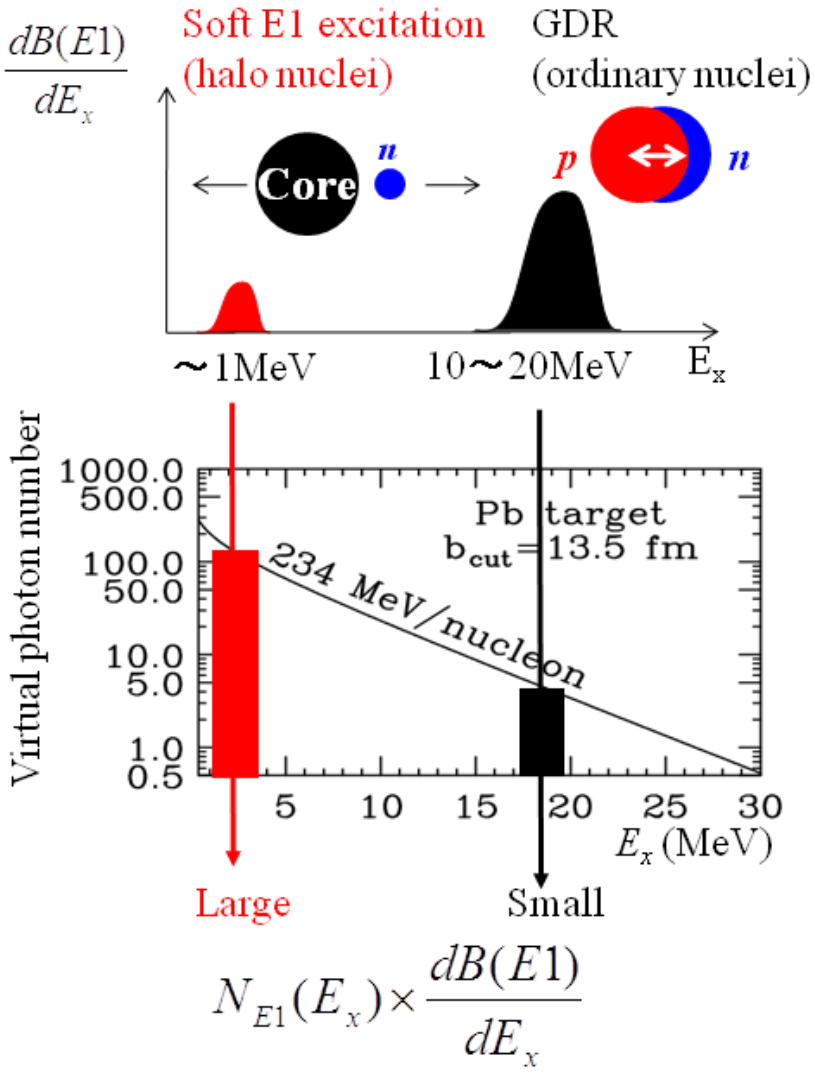

Figure 2.2: Schematic figure of inclusive Coulomb breakup cross section for halo nuclei.

In the present experiment, the one-neutron removal channel is measured (e.g., Pb(^{37}Mg, ^{36}Mg)). Thus, measured quantity is an inclusive Coulomb breakup cross section for one-neutron removal channel, $\sigma_{-1n}(E1)$, which is described as Eq. (2.8):

$$\sigma_{-1n}(E1) = \int_{S_{1n}}^{S_{2n}} \frac{16\pi^3}{9\hbar c} N_{E1}(E_x) \frac{dB(E1)}{dE_x} dE_x, \tag{2.8}$$

where, S_{2n} represents two-neutron separation energy. If the projectile nucleus is excited higher than the two-neutron separation energy S_{2n}, three or more neutron removal channel is open. Hence, $\sigma_{-1n}(E1)$ reflects the enhancement of low-lying soft $E1$ excitation well, while the contribution of Giant Dipole Resonance (GDR) at $E_x \approx 10 - 20$ MeV can be ignored in $\sigma_{-1n}(E1)$.

2.2 Neutron Removal Nuclear Breakup Reactions

2.2.1 General Description

Over the last decade, nucleon removal reactions have become a powerful spectroscopic tool to explore the structure of nuclei far from stability. Figure 2.3 shows a schematic view of one-

neutron removal reaction. On a low-Z target (e.g., carbon target), the valence neutron of the projectile is "knocked" out by nuclear interaction. Then, the core fragment comes out. By counting the numbers of the projectiles and core fragments, the neutron removal cross section is obtained. In addition, a fragment momentum distribution is obtained from measurement of the core fragment momentum $P_{||}^{\rm lab}$. The fragment momentum distributions and associated cross sections offer a means to probe the active single-particle orbitals near the Fermi surface, whereby the shapes of the momentum distributions reflect the orbital angular momentum of the removed nucleon(s) and cross sections the spectroscopic strengths [16–21]. In the present analysis, the measured cross section is compared with the theoretical calculation based on an eikonal model. Details about the eikonal model is described in Sec. 2.2.2. Details about the momentum distribution is described in Sec. 2.2.3.

2.2.2 Reaction Theory

We adopt an eikonal model description of the reaction mechanisms. Given a nucleon- or nucleus-target interaction description, the eikonal approximation has been shown [22, 23] to provide a rather accurate description of the elastic S-matrix and derived observables for incident projectile energies of order 50 MeV/nucleon and greater. As noted earlier, at the energy of the current experiments (around 240 MeV/nucleon) the sudden and eikonal approximations of the reaction model are very accurate.

The removal reaction cross sections for one-neutron knockout to a given final state, with spin-parity J^π, are calculated using [19]

$$\sigma_{-1n} = \sum_{n\ell j} \left[\frac{A}{A-1}\right]^N C^2S(J^\pi, n\ell j)\ \sigma_{\rm sp}(n\ell j, S_n^{\rm eff}), \tag{2.9}$$

where the C^2S are the shell-model spectroscopic factors and the single-particle cross section $\sigma_{\rm sp}$ is calculated using the eikonal model assuming unit spectroscopic factor. The quantum numbers of the removed neutron are denoted by $n\ell j$ and $S_n^{\rm eff}$ is the effective separation energy for the removal of the neutron leaving the residue in the given final state. The single-particle cross sections, $\sigma_{\rm sp}$, include the contributions from both the stripping (inelastic breakup) and diffractive dissociation (elastic breakup) mechanisms. Details of calculations of these two distinct and (incoherent) additive contributions can be found in Ref. [24]. For convenience sake, the one-

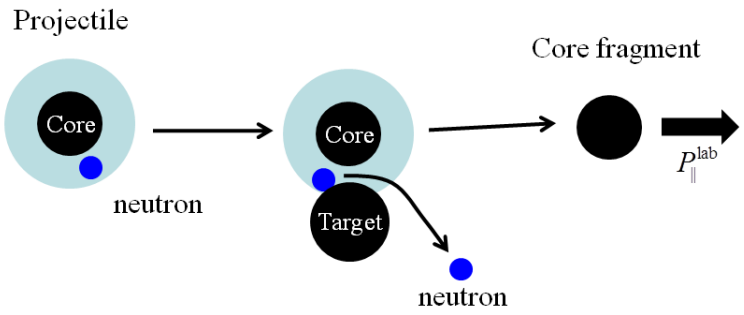

Figure 2.3: Schematic figure of Nuclear breakup reaction is shown. To avoid the Coulomb breakup contribution, low-Z target is used. The momentum of core fragment reflects the angular momentum of the valence neutron orbital, hence the measurement of fragment momentum distribution is a good spectroscopic tool.

neutron knockout cross section on C target is represented as follows:

$$\sigma_{-1n}(\mathrm{C}) = \sum_{n\ell j} \left[\frac{A}{A-1}\right]^N C^2S(J^\pi, n\ell j)\ \sigma_{\mathrm{sp}}(\mathrm{C}, n\ell j, S_n^{\mathrm{eff}}). \tag{2.10}$$

In direct two-neutron removal the theoretical cross sections do not in general (e.g., when there are several active orbitals) factorize into a structural (spectroscopic) factor and a single-particle cross section. The cross sections involve coherent contributions from all active shell-model two-nucleon configurations with non-vanishing two-nucleon amplitudes (TNA). Details of their definitions and the phase conventions used can be found in Ref. [25]. Here we will calculate the single-step direct two-neutron removal yields arising from both (a) two-neutron stripping and (b) one neutron being stripped and the second being elastically dissociated (diffracted) [26]. Since these direct two-neutron removal cross sections are small compared to the cross sections arising from single-neutron removal, we do not expand upon these formal aspects here. Full details of the necessary eikonal formalism, as is applied to direct two-nucleon removal events, can be found in Refs. [25, 26].

For both the one- and two-neutron removal calculations, the required neutron- and residue-target elastic S-matrices were calculated using the static density limit of the eikonal model, e.g., [27], also known as the $t\rho\rho$ limit of the Glauber multiple scattering series. That is, we used the single-folding model (nucleon-target) and double-folding model (residue-target) for the absorptive optical model interactions with the carbon target. The inputs needed were the residue and target point neutron and proton one-body densities and an effective nucleon-nucleon (NN) interaction. The densities of the fragments were estimated from spherical Skyrme Hartree-Fock (HF) calculations using the SkX interaction [28].

All calculations assumed the following. The density of the carbon target nuclei was taken to be of Gaussian form with a point-nucleon root-mean squared radius of 2.32 fm. A zero-range NN effective interaction was used with its strength calculated from the free neutron-neutron and neutron-proton cross sections at the beam energy and from the real-to-imaginary ratios of the NN forward scattering amplitudes at 240 MeV, interpolated (using a polynomial fit) from the values tabulated by Ray [29]. The use of these inputs, as a standard parameter set in the eikonal reaction model, was shown to accurately reproduce the recently-measured [30] ratios of the diffraction to stripping reaction mechanism yields in the cases of ^{8}B and ^{9}C induced proton-removal reactions. A recent careful analysis by Bertulani and De Conti [31] confirms that corrections to this adopted procedure, due to Pauli blocking corrections to the NN effective interaction, are negligible at the energy of the present study.

We assume here that the heavy residue-target interactions and their S-matrices are diagonal with respect to the different final states of the residue, and thus that there is no reaction-induced dynamical excitation of the residues during the collision. For the odd-A carbon projectiles, where different neutron orbitals ($n\ell j$) may then contribute to a given J^π final state, this implies that these different $n\ell j$ contributions are incoherent and should be summed.

2.2.3 Fragment Momentum Distribution

Fragment momentum distributions following the nuclear breakup of nuclei far from stability have long been recognized as probes to investigate the spectroscopic information of valence neutron wave functions [4,5]. On a low-Z target (e.g., carbon target), the valence neutron of the projectile is removed by nuclear interaction (Fig. 2.3). Then, the core fragment comes out. If the valence neutron and core in the projectile have the momenta of $\boldsymbol{P}^{\mathrm{neut}}$ and $\boldsymbol{P}^{\mathrm{core}}$, respectively, the sum of momenta is zero in the projectile rest frame:

$$\boldsymbol{P}^{\mathrm{neut}} + \boldsymbol{P}^{\mathrm{core}} = 0. \tag{2.11}$$

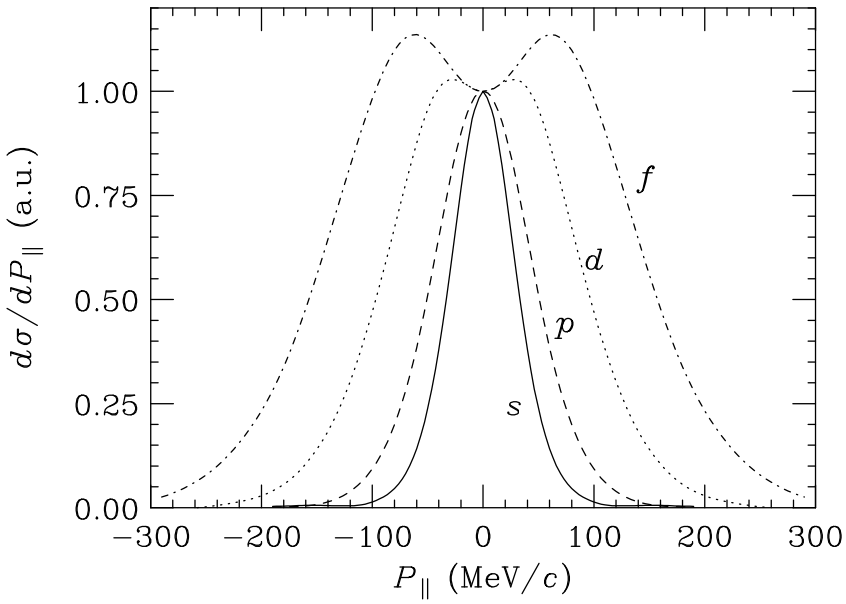

Figure 2.4: Momentum distributions of fragments for one-neutron removal reactions from the s-, p-, d-, and f-wave valence neutron configurations. The solid, dashed, dotted, and dot-dashed lines represent the s-, p-, d-, and f-wave valence neutron configurations, respectively.

If the momentum of core $\boldsymbol{P}^{\rm core}$ is divided into $\boldsymbol{P}^{\rm core}_{\perp}$ in a vertical direction to the beam direction and $\boldsymbol{P}^{\rm core}_{||}$ in a parallel direction to the beam direction, $\boldsymbol{P}^{\rm neut}$ is described as follows:

$$\boldsymbol{P}^{\rm neut} = \boldsymbol{P}^{\rm core}_{\perp} + \boldsymbol{P}^{\rm core}_{||}. \tag{2.12}$$

Both $\boldsymbol{P}^{\rm core}_{||}$ and $\boldsymbol{P}^{\rm neut}$ include spectroscopic information of the valence neutron. Figure 2.4 shows the calculated distributions of magnitude $P_{||}$ of $\boldsymbol{P}^{\rm core}_{||}$ ($|\boldsymbol{P}^{\rm core}_{||}| = P_{||}$) for s-, p-, d-, and f-wave valence neutron configurations. In the present experiment, a parallel momentum ($P^{\rm lab}_{||}$) of the core fragment in the laboratory frame is measured, then the momentum $P_{||}$ in the projectile rest frame is obtained.

2.3 Separation Energy

In this section, the neutron separation energies for the nuclei related to this thesis are shown. Table 2.1 lists the separation energies taken from Refs. [32–34]. Figure 2.5 shows the systematics of the separation energies. It is noted that, in general, small separation energy less than about 1 MeV is needed to form halo structure.

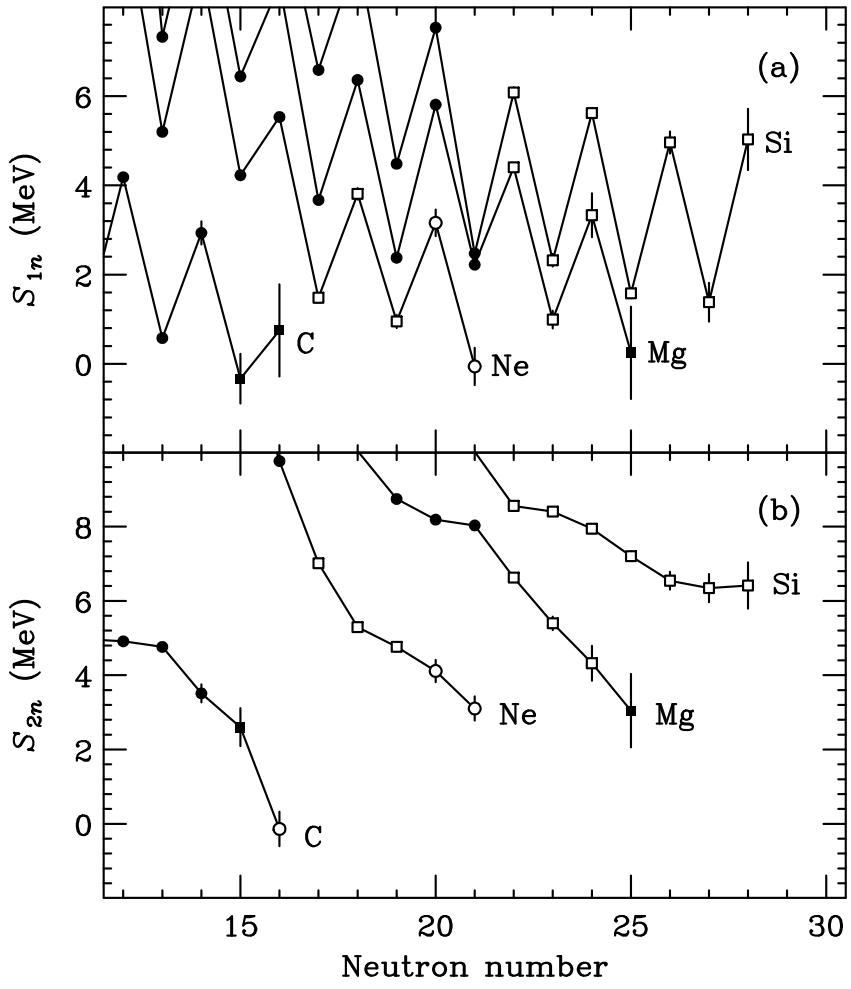

Figure 2.5: (a) One-neutron separation energy (S_{1n}) and (b) Two-neutron separation energy (S_{2n}) as a function of neutron number for C, Ne, Mg, and Si isotopes. Closed circles were extracted from measured masses and closed squares were extracted from the masses estimated on the basis of extrapolation [32]. Open circles and squares are obtained from the Ref. [33] and [34].

Table 2.1: One-neutron separation energy (S_{1n}) and two-neutron separation energy (S_{2n}) extracted from Refs. [32–34] are listed. The characters of '#' represent the estimated values on the basis of extrapolation [32].

	S_{1n} (MeV)			S_{2n} (MeV)		
Nucleus	Ref. [32]	Ref. [33]	Ref. [34]	Ref. [32]	Ref. [33]	Ref. [34]
^{19}C	0.58(9)			4.76(10)		
^{20}C	2.93(26)			3.51(24)		
^{22}C	0.75(1.03)#			0.42(94)#		-0.14(47)
^{29}Ne	1.26(31)	0.95(15)		4.29(59)	4.76(12)	
^{31}Ne	0.33(1.07)#	0.29(1.64)	-0.06(42)	3.36(94)#	3.72(1.62)	3.10(33)
^{33}Mg	2.22(3)			8.03(2)		
^{35}Mg	0.73(46)#	0.99(20)		4.89(40)#	5.40(18)	
^{37}Mg	0.25(1.03)#			3.05(99)#		
^{39}Si	2.08(36)	1.58(11)		7.63(38)	7.20(13)	
^{41}Si	-0.02(1.93)	1.38(44)		6.61(57)	6.34(38)	

Chapter 3

Experiment

This chapter describes the experiment: the measured reaction channels, primary- and secondary-beam properties, production and reaction targets, and detector setups. In this thesis, the results of two experiments are analyzed. Section 3.1 describes the two experiments. Since many reaction channels are measured, the channels are listed first in Sec 3.2. Section 3.3 describe the production and reaction targets. The production target was used to produce the secondary radioactive beams, e.g., ^{22}C, ^{31}Ne, and ^{37}Mg beams, from the primary beam. The reaction targets of Pb and C were used to measure the Coulomb and nuclear breakup reactions. Section 3.4 describes the primary and secondary beam properties. Section 3.5 describes the devices used in this experiments. At the end, Section 3.6 shows the trigger logic.

3.1 General Description

We performed two experiments at the RI Beam factory (RIBF) [35] operated by the RIKEN Nishina Center and the Center for Nuclear Study, University of Tokyo. One is the experiment of Coulomb and nuclear breakup for ^{19,20,22}C and ^{31}Ne in Nov. 2008, which is called "Day One" experiment. The other is the experiment of Coulomb and nuclear breakup for ^{29}Ne, ^{33,35,37}Mg, and ^{39,41}Si in Dec. 2010, which is called "Day Three" experiment. Basically, setup of the latter experiment is the same as that of the former experiment. The layout of RIBF is shown in Fig. 3.1. The primary beam of ^{48}Ca was delivered by Superconducting Ring Cyclotron (SRC), entering the RI beam Projectile fragment Separator (BigRIPS) [36–38]. The secondary beam was produced and identified event-by-event by BigRIPS, entering a reaction target. After reaction, fragments were identified by Zero Degree Spectrometer (ZDS). The detectors and setups are detailed in the following sections.

3.2 Measured Reaction Channels

We measured the inclusive one-neutron removal reactions from ^{19,20,22}C, ^{29,31}Ne, ^{37,35,33}Mg, ^{41,39}Si on carbon and lead targets, which are listed in Table 3.1. The mid-target energy are also shown in Table 3.1. In the inclusive measurement, only the core fragment and gamma-ray(s) were identified. Namely, neither the neutrons nor target nuclei emitted by reaction were measured. We should note that since the analysis of Coulomb breakup reaction for ^{19,20,22}C is in progress, the discussion for the results is out of the scope of this thesis.

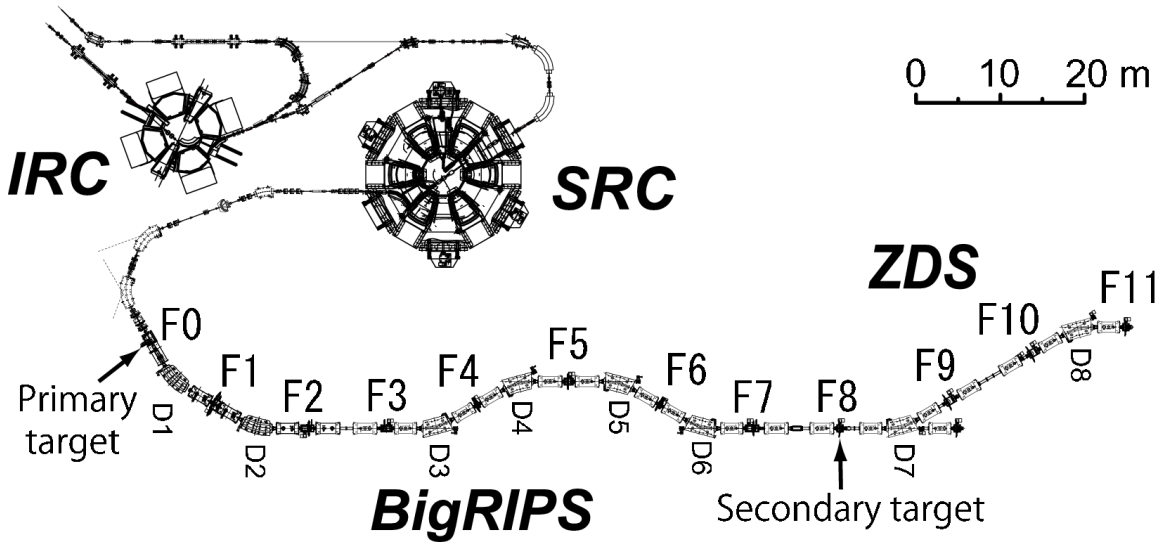

Figure 3.1: The layout of BigRIPS (F0-F8) and zero degree spectrometer, ZDS (F8-F11), where F1 through F11 represent each focal plane. The reaction target was mounted at the achromatic focal plane F8. The fragments were identified using the ZDS.

Reaction	Experiment	Mid-target energy
^{19}C + Pb → ^{18}C + X	Day One	242 MeV/nucleon
^{19}C + C → ^{18}C + X	Day One	242 MeV/nucleon
^{20}C + Pb → ^{18}C + X	Day One	241 MeV/nucleon
^{20}C + C → ^{18}C + X	Day One	240 MeV/nucleon
^{20}C + Pb → ^{19}C + X	Day One	241 MeV/nucleon
^{20}C + C → ^{19}C + X	Day One	240 MeV/nucleon
^{22}C + Pb → ^{20}C + X	Day One	240 MeV/nucleon
^{22}C + C → ^{20}C + X	Day One	239 MeV/nucleon
^{29}Ne + Pb → ^{28}Ne + X	Day Three	244 MeV/nucleon
^{29}Ne + C → ^{28}Ne + X	Day Three	240 MeV/nucleon
^{31}Ne + Pb → ^{30}Ne + X	Day One	234 MeV/nucleon
^{31}Ne + C → ^{30}Ne + X	Day One	230 MeV/nucleon
^{33}Mg + Pb → ^{32}Mg + X	Day Three	234 MeV/nucleon
^{33}Mg + C → ^{32}Mg + X	Day Three	229 MeV/nucleon
^{35}Mg + Pb → ^{34}Mg + X	Day Three	245 MeV/nucleon
^{35}Mg + C → ^{34}Mg + X	Day Three	241 MeV/nucleon
^{37}Mg + Pb → ^{36}Mg + X	Day Three	244 MeV/nucleon
^{37}Mg + C → ^{36}Mg + X	Day Three	240 MeV/nucleon
^{39}Si + Pb → ^{38}Si + X	Day Three	224 MeV/nucleon
^{39}Si + C → ^{38}Si + X	Day Three	218 MeV/nucleon
^{41}Si + Pb → ^{40}Si + X	Day Three	229 MeV/nucleon
^{41}Si + C → ^{40}Si + X	Day Three	224 MeV/nucleon

Table 3.1: The measured reaction channels and the mean mid-target energies are shown. The character of X represents the undetected reactions products. We should note that the analysis of Coulomb breakup reaction for ^{19,20,22}C is in progress, thus the results are not presented here.

Secondary beam	Production target of Be	Reaction target of Pb	Reaction target of C
^{19,20,22}C	3.62 g/cm^2	6.74 g/cm^2	4.02 g/cm^2
^{29,31}Ne, ^{33,35,37}Mg, ^{39,41}Si	2.76 g/cm^2	3.37 g/cm^2	2.54 g/cm^2

Table 3.2: Thickness of each target. Considering the resolution of the fragment momentum distribution and the reaction rate, the target thickness was optimized.

	Production target	Reaction targets
Position	F0	F8
Material	Be	Pb, C, empty
Type	Rotating target	Fixed target
Shape	Fig. 3.3	Circle (radius: 15 mm)

Table 3.3: Property of the production target and reaction targets. The schematic picture of the production target is shown in Fig. 3.3. To measure the background, we located only the target holder without the target, which is represented as "empty" in the table.

3.3 Production and reaction targets

Property about a production target and reaction targets is listed in Table 3.3. The thickness of each target is listed in Table 3.3. To prevent melting the production target, the target was rotated and cooled by water as shown in Fig 3.2.

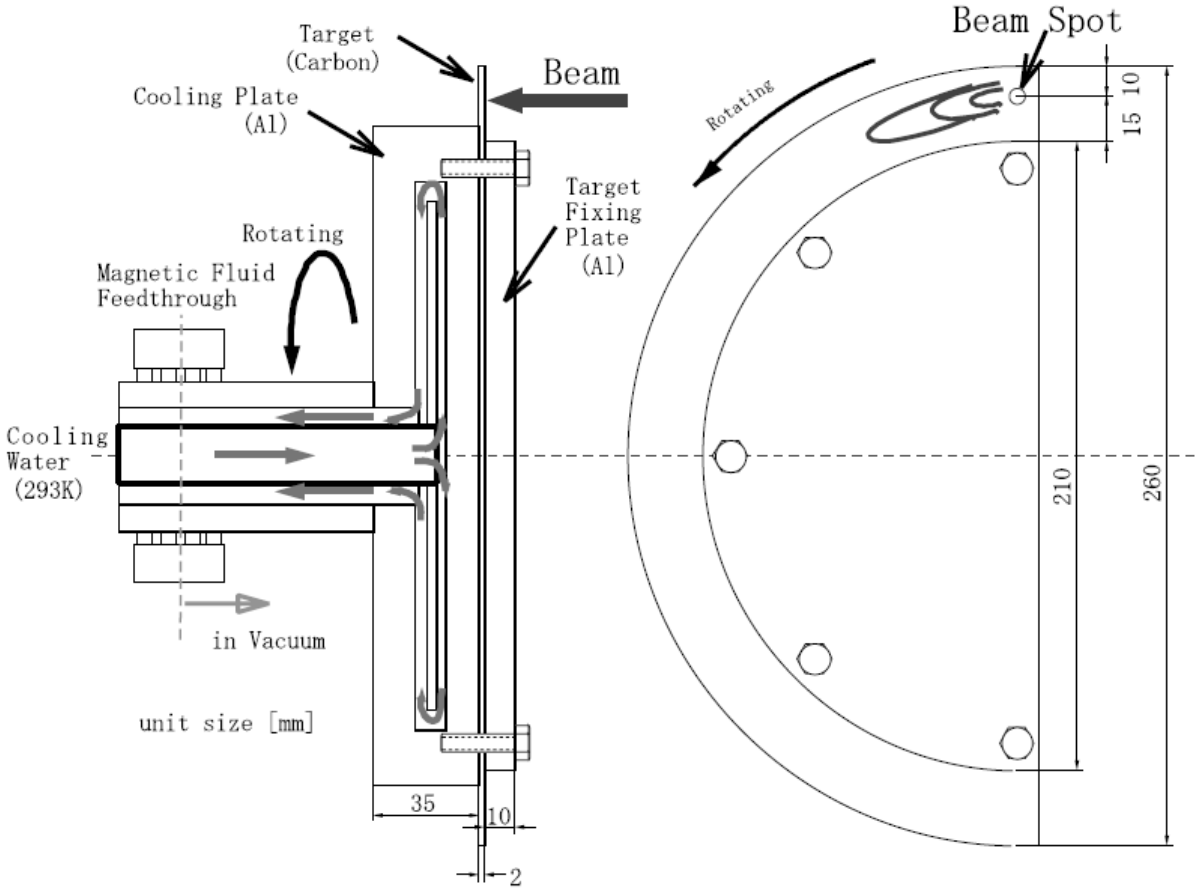

Figure 3.2: A schematic picture of the production target. To prevent melting the production target, the target was rotated and cooled by water during the experiment.

3.4 Property of beams

	Nuclide	Energy	Typical Intensity
Day One	^{48}Ca	345 MeV/nucleon	≈60 pnA
Day Three	^{48}Ca	345 MeV/nucleon	≈120 pnA

Table 3.4: Profile of the primary beam.

3.4.1 Primary beam

The ^{48}Ca primary beam at 345 MeV/nucleon was delivered from Superconducting Ring Cyclotron (SRC). The typical beam intensity was about 60 pnA for the Day One experiment and 120 pnA for the Day Three experiment, which are shown in Table 3.4.

3.4.2 Secondary beams

Secondary beams of ^{19,20,22}C, ^{29,31}Ne, ^{33,35,37}Mg, and ^{39,41}Si were produced by fragmentation of a ^{48}Ca beam at 345 MeV/nucleon on a 20-mm-thick rotating Be target. The secondary beams were separated using the superconducting separator BigRIPS [36–38] whose layout is shown in Fig. 3.1. The secondary beam particles were identified event-by-event by combining the measured time-of-flight (TOF), energy loss (ΔE), and magnetic rigidity ($B\rho$). The TOF was recorded between two plastic scintillators at the achromatic focal planes F3 and F7, ΔE was measured using a plastic scintillator at F7, and $B\rho$ was determined from a position measurement using a plastic scintillator read out on both sides by photomultiplier tubes at F5. The secondary beam intensities (I_2) and momentum spread ($\Delta P/P$) of the beams are listed in Table 3.5.

Table 3.5: The typical ^{48}Ca primary beam intensity (I_1) for each setting and typical secondary beam intensity (I_2). Also tabulated are the momentum spread ($\Delta P/P$) of the secondary beams.

Secondary beam	I_1 (pnA)	I_2 (particles/s)	$\Delta P/P$
^{19}C	≈4	$\approx 1 \times 10^3$	±2%
^{20}C	≈6	$\approx 6 \times 10^2$	±3%
^{22}C	≈80	≈6	±3%
^{29}Ne	≈50	$\approx 1 \times 10^2$	±0.5%
^{31}Ne	≈60	≈5	±3%
^{33}Mg	≈60	$\approx 6 \times 10^2$	±0.1%
^{35}Mg	≈40	$\approx 2 \times 10^2$	±3%
^{37}Mg	≈120	≈6	±3%
^{39}Si	≈100	$\approx 4 \times 10^2$	±0.1%
^{41}Si	≈130	$\approx 3 \times 10^2$	$-2\% \leq \Delta P/P \leq 3\%$

3.5 Detector setup

3.5.1 Big RIKEN Projectile fragment Separator (BigRIPS)

BigRIPS (Fig. 3.1) is the device to separate and identify the projectile fragment, producing radioactive isotope beams. The beam line has 9 focal planes (F0–F8), 6 dipole magnets (D1–D6), and 16 superconducting triplet quadrupole magnets (STQ1–STQ16). An aluminum degrader can be mounted at the dispersive focal plane F1, which is used to obtain a secondary beam with good purity. Thanks to the dipole magnets and degrader, projectile fragments were separated, and secondary beams were produced.

The secondary beam particles were identified event-by-event by combining the measured time-of-flight (TOF), energy loss (ΔE), and magnetic rigidity ($B\rho$). To measure each value, various detectors were installed at some focal planes. Detailed property of each detector is described in fallowing sections.

3.5.2 Zero Degree Spectrometer (ZDS)

ZDS (Fig. 3.1) is the device to identify the fragments following reactions and measure the each momentum of the fragments. The beam line has 4 focal planes (F8–F11), 2 dipole magnets (D7 and D8), and 6 superconducting triplet quadrupole magnets (STQ17–STQ22). The fragments were collected by tuning the rigidity of ZDS to center the momentum distribution. The fragments as well as the secondary beam particles were identified event-by-event by combining TOF, ΔE, and $B\rho$.

3.5.3 Plastic scintillators

The plastic scintillators were used to measure the time of flight of the secondary beam particles and the fragments following the reactions. Additionally, the energy loss ΔE in the scintillator was measured redundantly. The property about the scintillators is listed in Table 3.6. The light emitted from the scintillator was directly read out on both sides by photomultiplier tubes (PMT). The scintillators were connected by optical grease to PMTs. The chambers enclosing the scintillators at focal planes prevented the entrance of outside light. Therefore, the scintillators were mounted without light shielding. It should be note that no scintillator was installed near the F8 target position in order to reduce any backgrounds arising from reactions on materials other than the target except for the setting of ^{31}Ne. The significant background contribution of the F8 plastic scintillator was found from the runs of ^{31}Ne.

Focal Plane	Optics	Thickness	Active area (height × width)
F3	achromatic	3 mm (Day One)	90 mm × 100 mm
		1 mm (Day Three)	90 mm × 100 mm
F5	dispersive	1 mm	100 mm × 240 mm
F7	achromatic	3 mm (Day One)	100 mm × 240 mm
		1 mm (Day Three)	100 mm × 240 mm
F8	achromatic	1 mm	90 mm × 100 mm
F11	achromatic	1 mm	90 mm × 100 mm

Table 3.6: Property of plastic scintillators. The scintillators were mounted without light shielding. The F8 scintillator was used only for the setting of ^{31}Ne.

3.5.4 Ionization chambers

Ionization chambers [39,40] (Fig. 3.3) were used to measure the energy loss ΔE of projectiles at F7 and fragments at F11. Each ionization chamber consists of the housing, inner gas, and a set of electrodes. The electrodes consist of 12 anodes sandwiched between 13 cathodes. The effective areas of electrodes are 232 mmϕ for the ionization chamber at F7 and 260×170 mm^2 for that at F11. The Path lengths for the ionization chambers at F7 and F11 are 586 mm and 600 mm, respectively. The ionization chambers were filled with the P10 gas (Ar(90 %)+CH_4(10%)).

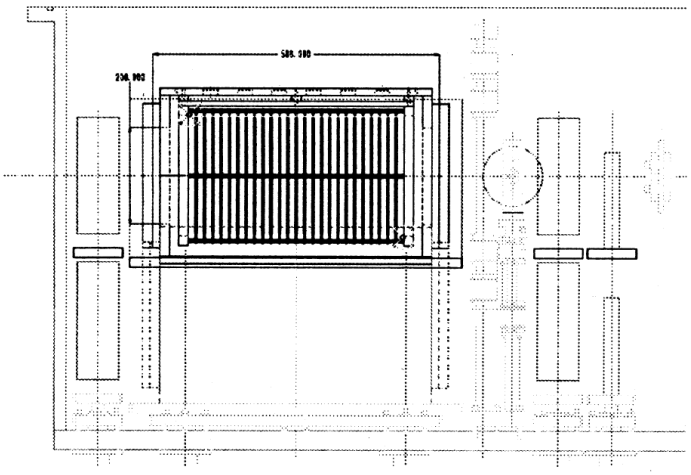

Figure 3.3: Side view of the ionization chamber at the F7 focal plane on the BigRIPS beam line.

3.5.5 Gamma-ray detector array (DALI2)

DALI2 was placed around reaction target at F8 to measure the gamma-rays emitted from the fragments following the reactions. The figure of DALI2 of the Day Three experiment shown in Fig. 3.5.5. The Day One setup is similar with the Day Three setup. The DALI2 had 12 layers and 186 NaI(Tl) crystals. Each crystal was read out on one side by a PMT. We used three kinds of modules, which were named "red module", "white module" and "old module". Here, "module" means a housed crystal attached with PMT. To reduce the atomic background, 1 mm thick lead shield covered the target chamber. Property of each module is listed in Table 3.5.5.

Name	Crystal size	Number of crystals
Red module	$80 \times 40 \times 160$ mm^3	66
White module	$80 \times 45 \times 160$ mm^3	88
Old module	$61 \times 61 \times 122$ mm^3	32

Table 3.7: Property of modules of DALI2. Here, "module" means a housed crystal attached with PMT. There were three kinds of modules, which were named "white module", "red module" and "old module".

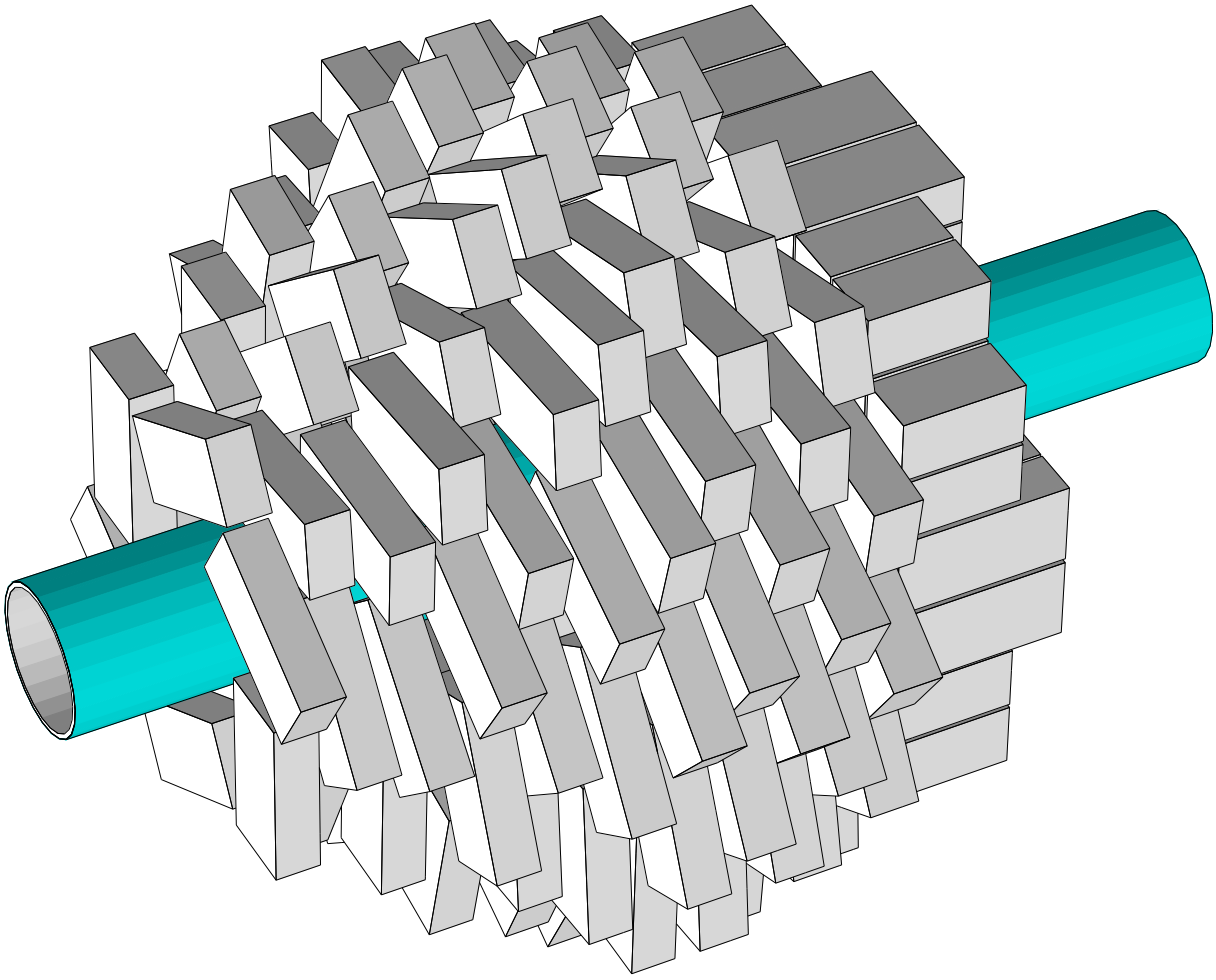

Figure 3.4: Figure of DALI2. DALI2 had 12 layers and 186 NaI(Tl) crystals. There were three kinds of crystals, which were named “white module”, “red module” and “old module”.

3.5.6 Parallel plate avalanche counters (PPAC)

The PPACs located at some focal planes measured position and angle of beams. A PPAC has an anode sandwiched between two cathodes measuring X and Y positions as shown in Fig. 3.5. The cathode layer has 2.40-mm-width strips with 0.15-mm gaps. These strips are connected by a delay-line, whose timing signals are read out on both sides. The difference between the timing signals is proportional to the hit position. Therefore, a PPAC outputs X and Y position information. The position resolution is about 1 mm. In the present experiment, we installed "Double PPAC", which had two PPACs in one housing. Two Double PPACs were installed at the each focal plane. The property of the PPACs are listed in Table 3.8.

Focal plane	Optics	Position	Active are (height × width)
F3	achromatic	Upstream	150 mm × 150 mm
		Downstream	150 mm × 240 mm
F5	dispersive	Upstream	150 mm × 240 mm
		Downstream	150 mm × 240 mm
F7	achromatic	Upstream	150 mm × 240 mm
		Downstream	150 mm × 150 mm
F8	achromatic	Upstream	150 mm × 240 mm
		Downstream	150 mm × 150 mm
F9	dispersive	Upstream	150 mm × 240 mm
		Downstream	150 mm × 240 mm
F10	dispersive	Upstream	150 mm × 240 mm
		Downstream	150 mm × 240 mm
F11	achromatic	Upstream	150 mm × 240 mm
		Downstream	150 mm × 240 mm

Table 3.8: Information about PPACs. The size of a PPAC was selected according to the optics of the focal plane.

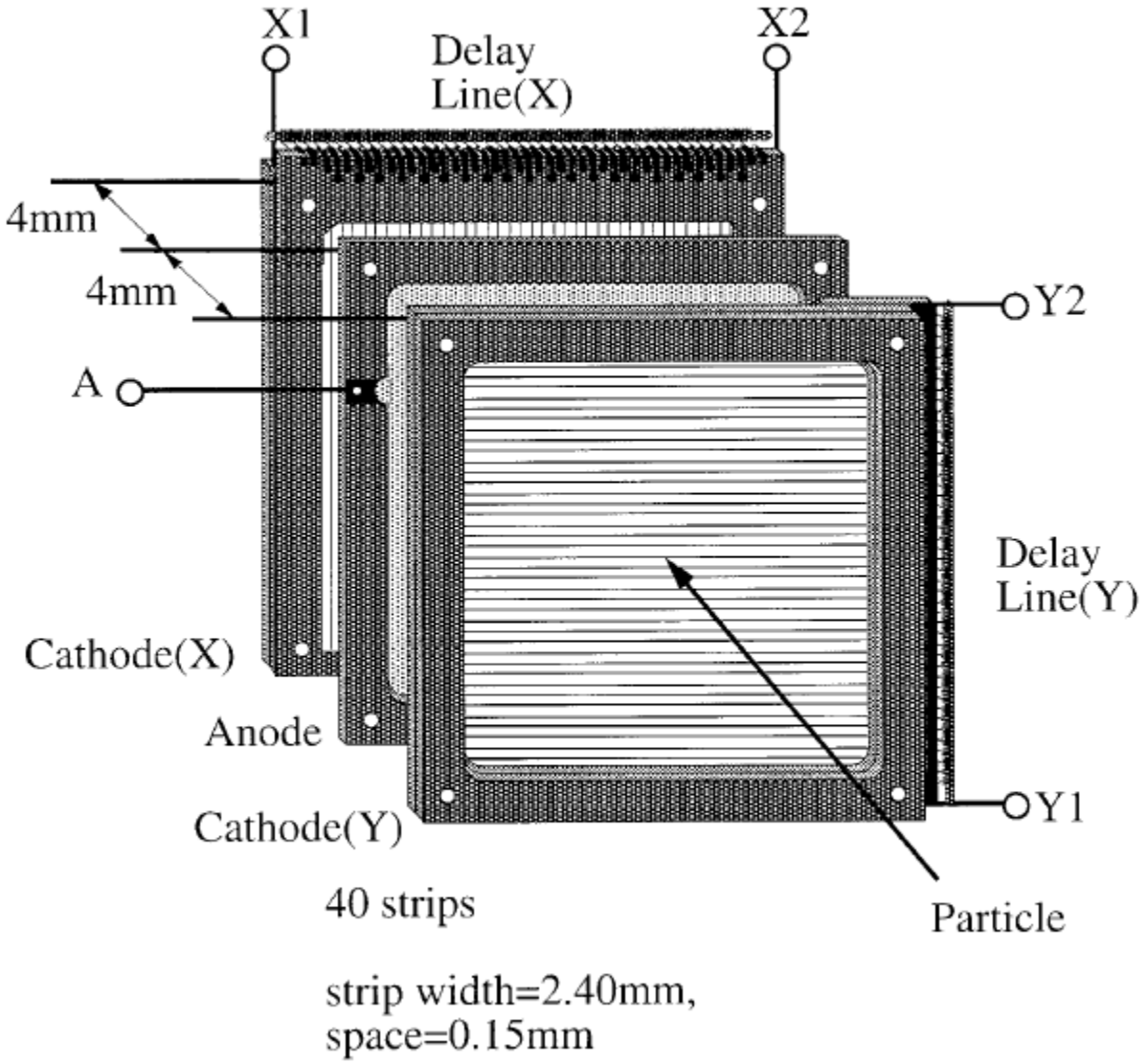

Figure 3.5: Structure of the PPAC. The PPACs located at some focal planes measured position and angle of beams. A PPAC has an anode sandwiched between two cathodes. The cathode layer has 2.40-mm-width strips with 0.15-mm gaps.

3.6 Trigger

In the present experiment, a beam trigger, most simple trigger, was used except for ^{19,20}C setting. For ^{19,20}C setting, the beam intensity was high, thus the master trigger is OR of ZDS trigger and down scale beam trigger. The beam trigger was defined as the coincidence of F3 and F7 plastic hits for ^{19,20}C, ^{29}Ne, ^{33,35,37}Mg, and ^{39,41}Si setting. For ^{22}C and ^{31}Ne setting, the beam trigger was defined as the coincidence of F3 and F5 plastic hits. The schematic view of the trigger logic are shown in Fig. 3.6.

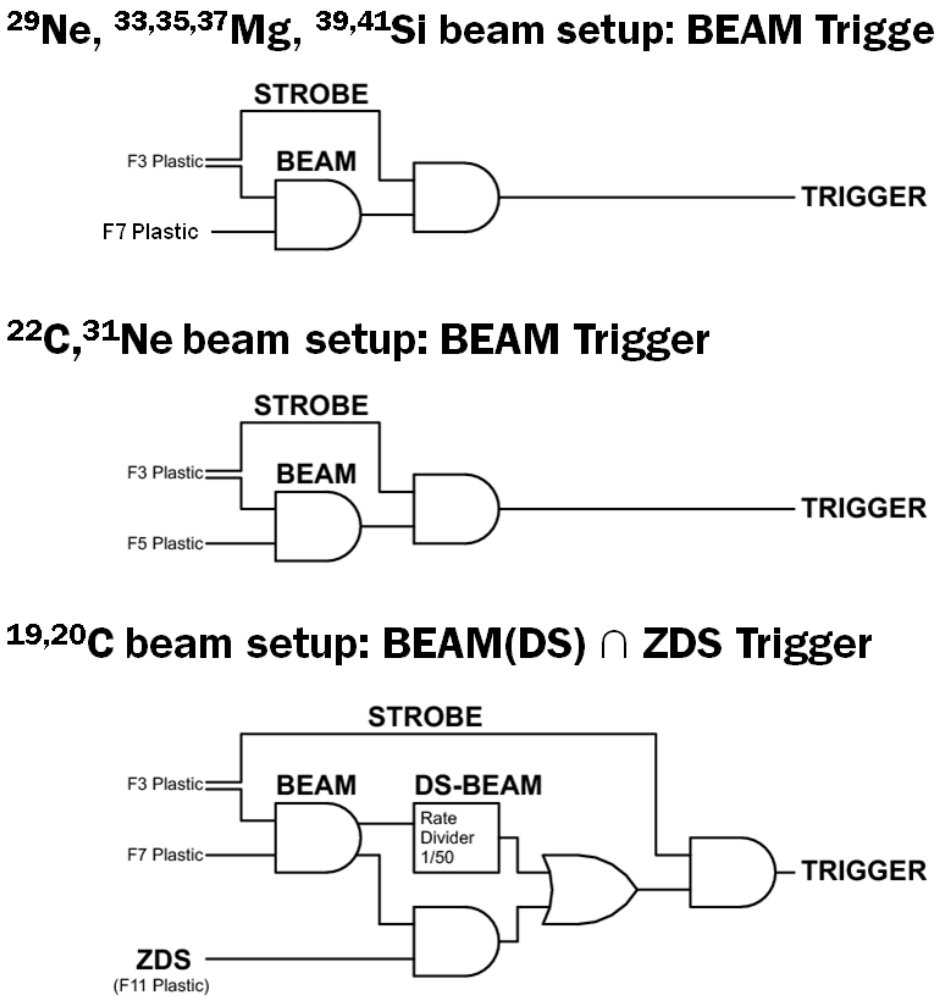

Figure 3.6: Trigger logic. F3, F5, and F7 mean the hit signals from F3, F5, and F7 plastics, respectively. The hit means that the sum of two PMT's signals on both sides of the plastic exceeds a threshold.

Chapter 4

Data Analysis

This chapter describes the particle identification, transmission estimation of ZDS, extraction of one- and two-neutron removal cross sections, γ-ray analysis, and momentum distribution of the fragment. The one- and two neutron removal cross sections are derived from counting the projectiles and fragments as shown in Sec. 4.3. Science all the fragments were not accepted in ZDS with the restricted acceptance, the number of fragments have to be corrected by transmission estimation of ZDS. Section 4.2 shows the transmutation efficiency. Section 4.6 describes the analysis of γ-rays emitted from the fragments of Coulomb and nuclear breakup reaction. The section involves the results of cross sections in coincidence with γ-rays. Section 4.5 describes the analysis of the momentum distributions of the fragment. Each width of the distributions is also shown. At the end, the shell model levels for the nuclei concerning this thesis are shown in Sec. 4.7.

4.1 Particle identification

Figure 4.1 shows the particle identification spectrum for ^{37}Mg projectiles as a function of Z vs. A/Z. The Z value was reconstructed from energy loss (ΔE) in the ionization chamber and velocity calculated from time-of-flight (TOF) . The A/Z value was reconstructed from TOF between F3 and F7 plastics and magnetic rigidity ($B\rho$) at F5. As well as the projectile, the fragment was identified at ZDS by the ΔE, TOF, and $B\rho$ information.

In practical analysis, the Z value for each particle was obtained from Eq. (4.1) based on Bethe-Bloch formula.

$$\Delta E = aZ^2 F(\beta_{\mathrm{F7}}) + b, \tag{4.1}$$

$$F(\beta_{\mathrm{F7}}) = \frac{1}{\beta_{\mathrm{F7}}^2} \ln\left(\frac{2m_e c^2 \beta_{\mathrm{F7}}^2}{I(1-\beta_{\mathrm{F7}}^2)} - \beta_{\mathrm{F7}}^2\right). \tag{4.2}$$

Here,

ΔE	:	energy loss in the ionization chamber at F7,
m_e	:	electron mass,
I	:	ionization potential,
c	:	the speed of light,
β_{F7}	:	the velocity of the projectile over the speed of light (v/c) at F7.

Furthermore, a and b were decided so as to obtain the proper Z value. The β_{F7} was obtained from the time-of-flight (TOF) between F3 and F7.

The A/Z value was obtained from

$$B\rho = \frac{A}{Z}\frac{m_{\mathrm{amu}} c \gamma_{\mathrm{F5}} \beta_{\mathrm{F5}}}{e}. \tag{4.3}$$

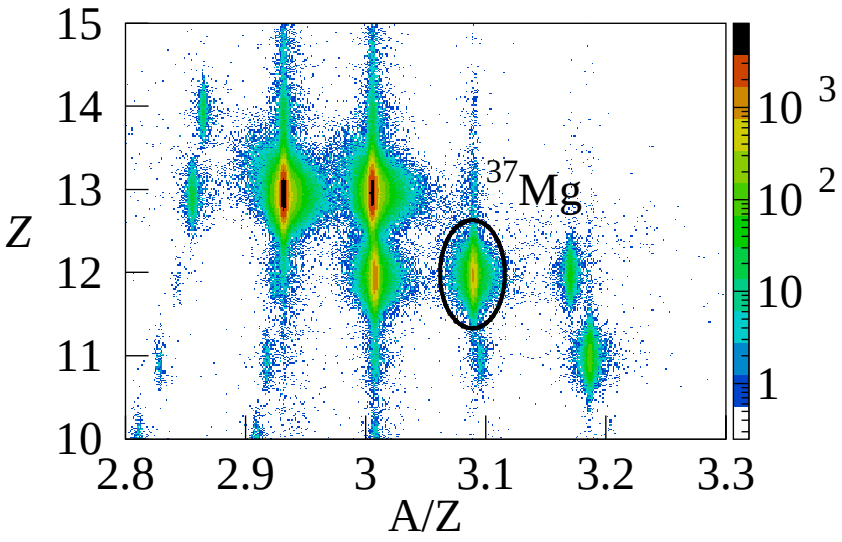

Figure 4.1: Particle identification spectrum for ^{37}Mg projectiles as a function of A/Z vs. Z. The Z value was reconstructed from energy loss (ΔE) in the ionization chamber. The A/Z value was reconstructed from time-of-flight (TOF) between F3 and F7 plastics and magnetic rigidity ($B\rho$) at F5.

Here,

$B\rho$	:	the magnetic rigidity of the projectile,
c	:	the speed of light,
β_{F5}	:	the velocity of the projectile over the speed of light (v/c) at F5,
γ_{F5}	:	$1/\sqrt{1-\beta_{\mathrm{F5}}^2}$,
m_{amu}	:	the atomic mass unit,
e	:	the elementary charge.

The $B\rho$ value was extracted from the horizontal position x_{F5} at the dispersive focal plane F5:

$$x_{F5} = (x|\delta)\delta, \tag{4.4}$$

$$\delta = \frac{B\rho}{B\rho_0}. \tag{4.5}$$

Here, $B\rho_0$ was the magnetic rigidity of the projectile along the center of the beam line. The $(x|\delta)$ value was 33 mm/%, which is the element of the first order transfer matrix.

In the same manner, the particle identification spectrum at ZDS is shown in Fig. 4.1.

4.2 Analysis of the transmission of ZDS

The transmission of ZDS was estimated using a Monte Carlo simulation. In the following, the simulation of Day Three experiment is described as an example. The inputs to the simulation were angular and momentum acceptances of ZDS. The angular acceptance of the ZDS was obtained by calibration runs, where the incident angle to target was broadened by tuning the STQ before the target.

The angular acceptances in x axis and y axis were obtained shown in Fig. 4.3 (x-angle broadened run) and Fig. 4.4 (y-angle broadened run), respectively. The right panel of Fig. 4.3

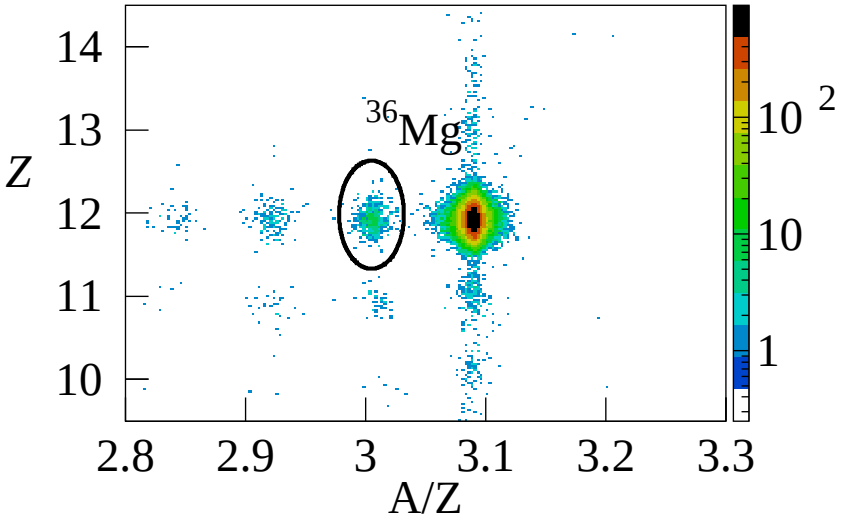

Figure 4.2: Particle identification spectrum for ^{36}Mg projectiles as a function of A/Z vs. Z The Z value was reconstructed from energy loss (ΔE) in the ionization chamber and velocity calculated from time-of-flight (TOF). The A/Z value was reconstructed from TOF between F7 and F11 plastics and magnetic rigidity ($B\rho$) at F9.

shows the x-axis angular acceptance. From the fitting result, the angular acceptance is found to be -40 $\leq \theta_x \leq$ +52. The fitting function $f(x)$ is as follows:

$$f(x) = C\int_{-\infty}^{-\infty} \mathrm{rect}(t)\mathrm{gauss}(x-t)dt \tag{4.6}$$

$$\mathrm{rect}(t) = \begin{cases} 1 & \text{if} \quad \Gamma_{\mathrm{FWHM}}/2 \leq t \leq \Gamma_{\mathrm{FWHM}}/2, \\ 0 & \text{otherwise}, \end{cases} \tag{4.7}$$

$$\mathrm{gauss}(x) = \frac{1}{\sqrt{2\pi}\sigma}\exp\left(-\frac{x^2}{2\sigma^2}\right), \tag{4.8}$$

where,

$f(x)$	:	folded rectangle function,
rect(x)	:	rectangular function,
gauss(x)	:	Gaussian function.

It is noted that the x-axis angular distribution is not centered, hence the function rect(x) is shifted by +6 mrad. In the same manner, the y-axis the angular acceptance is found to be -30 $\leq \theta_y \leq$ +30.

The upper and lower limits of momentum acceptance were obtained shown in Fig. 4.5 and Fig. 4.6, respectively. The left panel of Fig. 4.5 shows the momentum distributions of beam without (black points) and with (red points) the ZDS accepted gate. It is noted that the high momentum beam is larger than the acceptance of ZDS. On the other hand, the right panel shows the ratio of the two distributions. From the fitting result by the function $f(x)$ above, the upper limit of momentum acceptance is found to be $P_{||} \leq +4.8$ %.

The left panel of Fig. 4.6 shows the momentum distributions of fragment without (black points) and with (red points) the ZDS accepted gate. From the fitting result of the right panel by the function $f(x)$ above, the lower limit of momentum acceptance is found to be $P_{||} \geq$ -4.3 %.

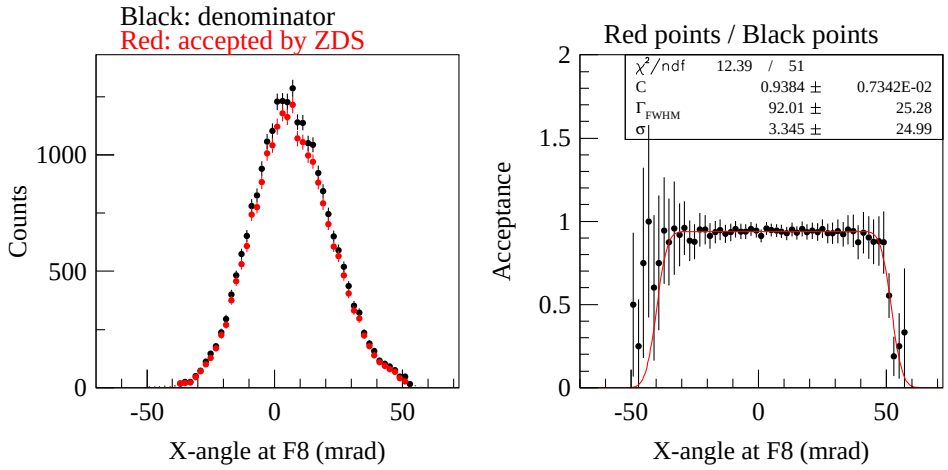

Figure 4.3: Left: x-axis angular distributions without (black point) and with (red point) the ZDS accepted gate. Right: ratio of the two distribution of left panel.

By inputting these data to simulation code, the transmission of ZDS for each reaction channel was calculated. The results are shown in Table. 4.1. These are used in the correction of the reaction cross sections.

4.3 Extraction of Inclusive Cross Section

The present study measured one- and two-neutron removal cross sections ($\sigma^{\rm exp}_{-xn}$, $x = 1$ or 2). The cross sections were derived from the numbers of the beam particles counted before the secondary target and those of the residues registered at the final focal plane F11 of the ZDS, using

$$\sigma^{\rm exp}_{-xn} = \left(\frac{N'_i}{N_i} - \frac{N'_o}{N_o}\right)\left(\frac{\sigma_R - \sigma'_R}{e^{-\sigma'_R N_t} - e^{-\sigma_R N_t}}\right) . \tag{4.9}$$

Here N_i (N_o) represents the number of projectiles and N'_i (N'_o) the number of residues for target-in (i) (target-out (o)) runs. N_t and σ_R (σ'_R) are the number of target nuclei per unit area and reaction cross section of the projectile (residue). The details are shown in Sec. A. The background events were subtracted by using target-out runs. Owing to the substantial thickness of the carbon target, such a correction had to be applied to account for the losses in the number of projectiles and residues owing to reactions in the target. It should be noted that a 10% deviation in these reaction cross section values translates into an essentially negligible 1% deviation of the deduced one- and two-neutron removal cross sections.

In the analysis, the theoretical reaction cross section on a lead target ($\sigma^{\rm nucl}_R$(Pb)) and a carbon target (σ_R(C)) listed in Table 4.2 are used. The calculation do not include the Coulomb breakup contribution. Therefore, the reaction cross section $\sigma_{\rm R}$(Pb) calculated by Eq. (4.10) is used as an input of Eq. 4.9.

$$\sigma_R({\rm Pb}) = \sigma^{\rm nucl}_R({\rm Pb}) + \sigma^{\rm coul}_R({\rm Pb}), \tag{4.10}$$

where $\sigma^{\rm nucl}_R$(Pb) represents the reaction cross section by nuclear interaction, and $\sigma^{\rm coul}_R$(Pb) represents the Coulomb breakup cross section for all decay channels. Since the main part of $\sigma^{\rm coul}_R$(Pb) is exhausted by one- or two-neutron removal Coulomb breakup cross section ($\sigma^{\rm exp}_{-xn}(E1)$, $x = 1$ or 2), $\sigma^{\rm exp}_{-xn}(E1)$ is adopted as $\sigma^{\rm nucl}_R$(Pb). $\sigma^{\rm exp}_{-xn}(E1)$ and $\sigma^{\rm nucl}_R$(Pb) should be calculated iteratively until convergence.

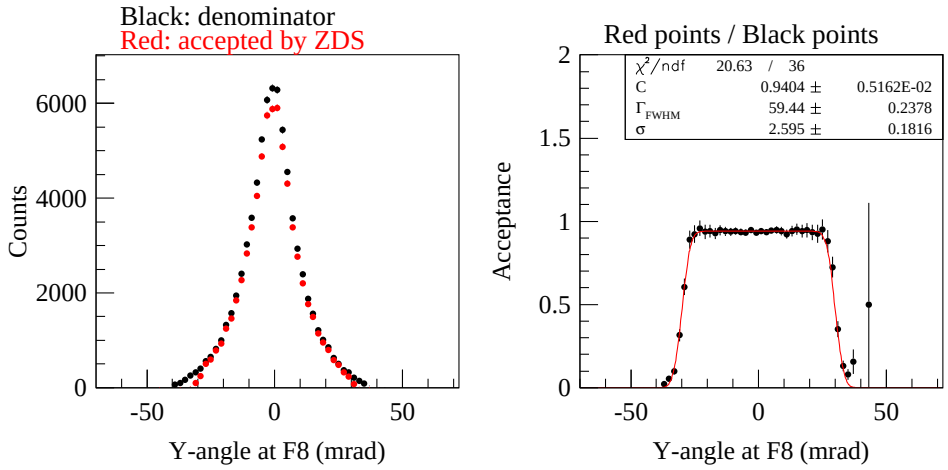

Figure 4.4: Left: y-axis angular distributions without (black point) and with (red point) the ZDS accepted gate. Right: ratio of the two distribution of left panel.

4.4 Analysis of the parallel momentum

The parallel momentum ($P_{||}$) was obtained by

$$P_{||} = \gamma_{\rm proj}(P_{\rm frag} - \beta_{\rm proj} E_{\rm frag}). \tag{4.11}$$

Here,

$P_{\rm frag}$: the momentum of the fragment at the center of the target,
$E_{\rm frag}$: the total energy of the fragment at the center of the target,
$\beta_{\rm proj}$: the velocity of the projectile over the speed of light (v/c) at the center of the target,
$\gamma_{\rm proj}$: $1/\sqrt{1-\beta^2_{\rm proj}}$.

The $P_{\rm frag}$ and $E_{\rm frag}$ values were obtained from the β of the fragment at the center of the target which was extracted from the the time-of-flight (TOF) between F8 and F11. The $\beta_{\rm proj}$ was extracted from the time-of-flight (TOF) between F3 and F7.

The resolution of momentum is obtained by calibration runs where the $B\rho$ setting of ZDS is adjusted to the $B\rho$ of secondary beam after carbon target. Figure 4.7 shows the momentum distribution for the run of the direct ^{37}Mg beam with the C target. The width $\sigma_{\rm beam}$ corresponds the resolution including the whole system resolution and energy straggling in the target. For the resolution $\sigma_{\rm reac}$ of reaction channels, the effect of energy-loss difference $\sigma_{\rm loss}$ is added to $\sigma_{\rm beam}$:

$$\sigma_{\rm reac} = \sqrt{\sigma^2_{\rm loss} + \sigma^2_{\rm beam}} \tag{4.12}$$

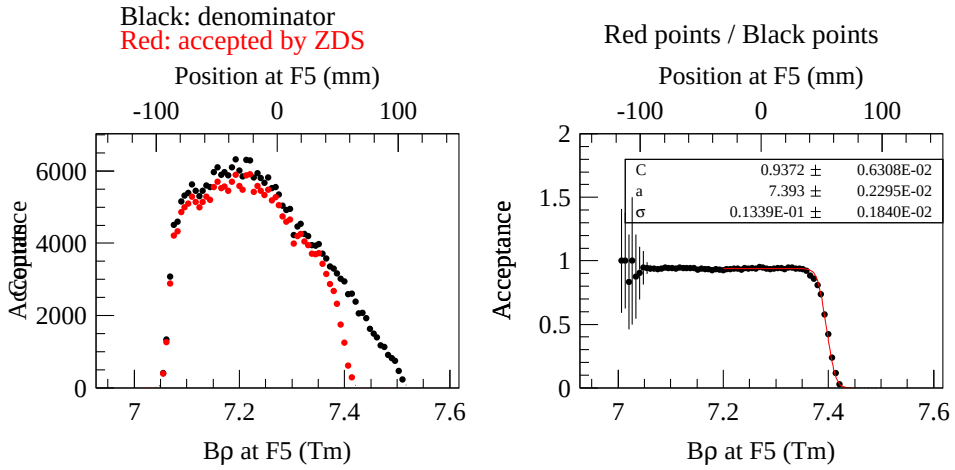

Figure 4.5: Left: the momentum distributions of beam without (black points) and with (red points) the ZDS accepted gate. Right: ratio of the two distribution of left panel.

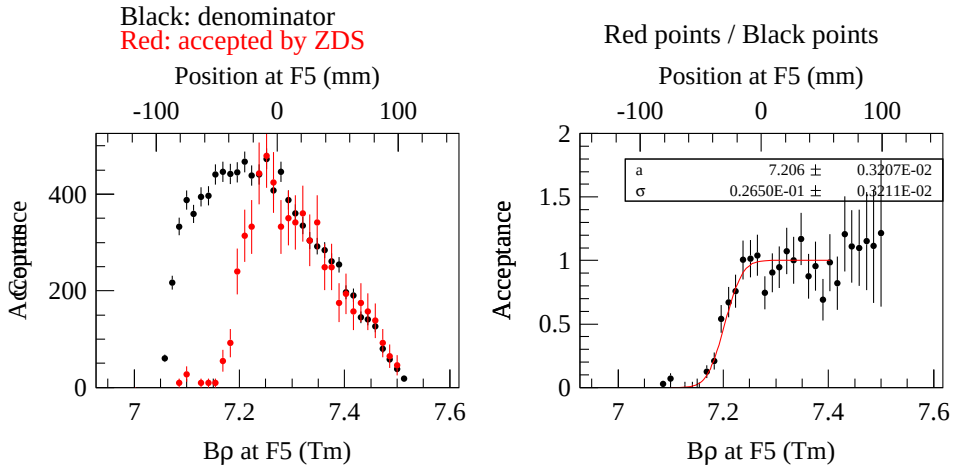

Figure 4.6: Left: the momentum distributions of fragments without (black points) and with (red points) the ZDS accepted gate. Right: ratio of the two distribution of left panel.

Channel	Transmission
Pb(^{19}C, ^{18}C)	94.4 %
C(^{19}C, ^{18}C)	98.7 %
Pb(^{20}C, ^{18}C)	96.1 %
C(^{20}C, ^{18}C)	88.1 %
Pb(^{20}C, ^{19}C)	95.2 %
C(^{20}C, ^{19}C)	95.0 %
Pb(^{22}C, ^{20}C)	97.2 %
C(^{22}C, ^{20}C)	91.7 %
Pb(^{29}Ne, ^{28}Ne)	97.2 %
C(^{29}Ne, ^{28}Ne)	99.3 %
Pb(^{31}Ne, ^{30}Ne)	96.1 %
C(^{31}Ne, ^{30}Ne)	95.3 %
Pb(^{33}Mg, ^{32}Mg)	97.9 %
C(^{33}Mg, ^{32}Mg)	99.6 %
Pb(^{35}Mg, ^{34}Mg)	98.4 %
C(^{35}Mg, ^{34}Mg)	99.8 %
Pb(^{37}Mg, ^{36}Mg)	98.8 %
C(^{37}Mg, ^{36}Mg)	99.9 %
Pb(^{39}Si, ^{38}Si)	97.4 %
C(^{39}Si, ^{38}Si)	99.6 %
Pb(^{41}Si, ^{40}Si)	97.7 %
C(^{41}Si, ^{40}Si)	99.7 %

Table 4.1: Transmission of ZDS for each channel is listed. The results are calculated by simulation whose inputs are the angular and momentum acceptances.

	Theoretical				Experimental		
Nucleus	Energy (MeV/u)	$\sigma_R^{\rm nucl}$(Pb) (mb)	Energy (MeV/u)	σ_R(C) (mb)	Energy (MeV/u)	σ_I(C) (mb)	Reference
^{18}C	240	3566	240	1023		-	
^{19}C	240	4085	240	1139		-	
^{20}C	240	3711	240	1090		-	
^{22}C	240	5208	240	1375		-	
^{28}Ne	244	3965	240	1231	240	1274(10)	[41]
^{29}Ne	244	4028	240	1262	240	1344(13)	[41]
^{30}Ne	234	4086	230	1294	240	1349(17)	[41]
^{31}Ne	234	4149	230	1321	240	1435(22)	[41]
^{32}Mg	234	4044	229	1289		-	
^{33}Mg	234	4099	229	1315		-	
^{34}Mg	245	4153	241	1338		-	
^{35}Mg	245	4202	241	1362		-	
^{36}Mg	244	4251	240	1386		-	
^{37}Mg	244	4301	240	1410		-	
^{38}Mg	224	4209	218	1385		-	
^{39}Mg	224	4248	218	1406		-	
^{40}Mg	229	4287	224	1424		-	
^{41}Mg	229	4326	224	1445		-	

Table 4.2: Table shows the theoretical total reaction cross sections for nuclear interaction induced reactions on a lead target ($\sigma_R^{\rm nucl}$(Pb)) and a carbon target (σ_R(C)) at listed energies. Experimental interaction cross sections (σ_I(C)) on a carbon target are also listed. The cross sections of $\sigma_R^{\rm nucl}$(Pb) and σ_R(C) are calculated based on the eikonal model as was shown in Sec. 2.2.2. These cross sections do not include the Coulomb breakup contribution.

Reaction	$\sigma_{\rm loss}$ (MeV/c)	$\sigma_{\rm beam}$ (MeV/c)	$\sigma_{\rm reac}$ (MeV/c)
C(^{19}C, ^{18}C)	20.0	10.3	23
C(^{20}C, ^{18}C)	20.2	19.6	28
C(^{20}C, ^{19}C)	20.2	9.82	23
C(^{22}C, ^{20}C)	20.2	18.0	27
C(^{29}Ne, ^{28}Ne)	21.6	12.0	25
C(^{31}Ne, ^{30}Ne)	21.5	11.8	25
C(^{33}Mg, ^{32}Mg)	23.9	16.0	29
C(^{35}Mg, ^{34}Mg)	27.3	14.2	31
C(^{37}Mg, ^{36}Mg)	28.3	13.6	31
C(^{39}Si, ^{38}Si)	29.5	19.6	35
C(^{41}Si, ^{40}Si)	32.4	18.1	37

Table 4.3: List of momentum resolution. The width $\sigma_{\rm beam}$ corresponds the resolution of beam runs including the whole system resolution and energy straggling in the target. The resolution $\sigma_{\rm reac}$ is resolution for reaction channels. $\sigma_{\rm loss}$ is the broadening effect by energy-loss difference.

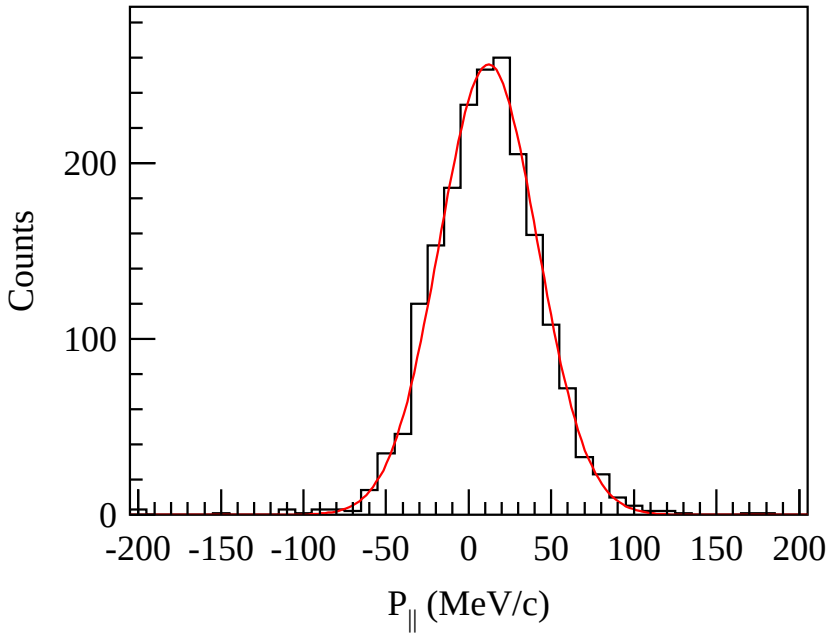

Figure 4.7: Momentum distribution for the direct ^{37}Mg beam with the C target. The width ($\sigma = 13.6$ MeV/c) corresponds the resolution including the whole system resolution and energy straggling in the target.

4.5 Width of momentum distributions

The parallel momentum ($P_{||}$) distributions of the fragments for (^{29}Ne, ^{28}Ne), (^{33}Mg, ^{32}Mg), (^{35}Mg, ^{34}Mg), (^{37}Mg, ^{36}Mg), (^{39}Si, ^{38}Si), and (^{41}Si, ^{40}Si) on the C target are shown in Figs. 4.8–4.10. The closed circles show the measured momentum distributions. The each black solid curve shows the fit result by a Gaussian function folded by experimental resolution listed in Table. 4.3. The fitting range is ±80 MeV for (^{31}Ne, ^{30}Ne) and ±100 MeV for the other channels, avoid the broadening effect by the tail component. Table 4.4 shows the deduced FWHMs of distribution for each reaction. The comparisons between measured distributions and theoretical ones is made in Chapters. 5 and 6.

So far, only the momentum distribution for the reaction C(^{33}Mg, ^{32}Mg) has been measured [42] elsewhere, where a width of 147(2) MeV/c (FWHM), which is consistent with our result of 148(4) MeV/c (FWHM), was found.

Reaction	Energy (MeV/nucleon)	FWHM (MeV/c)
C(^{29}Ne, ^{28}Ne)	240	128(5)
C(^{31}Ne, ^{30}Ne)	230	105(14)
C(^{33}Mg, ^{32}Mg)	229	148(4)
C(^{35}Mg, ^{34}Mg)	241	150(5)
C(^{37}Mg, ^{36}Mg)	240	121(10)
C(^{39}Si, ^{38}Si)	218	181(7)
C(^{41}Si, ^{40}Si)	224	170(6)

Table 4.4: The FWHM of Parallel momentum distribution of fragments for one-neutron removal from ^{29,31}Ne, ^{33,35,37}Mg, and ^{39,41}Si are shown. These values are obtained from the fit results by Gaussian function folded by experimental resolution listed in Table. 4.3.

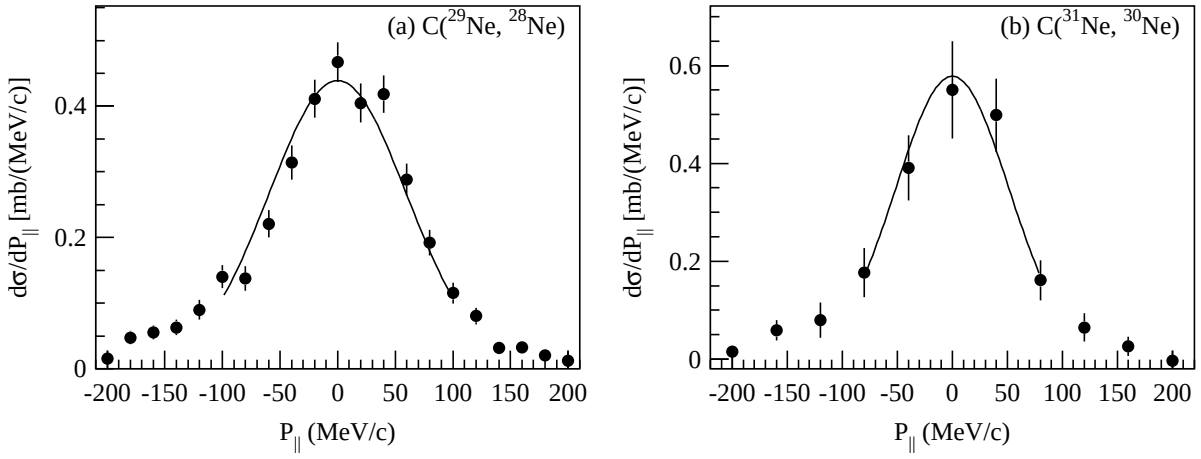

Figure 4.8: Parallel momentum distributions of the fragments for one-neutron removal from ^{29}Ne and (b) ^{31}Ne are shown. The black solid curves show the fitting results, to the central regions of the distributions, for Gaussian line shapes folded with the experimental resolutions listed in Table. 4.3.

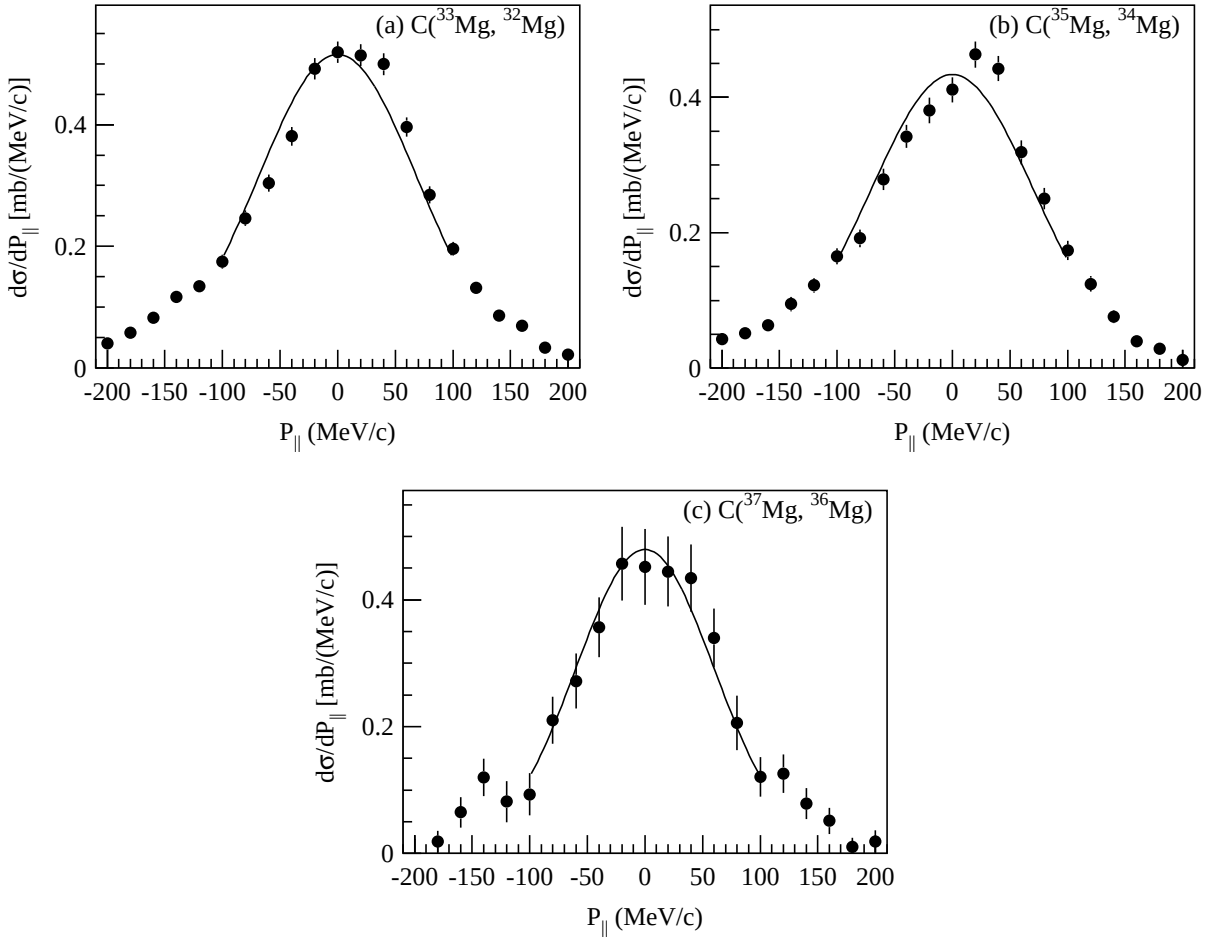

Figure 4.9: Parallel momentum distributions of the fragments for one-neutron removal from (a) ^{33}Mg, (b) ^{35}Mg, and (c) ^{37}Mg are shown. The black solid curves show the fitting results, to the central regions of the distributions, for Gaussian line shapes folded with the experimental resolutions listed in Table. 4.3.

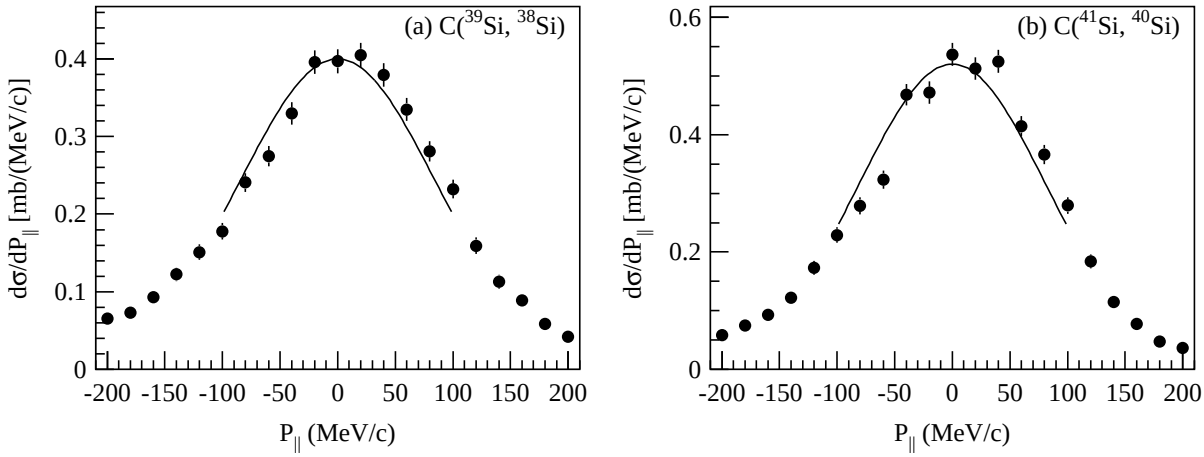

Figure 4.10: Parallel momentum distributions of the fragments for one-neutron removal from (a) ^{39,41}Si and (b) ^{41}Si are shown. The black solid curves show the fitting results, to the central regions of the distributions, for Gaussian line shapes folded with the experimental resolutions listed in Table. 4.3.

4.6 γ-ray analysis

The measured Doppler corrected γ-ray spectra on the lead and carbon targets are shown in Fig. 4.11 for the reactions (^{29}Ne, ^{28}Ne) and (^{31}Ne, ^{30}Ne), in Fig. 4.12 for (^{33}Mg, ^{32}Mg), (^{35}Mg, ^{34}Mg), (^{37}Mg, ^{36}Mg), and in Fig. 4.13 for (^{39}Si, ^{38}Si) and (^{41}Si, ^{40}Si). The red solid lines show the results of fits by the response function of Geant4 (red doted curves) with exponential background (red dashed curves). All of the γ-ray peaks in the present experiment are known. In the fitting procedure, the peak positions are fixed to the known energies listed in Table 4.5.

The fit results for the γ-ray spectra provides the cross section associated with the feeding from the 2_1^+ state to the ground state of the core fragment, which is shown in the columns of "Cross section (mb)" in the Table. 4.5. The error of each cross section includes the systematic error of 7 % for the Day One setup and 12 % for the Day Three setup. The systematic error arose from the efficiency simulation by Geant4 [43]. We should note that each cross section may include a contribution arising from feeding from higher lying states, populated in the reaction, which we do not observe in the γ-ray spectrum. For instance, the cross sections to 2_1^+ states in the table include also the cross sections to 4_1^+ states, which decay to the 2_1^+ states of core fragment. Finally, we note that in the later interpretation of our results we assume that dynamical excitations of the core fragment are negligible.

				Cross section (mb)	
Reaction	Peak (keV)	Transition	Reference	Pb target	C target
(^{29}Ne, ^{28}Ne)	1293(8)	$2_1^+ \rightarrow 0^+_{\text{g.s.}}$	[44]	111(42)	28(7)
(^{31}Ne, ^{30}Ne)	791(26)	$2_1^+ \rightarrow 0^+_{\text{g.s.}}$	[45]	202(82)	57(13)
(^{33}Mg, ^{32}Mg)	885.0(0.5)	$2_1^+ \rightarrow 0^+_{\text{g.s.}}$	[46]	322(46)	53(7)
(^{35}Mg, ^{34}Mg)	660(10)	$2_1^+ \rightarrow 0^+_{\text{g.s.}}$	[47]	350(67)	50(7)
(^{37}Mg, ^{36}Mg)	660(6)	$2_1^+ \rightarrow 0^+_{\text{g.s.}}$	[48]	181(81)	48(8)
(^{39}Si, ^{38}Si)	1071(12)	$2_1^+ \rightarrow 0^+_{\text{g.s.}}$	[49]	336(46)	71(9)
(^{39}Si, ^{38}Si)	1168(22)	$4_1^+ \rightarrow 2_1^+$	[49,50]	209(33)	38(5)
(^{39}Si, ^{38}Si)	1284(26)	-	[50]	34(19)	2(4)
(^{41}Si, ^{40}Si)	629(8)	$(0^+,2^+) \rightarrow 2_1^+$	[49,51]	83(32)	15(3)
(^{41}Si, ^{40}Si)	985(11)	$2_1^+ \rightarrow 0^+_{\text{g.s.}}$	[49]	295(48)	62(8)

Table 4.5: γ-ray peaks used by fitting and corresponding transitions are shown. The partial cross sections to excitation states by fitting results are also shown.

4.7 Shell model results

We summarize the shell-model predictions for the nuclei studied here. The ground and low-lying excitation states calculated with the SDPF-M interaction for ^{29,31}Ne and ^{33,35,37}Mg and with the SDPF-MU interaction for ^{39,41}Si [52,53] are listed in Table. 4.6. Figure 4.14 shows the levels tabulated in Table 4.6. The states of 0.00 MeV correspond to the predicted ground states. Only the yrast states are shown.

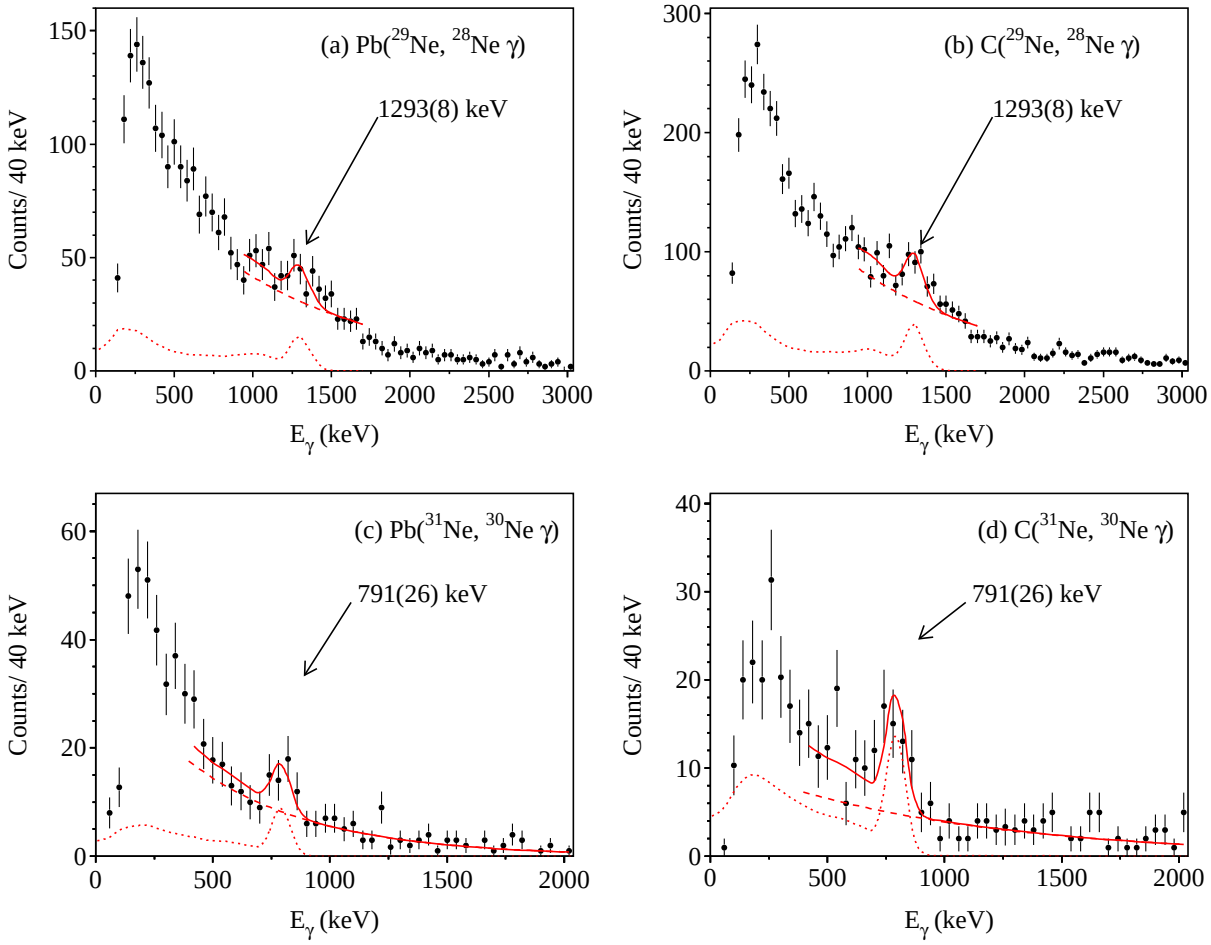

Figure 4.11: Doppler-shift corrected γ-ray spectrum obtained for the reactions of (a) Pb(^{29}Ne, ^{28}Ne), (b) C(^{29}Ne, ^{28}Ne), (c) Pb(^{31}Ne, ^{30}Ne), and (d) C(^{31}Ne, ^{30}Ne) are shown. The red solid lines show the results of fits by the response function of Geant4 (red doted curves) and exponential background (red dashed curves). All of the measure γ-ray peaks in the present experiment are known so far. In the fitting procedure, the peak positions are fixed to the known energy listed in 4.5

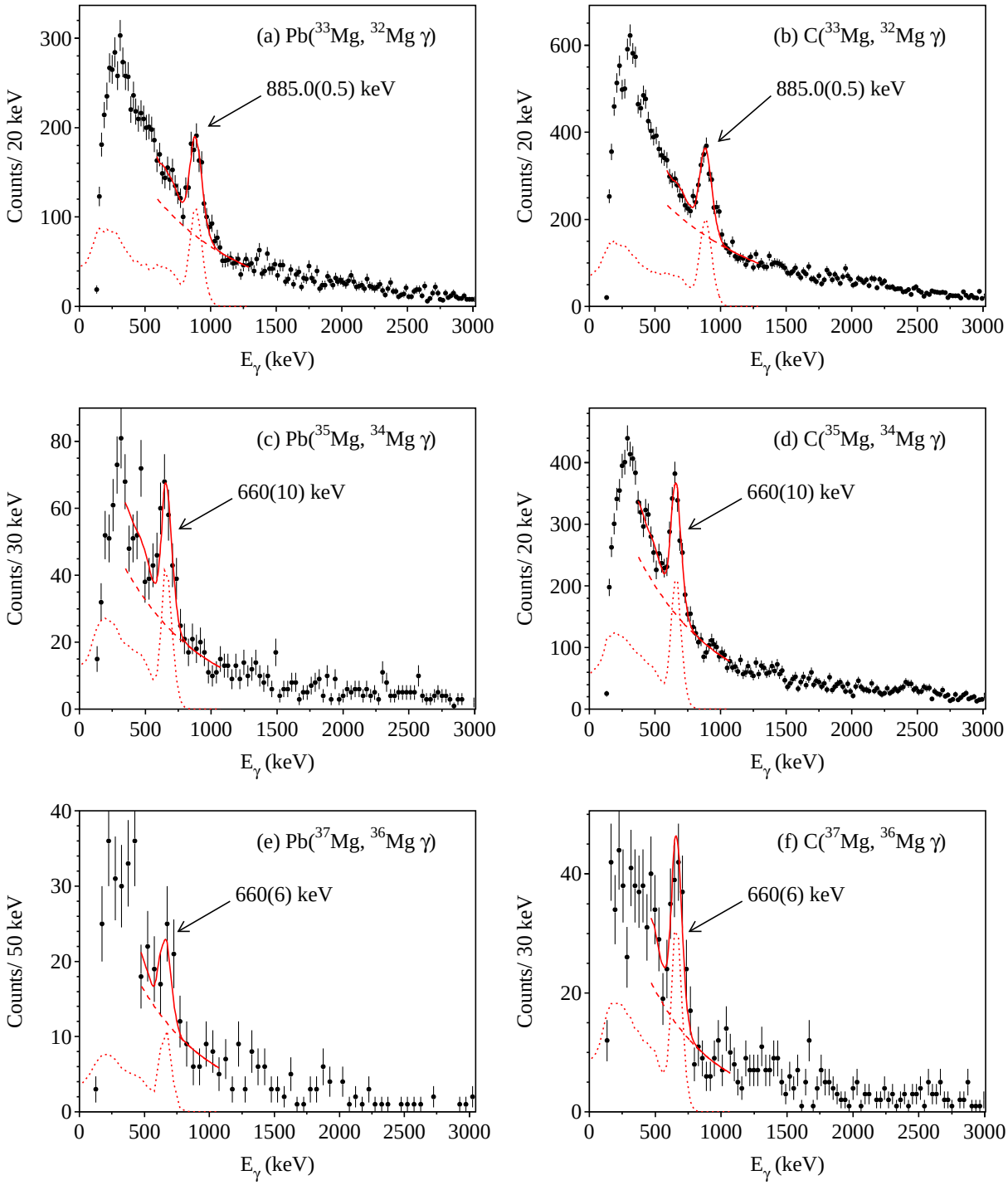

Figure 4.12: Doppler-shift corrected γ-ray spectrum obtained for the reactions of (a) Pb(^{33}Mg, ^{32}Mg), (b) C(^{33}Mg, ^{32}Mg), (c) Pb(^{35}Mg, ^{34}Mg), (d) C(^{35}Mg, ^{34}Mg), (e) Pb(^{37}Mg, ^{36}Mg), and (f) C(^{37}Mg, ^{36}Mg) are shown. The red solid lines show the results of fits by the response function of Geant4 (red doted curves) and exponential background (red dashed curves). All of the measure γ-ray peaks in the present experiment are known so far. In the fitting procedure, the peak positions are fixed to the known energy listed in 4.5

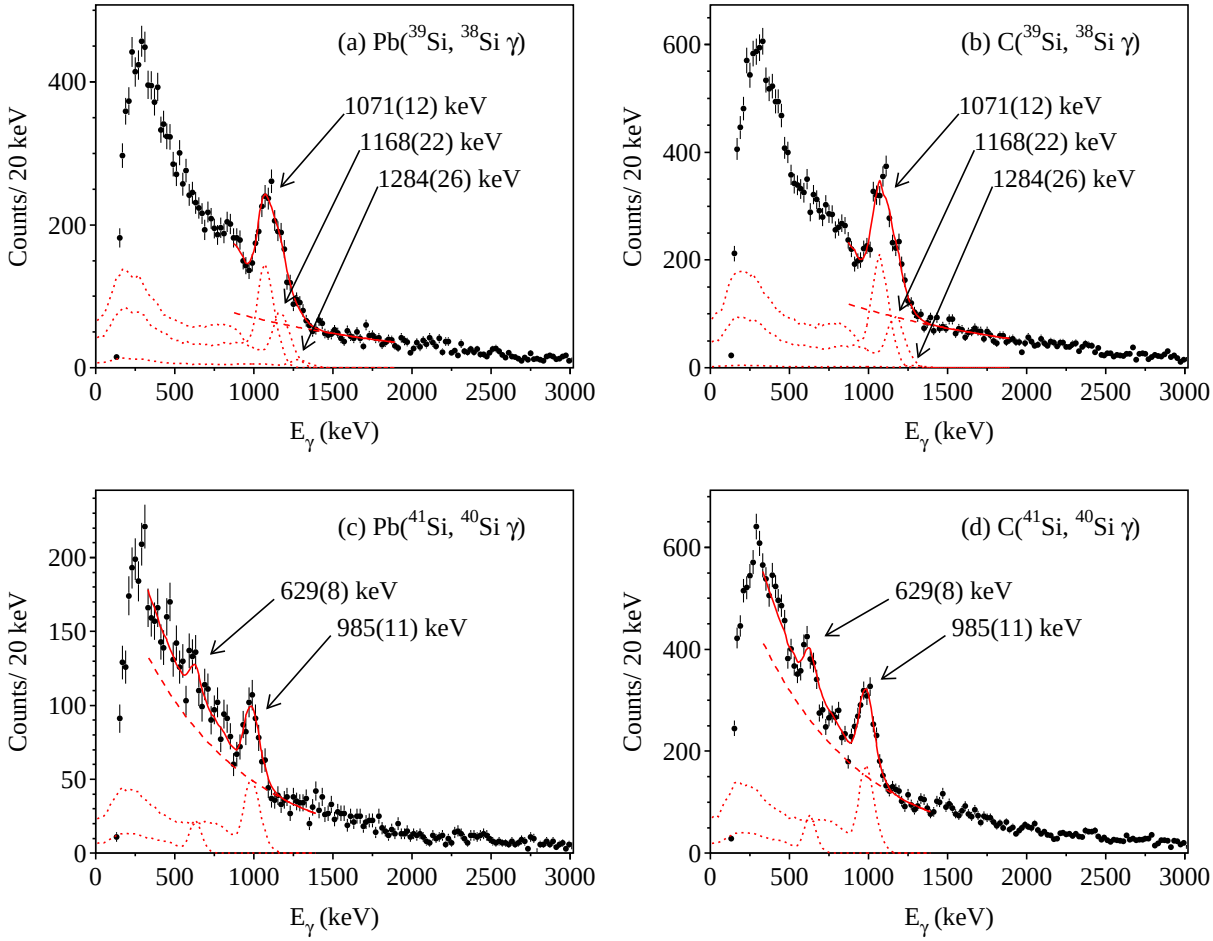

Figure 4.13: Doppler-shift corrected γ-ray spectrum obtained for the reactions of (a) Pb(^{39}Si, ^{38}Si), (b) C(^{39}Si, ^{38}Si), (c) (^{41}Si, ^{40}Si), and (d) (^{41}Si, ^{40}Si) are shown. The red solid lines show the results of fits by the response function of Geant4 (red doted curves) and exponential background (red dashed curves). All of the measure γ-ray peaks in the present experiment are known so far. In the fitting procedure, the peak positions are fixed to the known energy listed in 4.5

Nucleus	J^π	Energy (MeV)
^{29}Ne	$3/2^+$	0.00
	$3/2^-$	0.07
	$7/2^-$	0.12
	$1/2^+$	0.56
	$5/2^-$	0.70
	$5/2^+$	1.46
	$1/2^-$	2.09
^{31}Ne	$3/2^-$	0.00
	$7/2^-$	0.65
	$3/2^+$	0.68
	$1/2^+$	0.99

Nucleus	J^π	Energy (MeV)
^{33}Mg	$3/2^-$	0.00
	$3/2^+$	0.99
^{35}Mg	$3/2^-$	0.00
	$5/2^-$	0.09
	$7/2^-$	0.35
	$1/2^-$	0.43
	$5/2^+$	1.01
	$1/2^+$	2.25
^{37}Mg	$3/2^-$	0.00
	$5/2^-$	0.50
	$7/2^-$	0.50
	$1/2^-$	0.56
	$3/2^+$	0.81
	$5/2^+$	1.34
	$1/2^+$	1.76

Nucleus	J^π	Energy (MeV)
^{39}Si	$5/2^-$	0.00
	$7/2^-$	0.04
	$3/2^-$	0.10
	$1/2^-$	0.38
^{41}Si	$3/2^-$	0.00
	$7/2^-$	0.23
	$5/2^-$	0.52
	$1/2^-$	0.61

Table 4.6: Low-lying shell-model levels for ^{29,31}Ne, ^{33,35,37}Mg, and ^{39,41}Si calculated by Utsuno et al. [52, 53] are listed. The states of 0.00 MeV correspond the ground states. Only the yrast states are shown. For ^{31}Ne and ^{33,35,37}Mg, only the ground state is listed.

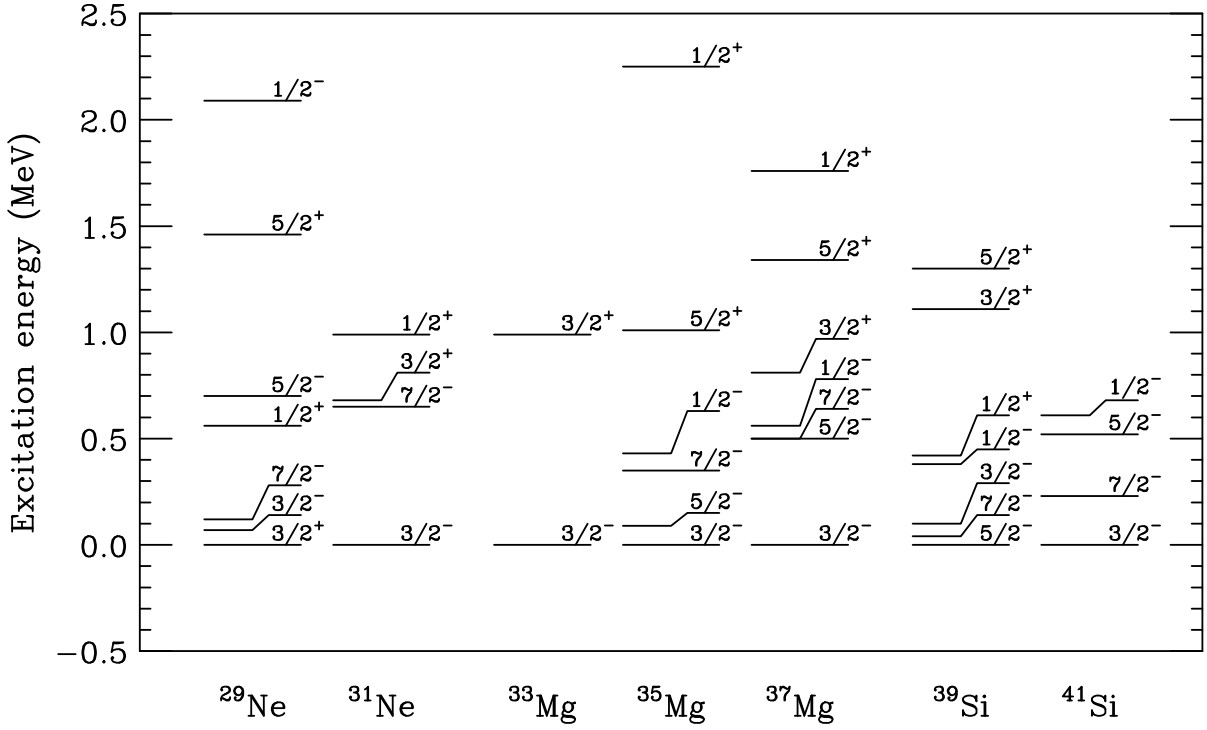

Figure 4.14: Low-lying shell-model level scheme calculated with the SDPF-M interaction for ^{29,31}Ne and ^{33,35,37}Mg and with the SDPF-MU interaction for ^{39,41}Si [52, 53]. Only the yrast states are shown.

Chapter 5

Experimental Results and Discussions for ^{31}Ne

5.1 General description

We analyze the microscopic structure of $N = 21$ weakly bound nucleus ^{31}Ne by utilizing the different sensitivities of the response to Coulomb and nuclear breakup. Section 5.2 shows the inclusive and semi-inclusive cross sections, which were obtained in coincidence with the associated γ-ray, on the lead and carbon targets. From the cross sections, the spectroscopic factors of ^{31}Ne are obtained as shown in Sec. 5.3. In Sec. 5.4, we compare the inclusive and semi-inclusive cross sections with theoretical calculations based on shell model and eikonal reaction model, and discuss the shell structure. The momentum distributions are also compared with the calculations.

5.2 Inclusive Breakup Cross Sections

The measured inclusive one-neutron removal cross sections of ^{31}Ne with the lead target, $\sigma^{\rm exp}_{-1n}$(Pb), and carbon target, $\sigma^{\rm exp}_{-1n}$(C), are listed in Table 5.1, which are labeled as "(Inclusive)". In the table, cross sections of ^{19}C measured in the same experiment are also listed for reference purposes. The table also shows the Coulomb breakup cross sections, $\sigma^{\rm exp}_{-1n}(E1)$, which are obtained from the cross sections $\sigma^{\rm exp}_{-1n}$(Pb) and $\sigma^{\rm exp}_{-1n}$(C) by

$$\sigma^{\rm exp}_{-xn}(E1) = \sigma^{\rm exp}_{-xn}({\rm Pb}) - \Gamma\sigma^{\rm exp}_{-xn}({\rm C}), \tag{5.1}$$

where, Γ was estimated to be $\approx$1.7–2.6. The lower limit $\Gamma_{\rm min}$ is from the ratio of target + projectile radii, as in Ref. [54], while the upper limit $\Gamma_{\rm max}$ is derived from the Serber model [55]:

$$\Gamma = \frac{\Gamma_{\rm min} + \Gamma_{\rm max}}{2} \tag{5.2}$$

$$\Gamma_{\rm min} = \frac{R({\rm Pb}) + R({\rm Proj.})}{R({\rm C}) + R({\rm Proj.})} \tag{5.3}$$

$$\Gamma_{\rm max} = \frac{R({\rm Pb})}{R({\rm C})} \tag{5.4}$$

$$R \propto A^{1/3}, \tag{5.5}$$

where, R(Pb), R(C), and R(Proj.) represent nuclear radii of lead, carbon, and projectile ^{31}Ne, respectively, and each is proportional to the mass number A to the power of 1/3. The ambiguity due to the two choices is included in the uncertainty of $\sigma^{\rm exp}_{-xn}(E1)$.

In Table 5.1, the cross sections corresponding to the transitions of $2^+_1 \rightarrow 0^+_{\rm g.s.}$ are listed, which are labeled as "(2^+, 4^+, etc.)" with the fragment nuclei. This label is used since hereafter we assume that this γ-ray line ($2^+ \rightarrow 0^+$) contains all the contributions from the bound states below two neutron decay threshold. By subtracting the cross sections corresponding to the transitions $2^+_1 \rightarrow 0^+_{\rm g.s.}$ from the inclusive cross sections, we estimate the cross sections to the $0^+_{\rm g.s.}$ state of the fragments. The cross sections are listed in Table 5.1, which are labeled as "($0^+_{\rm g.s.}$)" for the fragment nuclei. In this estimation, we assumed that the direct decay from excited states higher than 2^+_1 state to the ground state can be neglected.

The inclusive Coulomb breakup cross section $\sigma^{\rm exp}_{-1n}(E1)$ = 529(63) mb is obtained for ^{31}Ne (S_{1n} = -0.06(42) MeV [34]). This value is significantly larger than that of ordinary nuclei and is close to that of ^{19}C which is an established halo nucleus. This suggests that ^{31}Ne has $1n$ halo structure.

	$\bar{E}/A$ (MeV)		$\sigma^{\rm exp}_{-1n}$(Pb)	$\sigma^{\rm exp}_{-1n}$(C)	$\sigma^{\rm exp}_{-1n}(E1)$
Reaction	Pb	C	(mb)	(mb)	(mb)
(^{31}Ne, ^{30}Ne) (Inclusive)	234	230	720(61)	90(7)	529(63)
(^{31}Ne, ^{30}Ne(2^+, 4^+, etc.))			202(83)	57(13)	81(87)
(^{31}Ne, ^{30}Ne($0^+_{\rm g.s.}$))			518(103)	33(15)	448(108)
(^{19}C, ^{18}C) (Inclusive)	243	238	969(64)	132(4)	690(70)

Table 5.1: The one-neutron removal cross sections for each reaction channel at the mid-target energies ($\bar{E}/A$) are shown. The inclusive cross sections are labeled as "(inclusive)". The partial semi-inclusive cross sections connecting to the excited states of the fragments are labeled as "(2^+, 4^+, etc.)". The $0^+_{\rm g.s.}$ partial cross sections are labeled as "($0^+_{\rm g.s.}$)".

To interpret the experimental Coulomb breakup cross section, it is compared with calculations based on the direct breakup model shown in Sec. 2.1.2. Figure 5.1 shows a comparison of the experimental Coulomb breakup cross section of 529(63) mb (hatched area) with the cross sections calculated for possible valence neutron configurations. The separation energy of ^{31}Ne ($S_n = -0.06(42)$) reported recently by Gardefroy *et al.* [34] still has a large uncertainty. Hence, these cross sections are calculated as a function of S_{1n}.

The calculations have been made in the following manner. The wave function of the ground state of ^{31}Ne with spin parity J^π is modeled as a linear combination of single-particle configurations: $^{30}{\rm Ne}(0^+_1) \otimes \phi_{n\ell j}$, $^{30}{\rm Ne}(2^+_1) \otimes \phi_{n'\ell'j'}$, ..., where $\phi_{n\ell j}$ represents the valence neutron in the $n\ell j$ orbital. The first configuration describes a valence neutron coupled to the ground state of the $^{30}{\rm Ne}(0^+_1)$ core. The second describes coupling to the first excited state of $^{30}{\rm Ne}(2^+_1)$ with E_x = 0.801(7) MeV [45,56]. Given the large effective neutron binding energies, higher-lying core states will not contribute significantly to $\sigma^{\rm exp}_{-1n}(E1)$. Therefore, we consider only the $^{30}{\rm Ne}(0^+_1)$ and $^{30}{\rm Ne}(2^+_1)$ states couples to a $2s_{1/2}$, $2p_{3/2}$, $1d_{3/2}$, and $1f_{7/2}$ valence neutron. The single-particle wave functions were derived for a Woods-Saxon potential with r_0 = 1.24 fm, diffuseness a = 0.62 fm and spin-orbit potential V_{SO} = 7.0 MeV [57].

The $E1$ strength function is estimated based on the Coulomb direct-breakup model of a core + $1n$ system [7, 13–15, 58] as shown in Sec 2.1.2,

$$\frac{dB(E1)}{dE_x} = \sum_{n\ell j J^\pi} C^2S(J^\pi, n\ell j) \sum_{\ell_f j_f} |\langle \psi_{\ell_f j_f} | \hat{T}^{(E1)} | \phi_{n\ell j} \rangle|^2, \tag{5.6}$$

where $C^2S(J^\pi, n\ell j)$ denotes the spectroscopic factor for $^{30}{\rm Ne}(J^\pi) \otimes \phi_{n\ell j}$, and the $E1$ operator $\hat{T}^{(E1)}$ involves r, the relative distance between the core and valence neutron. The wave function

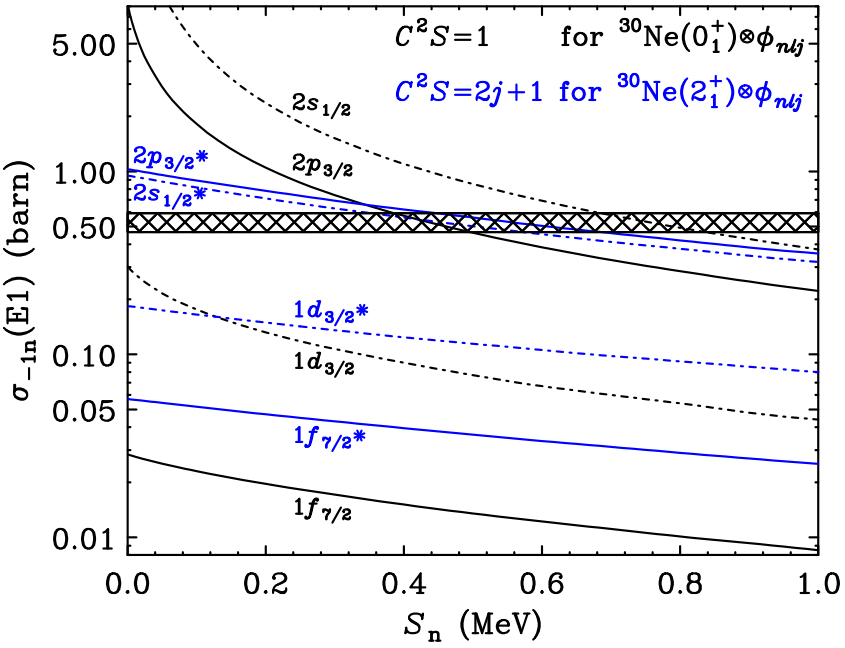

Figure 5.1: The Coulomb breakup cross section for ^{31}Ne of 529(63) mb is compared with calculations for possible configurations of the valence neutron for the sum-rule limits of C^2S as a function of S_{1n}. The solid curves are for the negative parity states, $2p_{3/2}$ and $1f_{7/2}$ coupled to $^{30}\mathrm{Ne}(0^+_1)$, while the dot-dashed curves are for the positive parity states, $2s_{1/2}$ and $1d_{3/2}$. The blue lines labeled with an asterisk are for the configurations coupled to $^{30}\mathrm{Ne}(0^+_1)$.

$\psi_{\ell_f j_f}$ represents the neutron scattering state in the exit channel. The core is considered to be a spectator in the reaction. As the matrix element is related to the Fourier transformation of $r\phi(r)$, the $B(E1)$ enhances at low E_x for a halo system [7, 13–15].

The cross section $\sigma_{-1n}(E1)$ for each configuration is then calculated by

$$\sigma_{-1n}(E1) = \int_{S_{1n}}^{S_{2n}} \frac{16\pi^3}{9\hbar c} N_{E1}(E_x) \frac{dB(E1)}{dE_x} dE_x, \tag{5.7}$$

where integration is made up to $E_x = S_{1n} + 3.4$ MeV(S_{2n}), assuming that above this energy decay occurs to a channel other than $1n$ emission. For C^2S, we use the maximum value of $C^2S = 1$ for a state coupled to $^{30}\mathrm{Ne}(0^+_1)$ and $C^2S = 2j + 1$ for a state coupled to $^{30}\mathrm{Ne}(2^+_1)$, which are the sum-rule limits as shown in Ref. [59].

According to Fig. 5.1, for the configurations coupled to $^{30}\mathrm{Ne}(0^+_1)$, the experimental cross section is well explained for the low-ℓ angular orbital configurations $^{30}\mathrm{Ne}(0^+_1) \otimes 2s_{1/2}$ at $S_{1n} \approx 0.7$ MeV and $^{30}\mathrm{Ne}(0^+_1) \otimes 2p_{3/2}$ at $S_{1n} \approx 0.4$ MeV. On the other hand, the experimental cross section can not be reproduced by the high-ℓ configurations $^{30}\mathrm{Ne}(0^+_1)\otimes 1d_{3/2}$ and $^{30}\mathrm{Ne}(0^+_1)\otimes 1f_{7/2}$.

For the configurations coupled to $^{30}\mathrm{Ne}(2^+_1$, $E_x = 0.801(7)$ MeV), since the separation energy of the valence neutron is 0.801-MeV deeper than the case of $^{30}\mathrm{Ne}(0^+_1)$, the Coulomb breakup cross section is reduced. On the other hand, the maximum C^2S of $^{30}\mathrm{Ne}(2^+_1)$ configurations is $2j + 1$ times larger than that of $^{30}\mathrm{Ne}(0^+_1)$. As similar to the case of $^{30}\mathrm{Ne}(2^+_1)$, the experimental cross section is explained only for the low-ℓ configurations $^{30}\mathrm{Ne}(2^+_1) \otimes 2s_{1/2}$ at $S_{1n} \approx 0.4$ MeV and $^{30}\mathrm{Ne}(0^+_1) \otimes 2p_{3/2}$ at $S_{1n} \approx 0.5$ MeV. The experimental cross section can not be reproduced by the high-ℓ configurations $^{30}\mathrm{Ne}(2^+_1) \otimes 1d_{3/2}$ and $^{30}\mathrm{Ne}(2^+_1) \otimes 1f_{7/2}$.

As a result, the accepted configurations are $^{30}\mathrm{Ne}(0^+_1) \otimes 2s_{1/2}$, $^{30}\mathrm{Ne}(0^+_1) \otimes 2p_{3/2}$, $^{30}\mathrm{Ne}(2^+_1) \otimes 2s_{1/2}$, and $^{30}\mathrm{Ne}(2^+_1) \otimes 2p_{3/2}$. All of these include a low-ℓ valence neutron. In the low-ℓ configurations, the effective potential binding the valence neutron has no or very low centrifugal barrier.

Hence, the wave function of the valence neutron extends out of the core, which causes development of halo structure and enhancement of the large Coulomb breakup cross section. We should note that the dominance of $^{30}\mathrm{Ne}(0_1^+) \otimes 1f_{7/2}$ configuration expected from the conventional shell order is fully excluded, which is in line with the melting of the shell gaps in $N = 20$ and 28.

However, the inclusive cross section offers only a qualitative picture of ^{31}Ne halo state. In order to discuss the structure of ^{31}Ne more quantitatively, it is necessary to use additional information of semi-inclusive cross sections both on carbon and lead targets. The results for this analysis will be given in the next section.

5.3 Combined Analysis of the Coulomb and Nuclear Breakup

From Eq. (4.9), the spectroscopic factor $C^2S(0^+, n\ell j)$ between the ground state of the projectile and 0^+ state of the fragment in the $1n$ removal reaction with a carbon target is obtained from the ratio of $\sigma^{\rm exp}_{-1n}({\rm C},\ 0^+_{\rm g.s.})$ to the single-particle cross section $\sigma_{\rm sp}({\rm C}, n\ell j, S_n)$. Here, we denote the spectroscopic factor by $C^2S(C, 0^+, n\ell j, S_{1n})$:

$$C^2S(C, 0^+, n\ell j, S_{1n}) = \left[\frac{A-1}{A}\right]^N \frac{\sigma^{\rm exp}_{-1n}({\rm C}, 0^+_{\rm g.s.})}{\sigma_{\rm sp}({\rm C}, n\ell j, S_{1n})}. \tag{5.8}$$

On the other hand, the spectroscopic factor is also obtained from the Coulomb breakup cross section $\sigma^{\rm exp}_{-1n}(E1,\ 0^+_{\rm g.s.})$ and the single-particle cross section $\sigma_{\rm sp}(E1, n\ell j, S_n)$ as

$$C^2S(E1, 0^+, n\ell j, S_{1n}) = \frac{\sigma^{\rm exp}_{-1n}(E1, 0^+_{\rm g.s.})}{\sigma_{\rm sp}(E1, n\ell j, S_{1n})}, \tag{5.9}$$

where, $\sigma_{\rm sp}(E1, n\ell j, S_n)$ is calculated by

$$\sigma_{\rm sp}(E1, n\ell j, S_{1n}) = \int_{S_{1n}}^{S_{2n}} \frac{16\pi^3}{9\hbar c} N_{E1}(E_x) \sum_{\ell_f j_f} |\langle \psi_{\ell_f j_f}(E_x)|\hat{T}^{(E1)}|\phi_{n\ell j}(S_{1n})\rangle|^2 dE_x. \tag{5.10}$$

Here, the wave function $\psi_{\ell_f j_f}$ represents the neutron scattering state in the exit channel, and the $E1$ operator is denoted as $\hat{T}^{(E1)}$. N_{E1} represents the virtual photon number as a function of excitation energy E_x.

Figure 5.2 (b-1) shows the single-particle cross section $\sigma_{\rm sp}(E1, 2p_{3/2}, S_n)$ for the $2p_{3/2}$ neutron removal from ^{31}Ne as a function of S_n (red curve) and measured Coulomb breakup cross section $\sigma^{\rm exp}_{-1n}(E1, 0^+_{\rm g.s.})$ (red hatched area). Similarly, Figure 5.2 (b-2) shows the single-particle cross section $\sigma_{\rm sp}({\rm C}, 2p_{3/2}, S_n)$ as a function of S_n (blue curve) and measured one-neutron removal cross section $\sigma^{\rm exp}_{-1n}({\rm C}, 0^+_{\rm g.s.})$ (blue hatched area). In Fig. 5.2 (b-3), the red and blue hatched areas show the possible area of C^2S values obtained from Eqs. (5.8) and (5.9), respectively, for the $2p_{3/2}$ neutron removal reactions. In addition, the green area shows the separation energy from the mass measurement [34]. The overlapped area of the red, blue, and green hatched areas is experimentally accepted if the $2s_{1/2}$- and $2p_{3/2}$-neutron removal is assumed. The figures labeled as (a), (c), and (d) in Fig. 5.2 show the results for the $2s_{1/2}$-, $1d_{3/2}$-, and $1f_{7/2}$-neutron removal, respectively. We should note that since the maximum of the spectroscopic factor of $^{30}{\rm Ne}(0^+_1) \otimes \phi_{\phi_{n\ell j}}$ is unity, the $C^2S(0^+, n\ell j)$ should be less than one.

In Figs. (a-3) and (b-3) of Fig. 5.2, the blue, red, and green hatched areas can have an overlap. In Figs. (c-3) and (d-3) of Fig. 5.2, there is no overlap between the blue and red hatched areas. Therefore, the possible configurations are $^{30}{\rm Ne}(0^+) \otimes 2s_{1/2}$ with $J^\pi = 1/2^+$ and $^{30}{\rm Ne}(0^+) \otimes 2p_{3/2}$ with $J^\pi = 3/2^-$.

Each black line in Figs. (a-3) and (b-3) shows the 68% confidential level obtained from $\chi^2 = \chi^2_{\rm min} + 2.3$ for two parameters of C^2S and S_{1n}. The details are described in Sec. B. From the χ^2 analysis in Fig. (a-3), the spectroscopic factor $C^2S(0^+, 2s_{1/2}))$ is $0.23^{+0.17}_{-0.13}$, and the separation energy S_{1n} is $0.23^{+0.18}_{-0.13}$ MeV. For Fig. (b-3), $C^2S(0^+, 2p_{3/2}))$ is $0.26^{+0.17}_{-0.14}$, and the separation energy S_{1n} is $0.11^{+0.12}_{-0.08}$ MeV.

5.4 Comparison with shell model

To clarify the spin parity of the ground state of ^{31}Ne, large-scale Monte Carlo Shell Model (MCSM) calculations employing the SDPF-M effective interaction [52] were performed. The shell-model levels are listed in Table 5.2 and shown in Fig 5.3. According to the shell model, the spin parity of the ground state of ^{31}Ne is $3/2^-$. The $1/2^+$ shell-model state is lying at $E_{\rm x} = 0.99$ MeV. This suggests that the $3/2^-$ shell-model state is favored as the ground state of ^{31}Ne, which is consistent with the result of the combined analysis for the case of $3/2^-$ in the previous section.

To confirm the result, the inclusive and semi-inclusive cross sections are calculated. Table 5.4 shows the comparison between the experimental results and theoretical calculations for nuclear breakup reactions. The calculations were carried out for the $1/2^+$ and $3/2^-$ shell-model states of ^{31}Ne. The measured inclusive and semi-inclusive cross sections of 90(7) mb and 33(15) mb are in good agreement with those of calculated values 92.02 and 24.61 mb, respectively. Therefore, the ground state with $J^\pi = 3/2^-$ is concluded. On the other hand, for the other possibility of $1/2^+$ obtained in the combined analysis, we find large discrepancy between the experimental cross sections (90(7) and 33(15) mb) and the calculations (52.6 and 1.78 mb). We note that the discrepancy is extremely large in particular for the semi-inclusive result. From these comparisons, we conclude that the $3/2^+$ ground state of ^{31}Ne is most likely, where the halo is found in p-wave as shown in Table 5.4.

Reaction	E_x (MeV)	J^π	ℓ_j	σ_{sp} (mb)	C^2S	σ^{th}_{-1n}(C) (mb)	σ^{exp}_{-1n}(C) (mb)	R_s
C(^{31}Ne($3/2^-$),^{30}Ne)	0.00	0^+_1	$p_{3/2}$	109.66	0.212	25.65	33(15)	1.29(58)
S_{1n}(^{31}Ne) = 0.11 MeV	1.05	2^+_1	$p_{3/2}$	58.50	0.265	17.10		
			$f_{7/2}$	23.86	0.158	4.16		
	2.42	4^+_1	$f_{7/2}$	20.61	0.592	13.46		
	2.68	0^+_2	$p_{3/2}$	39.67	0.013	0.57		
	3.08	2^-_1	$s_{1/2}$	31.78	0.019	0.64		
			$d_{3/2}$	18.43	0.618	12.16		
			$d_{5/2}$	20.15	0.000	0.00		
	3.10	2^+_2	$p_{3/2}$	36.99	0.058	2.37		
			$f_{7/2}$	19.44	0.053	1.14		
	3.27	3^-_1	$d_{3/2}$	18.00	0.528	10.15		
			$d_{5/2}$	19.67	0.006	0.13		
	3.33	1^-_1	$s_{1/2}$	30.20	0.075	2.42		
			$d_{3/2}$	17.87	0.181	3.45		
			$d_{5/2}$	19.52	0.001	0.02		
		Inclusive				93.42	90(7)	0.96(7)
C(^{31}Ne($1/2^+$),^{30}Ne)	0.00	0^+_1	$s_{1/2}$	151.48	0.011	1.78	33(15)	19(8)
S_{1n}(^{31}Ne) = 0.11 MeV	1.05	2^+_1	$d_{3/2}$	26.20	0.255	7.13		
			$d_{5/2}$	28.66	0.001	0.03		
	2.68	0^+_2	$s_{1/2}$	34.73	0.100	3.71		
	3.08	2^-_1	$p_{3/2}$	37.11	0.072	2.95		
	3.10	2^+_2	$d_{3/2}$	18.38	0.291	5.71		
			$d_{5/2}$	20.10	0.000	0.00		
	3.27	3^-_1	$f_{7/2}$	19.18	1.141	24.15		
	3.33	1^-_1	$p_{3/2}$	36.81	0.175	7.11		
		Inclusive				52.56	90(7)	1.71(13)

Table 5.3: Results for one-neutron removal reaction from ^{31}Ne on the C target. Tabulated are the one-neutron removal cross sections to assumed bound states in the mass $A-1$ systems, ^{30}Ne, of 3.16(30) MeV. The final theoretical cross sections, σ^{th}_{-1n}, include the center-of-mass correction factor $[A/(A-1)]^N$. The errors shown for the ratio of cross sections, $R_s = \sigma^{exp}_{-1n}/\sigma^{th}_{-1n}$, reflect only the errors quoted on the measurements.

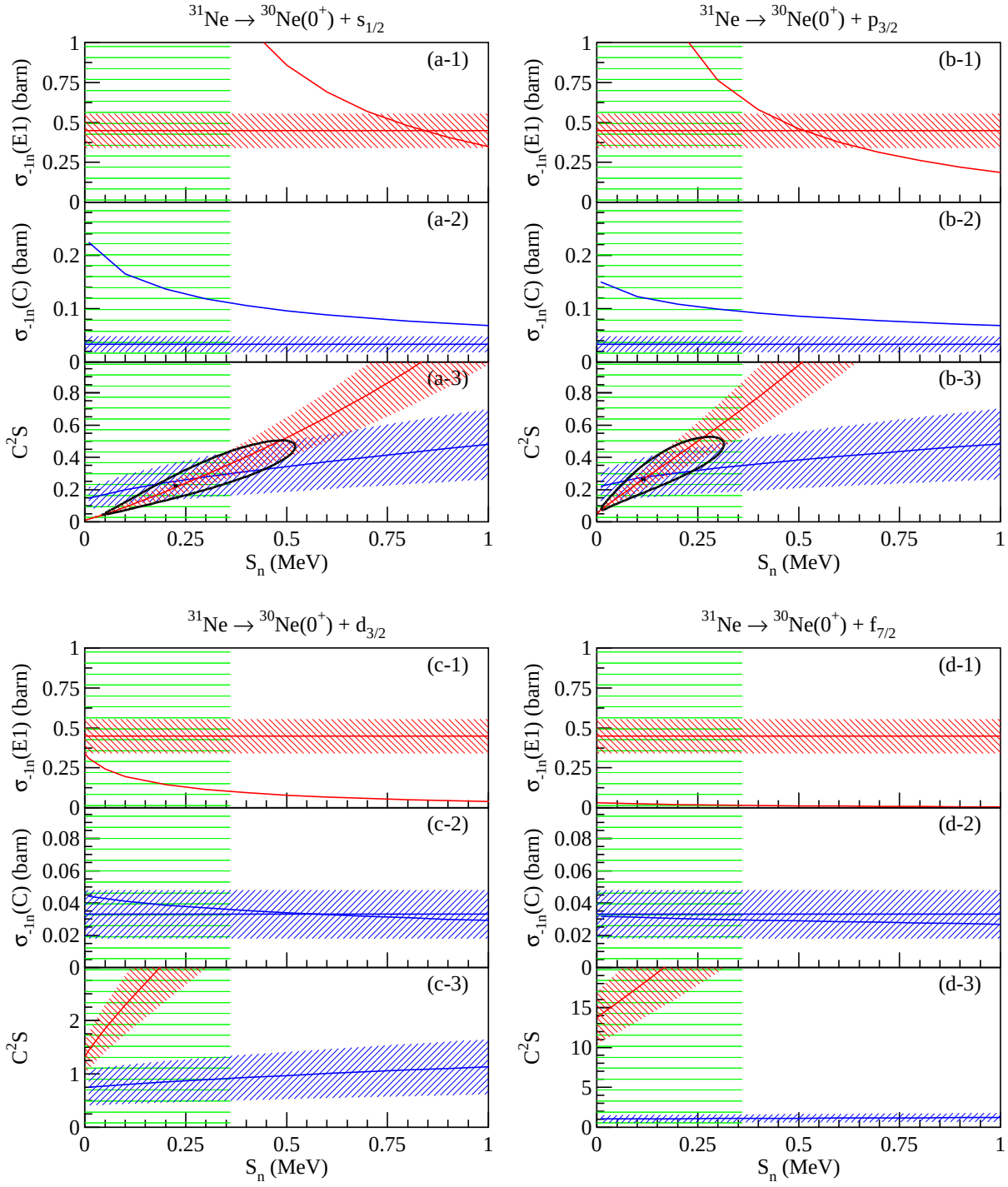

Figure 5.2: (a-1) The single-particle cross section $\sigma_{\rm sp}(E1, 2s_{1/2}, S_n)$ for the $2s_{1/2}$ neutron removal from ^{31}Ne as a function of S_n (red curve) and measured Coulomb breakup cross section $\sigma^{\rm exp}_{-1n}(E1, 0^+_{\rm g.s.})$ (red hatched area) are shown. (a-2) The single-particle cross section $\sigma_{\rm sp}({\rm C}, 2s_{1/2}, S_n)$ as a function of S_n (blue curve) and measured one-neutron removal cross section $\sigma^{\rm exp}_{-1n}({\rm C}, 0^+_{\rm g.s.})$ (blue hatched area) are shown. (a-3) The red and blue hatched areas show the possible C^2S values obtained from Eqs. 5.8 and 5.9, respectively, for the $2s_{1/2}$ neutron removal reactions. The green area shows the separation energy value from the mass measurement. The overlap area among red, blue, and green hatched areas is experimentally accepted if the $2s_{3/2}$ neutron removal is assumed. The figures labeled as (b), (c), and (d) show the results for the $2s_{1/2}$-, $1d_{3/2}$-, and $1f_{7/2}$-neutron removal reactions, respectively. Each black line represents the 68 % confidence levels.

Nucleus	J^π	Energy (MeV)
^{31}Ne	$3/2^-$	0.00
	$7/2^-$	0.65
	$3/2^+$	0.68
	$1/2^+$	0.99

Table 5.2: Low-lying shell-model levels for ^{31}Ne calculated with the SDPF-M interaction [52] are listed. The state of 0.00 MeV corresponds the ground states. Only the yrast states are shown.

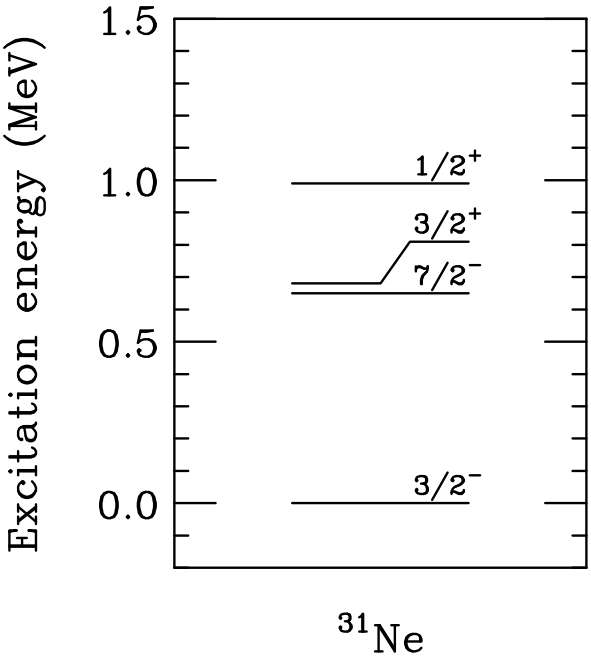

Figure 5.3: Low-lying shell-model level scheme for ^{31}Ne with the SDPF-M interaction [52] are listed. The state of 0.00 MeV corresponds the ground states. Only the yrast states are shown.

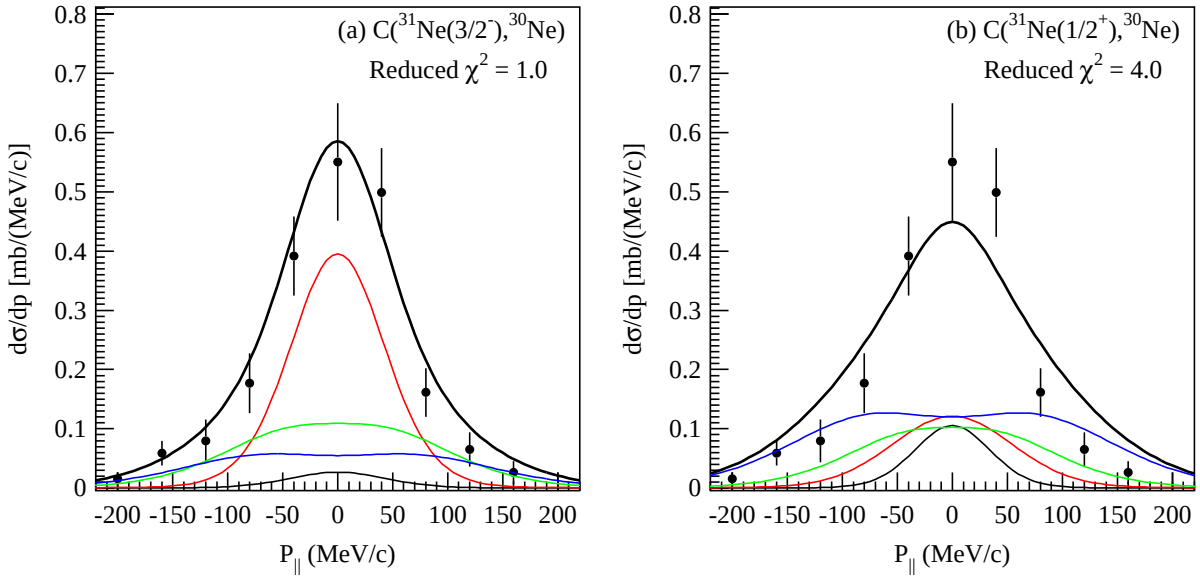

Figure 5.4: Measured parallel momentum distribution of one-neutron removal form ^{31}Ne and corresponding theoretical distribution for (a) $1/2^+$ and (b) $3/2^-$ shell model states of ^{30}Ne. The black, red, green, and blue thin lines show the s-, p-, d-, and f-wave component tabulated in Table 5.4. Each partial cross section is the sum of the same angular orbital components. The black thick line shows a sum of the four lines. The theoretical momentum distribution curves are normalised to the measured inclusive cross section.

5.5 Momentum distributions

We now examine the momentum distribution of ^{31}Ne + C $\rightarrow$ ^{30}Ne + X (inclusive) with the shell model calculations. Figure 5.4 shows the obtained momentum distribution compared with those calculations based on the eikonal model with the shell model calculations shown in Table 5.4. The theoretical momentum distributions for (a) $3/2^-$ and (b) $1/2^+$ shell-model states are shown. Black, red, green, and blue thin lines show the s-, p-, d-, and f-neutron removal components tabulated in Table 5.4. Here, we normalized the calculated cross sections to match the experimental one as in $R_s = \sigma^{\rm exp}_{-1n}({\rm C})/\sigma^{\rm th}_{-1n}({\rm C})$. Each partial cross section is the sum of the same angular orbital components. The distributions are calculated based on the eikonal-reaction model. The good agreement in the result for $3/2^-$ shell model state supports the $3/2^-$ ground state of ^{30}Ne.

To check the consistency of the results, we now use C^S values obtained from the combined analysis for the $^{30}{\rm Ne}(0^+_1) \otimes \phi_{n\ell j}$. Table 5.5 shows the such results, where only C^2S for the $^{30}{\rm Ne}(0^+_1) \otimes 2p_{3/2}$ and the experimental E_x of the first excited state is used The change from Table 5.4 is shown by red numbers. Table 5.5 includes C^2S coupled to the first 0^+ state, 0^+_1, of 0.26, which obtained from the combined analysis. Furthermore, the measured excitation energy of 2^+ of $E_x = 0.801(7)$ MeV [45,56] is adapted. Similarly, Table 5.5 shows the case of Coulomb breakup reaction. The theoretical cross sections are in agreement with the experimental values within errors. Using these cross sections, the momentum distribution of ^{30}Ne is plotted in Figure 5.5. In the figure, the p-neutron removal components coupled to 0^+ and 2^+ final states are plotted exclusively. The red dashed- and doted-lines show the p-wave components to the 0^+ and 2^+state of the fragment, respectively. The experimental data are found to be explained well by the calculations. All of these results are consistent with the calculations for $3/2^-$ ground state of ^{31}Ne. Therefore, the $3/2^-$ ground state is suggested.

Reaction	E_x (MeV)	J^π	ℓ_j	σ_{sp} (mb)	C^2S	σ^{th}_{-1n}(C) (mb)	σ^{exp}_{-1n}(C) (mb)	R_s
C(^{31}Ne(3/2$^-$),^{30}Ne)	0.00	0^+_1	$p_{3/2}$	109.66	0.26	31.4	33(15)	1.05(48)
S_{1n}(^{31}Ne) = 0.11 MeV	0.80	2^+_1	$p_{3/2}$	64.10	0.265	18.74		
			$f_{7/2}$	24.66	0.158	4.30		
	2.42	4^+_1	$f_{7/2}$	20.61	0.592	13.46		
	2.68	0^+_2	$p_{3/2}$	39.67	0.013	0.57		
	3.08	2^-_1	$s_{1/2}$	31.78	0.019	0.64		
			$d_{3/2}$	18.43	0.618	12.16		
			$d_{5/2}$	20.15	0.000	0.00		
	3.10	2^+_2	$p_{3/2}$	36.99	0.058	2.37		
			$f_{7/2}$	19.44	0.053	1.14		
	3.27	3^-_1	$d_{3/2}$	18.00	0.528	10.15		
			$d_{5/2}$	19.67	0.006	0.13		
	3.33	1^-_1	$s_{1/2}$	30.20	0.075	2.42		
			$d_{3/2}$	17.87	0.181	3.45		
			$d_{5/2}$	19.52	0.001	0.02		
		Inclusive				101.01	90(7)	0.89(7)

Table 5.4: Results for one-neutron removal reaction from ^{31}Ne on the C target. Tabulated are the one-neutron removal cross sections to assumed bound states in the mass $A-1$ systems, ^{30}Ne, of 3.16(30) MeV. The final theoretical cross sections, σ^{th}_{-1n}, include the center-of-mass correction factor $[A/(A-1)]^N$. The errors shown for the ratio of cross sections, $R_s = \sigma^{exp}_{-1n}/\sigma^{th}_{-1n}$, reflect only the errors quoted on the measurements.

Reaction	E_x (MeV)	J^π	ℓ_j	σ_{sp} (mb)	C^2S	$\sigma^{th}_{-1n}(E1)$ (mb)	$\sigma^{exp}_{-1n}(E1)$ (mb)	R_s
Pb(^{31}Ne(3/2$^-$),^{30}Ne)	0.00	0^+_1	$p_{3/2}$	1564.74	0.26	468.64	448(108)	0.96(23)
S_{1n}(^{31}Ne) = 0.11 MeV	0.80	2^+_1	$p_{3/2}$	218.01	0.265	57.77		
			$f_{7/2}$	6.27	0.158	0.99		
	2.42	4^+_1	$f_{7/2}$	0.06	0.592	0.04		
	2.68	0^+_2	$p_{3/2}$	4.19	0.013	0.05		
	3.08	2^-_1	$s_{1/2}$	0.14	0.019	0.00		
			$d_{3/2}$	0.02	0.618	0.01		
			$d_{5/2}$	0.01	0.000	0.00		
	3.10	2^+_2	$p_{3/2}$	0.45	0.058	0.03		
			$f_{7/2}$	0.00	0.053	0.00		
	3.27	3^-_1	$d_{3/2}$	0.01	0.528	0.01		
			$d_{5/2}$	0.00	0.006	0.00		
	3.33	1^-_1	$s_{1/2}$	0.03	0.075	0.00		
			$d_{3/2}$	0.00	0.181	0.00		
			$d_{5/2}$	0.00	0.001	0.00		
		Inclusive				527.54	529(63)	1.00(12)

Table 5.5: Results for one-neutron removal Coulomb breakup reaction from ^{31}Ne. Tabulated are the one-neutron removal cross sections to assumed bound states in the mass $A-1$ systems, ^{30}Ne, of 3.16(30) MeV. The final theoretical cross sections, σ^{th}_{-1n}, include the center-of-mass correction factor $[A/(A-1)]^N$. The errors shown for the ratio of cross sections, $R_s = \sigma^{exp}_{-1n}/\sigma^{th}_{-1n}$, reflect only the errors quoted on the measurements.

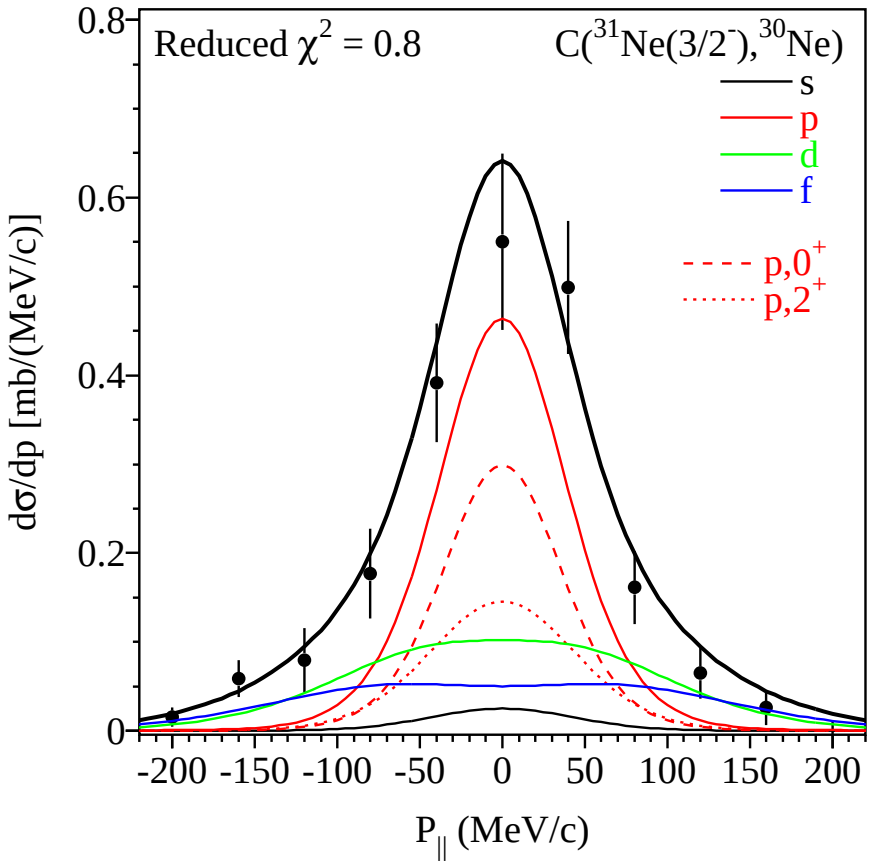

Figure 5.5: Measured parallel momentum distribution of one-neutron removal form ^{31}Ne and corresponding theoretical distribution for the $3/2^-$ ground state of ^{31}Ne. The black, red, green, and blue thin solid lines show the s-, p-, d-, and f-wave components tabulated in Table 5.5. Each partial cross section is the sum of the same angular orbital components. The black thick line shows a sum of the four lines. The red dashed- and doted-lines show the p-wave components to the 0^+ and 2^+state of the fragment, respectively.

5.6 Comparison with Nilsson model

The results in Table 5.5 show that the spectroscopic factors are fragmented among many states. The mixed ground-state configuration is consistent with ^{31}Ne lying within the island of inversion and, as such, suggests that it will be strongly deformed. It is thus interesting to describe the structure of ^{31}Ne as a weakly bound neutron in a deformed potential [60–62]. For instance, the Nilsson diagram in Fig. 5.6 show that the 21th neutron with $J^\pi = 3/2^-$ should be located at the [330 1/2] level with $J^\pi = 3/2^-$ ($0.23 \leq \beta \leq 0.29$) or [321 3/2] level with $J^\pi = 3/2^-$ ($0.40 \leq \beta \leq 0.59$) which involve the $p_{3/2}$ configuration. The [330 1/2] level with $J^\pi = 3/2^-$ is corresponding to the 1 particle -0 hole (1p-0h) state $[(\nu p_{3/2})^1]$. The [321 3/2] level with $J^\pi = 3/2^-$ is corresponding to the 3p-2h state $[(\nu p_{3/2})^3(\nu d_{3/2})^{-2}]$ or $[(\nu p_{3/2})^1(\nu f_{7/2})^2(\nu d_{3/2})^{-2}]$. In both cases of [330 1/2] and [321 3/2], $\nu p_{3/2}$ orbital is dominant over the $\nu f_{3/2}$ orbital. This suggests that the $N = 20$ and 28 shell gaps are melting. To occupy the levels, the ground state of ^{31}Ne needs to be deformed. As a result, ^{31}Ne is found to be a deformed p-wave neutron halo nucleus with $J^\pi = 3/2^-$ in the island of inversion. It should be noted that in Refs. [60, 61] the low-ℓ configurations are shown to become dominant as the separation energy approaches zero.

According to reaction cross section measurement by Takechi *et al.*, they suggest that the

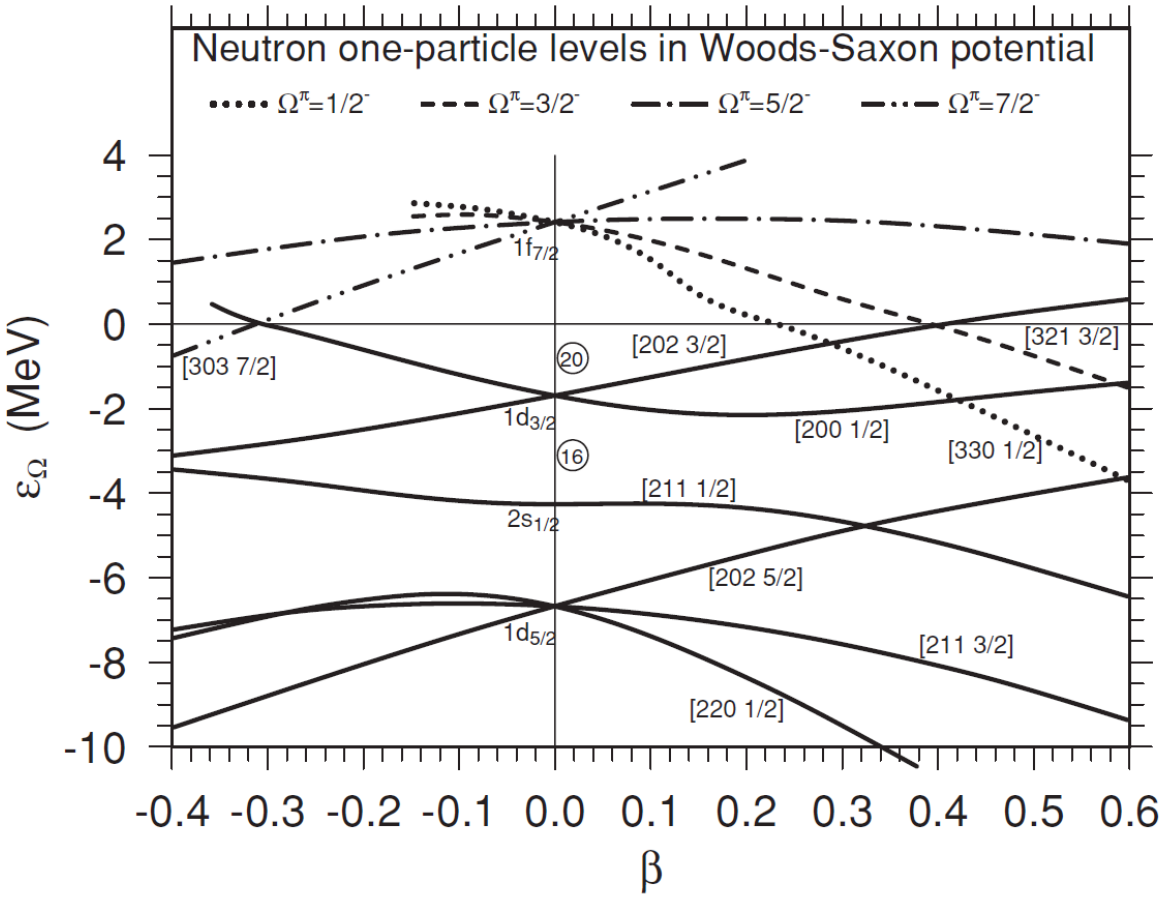

Figure 5.6: Nilsson diagram for ^{31}Ne taken from [62]. The figure shows the neutron one-particle levels as a function of quadrupole deformation. Parameters of the Woods-Saxson potential are designed approximately for the nucleus ^{31}Ne. One-particle levels are denoted by the asymptotic quantum numbers $[Nn_z\Lambda\Omega]$. The $\Omega^\pi = 1/2^-$ levels are denoted by dotted curves, the $3/2^-$ levels by dashed curves, the $5/2^-$ levels by dot-dashed curves, the $7/2^-$ levels by dot-dot-dashed curves, while positive-parity levels are plotted by solid curves.

21th neutron is considered to be located in the Nilsson level of [330 1/2] with $J^\pi = 3/2^-$, [321 3/2] with $J^\pi = 3/2^-$, or [200 1/2] with $J^\pi = 1/2^+$, which is consistent with our results.

Chapter 6

Experimental Results and Discussions for ^{29}Ne, ^{33,35,37}Mg, and ^{39,41}Si

6.1 General description

This Chapter describes the results and discussions on the Coulomb and nuclear breakup of neutron-rich even-odd nucleus ^{29}Ne, ^{33,35,37}Mg, and ^{39,41}Si isotopes near $N = 20$ and 28. Sections 6.2 and 6.3 show the inclusive and semi-inclusive cross sections, respectively, with the lead and carbon targets. Section 6.4 shows how the combination of inclusive and semi-inclusive Coulomb and nuclear breakup can clarify the single-particle state of these nuclei, as demonstrated for the case of ^{31}Ne shown in the previous chapter (Chapter 5). In Sec. 6.5–6.10, we compare the inclusive and semi-inclusive cross sections of ^{29,31}Ne, ^{33,35,37}Mg, and ^{39,41}Si isotopes with shell-model calculations and discuss the shell structure of each nucleus. The momentum distributions are also compared with the calculations based on eikonal reaction model and shell model.

6.2 Inclusive Breakup Cross Sections

The measured inclusive one-neutron removal cross sections of the ^{29,31}Ne, ^{33,35,37}Mg, and ^{39,41}Si isotopes with the lead target, $\sigma^{\rm exp}_{-1n}$(Pb), and carbon target, $\sigma^{\rm exp}_{-1n}$(C), are listed in Table 6.1, which are labeled as "(Inclusive)". The table also shows the Coulomb breakup cross sections, $\sigma^{\rm exp}_{-1n}(E1)$, which are obtained from the cross sections $\sigma^{\rm exp}_{-1n}$(Pb) and $\sigma^{\rm exp}_{-1n}$(C) according to Eq. (5.2–5.5). Figure 6.1 (a) shows the systematics of these cross sections.

The Coulomb breakup cross section $\sigma^{\rm exp}_{-1n}(E1)$ of 222(36) mb for ^{29}Ne ($S_{1n} = 0.95(15)$ MeV) is much smaller than that for ^{31}Ne of 529(60) mb, although it is significantly larger than that for the ordinary nuclei. This may show that ^{29}Ne has a moderate strength of soft $E1$ excitation. The cross section $\sigma^{\rm exp}_{-1n}(E1)$ of 491(54) mb for ^{37}Mg ($S_{1n} = 0.25(1.03)$ MeV) is almost as large as that for the one-neutron halo nucleus ^{31}Ne and ^{19}C (see Table. 5.1). This result suggests that ^{37}Mg has halo structure. On the other hand, $\sigma^{\rm exp}_{-1n}(E1)$ for ^{33}Mg ($S_{1n} = 2.22(3)$ MeV) and ^{35}Mg ($S_{1n} = 0.99(20)$ MeV) are 250(47) mb and 242(43) mb, respectively, smaller than that for ^{37}Mg, although these $\sigma^{\rm exp}_{-1n}(E1)$ values are significantly larger than the ordinary nuclei. In general, the Coulomb breakup cross section is sensitive to the separation energy and angular momentum of the valence neutron and hence the spin-parity of the ground state. We should note that although the separation energy of ^{33}Mg is about twice that of ^{35}Mg, the cross sections are almost identical. In Si isotopes, the cross section of ^{41}Si ($S_{1n} = 1.38(44)$ MeV) is larger than

that of ^{39}Si (S_{1n} = 1.58(11) MeV). In the following sections, further analysis is made to extract the single-particle configuration of the ground state of these nuclei.

	$\bar{E}/A$ (MeV)		$\sigma^{\rm exp}_{-1n}$(Pb)	$\sigma^{\rm exp}_{-1n}$(C)	$\sigma^{\rm exp}_{-1n}(E1)$
Reaction	Pb	C	(mb)	(mb)	(mb)
(^{29}Ne, ^{28}Ne) (Inclusive)	244	240	379(14)	74(2)	222(36)
(^{29}Ne, ^{28}Ne(2^+, 4^+, etc.))			113(43)	28(7)	53(47)
(^{29}Ne, ^{28}Ne(0^+))			266(45)	45(7)	169(59)
(^{31}Ne, ^{30}Ne) (Inclusive)	234	230	720(61)	90(7)	529(63)
(^{31}Ne, ^{30}Ne(2^+, 4^+, etc.))			202(83)	57(13)	81(87)
(^{31}Ne, ^{30}Ne(0^+))			518(103)	33(15)	448(108)
(^{33}Mg, ^{32}Mg) (Inclusive)	234	229	461(9)	99(1)	250(47)
(^{33}Mg, ^{32}Mg(2^+, 4^+, etc.))			328(47)	54(7)	213(55)
(^{33}Mg, ^{32}Mg(0^+))			133(47)	45(7)	38(72)
(^{35}Mg, ^{34}Mg) (Inclusive)	245	241	420(18)	84(1)	242(43)
(^{35}Mg, ^{34}Mg(2^+, 4^+, etc.))			351(67)	51(7)	243(72)
(^{35}Mg, ^{34}Mg(0^+))			69(69)	33(7)	-2(84)
(^{37}Mg, ^{36}Mg) (Inclusive)	244	240	660(38)	80(4)	491(54)
(^{37}Mg, ^{36}Mg(2^+, 4^+, etc.))			182(84)	48(10)	79(90)
(^{37}Mg, ^{36}Mg(0^+))			479(92)	32(11)	411(105)
(^{39}Si, ^{38}Si) (Inclusive)	224	218	390(7)	94(1)	193(45)
(^{39}Si, ^{38}Si(2^+, 4^+, etc.))			343(47)	71(9)	193(61)
(^{39}Si, ^{38}Si(0^+))			47(48)	22(9)	0(76)
(^{41}Si, ^{40}Si) (Inclusive)	229	224	516(13)	110(1)	284(54)
(^{41}Si, ^{40}Si(2^+, 4^+, etc.))			299(49)	62(8)	169(59)
(^{41}Si, ^{40}Si(0^+))			217(50)	48(8)	115(80)

Table 6.1: One- and two-neutron removal cross sections for each reaction channel at the mid-target energies ($\bar{E}/A$) are shown. The inclusive cross sections are labeled as "(inclusive)". The partial semi-inclusive cross sections connecting to the excited states of the fragments are labeled as "(2^+, 4^+, etc.)". The 0^+ partial cross sections are labeled as "(0^+)". As is discussed in Sec. 6.3, the 0^+ partial cross sections $\sigma^{\rm exp}_{-1n}$(Pb) and $\sigma^{\rm exp}_{-1n}$(C) can be suppressed. Therefore, the cross sections in the table represent an upper limit.

6.3 Semi-Inclusive Breakup Cross Sections

In Table 6.1, the cross sections corresponding to the transitions of $2^+_1 \rightarrow 0^+_{\rm g.s.}$ obtained from γ-ray analysis in Sec. 4.6 are listed. The cross sections are labeled as "(2^+, 4^+, etc.)" with the fragment nuclei. By subtracting the cross sections of $2^+_1 \rightarrow 0^+_{\rm g.s.}$ from the inclusive cross sections, we estimate the cross sections to $0^+_{\rm g.s.}$ state of the fragments. The cross sections are listed in Table 6.1, which are labeled as "(0^+)" for the fragment nuclei. This estimation assumes that the direct decay from the sates higher than 2^+_1 state can be neglected. If this assumption Therefore, the listed values in the table show the upper limits of the cross sections to the 0^+ ground state.

The semi-inclusive one-neutron removal cross sections to the 0^+ ground states for the reactions on the lead target, $\sigma^{\rm exp}_{-1n}$(Pb, $0^+_{\rm g.s.}$), nuclear breakup reactions on the C target, $\sigma^{\rm exp}_{-1n}$(C, $0^+_{\rm g.s.}$), and the Coulomb breakup reactions , $\sigma^{\rm exp}_{-1n}(E1,\ 0^+_{\rm g.s.})$, are summarized in Fig. 6.1 (b). We found that the cross sections $\sigma^{\rm exp}_{-1n}(E1,\ 0^+_{\rm g.s.})$ for ^{29}Ne, ^{37}Mg, and ^{41}Si are significantly large, which suggest that these nuclei have a configuration that the valence neutron with low-ℓ angular momentum is coupled to the ground state as in the case of ^{31}Ne. The Coulomb breakup cross sections for ^{35}Mg and ^{39}Si are consistent with 0 mb, which suggest that these nuclei have a configuration that the valence neutron with low-ℓ angular momentum is coupled to the 2^+ or higher excited states, or the enhancement of $E1$ strength is due to other mechanism than the soft $E1$ excitation.

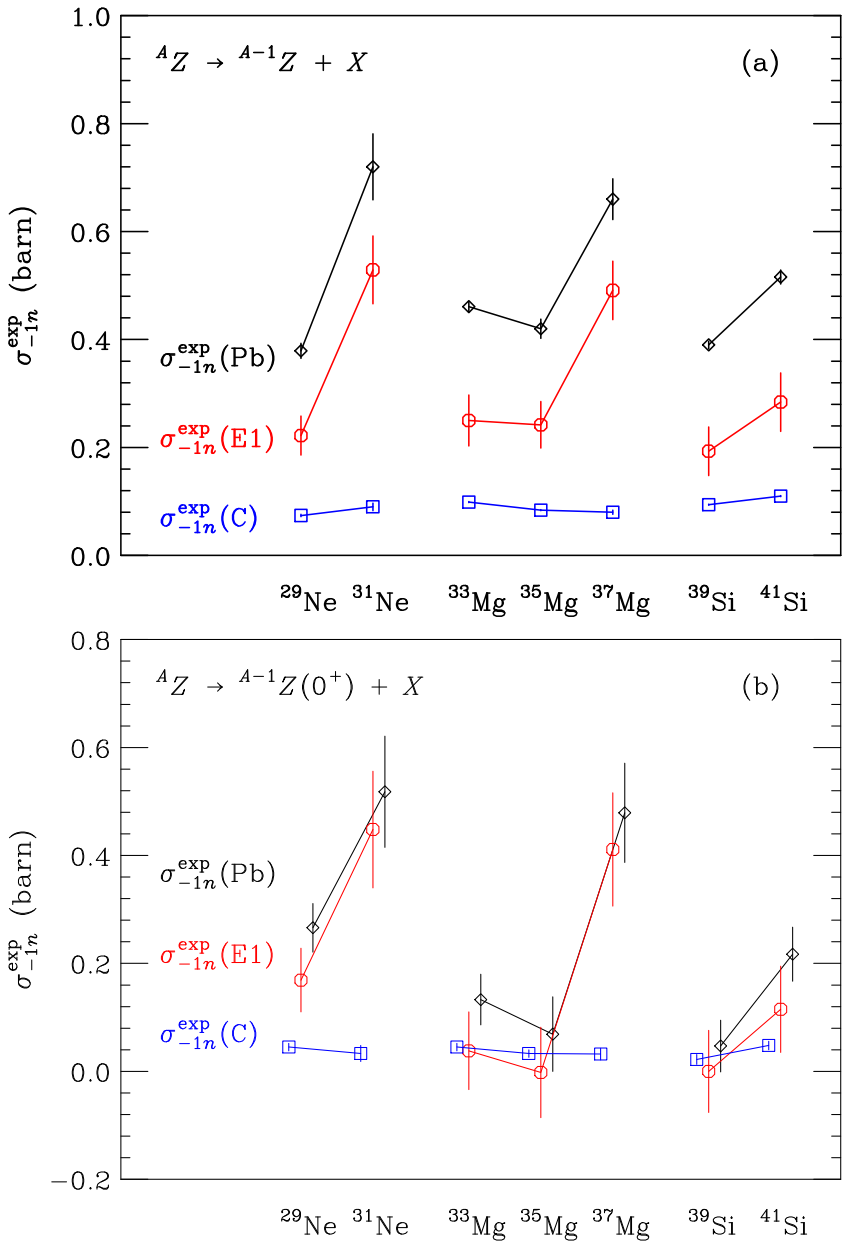

Figure 6.1: The figure shows (a) experimental inclusive one-neutron cross sections of ^{29,31}Ne, ^{33,35,37}Mg, and ^{39,41}Si and (b) experimental partial cross sections connecting to 0^+ of the fragments for each reactions. The black diamonds, blue squares, and red circles represent $\sigma^{\rm exp}_{-1n}(Pb)$, $\sigma^{\rm exp}_{-1n}(C)$, and $\sigma^{\rm exp}_{-1n}(E1)$, respectively.

6.4 Combined Analysis of the Coulomb and Nuclear Breakup

In the same manner as in Sec. 5.3, the spectroscopic factor $C^2S(0^+, n\ell j)$ and separation energy S_{1n} are estimated. Figures 6.2, 6.3, 6.4, 6.5, 6.6, and 6.7 show the cases for one-neutron removal from ^{29}Ne, ^{33,35,37}Mg and ^{39,41}Si, respectively. Each result is discussed in Secs. 6.5–6.10.

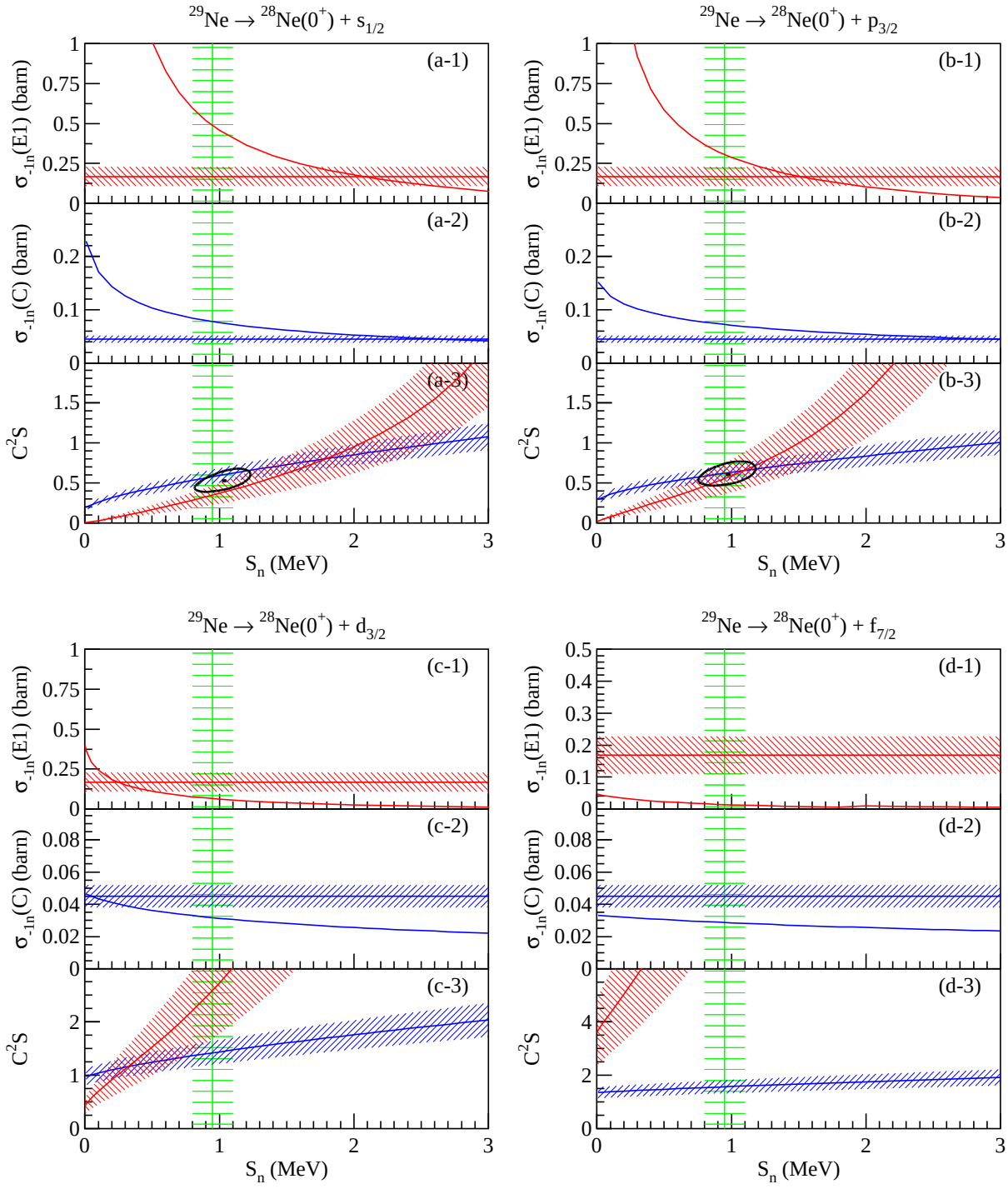

Figure 6.2: (a-1) The single-particle cross section $\sigma_{\rm sp}(E1, 2s_{1/2}, S_{1n})$ for the $2s_{1/2}$ neutron removal from ^{29}Ne as a function of S_{1n} (red curve) and measured Coulomb breakup cross section $\sigma^{\rm exp}_{-1n}(E1, 0^+_{\rm g.s.})$ (red hatched area) are shown. (a-2) The single-particle cross section $\sigma_{\rm sp}({\rm C}, 2s_{1/2}, S_{1n})$ as a function of S_{1n} (blue curve) and measured one-neutron removal cross section $\sigma^{\rm exp}_{-1n}({\rm C}, 0^+_{\rm g.s.})$ (blue hatched area) are shown. (a-3) The red and blue hatched areas show the possible C^2S values obtained from Eqs. 5.8 and 5.9, respectively, for the $2s_{1/2}$ neutron removal reactions. The green area shows the separation energy value from the mass measurement. The figures labeled as (b), (c), and (d) show the results for the $2s_{1/2}$-, $1d_{3/2}$-, and $1f_{7/2}$-neutron removal reactions, respectively. The black line represents the 68 % confidence level.

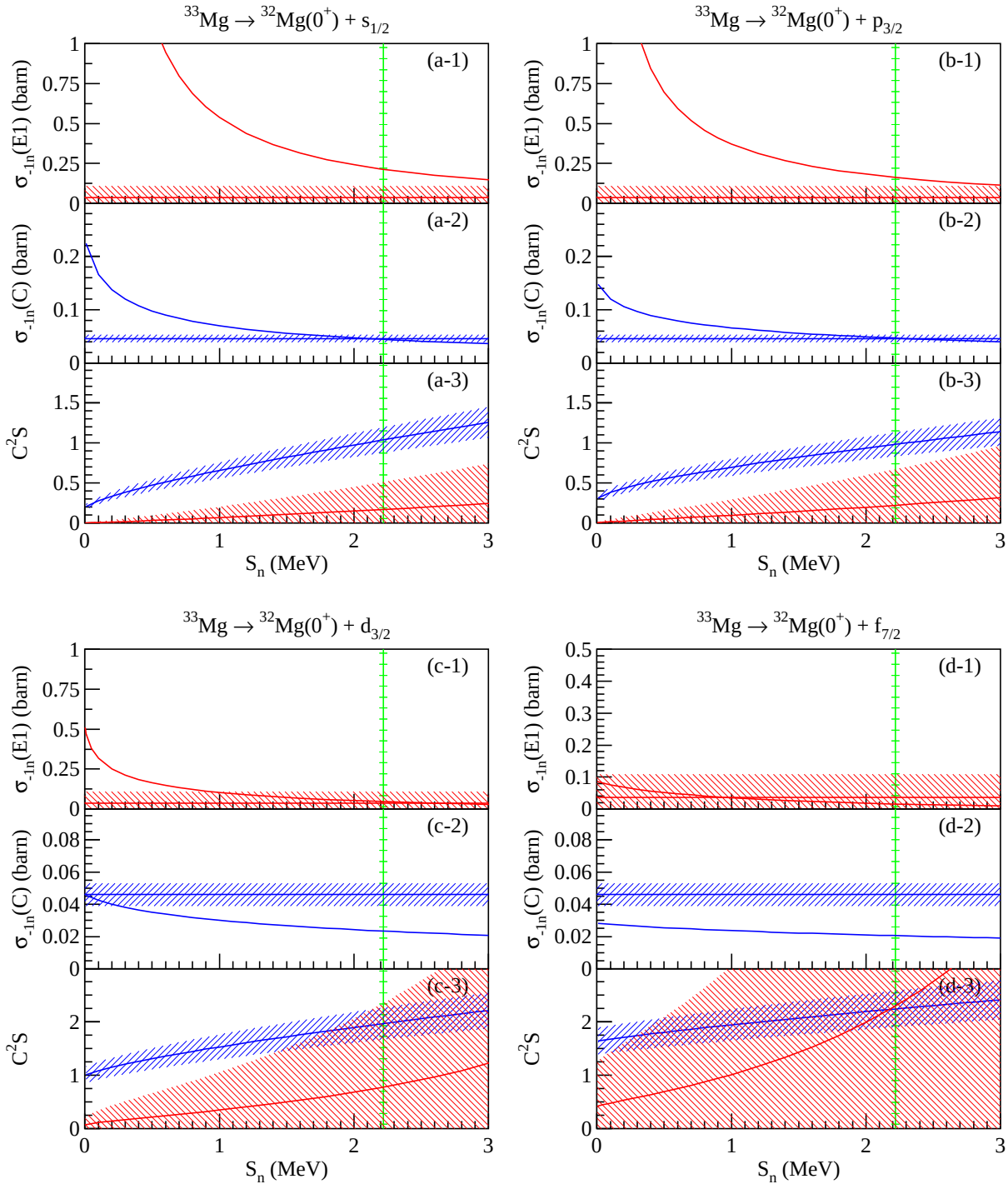

Figure 6.3: (a-1) The single-particle cross section $\sigma_{\rm sp}(E1, 2s_{1/2}, S_{1n})$ for the $2s_{1/2}$ neutron removal from ^{33}Mg as a function of S_{1n} (red curve) and measured Coulomb breakup cross section $\sigma^{\rm exp}_{-1n}(E1, 0^+_{\rm g.s.})$ (red hatched area) are shown. (a-2) The single-particle cross section $\sigma_{\rm sp}({\rm C}, 2s_{1/2}, S_{1n})$ as a function of S_{1n} (blue curve) and measured one-neutron removal cross section $\sigma^{\rm exp}_{-1n}({\rm C}, 0^+_{\rm g.s.})$ (blue hatched area) are shown. (a-3) The red and blue hatched areas show the possible C^2S values obtained from Eqs. 5.8 and 5.9, respectively, for the $2s_{1/2}$ neutron removal reactions. The green area shows the separation energy value from the mass measurement. The figures labeled as (b), (c), and (d) show the results for the $2s_{1/2}$-, $1d_{3/2}$-, and $1f_{7/2}$-neutron removal reactions, respectively.

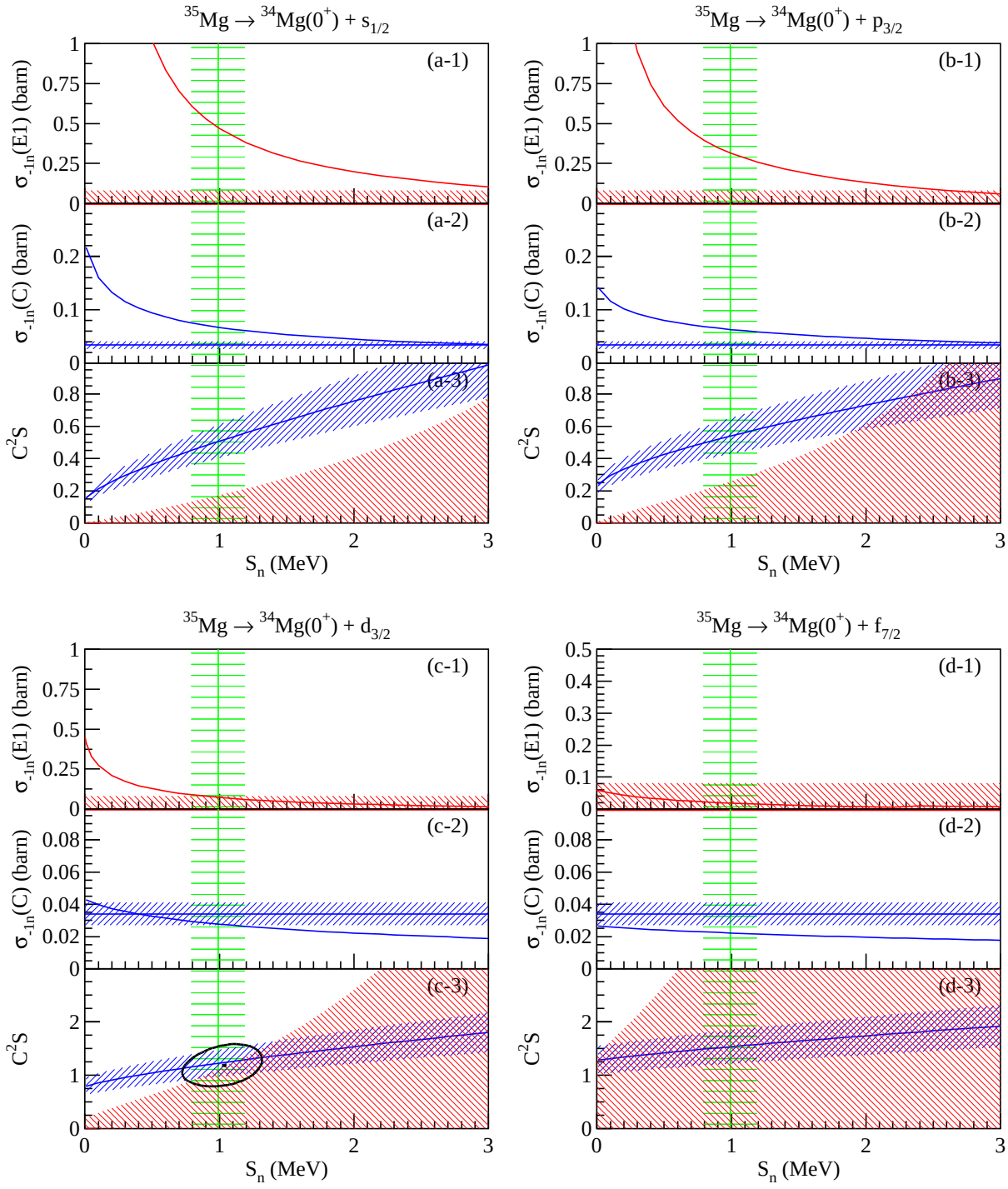

Figure 6.4: (a-1) The single-particle cross section $\sigma_{\rm sp}(E1, 2s_{1/2}, S_{1n})$ for the $2s_{1/2}$ neutron removal from ^{35}Mg as a function of S_{1n} (red curve) and measured Coulomb breakup cross section $\sigma^{\rm exp}_{-1n}(E1, 0^+_{\rm g.s.})$ (red hatched area) are shown. (a-2) The single-particle cross section $\sigma_{\rm sp}({\rm C}, 2s_{1/2}, S_{1n})$ as a function of S_{1n} (blue curve) and measured one-neutron removal cross section $\sigma^{\rm exp}_{-1n}({\rm C}, 0^+_{\rm g.s.})$ (blue hatched area) are shown. (a-3) The red and blue hatched areas show the possible C^2S values obtained from Eqs. 5.8 and 5.9, respectively, for the $2s_{1/2}$ neutron removal reactions. The green area shows the separation energy value from the mass measurement. The figures labeled as (b), (c), and (d) show the results for the $2s_{1/2}$-, $1d_{3/2}$-, and $1f_{7/2}$-neutron removal reactions, respectively. Each black line represents the 68 % confidence level.

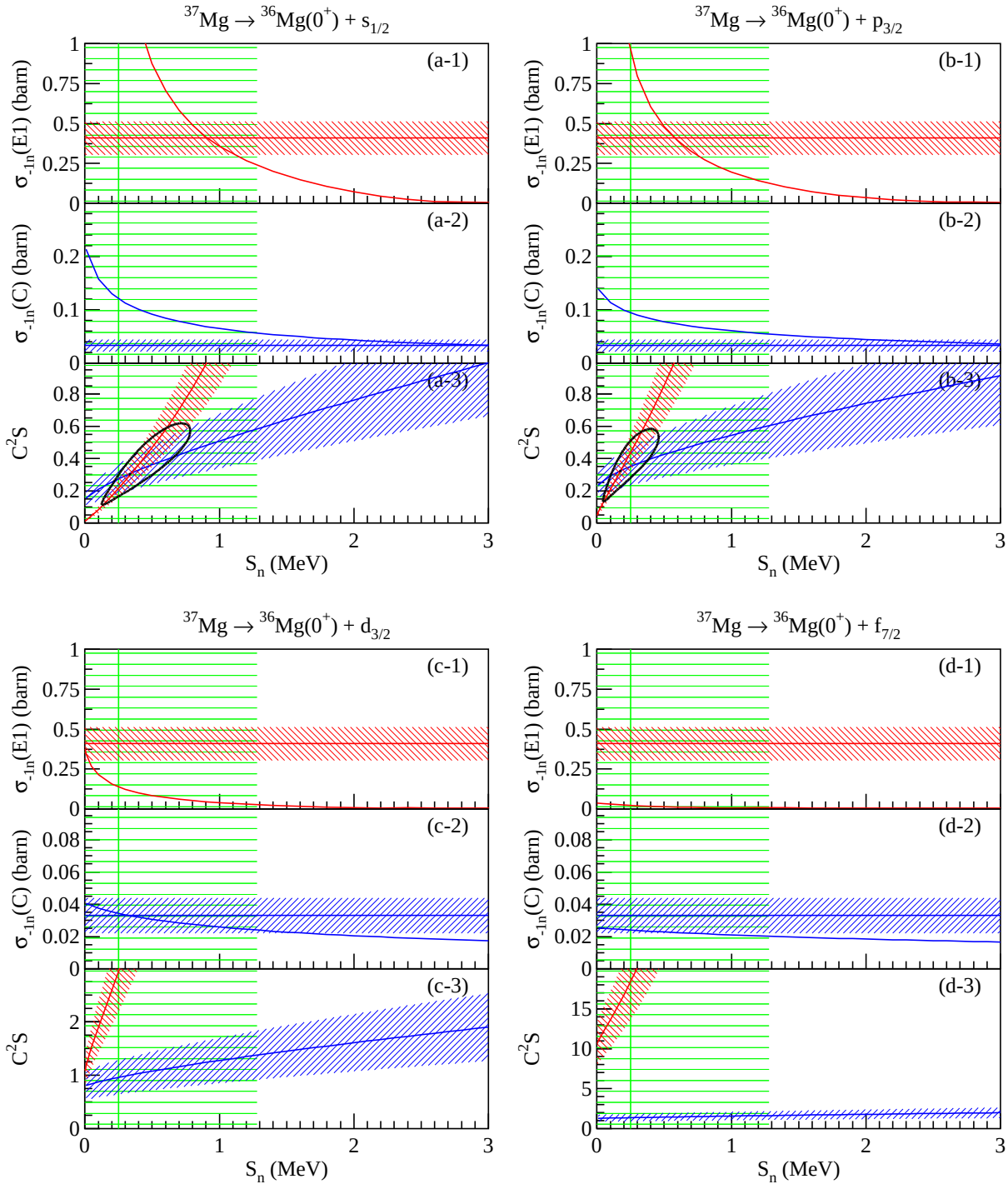

Figure 6.5: (a-1) The single-particle cross section $\sigma_{\rm sp}(E1, 2s_{1/2}, S_{1n})$ for the $2s_{1/2}$ neutron removal from ^{37}Mg as a function of S_{1n} (red curve) and measured Coulomb breakup cross section $\sigma^{\rm exp}_{-1n}(E1, 0^+_{\rm g.s.})$ (red hatched area) are shown. (a-2) The single-particle cross section $\sigma_{\rm sp}({\rm C}, 2s_{1/2}, S_{1n})$ as a function of S_{1n} (blue curve) and measured one-neutron removal cross section $\sigma^{\rm exp}_{-1n}({\rm C}, 0^+_{\rm g.s.})$ (blue hatched area) are shown. (a-3) The red and blue hatched areas show the possible C^2S values obtained from Eqs. 5.8 and 5.9, respectively, for the $2s_{1/2}$ neutron removal reactions. The green area shows the separation energy value from the mass measurement. The figures labeled as (b), (c), and (d) show the results for the $2s_{1/2}$-, $1d_{3/2}$-, and $1f_{7/2}$-neutron removal reactions, respectively. Each black line represents the 68 % confidence level.

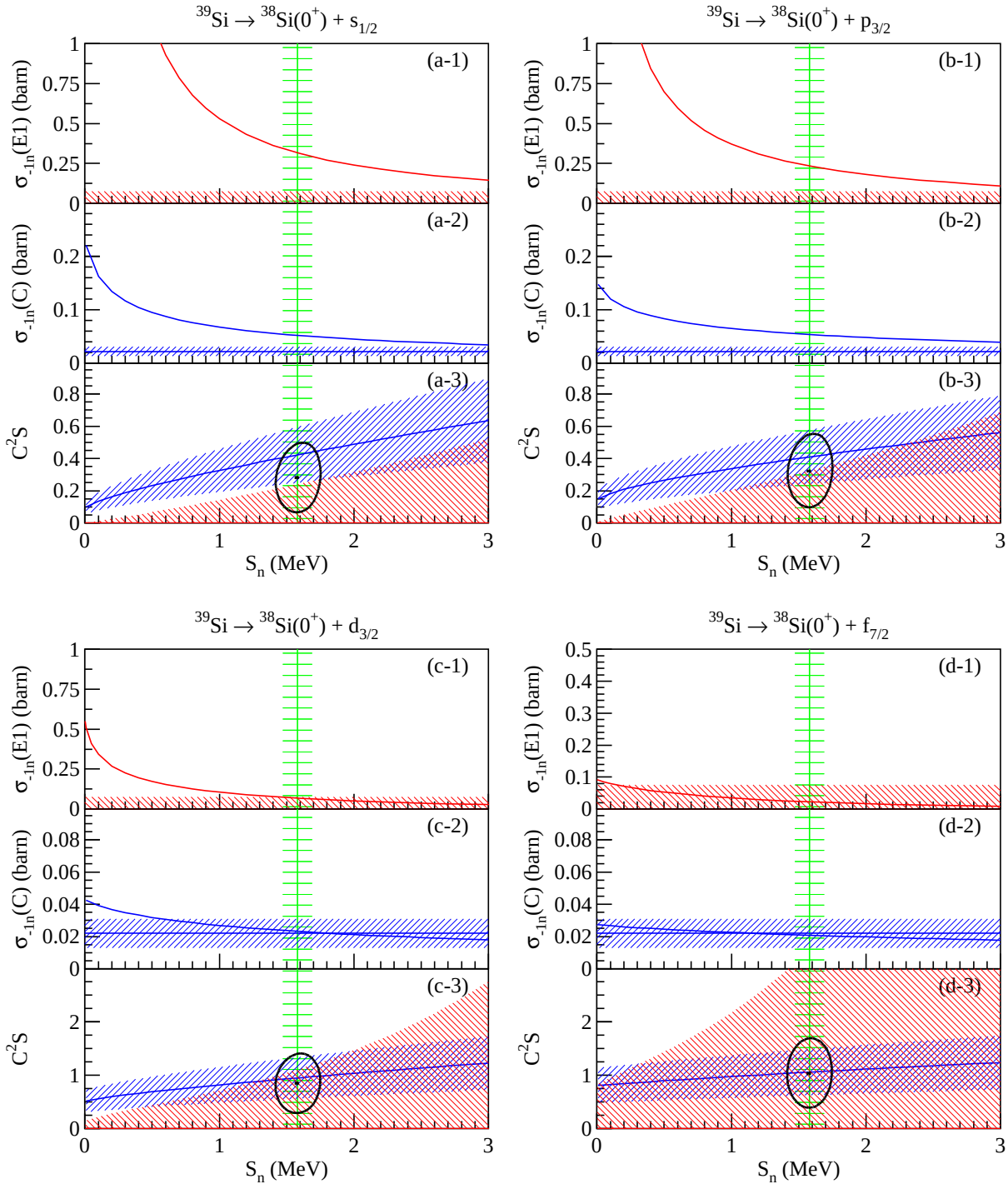

Figure 6.6: (a-1) The single-particle cross section $\sigma_{\rm sp}(E1, 2s_{1/2}, S_{1n})$ for the $2s_{1/2}$ neutron removal from ^{39}Si as a function of S_{1n} (red curve) and measured Coulomb breakup cross section $\sigma^{\rm exp}_{-1n}(E1, 0^+_{\rm g.s.})$ (red hatched area) are shown. (a-2) The single-particle cross section $\sigma_{\rm sp}({\rm C}, 2s_{1/2}, S_{1n})$ as a function of S_{1n} (blue curve) and measured one-neutron removal cross section $\sigma^{\rm exp}_{-1n}({\rm C}, 0^+_{\rm g.s.})$ (blue hatched area) are shown. (a-3) The red and blue hatched areas show the possible C^2S values obtained from Eqs. 5.8 and 5.9, respectively, for the $2s_{1/2}$ neutron removal reactions. The green area shows the separation energy value from the mass measurement. The figures labeled as (b), (c), and (d) show the results for the $2s_{1/2}$-, $1d_{3/2}$-, and $1f_{7/2}$-neutron removal reactions, respectively. Each black line represents the 68 % confidence level.

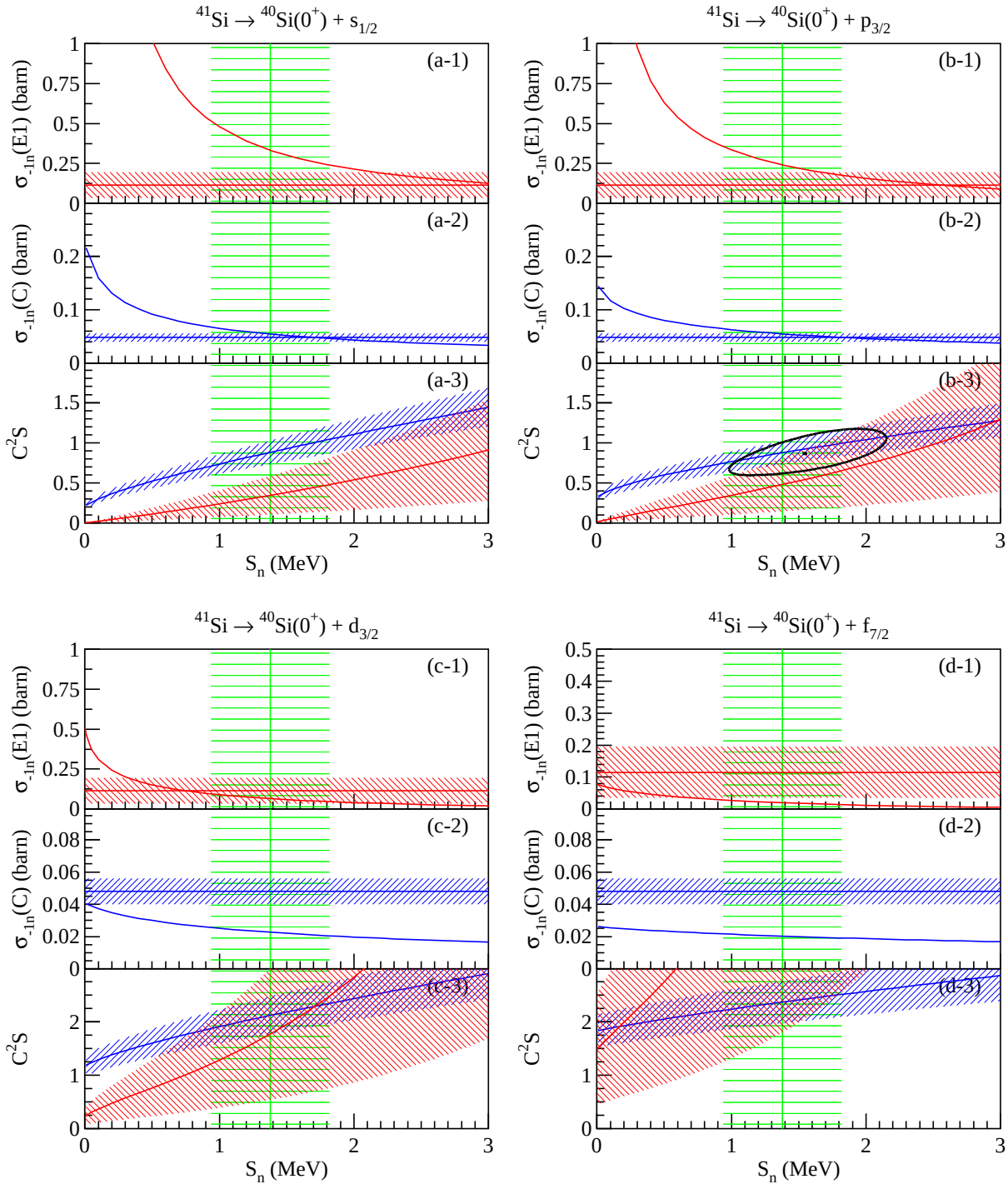

Figure 6.7: (a-1) The single-particle cross section $\sigma_{\rm sp}(E1, 2s_{1/2}, S_{1n})$ for the $2s_{1/2}$ neutron removal from ^{41}Si as a function of S_{1n} (red curve) and measured Coulomb breakup cross section $\sigma^{\rm exp}_{-1n}(E1, 0^+_{\rm g.s.})$ (red hatched area) are shown. (a-2) The single-particle cross section $\sigma_{\rm sp}({\rm C}, 2s_{1/2}, S_{1n})$ as a function of S_{1n} (blue curve) and measured one-neutron removal cross section $\sigma^{\rm exp}_{-1n}({\rm C}, 0^+_{\rm g.s.})$ (blue hatched area) are shown. (a-3) The red and blue hatched areas show the possible C^2S values obtained from Eqs. 5.8 and 5.9, respectively, for the $2s_{1/2}$ neutron removal reactions. The green area shows the separation energy value from the mass measurement. The figures labeled as (b), (c), and (d) show the results for the $2s_{1/2}$-, $1d_{3/2}$-, and $1f_{7/2}$-neutron removal reactions, respectively. Each black line represents the 68 % confidence level.

6.5 Results for ^{29}Ne

The separation energy of ^{29}Ne ($S_{1n} = 0.95(15)$) is known from the mass measurement by Jurado *et al.* [33]. According to Fig. 6.2, the allowed configurations are $^{28}\mathrm{Ne}(0^+_1) \otimes 2p_{3/2}$ with $J^\pi = 3/2^-$ and $^{28}\mathrm{Ne}(0^+_1)) \otimes 2s_{1/2}$ with $J^\pi = 1/2^+$. From the same analysis of χ^2 for two parameters as described in Sec. 5.3, the spectroscopic factor $C^2S(0^+, 2s_{1/2})$ is extracted to be $0.53^{+0.10}_{-0.09}$, and the separation energy S_{1n} is $1.02^{+0.14}_{-0.14}$ MeV. From Fig. (b-3), $C^2S(0^+, 2p_{3/2}$ is $0.61^{+0.10}_{-0.10}$, and the separation energy S_{1n} is $0.96^{+0.14}_{-0.14}$ MeV.

To clarify the spin parity of the ground state of ^{29}Ne, the large-scale Monte Carlo Shell Model (MCSM) calculations employing the SDPF-M effective interaction [52] were performed as in the discussion for ^{31}Ne. The shell-model levels are listed in Table 6.2 and shown in Fig 6.8. The $3/2^-$ and $1/2^+$ shell-model states are lying at $E_\mathrm{x} = 0.07$ MeV and 0.56 MeV, respectively. This suggests that the $3/2^-$ shell-model state is favored as the ground state of ^{29}Ne. Additionally, the shell-model calculation excludes the ground state with $J^\pi = 3/2^+$.

Table 6.5 shows the comparison between the experimental results and theoretical calculations for the shell model states with $J^\pi = 3/2^-$ and $1/2^+$ for nuclear breakup on carbon target. For the shell model state with $J^\pi = 3/2^-$, the measured inclusive and semi-inclusive cross sections of 74(2) and 45(7) mb are close to the theoretical results for the of 31.60 and 69.01 mb, respectively. On the other hand, for the $1/2^+$ shell model state, the calculations can not explain the experimental results. We thus concluded that the ground state with $J^\pi = 3/2^-$ is most likely. that Therefore, the ground state with $J^\pi = 3/2^-$ is concluded.

Figure 6.9 shows the inclusive momentum distribution of ^{28}Ne for ^{29}Ne + C, which is compared with the theoretical momentum distributions for (a) $3/2^-$ and (b) $1/2^+$ shell-model states. Black, red, green, and blue thin lines show the *s*-, *p*-, *d*-, and *f*-neutron removal component tabulated in Table 6.5. Each partial cross section is the sum of the same angular orbital components. The distributions are calculated based on the eikonal-reaction model. The good agreement for the result for $3/2^-$ shell model state supports the $3/2^-$ ground state of ^{29}Ne.

Nucleus	J^π	Energy (MeV)
^{29}Ne	$3/2^+$	0.00
	$3/2^-$	0.07
	$7/2^-$	0.12
	$1/2^+$	0.56
	$5/2^-$	0.70
	$5/2^+$	1.46
	$1/2^-$	2.09

Table 6.2: Low-lying shell-model levels for ^{29}Ne calculated with the SDPF-M interaction [52, 53] are listed. The state of 0.00 MeV corresponds the ground states. Only the yrast states are shown.

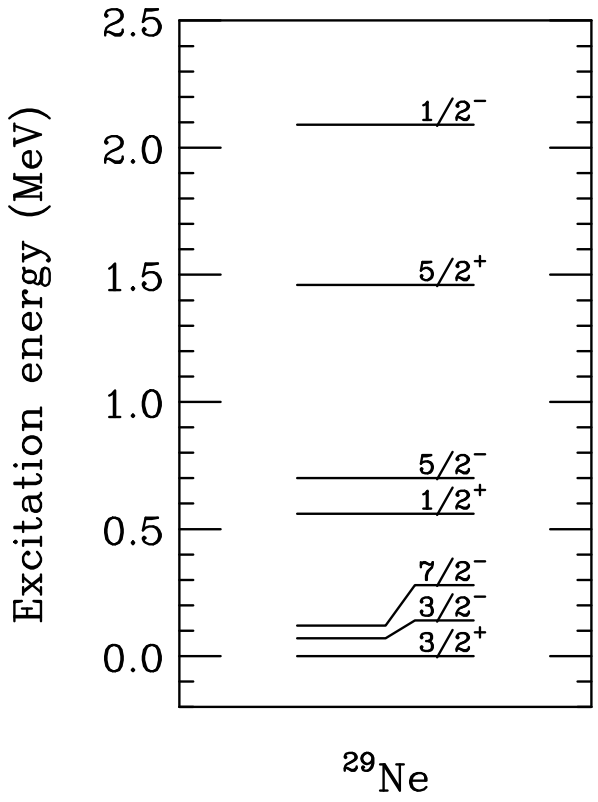

Figure 6.8: Low-lying shell-model level scheme for ^{29}Ne with the SDPF-M interaction [52, 53] are listed. The state of 0.00 MeV corresponds the ground states. Only the yrast states are shown.

Reaction	E_x (MeV)	J^π	ℓ_j	σ_{sp} (mb)	C^2S	σ^{th}_{-1n}(C) (mb)	σ^{exp}_{-1n}(C) (mb)	R_s
C(^{29}Ne($3/2^-$),^{28}Ne)	0.00	0^+_1	$p_{3/2}$	64.93	0.438	31.60	45(7)	1.42(22)
S_{1n}(^{29}Ne) = 0.95 MeV	1.36	2^+_1	$p_{3/2}$	45.45	0.072	3.64		
			$f_{7/2}$	22.33	0.167	4.14		
	2.21	0^+_2	$p_{3/2}$	39.26	0.005	0.22		
	2.76	4^+_1	$f_{7/2}$	19.97	0.417	9.25		
	2.99	2^+_2	$p_{3/2}$	35.19	0.066	2.58		
			$f_{7/2}$	19.65	0.015	0.33		
	3.57	2^-_1	$s_{1/2}$	30.20	0.036	1.17		
			$d_{3/2}$	17.45	0.035	0.66		
			$d_{5/2}$	19.80	0.000	0.00		
	3.69	3^-_1	$d_{3/2}$	17.25	0.236	4.37		
			$d_{5/2}$	19.58	0.017	0.36		
	3.98	2^+_3	$p_{3/2}$	31.35	0.153	5.33		
			$f_{7/2}$	18.43	0.005	0.10		
	3.99	4^+_2	$f_{7/2}$	18.42	0.258	5.28		
		Inclusive				69.01	74(2)	1.07(3)
C(^{29}Ne($1/2^+$),^{28}Ne)	0.00	0^+_1	$s_{1/2}$	72.27	0.035	2.71	45(7)	16.6(2.58)
S_{1n}(^{29}Ne) = 0.95 MeV	1.36	2^+_1	$d_{3/2}$	22.67	0.642	15.61		
			$d_{5/2}$	25.72	0.002	0.06		
	2.21	0^+_2	$s_{1/2}$	37.66	0.083	3.35		
	2.99	2^+_2	$d_{3/2}$	18.48	0.131	2.60		
			$d_{5/2}$	20.98	0.000	0.00		
	3.57	2^-_1	$p_{3/2}$	32.80	0.429	15.63		
	3.69	3^-_1	$f_{7/2}$	18.77	0.727	15.16		
	3.98	2^+_3	$d_{3/2}$	16.80	0.000	0.00		
			$d_{5/2}$	19.07	0.000	0.00		
		Inclusive				55.13	74(2)	1.32(4)

Table 6.3: Results for one-neutron removal reactions from ^{29}Ne. Tabulated are the one-neutron removal cross sections to assumed bound shell-model states near and below the neutron thresholds in the mass $A-1$ systems, ^{28}Ne, of 3.81(13) MeV. The final theoretical cross sections, σ^{th}_{-1n}, include the center-of-mass correction factor $[A/(A-1)]^N$. The errors shown for the ratio of cross sections, $R_s = \sigma^{exp}_{-1n}/\sigma^{th}_{-1n}$, reflect only the errors quoted on the measurements.

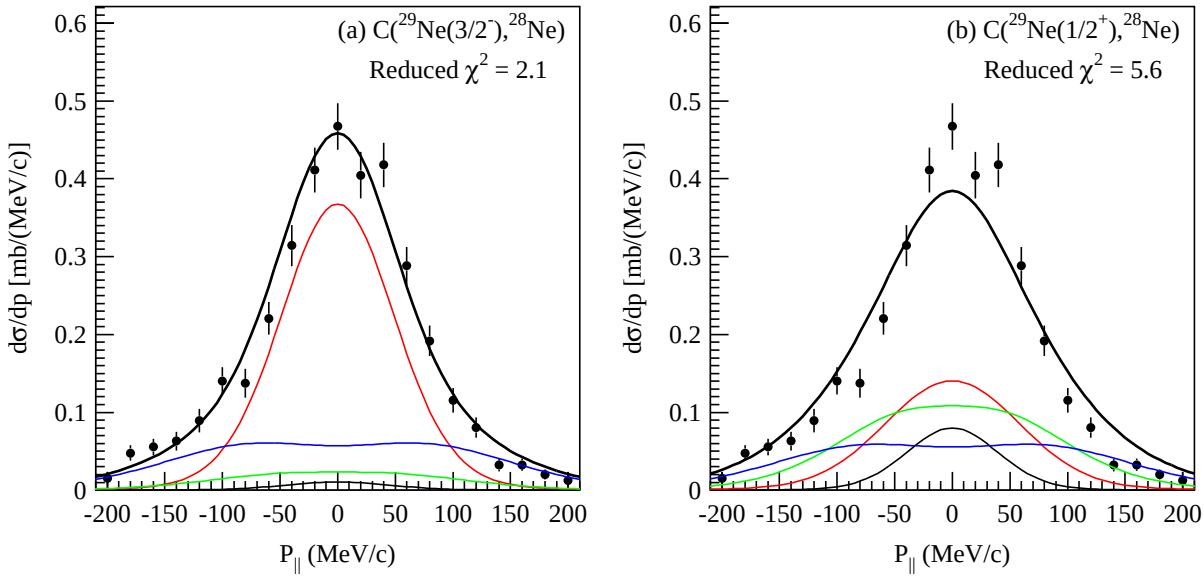

Figure 6.9: Measured parallel momentum distributions of one-neutron removal form ^{29}Ne and corresponding theoretical calculations for (a) $3/2^-$ ground state and (b) $1/2^+$ ground state. The black, red, green, and blue thin lines show the *s*-, *p*-, *d*-, and *f*-wave components. The thick black lines show the inclusive total distributions. The theoretical momentum distribution curves are normalised to the measured inclusive cross section.

To check the consistency of the results, we also calculated the cross sections when we use the C^2S of 0.61 for the ^{28}Ne$(0^+_1)\otimes 2p_{3/2}$ to be the one from the combined analysis, and we use the experimental excitation energy (E_x = 1.293(8) MeV) for the 2^+_1 state, as shown in Table 6.5. On the other hand, Table 6.5 shows the case of Coulomb breakup reaction in a similar way. The theoretical cross sections are consistent with the experimental values within errors. The momentum distribution of ^{28}Ne with these calculated cross sections is plotted in Figure 6.10. In the figure, the p-neutron removal components coupled to 0^+_1 and 2^+_1 final states are plotted exclusively. The red dashed- and doted-lines show the p-wave components to the 0^+ and 2^+state of the fragment, respectively. It is found that the experimental data are well explained by the calculations for the $3/2^-$ ground state of ^{29}Ne, which supports again the ground state with $J^\pi = 3/2^-$.

Reaction	E_x (MeV)	J^π	ℓ_j	σ_{sp} (mb)	C^2S	σ^{th}_{-1n}(C) (mb)	σ^{exp}_{-1n}(C) (mb)	R_s
C(^{29}Ne($3/2^-$),^{28}Ne)	0.00	0^+_1	$p_{3/2}$	64.93	0.61	44.01	45(7)	1.02(16)
S_{1n}(^{29}Ne) = 0.95 MeV	1.29	2^+_1	$p_{3/2}$	46.09	0.072	3.69		
			$f_{7/2}$	22.47	0.167	4.17		
	2.21	0^+_2	$p_{3/2}$	39.26	0.005	0.22		
	2.76	4^+_1	$f_{7/2}$	19.97	0.417	9.25		
	2.99	2^+_2	$p_{3/2}$	35.19	0.066	2.58		
			$f_{7/2}$	19.65	0.015	0.33		
	3.57	2^-_1	$s_{1/2}$	30.20	0.036	1.17		
			$d_{3/2}$	17.45	0.035	0.66		
			$d_{5/2}$	19.80	0.000	0.00		
	3.69	3^-_1	$d_{3/2}$	17.25	0.236	4.37		
			$d_{5/2}$	19.58	0.017	0.36		
	3.98	2^+_3	$p_{3/2}$	31.35	0.153	5.33		
			$f_{7/2}$	18.43	0.005	0.10		
	3.99	4^+_2	$f_{7/2}$	18.42	0.258	5.28		
		Inclusive				81.50	74(2)	0.91(2)

Table 6.4: Results for one-neutron removal reactions from ^{29}Ne. Tabulated are the one-neutron removal cross sections to assumed bound shell-model states near and below the neutron thresholds in the mass $A-1$ systems, ^{28}Ne, of 3.81(13) MeV. The final theoretical cross sections, σ^{th}_{-1n}, include the center-of-mass correction factor $[A/(A-1)]^N$. The errors shown for the ratio of cross sections, $R_s = \sigma^{exp}_{-1n}/\sigma^{th}_{-1n}$, reflect only the errors quoted on the measurements.

As in the case of ^{31}Ne, the spectroscopic factors are fragmented among many states. The mixed ground-state configuration is consistent with ^{29}Ne lying within the island of inversion and, as such, suggests that it will be strongly deformed as the structure of ^{31}Ne is described well in a deformed potential [60–62]. According to the Nilsson diagram shown in Fig. 6.11, the 19th neutron with $J^\pi = 3/2^-$ should be located at the [330 1/2] level with $J^\pi = 3/2^-$ ($0.29 \le \beta \le 0.40$) or [321 3/2] level with $J^\pi = 3/2^-$ ($0.59 \le \beta$) which involve the $p_{3/2}$ configuration. The [330 1/2] level with $J^\pi = 3/2^-$ is corresponding to the 1 particle-2 hole (1p-2h) state $[(\nu p_{3/2})^1(\nu d_{3/2})^{-2}]$. The [321 3/2] level with $J^\pi = 3/2^-$ is corresponding to the 3p-4h state $[(\nu p_{3/2})^3(\nu d_{3/2})^{-4}]$ or $[(\nu p_{3/2})^1(\nu f_{7/2})^2(\nu d_{3/2})^{-4}]$. In both cases of [330 1/2] and [321 3/2], $\nu p_{3/2}$ orbital is dominant over the $\nu f_{3/2}$ orbital. For the case of [321 3/2], $\nu d_{3/2}$ is not occupied at all, which suggest that $\nu d_{3/2}$ orbital locate above the $\nu p_{3/2}$ orbital. As a result, ^{29}Ne is found to be a deformed nucleus with $J^\pi = 3/2^-$ in the island of inversion.

Reaction	E_x (MeV)	J^π	ℓ_j	σ_{sp} (mb)	C^2S	$\sigma^{th}_{-1n}(E1)$ (mb)	$\sigma^{exp}_{-1n}(E1)$ (mb)	R_s
Pb(^{29}Ne($3/2^-$),^{28}Ne)	0.00	0^+_1	$p_{3/2}$	301.37	0.61	183.83	169(59)	0.92(33)
$S_{1n}(^{29}\text{Ne}) = 0.95$ MeV	1.29	2^+_1	$p_{3/2}$	76.07	0.072	5.48		
			$f_{7/2}$	2.91	0.167	0.49		
	2.21	0^+_2	$p_{3/2}$	29.37	0.005	0.15		
	2.76	4^+_1	$f_{7/2}$	0.20	0.417	0.08		
	2.99	2^+_2	$p_{3/2}$	8.87	0.066	0.59		
			$f_{7/2}$	0.08	0.015	0.00		
	3.57	2^-_1	$s_{1/2}$	1.15	0.036	0.04		
			$d_{3/2}$	1.90	0.035	0.07		
			$d_{5/2}$	0.09	0.000	0.00		
	3.69	3^-_1	$d_{3/2}$	1.41	0.236	0.33		
			$d_{5/2}$	0.06	0.017	0.00		
	3.98	2^+_3	$p_{3/2}$	0.20	0.153	0.03		
			$f_{7/2}$	0.00	0.005	0.00		
	3.99	4^+_2	$f_{7/2}$	0.00	0.258	0.00		
	Inclusive					191.53	222(36)	1.16(18)

Table 6.5: Results for one-neutron removal reactions from ^{29}Ne on the Pb target. Tabulated are the one-neutron removal cross sections to assumed bound shell-model states near and below the neutron thresholds in the mass $A-1$ systems, ^{28}Ne, of 3.81(13) MeV. The errors shown for the ratio of cross sections, $R_s = \sigma^{exp}_{-1n}/\sigma^{th}_{-1n}$, reflect only the errors quoted on the measurements.

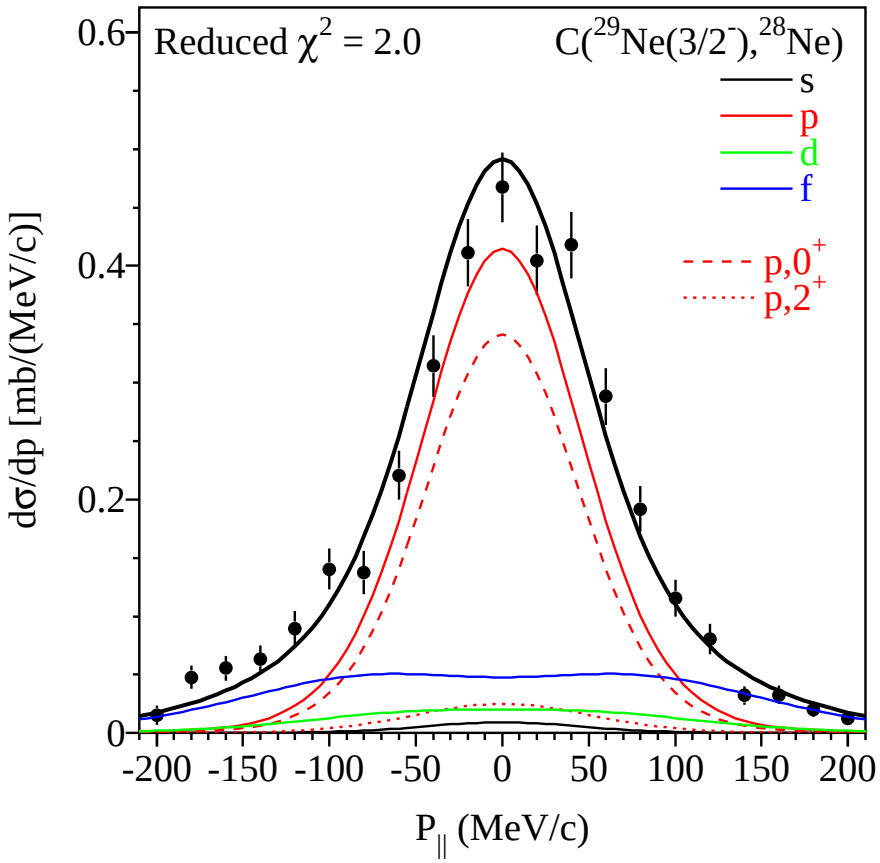

Figure 6.10: Measured parallel momentum distributions of one-neutron removal form ^{29}Ne and corresponding theoretical calculations for $3/2^-$ ground state. The black, red, green, and blue thin lines show the *s*-, *p*-, *d*-, and *f*-wave components. The red dashed- and doted-lines show the *p*-wave components to the 0^+ and 2^+state of the fragment, respectively. The thick black lines show the inclusive total distributions. The theoretical momentum distribution curves are normalised to the measured inclusive cross section.

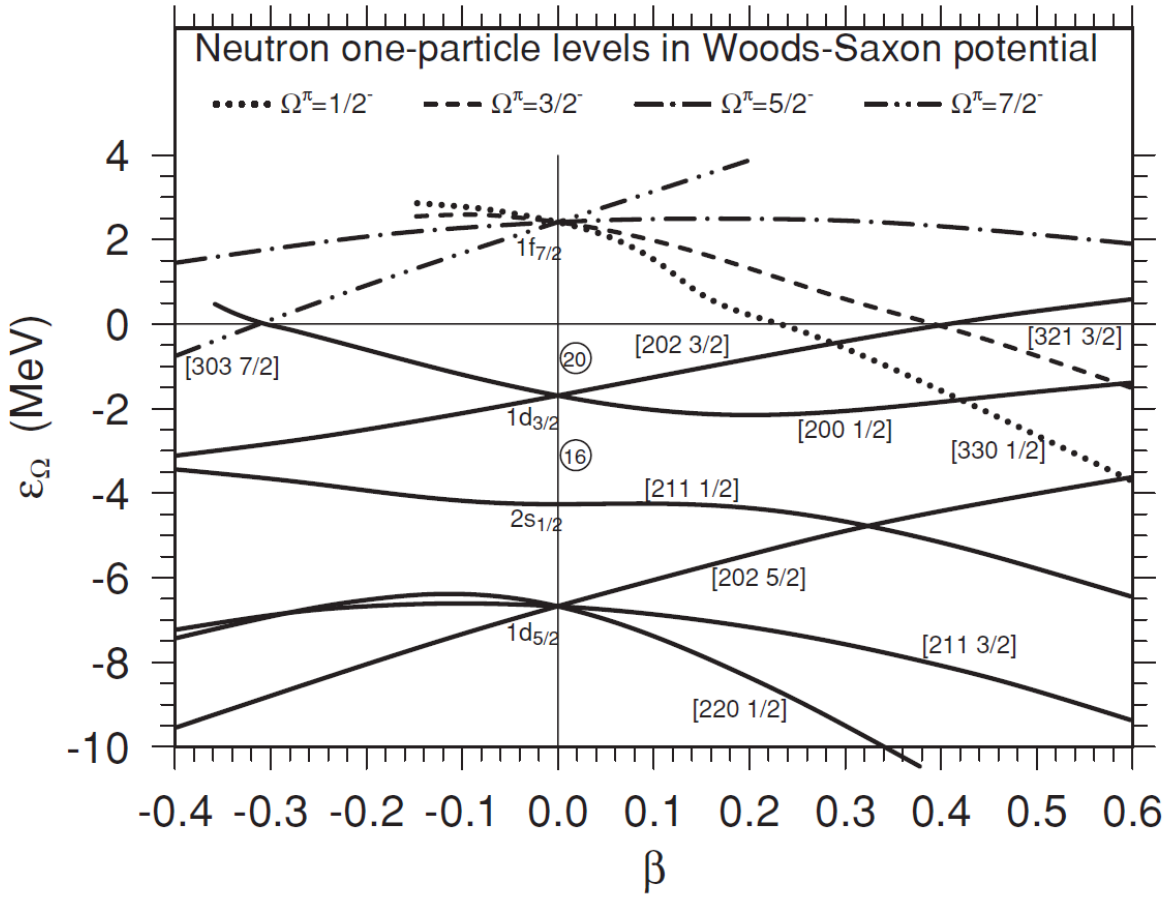

Figure 6.11: Nilsson diagram for ^{31}Ne taken from [62], which is used for ^{29}Ne here. The figure shows the neutron one-particle levels as a function of quadrupole deformation. Parameters of the Woods-Saxson potential are designed approximately for the nucleus ^{31}Ne. One-particle levels are denoted by the asymptotic quantum numbers $[Nn_z\Lambda\Omega]$. The $\Omega^\pi = 1/2^-$ levels are denoted by dotted curves, the $3/2^-$ levels by dashed curves, the $5/2^-$ levels by dot-dashed curves, the $7/2^-$ levels by dot-dot-dashed curves, while positive-parity levels are plotted by solid curves.

6.6 Results for ^{33}Mg

From the studies of even-even Mg isotopes [12, 63, 64], ^{33}Mg is likely to be in the island of inversion. According to the measurement of the magnetic moment by laser spectroscopy [65], the spin of the ground state was found to be $J = 3/2$, and the negative parity was suggested. On the other hand, a β study [66] suggested the positive parity of the ground state of ^{33}Mg. Thus, the ground-state parity is a subject of debate. In the following discussion, we consider only the ground states with $J^\pi = 3/2^+$ and $J^\pi = 3/2^-$. Hence, ^{33}Mg ground state should contain $^{32}\mathrm{Mg} \otimes 1d_{3/2}$ configuration for $J^\pi = 3/2^+$ or $^{32}\mathrm{Mg} \otimes 2p_{3/2}$ configuration for $J^\pi = 3/2^-$.

According to the large-scale Monte Carlo Shell Model (MCSM) calculation with the SDPF-M effective interaction [52], the excited states with $J^\pi = 3/2^-$ and $J^\pi = 3/2^+$ are listed in Table 6.6 and shown in Fig 6.12. In the calculation, the spin parity of the ground state is $3/2^-$, and the $3/2^+$ state is lying at $E_\mathrm{x} = 0.99$ MeV.

In Fig. 6.3 (a-3), (b-3), (c-3), and (d-3) for ^{33}Mg, there are no overlap area among blue, red, green areas in the region of $C^2S < 1$. Therefore, there are some other effects to be considered for ^{33}Mg. A possible reason is that, on the carbon target, the direct decay from ^{32}Mg excited states higher than the 2^+_1 state to the ground state are not any more negligible, which may be the reason for the fact that blue area is located over the possible true region. This consideration may be supported by the measurement of γ-ray spectroscopy of ^{32}Mg [46], where the direct decay branch was indeed observed.

Nucleus	J^π	Energy (MeV)
^{33}Mg	$3/2^-$	0.00
	$3/2^+$	0.99

Table 6.6: Low-lying shell-model levels for ^{33}Mg calculated with the SDPF-M interaction [52] are listed. The state of 0.00 MeV corresponds the ground states. Only the yrast states are shown.

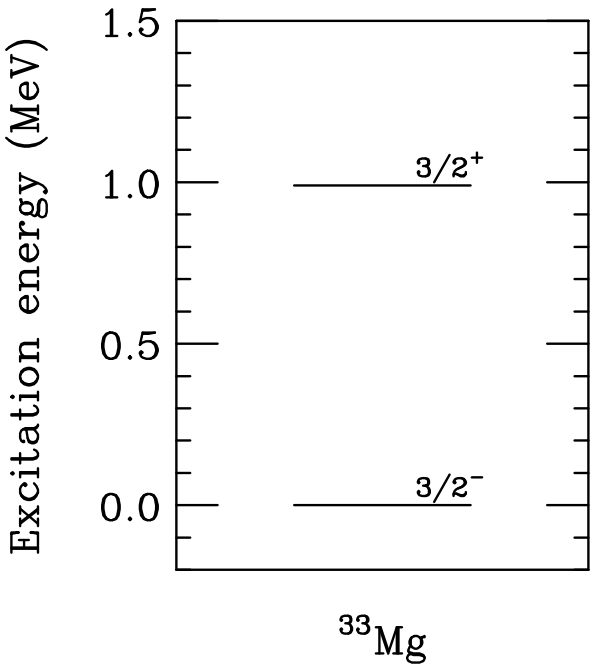

Figure 6.12: Low-lying shell-model level scheme for ^{33}Mg with the SDPF-M interaction [52] are listed. The state of 0.00 MeV corresponds the ground states. Only the yrast states are shown.

Table 6.6 shows the comparison between the experimental results and theoretical calculations for the shell model states of ^{33}Mg with $J^\pi = 3/2^-$ and $3/2^+$ for nuclear breakup on carbon target. Table 6.6 shows the case for Coulomb breakup. The experimental inclusive nuclear breakup cross section $\sigma^{\rm exp}_{-1n}$(C) of 99(1) mb is 44 % and 57 % larger than the theoretical cross sections $\sigma^{\rm th}_{-1n}$(C) of 69.01 mb and 63.07 mb, respectively. On the other hand, the experimental inclusive coulomb breakup cross section $\sigma^{\rm exp}_{-1n}(E1)$ of 222(36) mb is consistent with the theoretical cross section $\sigma^{\rm th}_{-1n}(E1)$ for the $3/2^-$ shell model state. Furthermore, Figure shows the theoretical fragment momentum distributions for (a) $3/2^-$ and (b) $3/2^+$ shell model states with experimental distributions. From the comparison, although the $3/2^-$ state is likely to be favored, further analysis or different approach is needed.

Reaction	$E_{\rm x}$ (MeV)	J^π	ℓ_j	$\sigma_{\rm sp}$ (mb)	C^2S	$\sigma^{\rm th}_{-1n}$(C) (mb)	$\sigma^{\rm exp}_{-1n}$(C) (mb)	R_s
C(^{33}Mg($3/2^-$),^{32}Mg)	0.00	0^+_1	$p_{3/2}$	42.78	0.114	5.35	45(7)	8.4(1.3)
S_{1n}(^{33}Mg) = 2.22 MeV	1.03	2^+_1	$p_{3/2}$	35.35	0.155	6.01		
			$f_{7/2}$	17.03	0.284	5.30		
	2.51	4^+_1	$f_{7/2}$	15.23	1.111	18.56		
	2.85	2^+_2	$p_{3/2}$	27.73	0.239	7.27		
	3.38	1^-_1	$s_{1/2}$	22.57	0.187	4.49		
			$d_{3/2}$	14.85	0.147	2.32		
	3.40	2^-_1	$d_{3/2}$	14.82	0.552	8.70		
	3.51	3^-_1	$d_{3/2}$	14.69	0.449	7.01		
	3.55	2^-_2	$s_{1/2}$	22.10	0.245	5.76		
	3.60	3^+_1	$f_{7/2}$	14.20	0.251	3.91		
	3.94	4^+_2	$f_{7/2}$	13.92	0.242	3.69		
	5.37	2^-_5	$s_{1/2}$	18.18	0.256	4.95		
		Inclusive				69.01	99(1)	1.44(1)
C(^{33}Mg($3/2^+$),^{32}Mg)	0.00	0^+_1	$d_{3/2}$	21.99	0.246	5.75	45(7)	7.8(1.2)
S_{1n}(^{33}Mg) = 2.22 MeV	3.40	0^+_3	$d_{3/2}$	14.82	0.150	2.36		
	3.40	2^-_1	$p_{3/2}$	26.14	0.115	3.30		
			$f_{7/2}$	14.37	0.134	2.11		
	3.51	3^-_1	$p_{3/2}$	25.85	0.230	6.52		
			$f_{7/2}$	14.28	0.220	3.44		
	3.55	2^-_2	$f_{7/2}$	14.24	0.402	6.28		
	3.86	2^+_4	$s_{1/2}$	21.31	0.225	5.10		
			$d_{3/2}$	14.28	0.121	1.84		
	4.09	3^-_2	$f_{7/2}$	13.80	0.231	3.50		
	4.24	2^+_5	$d_{3/2}$	13.86	0.128	1.89		
	4.41	4^-_2	$f_{7/2}$	13.55	0.115	1.71		
	4.59	4^-_3	$f_{7/2}$	13.42	0.247	3.63		
		Inclusive				63.07	99(1)	1.57(2)

Table 6.7: Results for one-neutron removal reactions from ^{33}Mg on the C target. Tabulated are the one-neutron removal cross sections to assumed bound shell-model states below the neutron thresholds in the mass $A-1$ systems, ^{32}Mg, of 5.81(2) MeV. The final theoretical cross sections, $\sigma^{\rm th}_{-1n}$, include the center-of-mass correction factor $[A/(A-1)]^N$. The errors shown for the ratio of cross sections, $R_s = \sigma^{\rm exp}_{-1n}/\sigma^{\rm th}_{-1n}$, reflect only the errors quoted on the measurements. Configurations with $C^2S \geq 0.1$ are shown.

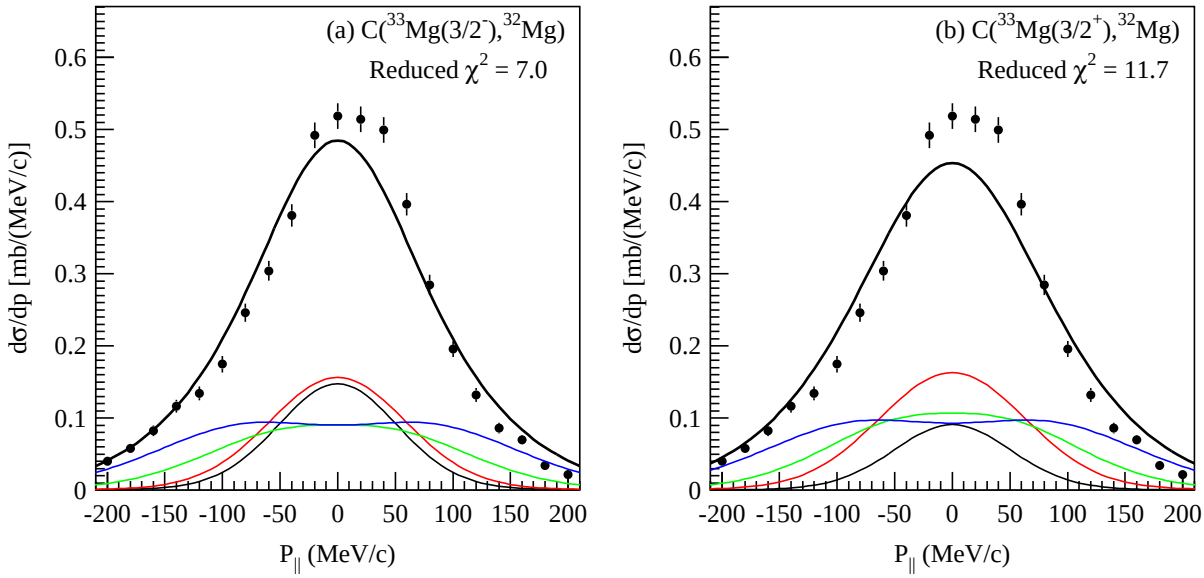

Figure 6.13: Measured parallel momentum distributions of one-neutron removal form ^{33}Mg and corresponding theoretical calculations for (a) $3/2^-$ ground state and (b) $3/2^+$ ground state. The black, red, green, and blue thin lines show the *s*-, *p*-, *d*-, and *f*-wave components. The thick black lines show the inclusive total distributions. The theoretical momentum distribution curves are normalised to the measured inclusive cross section.

Reaction	E_x (MeV)	J^π	ℓ_j	σ_{sp} (mb)	C^2S	$\sigma^{th}_{-1n}(E1)$ (mb)	$\sigma^{exp}_{-1n}(E1)$ (mb)	R_s
Pb(^{33}Mg($3/2^-$),^{32}Mg)	0.00	0^+_1	$p_{3/2}$	154.42	0.114	17.60	38(72)	2.16(4.09)
$S_{1n}(^{33}\text{Mg}) = 2.22$ MeV	1.03	2^+_1	$p_{3/2}$	93.40	0.155	14.48		
			$f_{7/2}$	103.22	0.284	29.31		
	2.51	4^+_1	$f_{7/2}$	58.73	1.111	65.25		
	2.85	2^+_2	$p_{3/2}$	33.38	0.239	7.98		
	3.38	1^-_1	$s_{1/2}$	61.69	0.187	11.54		
			$d_{3/2}$	10.12	0.147	1.49		
	3.40	2^-_1	$d_{3/2}$	9.91	0.552	5.47		
	3.51	3^-_1	$d_{3/2}$	8.73	0.449	3.92		
	3.55	2^-_2	$s_{1/2}$	58.43	0.245	14.32		
	3.60	3^+_1	$f_{7/2}$	36.25	0.251	9.10		
	3.94	4^+_2	$f_{7/2}$	28.94	0.242	7.00		
	5.37	2^-_5	$s_{1/2}$	15.82	0.256	4.05		
		Inclusive				218.86	222(36)	1.01(16)
Pb(^{33}Mg($3/2^+$),^{32}Mg)	0.00	0^+_1	$d_{3/2}$	77.22	0.246	19.00	38(72)	2.00(3.80)
$S_{1n}(^{33}\text{Mg}) = 2.22$ MeV	3.40	0^+_3	$d_{3/2}$	9.91	0.150	1.49		
	3.40	2^-_1	$p_{3/2}$	19.87	0.115	2.28		
			$f_{7/2}$	40.28	0.134	5.40		
	3.51	3^-_1	$p_{3/2}$	17.16	0.230	3.95		
			$f_{7/2}$	38.07	0.220	8.37		
	3.55	2^-_2	$f_{7/2}$	37.26	0.402	14.98		
	3.86	2^+_4	$s_{1/2}$	52.80	0.225	11.88		
			$d_{3/2}$	5.57	0.121	0.67		
	4.09	3^-_2	$f_{7/2}$	25.47	0.231	5.88		
	4.24	2^+_5	$d_{3/2}$	4.17	0.128	0.53		
	4.41	4^-_2	$f_{7/2}$	18.09	0.115	2.08		
	4.59	4^-_3	$f_{7/2}$	13.94	0.247	3.44		
		Inclusive				100.45	222(36)	2.21(36)

Table 6.8: Results for one-neutron removal reactions from ^{33}Mg on the Pb target. Tabulated are the one-neutron removal cross sections to assumed bound shell-model states below the neutron thresholds in the mass $A-1$ systems, ^{32}Mg, of 5.81(2) MeV. The final theoretical cross sections, σ^{th}_{-1n}, include the center-of-mass correction factor $[A/(A-1)]^N$. The errors shown for the ratio of cross sections, $R_s = \sigma^{exp}_{-1n}/\sigma^{th}_{-1n}$, reflect only the errors quoted on the measurements. Configurations with $C^2S \geq 0.1$ are shown.

6.7 Results for ^{35}Mg

According to the combined analysis of Coulomb and nuclear breakup in Fig. 6.4, there is an allowed area in Fig. (c-3). Therefore, the possible spin parity of the ground state is $3/2^+$, which corresponds to $^{34}\mathrm{Mg}(0^+) \otimes 1d_{3/2}$ neutron removal reaction. Additionally, since the calculation for the $1d_{5/2}$ neutron removal is almost the same as that for $1d_{3/2}$ neutron removal, $J^\pi = 5/2^+$ is also the possible spin parity of the ground state. According to the shell model calculation as shown in Table 6.9 and Fig 6.14, however, the ground state with $J^\pi = 3/2^+$ or $5/2^+$ are excluded. Considering the possibility that, on the carbon target, the direct decay from ^{34}Mg excited states higher than the 2^+_1 state to the ground state occurs as discussed in Sec. , the configurations $^{34}\mathrm{Mg}(0^+) \otimes 1s_{1/2}$, $^{34}\mathrm{Mg}(0^+) \otimes 1p_{3/2}$, and $^{34}\mathrm{Mg}(0^+) \otimes 1f_{5/2}$ in Fig. 6.4 may be allowed.

Table 6.7 shows the comparison between the experimental results and theoretical calculations for the lowest shell model states of ^{35}Mg with $J^\pi = 3/2^-$ and $5/2^-$ for nuclear breakup on carbon target. Table 6.7 shows the case for Coulomb breakup. From the comparison between the theoretical and experimental inclusive cross sections of nuclear and Coulomb breakup, these two shell model states are not excluded. From the comparisons of momentum distributions as shown in Fig. 6.15, on the other hand, the calculation for $J^\pi = 3/2^-$ can explain the experimental distribution.

As a result, there is a controversy between the results of combined analysis and momentum distribution analysis, and thus further analysis or different approach is needed.

Nucleus	J^π	Energy (MeV)
^{35}Mg	$3/2^-$	0.00
	$5/2^-$	0.09
	$7/2^-$	0.35
	$1/2^-$	0.43
	$5/2^+$	1.01
	$1/2^+$	2.25

Table 6.9: Low-lying shell-model levels for ^{35}Mg calculated with the SDPF-M interaction [52] are listed. The state of 0.00 MeV corresponds the ground states. Only the yrast states are shown.

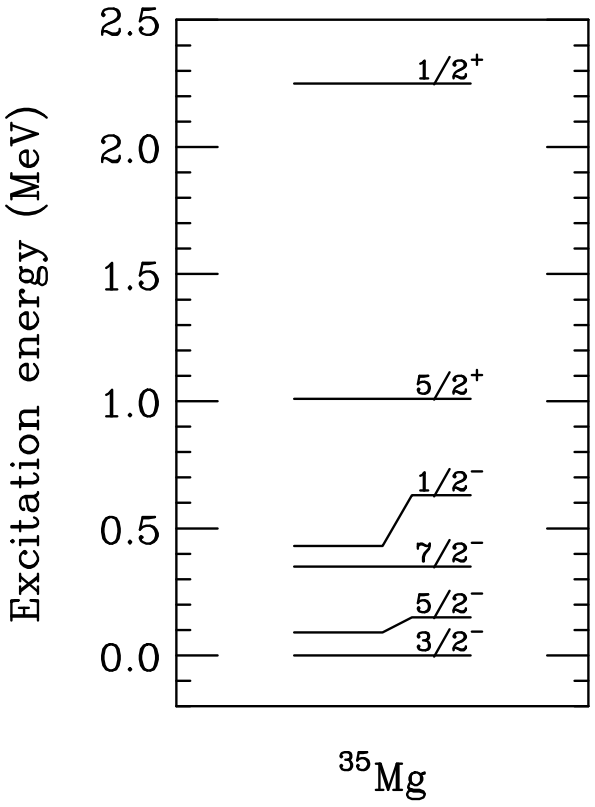

Figure 6.14: Low-lying shell-model level scheme for ^{35}Mg with the SDPF-M interaction [52] are listed. The state of 0.00 MeV corresponds the ground states. Only the yrast states are shown.

Reaction	E_x (MeV)	J^π	ℓ_j	σ_{sp} (mb)	C^2S	σ^{th}_{-1n}(C) (mb)	σ^{exp}_{-1n}(C) (mb)	R_s
C(^{35}Mg($3/2^-$),^{34}Mg)	0.00	0^+_1	$p_{3/2}$	57.85	0.527	33.26	33(7)	1.02 (21)
S_{1n}(^{35}Mg) = 0.99 MeV	0.74	2^+_1	$p_{3/2}$	45.65	0.118	5.88		
			$f_{7/2}$	18.50	0.260	5.25		
	2.01	4^+_1	$f_{7/2}$	16.24	0.107	1.90		
	3.57	3^+_1	$p_{3/2}$	27.67	0.210	6.34		
			$f_{7/2}$	14.32	0.266	4.16		
	3.67	2^+_4	$p_{3/2}$	27.33	0.189	5.63		
			$f_{7/2}$	14.22	0.443	6.87		
	4.08	4^+_4	$f_{7/2}$	13.82	0.337	5.08		
	4.21	5^+_1	$f_{7/2}$	13.70	0.634	9.47		
	4.30	5^+_2	$f_{7/2}$	13.62	0.534	7.93		
		Inclusive				102.5	84(1)	0.82(1)
C(^{35}Mg($5/2^-$),^{34}Mg)	0.00	0^+_1	-	-	0.000	0.00	33(7)	-
S_{1n}(^{35}Mg) = 0.99 MeV	0.74	2^+_1	$f_{7/2}$	18.50	0.745	15.03		
	2.01	4^+_1	$f_{7/2}$	16.24	0.667	11.82		
	3.70	4^+_2	$p_{3/2}$	27.23	0.280	8.32		
			$f_{7/2}$	14.19	0.594	9.19		
	4.21	5^+_1	$f_{7/2}$	13.70	0.393	5.87		
	4.24	2^-_2	$s_{1/2}$	22.35	0.184	4.36		
			$d_{3/2}$	13.85	0.270	3.96		
	4.30	5^+_2	$f_{7/2}$	13.62	0.354	5.26		
		Inclusive				78.85	84(1)	1.07(1)

Table 6.10: Results for one-neutron removal reactions from ^{35}Mg on the C target. Tabulated are the one-neutron removal cross sections to assumed bound shell-model states below the neutron thresholds in the mass $A-1$ systems, ^{34}Mg, of 4.41(9) MeV. The final theoretical cross sections, σ^{th}_{-1n}, include the center-of-mass correction factor $[A/(A-1)]^N$. The errors shown for the ratio of cross sections, $R_s = \sigma^{exp}_{-1n}/\sigma^{th}_{-1n}$, reflect only the errors quoted on the measurements. Configurations with $C^2S \geq 0.1$ are shown.

Reaction	E_x (MeV)	J^π	ℓ_j	σ_{sp} (mb)	C^2S	$\sigma^{th}_{-1n}(E1)$ (mb)	$\sigma^{exp}_{-1n}(E1)$ (mb)	R_s
Pb(^{35}Mg($3/2^-$),^{34}Mg)	0.00	0^+_1	$p_{3/2}$	309.05	0.527	162.87	-2(84)	-0.01(52)
S_{1n}(^{35}Mg) = 0.99 MeV	0.74	2^+_1	$p_{3/2}$	157.13	0.118	18.54		
			$f_{7/2}$	163.48	0.260	42.50		
	2.01	4^+_1	$f_{7/2}$	57.72	0.107	6.18		
	3.57	3^+_1	$p_{3/2}$	18.08	0.210	3.80		
			$f_{7/2}$	8.29	0.266	2.21		
	3.67	2^+_4	$p_{3/2}$	16.07	0.189	3.04		
			$f_{7/2}$	7.11	0.443	3.15		
	4.08	4^+_4	$f_{7/2}$	2.87	0.337	0.97		
	4.21	5^+_1	$f_{7/2}$	2.47	0.634	1.57		
	4.30	5^+_2	$f_{7/2}$	2.19	0.534	1.17		
		Inclusive				251.47	242(43)	0.96(17)
Pb(^{35}Mg($5/2^-$),^{34}Mg)	0.00	0^+_1	-	-	0.000	0.00	-2(84)	-
S_{1n}(^{35}Mg) = 0.99 MeV	0.74	2^+_1	$f_{7/2}$	163.48	0.745	121.79		
	2.01	4^+_1	$f_{7/2}$	57.72	0.667	38.50		
	3.70	4^+_2	$p_{3/2}$	15.47	0.280	4.33		
			$f_{7/2}$	6.75	0.594	4.01		
	4.21	5^+_1	$f_{7/2}$	2.47	0.393	0.97		
	4.24	2^-_2	$s_{1/2}$	3.85	0.184	0.71		
			$d_{3/2}$	0.20	0.270	0.05		
	4.30	5^+_2	$f_{7/2}$	2.19	0.354	0.78		
		Inclusive				180.45	242(43)	0.96(17)

Table 6.11: Results for one-neutron removal reactions from ^{35}Mg on the Pb target. Tabulated are the one-neutron removal cross sections to assumed bound shell-model states below the neutron thresholds in the mass $A-1$ systems, ^{34}Mg, of 4.41(9) MeV. The final theoretical cross sections, σ^{th}_{-1n}, include the center-of-mass correction factor $[A/(A-1)]^N$. The errors shown for the ratio of cross sections, $R_s = \sigma^{exp}_{-1n}/\sigma^{th}_{-1n}$, reflect only the errors quoted on the measurements. Configurations with $C^2S \geq 0.1$ are shown.

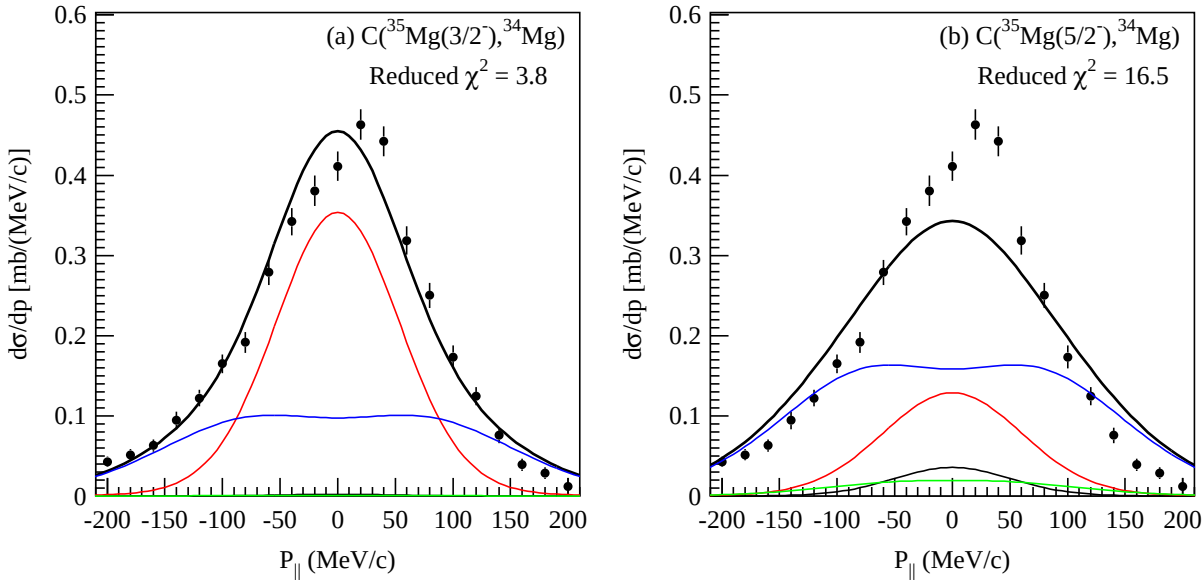

Figure 6.15: Measured parallel momentum distributions of one-neutron removal form ^{35}Mg and corresponding theoretical calculations for (a) $3/2^-$ and (b) $5/2^+$ shell model states. The black, red, green, and blue thin lines show the *s*-, *p*-, *d*-, and *f*-wave components. The thick black lines show the inclusive total distributions. The theoretical momentum distribution curves are normalised to the measured inclusive cross section.

6.8 Results for ^{37}Mg

The separation energy of ^{37}Mg is not known experimentally. The separation energy of S_{1n} = 0.95(15) used in Fig. 6.5 is an extrapolated value taken from Audi et al. [32]. In Figs. 6.5 (a-3) and (b-3), the possible configurations are $^{36}\mathrm{Mg}(0^+)\otimes 2s_{1/2}$ with $J^\pi = 1/2^+$ and $^{36}\mathrm{Mg}(0^+)\otimes 2p_{3/2}$ with $J^\pi = 3/2^-$. From the same analysis of χ^2 for two parameters as described in Sec. 5.3, the spectroscopic factor $C^2S(0^+, 2s_{1/2}))$ is $0.31^{+0.19}_{-0.14}$, and the separation energy S_{1n} is $0.34^{+0.25}_{-0.16}$ MeV. For Fig. (b-3), $C^2S(0^+, 2p_{3/2}))$ is $0.32^{+0.16}_{-0.13}$, and the separation energy S_{1n} is $0.18^{+0.16}_{-0.10}$ MeV. The configuration of $^{36}\mathrm{Mg}(0^+) \otimes 1d_{3/2}$ with $J^\pi = 3/2^+$ in Fig. (c-3) is also accepted at the very low separation energy, where the $C^2S(0^+, 1d_{3/2})$ is almost one.

According to the large-scale Monte Carlo Shell Model (MCSM) calculations employing the SDPF-M effective interaction [52], the spin parity of the ground state is $3/2^-$, which is consistent with the $^{36}\mathrm{Mg}(0^+) \otimes 2p_{3/2}$ configuration with $J^\pi = 3/2^-$ obtained from our combined analysis. The positive parity states are lying at high energies (> 0.81 MeV), and thus these states are unlikely to become the ground state.

Table 6.8 shows the comparison between the experimental results and theoretical calculations for the shell model states with $J^\pi = 3/2^-$, $1/2^+$, $3/2^+$ for nuclear breakup on carbon target. The experimental inclusive and semi-inclusive cross sections of 80(4) and 32(11) mb can only be explained by the theoretical cross sections for $^{37}\mathrm{Mg}(3/2^-)$ of 81.53 and 43.01 mb. Therefore, the ground state with $J^\pi = 3/2^-$ is concluded.

Figure. 6.17 show the theoretical momentum distributions for the $3/2^-$ shell-model state with measured momentum distribution. The distributions are calculated based on the eikonal-reaction model. The black, red, green, and blue thin lines show the s-, p-, d-, and f-neutron removal component tabulated in Table 6.8. Each partial cross section is the sum of the same angular orbital components. The red dashed- and doted-lines show the p-wave components to the 0^+ and 2^+state of the fragment, respectively. The agreement with experimental and theoretical distributions supports the $3/2^-$ ground state of ^{37}Mg. Furthermore, Table 6.8 shows the results of Coulomb breakup for $^{37}\mathrm{Mg}(3/2^-)$. The measured inclusive and semi-inclusive cross sections are consistent with the theoretical cross sections, which also supports the $3/2^-$ ground state.

Nucleus	J^π	Energy (MeV)
^{37}Mg	$3/2^-$	0.00
	$5/2^-$	0.50
	$7/2^-$	0.50
	$1/2^-$	0.56
	$3/2^+$	0.81
	$5/2^+$	1.34
	$1/2^+$	1.76

Table 6.12: Low-lying shell-model levels for ^{37}Mg calculated with the SDPF-M interaction [52] are listed. The state of 0.00 MeV corresponds the ground states. Only the yrast states are shown.

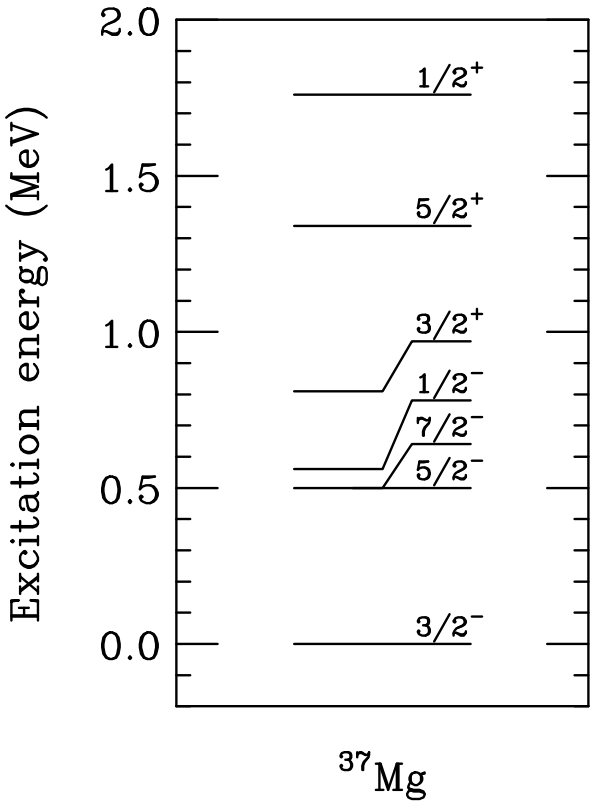

Figure 6.16: Low-lying shell-model level scheme for ^{37}Mg with the SDPF-M interaction [52] are listed. The state of 0.00 MeV corresponds the ground states. Only the yrast states are shown.

Reaction	E_x (MeV)	J^π	ℓ_j	σ_{sp} (mb)	C^2S	σ^{th}_{-1n}(C) (mb)	σ^{exp}_{-1n}(C) (mb)	R_s
C(^{37}Mg($3/2^-$),^{36}Mg)	0.00	0^+_1	$p_{3/2}$	89.43	0.443	43.01	32(11)	0.74(26)
S_{1n}(^{37}Mg) = 0.22 MeV	0.80	2^+_1	$f_{7/2}$	19.32	0.285	5.98		
	1.93	2^+_2	$f_{7/2}$	16.73	0.176	3.20		
	2.22	4^+_1	$f_{7/2}$	16.22	0.146	2.57		
	2.33	0^+_2	$p_{3/2}$	36.28	0.121	4.77		
	2.95	4^+_2	$f_{7/2}$	15.10	0.340	5.57		
	3.21	2^-_1	$d_{3/2}$	15.49	0.381	6.23		
		Inclusive				81.53	80(4)	0.98(5)
C(^{37}Mg($3/2^+$),^{36}Mg)	0.00	0^+_1	$d_{3/2}$	33.06	0.284	9.92	32(11)	3.23(1.11)
S_{1n}(^{37}Mg) = 0.22 MeV	0.80	2^+_1	$d_{3/2}$	24.37	0.332	8.55		
	2.83	2^+_3	$d_{3/2}$	16.34	0.115	1.98		
	3.21	2^-_1	$p_{3/2}$	31.72	0.296	10.19		
	3.22	4^-_1	$f_{7/2}$	14.95	0.420	6.82		
		Inclusive				43.48	80(4)	1.84(9)
C(^{37}Mg($1/2^+$),^{36}Mg)	0.00	0^+_1	$s_{1/2}$	119.72	0.003	0.38	32(11)	84(29)
S_{1n}(^{37}Mg) = 0.22 MeV	1.93	2^+_2	$d_{3/2}$	18.90	0.822	16.41		
	3.29	1^-_1	$p_{3/2}$	31.72	0.104	3.58		
		Inclusive				24.81	80(4)	3.22(16)

Table 6.13: Results for one-neutron removal reactions from ^{37}Mg on the C target. Tabulated are the one-neutron removal cross sections to assumed bound shell-model states below the neutron thresholds in the mass $A-1$ systems, ^{36}Mg, of 5.81(2) MeV. The final theoretical cross sections, σ^{th}_{-1n}, include the center-of-mass correction factor $[A/(A-1)]^N$. The errors shown for the ratio of cross sections, $R_s = \sigma^{exp}_{-1n}/\sigma^{th}_{-1n}$, reflect only the errors quoted on the measurements. Configurations with $C^2S \geq 0.1$ are shown.

According to the Nilsson diagram for ^{37}Mg shown in Fig. 6.18, the 25th neutron can be located in the [312 1/2] with $J^\pi = 3/2^-$ ($0.30 \leq \beta \leq 0.60$) level, which corresponds to the 5 particle-0 hole (5p-0h) state $[(\nu p_{3/2})^3(\nu f_{7/2})^2]$ or $[(\nu p_{3/2})^1(\nu f_{7/2})^4]$. In both cases of $[(\nu p_{3/2})^3(\nu f_{7/2})^2]$ and $[(\nu p_{3/2})^1(\nu f_{7/2})^4]$, $\nu p_{3/2}$ orbital is dominant over the $\nu f_{3/2}$ orbital, which cause the halo formation in ^{37}Mg. As a result, ^{37}Mg is found to be a deformed p-wave neutron halo nucleus with $J^\pi = 3/2^-$ in the island of inversion.

Reaction	E_x (MeV)	J^π	ℓ_j	σ_{sp} (mb)	C^2S	$\sigma^{th}_{-1n}(E1)$ (mb)	$\sigma^{exp}_{-1n}(E1)$ (mb)	R_s
Pb(^{37}Mg(3/2$^-$),^{36}Mg)	0.00	0^+_1	$p_{3/2}$	1067.68	0.443	472.98	411(105)	0.87(22)
$S_{1n}(^{37}\text{Mg}) = 0.22$ MeV	0.80	2^+_1	$p_{3/2}$	190.64	0.045	8.58		
		2^+_1	$f_{7/2}$	5.91	0.285	1.68		
	1.93	2^+_2	$f_{7/2}$	0.36	0.176	0.06		
	2.22	4^+_1	$f_{7/2}$	0.10	0.146	0.01		
	2.33	0^+_2	$p_{3/2}$	9.63	0.121	1.17		
	2.95	4^+_2	$f_{7/2}$	0.00	0.340	0.00		
	3.21	2^-_1	$d_{3/2}$	0.00	0.381	0.00		
		Inclusive				484.65	491(54)	1.01(11)

Table 6.14: Results for one-neutron removal reactions from ^{37}Mg of Coulomb breakup reaction. Tabulated are the one-neutron removal cross sections to assumed bound shell-model states below the neutron thresholds in the mass $A-1$ systems, ^{36}Mg, of 5.81(2) MeV. The final theoretical cross sections, σ^{th}_{-1n}, include the center-of-mass correction factor $[A/(A-1)]^N$. The errors shown for the ratio of cross sections, $R_s = \sigma^{exp}_{-1n}/\sigma^{th}_{-1n}$, reflect only the errors quoted on the measurements. Configurations with $C^2S \geq 0.1$ are shown.

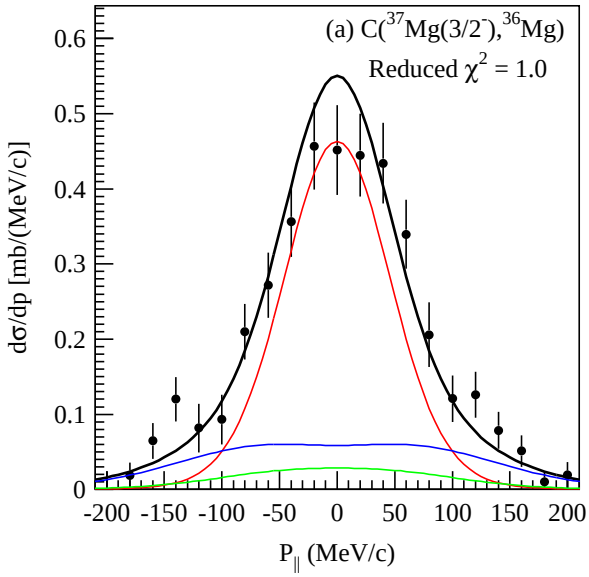

Figure 6.17: Measured parallel momentum distributions of one-neutron removal form ^{37}Mg and corresponding theoretical calculations for $3/2^-$. The black, red, green, and blue thin lines show the s-, p-, d-, and f-wave components. The thick black lines show the inclusive total distributions. The theoretical momentum distribution curves are normalised to the measured inclusive cross section. The theoretical momentum distribution curves are normalised to the measured inclusive cross section.

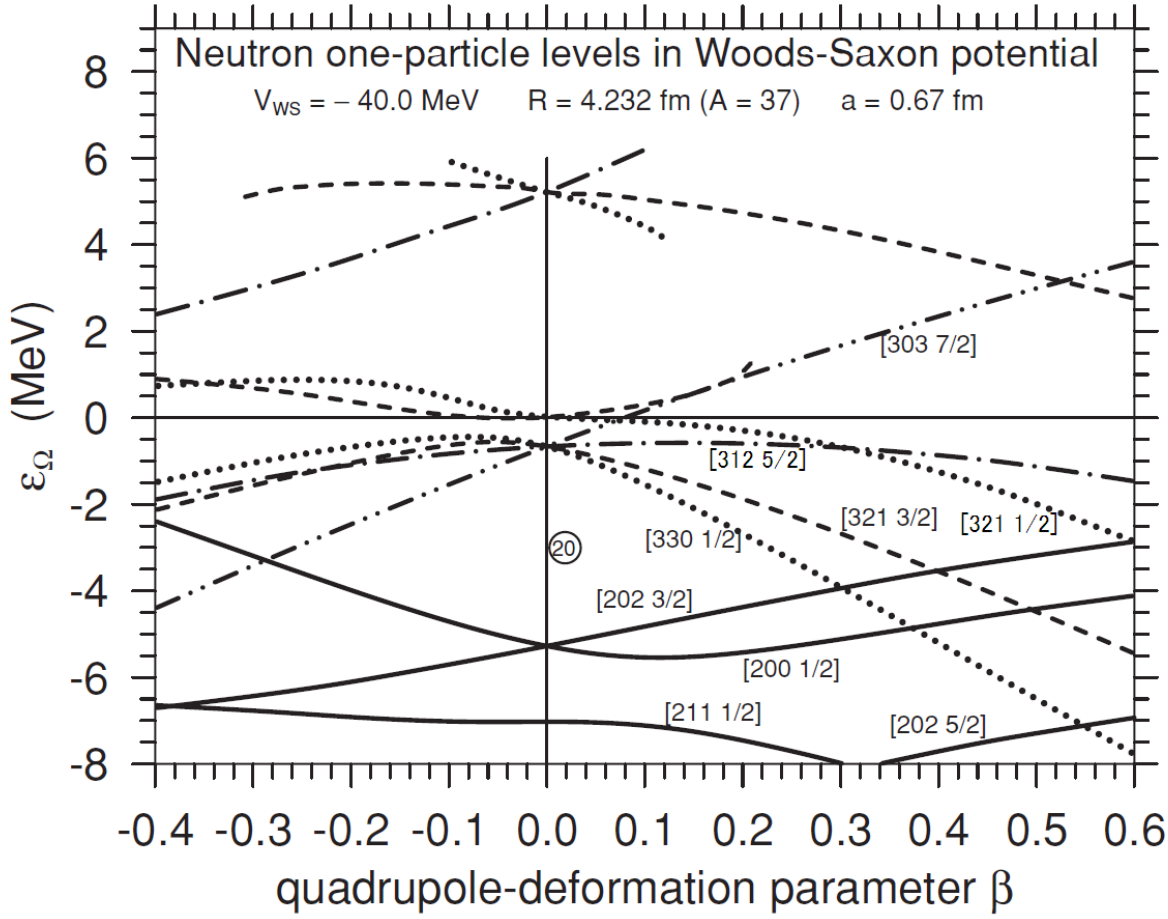

Figure 6.18: Nilsson diagram for ^{37}Mg taken from [62]. The figure shows the neutron one-particle levels as a function of quadrupole deformation. Parameters of the Woods-Saxson potential are designed approximately for the nucleus ^{37}Mg. One-particle levels are denoted by the asymptotic quantum numbers $[Nn_z\Lambda\Omega]$. The $\Omega^\pi = 1/2^-$ levels are denoted by dotted curves, the $3/2^-$ levels by dashed curves, the $5/2^-$ levels by dot-dashed curves, the $7/2^-$ levels by dot-dot-dashed curves, while positive-parity levels are plotted by solid curves. One-particle levels appearing at $\beta = 0$ are $2s_{1/2}$, $1d_{3/2}$, $1f_{7/2}$, $2p_{3/2}$, $1f_{5/2}$ levels at -7.02, -5.28, -0.66, +0.018 and +5.22 MeV, respectively. The $2p_{1/2}$ level is not obtained as a one-particle resonant level.

6.9 Results for ^{39}Si

In Figs. 6.6 (a-3), (b-3), (c-3), and (d-3) for ^{39}Si, all the configurations are seems to be allowed. Therefore, the combined analysis can not tell about the structure of the ground state of ^{39}Si. On the other hand, according to the large-scale Monte Carlo Shell Model (MCSM) calculation with the SDPF-MU effective interaction [52, 53] as listed in Table 6.15 and shown in Fig 6.19, the possible ground states are considered to be $1/2^+$, $1/2^-$, $3/2^-$, $5/2^-$, and $7/2^-$. In the following, the results of the theoretical calculations for these states are shown.

Tables 6.9, 6.9, and 6.9 show the comparison between the experimental nuclear breakup cross sections and theoretical calculations the shell model states with $J^\pi = 1/2^+$, $1/2^-$, $3/2^-$, $5/2^-$, and $7/2^-$. From the results, all the calculations can not well explain both experimental inclusive and semi-inclusive cross sections. Additionally, Tables 6.9, 6.9, and 6.9 shows the cases for Coulomb breakup cross sections. From the results, all cases can not well explain both experimental inclusive and semi-inclusive cross sections except for the case for $J^\pi = 1/2^-$.

Additionally, Figure 6.20 shows the inclusive momentum distribution of ^{39}Si, which is compared with the theoretical momentum distributions for (a) $1/2^+$, (b) $1/2^-$, (c) $3/2^-$, (d) $5/2^-$, and (e) $7/2^-$ shell-model states. Black, red, green, and blue thin lines show the s-, p-, d-, and f-neutron removal component tabulated in Tables 6.9, 6.9, and 6.9. Each partial cross section is the sum of the same angular orbital components. The distributions are calculated based on the eikonal-reaction model. For all cases, theoretical distributions describe the experimental data.

As a result, our analysis is not enough to describe the ground state of ^{39}Si, further analysis or different approach is needed.

Nucleus	J^π	Energy (MeV)
^{39}Si	$5/2^-$	0.00
	$7/2^-$	0.04
	$3/2^-$	0.10
	$1/2^-$	0.38
	$1/2^+$	0.42
	$3/2^+$	1.11
	$5/2^+$	1.30

Table 6.15: Low-lying shell-model levels for ^{39}Si calculated with the SDPF-MU interaction [52, 53] are listed. The state of 0.00 MeV corresponds the ground states. Only the yrast states are shown.

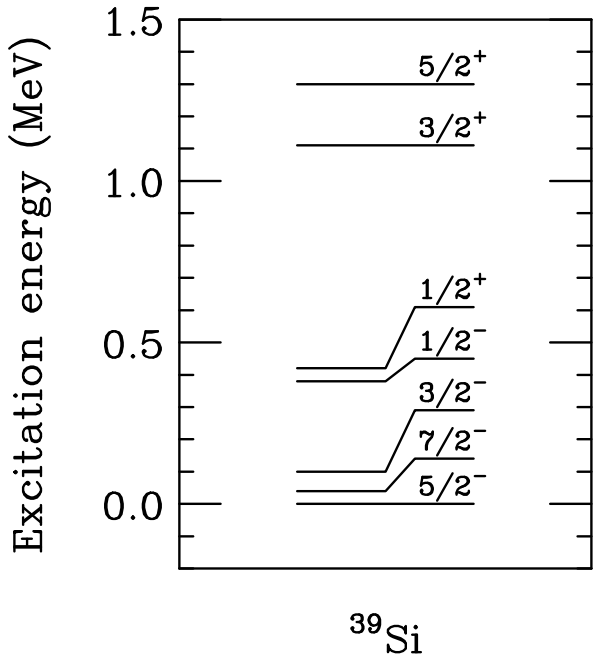

Figure 6.19: Low-lying shell-model level scheme for ^{39}Si with the SDPF-MU interaction [52, 53] are listed. The state of 0.00 MeV corresponds the ground states. Only the yrast states are shown.

Reaction	E_x (MeV)	J^π	ℓ_j	σ_{sp} (mb)	C^2S	σ^{th}_{-1n}(C) (mb)	σ^{exp}_{-1n}(C) (mb)	R_s
C(^{39}Si($3/2^+$),^{38}Si)	0.00	0^+_1	-	-	0.000	0.000	22(9)	-
S_{1n}(^{39}Si) = 1.58 MeV	3.57	3^-_1	$p_{3/2}$	26.87	0.351	10.20		
			$f_{5/2}$	13.78	0.060	0.89		
			$f_{7/2}$	13.78	0.134	2.00		
	3.61	4^-_1	$f_{7/2}$	13.74	0.277	4.11		
	3.70	2^-_1	$p_{3/2}$	26.48	0.169	4.84		
	3.74	5^-_1	$f_{7/2}$	13.62	0.763	11.23		
	3.95	2^-_2	$p_{3/2}$	25.77	0.105	2.93		
			$f_{7/2}$	13.42	0.260	3.77		
	4.08	3^-_2	$p_{3/2}$	25.42	0.138	3.79		
			$f_{5/2}$	13.30	0.101	1.45		
	4.16	4^-_2	$f_{7/2}$	13.23	0.452	6.46		
	4.25	2^-_3	$p_{3/2}$	24.97	0.142	3.83		
	4.54	3^-_4	$f_{7/2}$	12.91	0.402	5.61		
	4.63	1^-_4	$p_{3/2}$	24.04	0.102	2.65		
	4.76	4^-_3	$f_{7/2}$	12.73	0.177	2.44		
		Inclusive				82.70	94(1)	1.14(1)

Table 6.16: Results for one-neutron removal reactions from ^{39}Si on the C target. The ground state of ^{39}Si is assumed as the shell-model excited state with $J^\pi = 3/2^+$. Tabulated are the one-neutron removal cross sections to assumed bound shell-model states below the neutron thresholds in the mass $A-1$ systems, ^{38}Si, of 5.62(11) MeV. The final theoretical cross sections, σ^{th}_{-1n}, include the center-of-mass correction factor $[A/(A-1)]^N$. The errors shown for the ratio of cross sections, $R_s = \sigma^{exp}_{-1n}/\sigma^{th}_{-1n}$, reflect only the errors quoted on the measurements. Configurations with $C^2S \geq 0.1$ are shown.

Figs. 6.20 (a), (b) and (c) show the measured momentum distributions and theoretical calculation assuming $3/2^-$, $5/2^-$, and $7/2^-$ ground states. The $3/2^-$ calculation have too strong p-wave component with respect to the experimental distribution. On the other hand, the $5/2^-$ calculation have too small p-wave component. The experimental distribution would be located in the middle of $3/2^-$ and $5/2^-$ calculations. Namely, all cases are excluded. The expected configuration which has the small $C^2S(0^+, n\ell j)$ and large $C^2S(J^\pi, 2p_{3/2})$ component, as noted above, may agree with the experimental distribution.

Reaction	E_x (MeV)	J^π	ℓ_j	σ_{sp} (mb)	C^2S	σ^{th}_{-1n}(C) (mb)	σ^{exp}_{-1n}(C) (mb)	R_s
C(^{39}Si(1/2$^-$),^{38}Si)	0.00	0^+_1	$p_{1/2}$	48.38	0.103	5.39	22(9)	4.08(1.67)
S_{1n}(^{39}Si) = 1.58 MeV	1.26	2^+_1	$p_{3/2}$	37.37	0.435	17.57		
	2.72	2^+_2	$p_{3/2}$	29.81	0.333	10.73		
	3.51	3^+_1	$f_{7/2}$	13.84	1.140	17.06		
	3.70	2^-_1	$d_{3/2}$	12.98	0.681	9.31		
	3.82	4^+_3	$f_{7/2}$	13.54	0.505	7.39		
	3.95	2^-_2	$d_{3/2}$	12.67	0.107	1.43		
	4.23	1^-_2	$d_{3/2}$	12.35	0.731	9.51		
	4.25	2^-_3	$d_{3/2}$	12.33	0.374	4.86		
	4.45	1^-_3	$s_{1/2}$	20.11	0.101	2.14		
	4.47	4^+_5	$f_{7/2}$	12.97	0.337	4.73		
	4.63	1^-_4	$s_{1/2}$	19.68	0.102	2.11		
	4.75	3^+_4	$f_{7/2}$	12.74	0.142	1.96		
	4.89	2^-_5	$d_{3/2}$	11.66	0.114	1.40		
	5.05	2^-_6	$d_{3/2}$	11.51	0.440	5.33		
	5.45	4^+_8	$f_{7/2}$	12.21	0.223	2.94		
		Inclusive				131.34	94(1)	0.72(1)
C(^{39}Si(3/2$^-$),^{38}Si)	0.00	0^+_1	$p_{3/2}$	49.69	0.657	35.29	22(9)	0.62(26)
S_{1n}(^{39}Si) = 1.58 MeV	3.12	2^+_3	$f_{7/2}$	14.24	0.437	6.73		
	3.35	4^+_2	$f_{7/2}$	14.00	0.146	2.21		
	3.44	2^+_4	$f_{7/2}$	13.91	0.100	1.50		
	3.51	3^+_1	$f_{7/2}$	13.84	0.237	3.55		
	3.57	3^-_1	$d_{3/2}$	13.15	0.591	8.19		
	3.70	2^-_1	$d_{3/2}$	12.98	0.301	4.12		
	3.82	4^+_3	$f_{7/2}$	13.54	0.130	1.90		
	3.91	4^+_4	$f_{7/2}$	13.45	0.254	3.69		
	3.92	3^+_2	$f_{7/2}$	13.44	0.128	1.86		
	3.95	2^-_2	$d_{3/2}$	12.67	0.204	2.72		
	3.95	5^+_1	$f_{7/2}$	13.42	0.472	6.85		
	3.97	1^-_1	$d_{3/2}$	12.65	0.121	1.61		
	4.08	3^-_2	$d_{3/2}$	12.52	0.413	5.45		
	4.19	0^-_1	$d_{3/2}$	12.39	0.127	1.66		
	4.25	2^-_3	$d_{3/2}$	12.33	0.268	3.48		
	4.39	3^-_3	$d_{3/2}$	12.17	0.122	1.56		
	4.42	5^+_2	$f_{7/2}$	13.01	0.384	5.40		
	4.63	1^-_4	$d_{3/2}$	11.92	0.156	1.96		
	4.92	3^+_5	$f_{7/2}$	12.60	0.123	1.68		
	4.96	1^-_5	$d_{3/2}$	11.60	0.144	1.76		
		Inclusive				137.39	94(1)	0.68(1)

Table 6.17: Results for one-neutron removal reactions from ^{39}Si on the C target. The ground state of ^{39}Si is assumed as the shell-model excited state with $J^\pi = 1/2^-$ and $3/2^-$. Tabulated are the one-neutron removal cross sections to assumed bound shell-model states below the neutron thresholds in the mass $A-1$ systems, ^{38}Si, of 5.62(11) MeV. The final theoretical cross sections, σ^{th}_{-1n}, include the center-of-mass correction factor $[A/(A-1)]^N$. The errors shown for the ratio of cross sections, $R_s = \sigma^{exp}_{-1n}/\sigma^{th}_{-1n}$, reflect only the errors quoted on the measurements. Configurations with $C^2S \geq 0.1$ are shown.

Reaction	E_x (MeV)	J^π	ℓ_j	σ_{sp} (mb)	C^2S	σ^{th}_{-1n}(C) (mb)	σ^{exp}_{-1n}(C) (mb)	R_s
C(^{39}Si(5/2$^-$),^{38}Si)	0.00	0^+_1	$f_{5/2}$	16.44	0.010	0.18	22(9)	122(50)
S_{1n}(^{39}Si) = 1.58 MeV	1.26	2^+_1	$p_{3/2}$	37.37	0.110	4.44		
			$f_{7/2}$	16.70	0.731	13.20		
	2.24	4^+_1	$f_{7/2}$	15.27	0.691	11.41		
	3.12	2^+_3	$p_{3/2}$	28.33	0.131	4.01		
	3.35	4^+_2	$p_{3/2}$	27.56	0.153	4.56		
			$f_{7/2}$	14.00	0.698	10.56		
	3.57	3^-_1	$d_{3/2}$	13.15	0.218	3.02		
	3.61	4^-_1	$d_{3/2}$	13.09	0.947	13.06		
	3.70	2^-_1	$d_{3/2}$	12.98	0.121	1.65		
	3.90	6^+_1	$f_{7/2}$	13.46	0.250	3.64		
	3.95	2^-_2	$d_{3/2}$	12.67	0.169	2.26		
	3.95	5^+_1	$f_{7/2}$	13.42	0.406	5.89		
	3.97	1^-_1	$d_{3/2}$	12.65	0.192	2.56		
	4.01	3^+_3	$p_{3/2}$	25.60	0.121	3.35		
	4.08	3^-_2	$d_{3/2}$	12.52	0.220	2.90		
	4.42	5^+_2	$f_{7/2}$	13.01	0.103	1.45		
	4.54	3^-_4	$s_{1/2}$	19.89	0.111	2.33		
	4.69	3^-_5	$d_{3/2}$	11.86	0.187	2.34		
	4.76	4^-_3	$d_{3/2}$	11.79	0.107	1.33		
		Inclusive				121.66	94(1)	0.77(1)
C(^{39}Si(7/2$^-$),^{38}Si)	0.00	0^+_1	$f_{7/2}$	19.25	0.431	8.97	22(9)	2.45(1.00)
S_{1n}(^{39}Si) = 1.58 MeV	1.26	2^+_1	$f_{7/2}$	16.70	0.422	7.62		
	2.24	4^+_1	$f_{7/2}$	15.27	0.351	5.79		
	3.35	4^+_2	$f_{7/2}$	14.00	0.512	7.75		
	3.61	4^-_1	$d_{3/2}$	13.09	0.116	1.60		
	3.74	5^-_1	$d_{3/2}$	12.93	1.004	13.67		
	3.90	6^+_1	$f_{7/2}$	13.46	1.274	18.54		
	3.95	2^-_2	$d_{3/2}$	12.67	0.165	2.20		
	4.16	4^-_2	$d_{3/2}$	12.43	0.212	2.78		
	4.54	3^-_4	$d_{3/2}$	12.02	0.387	4.90		
	4.76	4^-_3	$d_{3/2}$	11.79	0.404	5.02		
	5.46	4^-_7	$s_{1/2}$	17.95	0.303	5.73		
		Inclusive				121.01	94(1)	0.78(1)

Table 6.18: Results for one-neutron removal reactions from ^{39}Si on the C target. The ground state of ^{39}Si is assumed as the shell-model excited state with $J^\pi = 5/2^-$ and $7/2^-$. Tabulated are the one-neutron removal cross sections to assumed bound shell-model states below the neutron thresholds in the mass $A-1$ systems, ^{38}Si, of 5.62(11) MeV. The final theoretical cross sections, σ^{th}_{-1n}, include the center-of-mass correction factor $[A/(A-1)]^N$. The errors shown for the ratio of cross sections, $R_s = \sigma^{exp}_{-1n}/\sigma^{th}_{-1n}$, reflect only the errors quoted on the measurements. Configurations with $C^2S \geq 0.1$ are shown.

Reaction	E_x (MeV)	J^π	ℓ_j	σ_{sp} (mb)	C^2S	$\sigma^{th}_{-1n}(E1)$ (mb)	$\sigma^{exp}_{-1n}(E1)$ (mb)	R_s
Pb(^{39}Si($3/2^+$),^{38}Si)	0.00	0^+_1	-	-	0.000	0.000	0(76)	-
$S_{1n}(^{39}\text{Si}) = 1.58$ MeV	3.57	3^-_1	$p_{3/2}$	38.38	0.351	13.47		
			$f_{5/2}$	2.22	0.060	0.13		
			$f_{7/2}$	1.11	0.134	0.15		
	3.61	4^-_1	$f_{7/2}$	1.07	0.277	0.30		
	3.70	2^-_1	$p_{3/2}$	34.71	0.169	5.87		
	3.74	5^-_1	$f_{7/2}$	0.92	0.763	0.70		
	3.95	2^-_2	$p_{3/2}$	27.65	0.105	2.90		
			$f_{7/2}$	0.69	0.260	0.18		
	4.08	3^-_2	$p_{3/2}$	23.97	0.138	3.31		
			$f_{5/2}$	1.09	0.101	0.11		
	4.16	4^-_2	$f_{7/2}$	0.46	0.452	0.21		
	4.25	2^-_3	$p_{3/2}$	19.17	0.142	2.72		
	4.54	3^-_4	$f_{7/2}$	0.15	0.402	0.06		
	4.63	1^-_4	$p_{3/2}$	11.87	0.102	1.21		
	4.76	4^-_3	$f_{7/2}$	0.11	0.177	0.02		
		Inclusive				35.14	193(45)	5.49(1.28)

Table 6.19: Results for one-neutron removal reactions from ^{39}Si on the Pb target. The ground state of ^{39}Si is assumed as the shell-model excited state with $J^\pi = 3/2^+$. Tabulated are the one-neutron removal cross sections to assumed bound shell-model states below the neutron thresholds in the mass $A-1$ systems, ^{38}Si, of 5.62(11) MeV. The final theoretical cross sections, σ^{th}_{-1n}, include the center-of-mass correction factor $[A/(A-1)]^N$. The errors shown for the ratio of cross sections, $R_s = \sigma^{exp}_{-1n}/\sigma^{th}_{-1n}$, reflect only the errors quoted on the measurements. Configurations with $C^2S \geq 0.1$ are shown.

Reaction	E_x (MeV)	J^π	ℓ_j	σ_{sp} (mb)	C^2S	$\sigma^{th}_{-1n}(E1)$ (mb)	$\sigma^{exp}_{-1n}(E1)$ (mb)	R_s
Pb(^{39}Si($1/2^-$),^{38}Si)	0.00	0^+_1	$p_{1/2}$	225.39	0.103	23.22	0(76)	0.00(3.27)
$S_{1n}(^{39}\text{Si}) = 1.58$ MeV	1.26	2^+_1	$p_{3/2}$	118.79	0.435	51.67		
	2.72	2^+_2	$p_{3/2}$	62.38	0.333	20.77		
	3.51	3^+_1	$f_{7/2}$	1.18	1.140	1.35		
	3.70	2^-_1	$d_{3/2}$	8.78	0.681	5.98		
	3.82	4^+_3	$f_{7/2}$	0.84	0.505	0.42		
	3.95	2^-_2	$d_{3/2}$	7.53	0.107	0.81		
	4.23	1^-_2	$d_{3/2}$	6.13	0.731	4.48		
	4.25	2^-_3	$d_{3/2}$	6.03	0.374	2.26		
	4.45	1^-_3	$s_{1/2}$	47.57	0.101	4.80		
	4.47	4^+_5	$f_{7/2}$	0.16	0.337	0.05		
	4.63	1^-_4	$s_{1/2}$	43.95	0.102	4.48		
	4.75	3^+_4	$f_{7/2}$	0.11	0.142	0.02		
	4.89	2^-_5	$d_{3/2}$	2.98	0.114	0.34		
	5.05	2^-_6	$d_{3/2}$	2.23	0.440	0.98		
	5.45	4^+_8	$f_{7/2}$	0.00	0.223	0.00		
	Inclusive					143.29	193(45)	1.35(31)
Pb(^{39}Si($3/2^-$),^{38}Si)	0.00	0^+_1	$p_{3/2}$	234.55	0.657	154.10	0(76)	0.00(0.49)
$S_{1n}(^{39}\text{Si}) = 1.58$ MeV	3.12	2^+_3	$f_{7/2}$	1.92	0.437	0.84		
	3.35	4^+_2	$f_{7/2}$	1.43	0.146	0.21		
	3.44	2^+_4	$f_{7/2}$	1.26	0.100	0.13		
	3.51	3^+_1	$f_{7/2}$	1.18	0.237	0.28		
	3.57	3^-_1	$d_{3/2}$	9.43	0.591	5.57		
	3.70	2^-_1	$d_{3/2}$	8.78	0.301	2.64		
	3.82	4^+_3	$f_{7/2}$	0.84	0.130	0.11		
	3.91	4^+_4	$f_{7/2}$	0.74	0.254	0.19		
	3.92	3^+_2	$f_{7/2}$	0.72	0.128	0.09		
	3.95	2^-_2	$d_{3/2}$	7.53	0.204	1.54		
	3.95	5^+_1	$f_{7/2}$	0.69	0.472	0.33		
	3.97	1^-_1	$d_{3/2}$	7.43	0.121	0.90		
	4.08	3^-_2	$d_{3/2}$	6.88	0.413	2.84		
	4.19	0^-_1	$d_{3/2}$	6.33	0.127	0.80		
	4.25	2^-_3	$d_{3/2}$	6.03	0.268	1.62		
	4.39	3^-_3	$d_{3/2}$	5.33	0.122	0.65		
	4.42	5^+_2	$f_{7/2}$	0.17	0.384	0.07		
	4.63	1^-_4	$d_{3/2}$	4.20	0.156	0.66		
	4.92	3^+_5	$f_{7/2}$	0.08	0.123	0.01		
	4.96	1^-_5	$d_{3/2}$	2.65	0.144	0.38		
	Inclusive					210.06	193(45)	0.92(21)

Table 6.20: Results for one-neutron removal reactions from ^{39}Si on the Pb target. The ground state of ^{39}Si is assumed as the shell-model excited state with $J^\pi = 1/2^-$ and $3/2^-$. Tabulated are the one-neutron removal cross sections to assumed bound shell-model states below the neutron thresholds in the mass $A-1$ systems, ^{38}Si, of 5.62(11) MeV. The final theoretical cross sections, σ^{th}_{-1n}, include the center-of-mass correction factor $[A/(A-1)]^N$. The errors shown for the ratio of cross sections, $R_s = \sigma^{exp}_{-1n}/\sigma^{th}_{-1n}$, reflect only the errors quoted on the measurements. Configurations with $C^2S \geq 0.1$ are shown.

Reaction	E_x (MeV)	J^π	ℓ_j	σ_{sp} (mb)	C^2S	$\sigma^{th}_{-1n}(E1)$ (mb)	$\sigma^{exp}_{-1n}(E1)$ (mb)	R_s
Pb(^{39}Si($5/2^-$),^{38}Si)	0.00	0^+_1	$f_{5/2}$	20.77	0.010	0.21	0(76)	0(362)
S_{1n}(^{39}Si) = 1.58 MeV	1.26	2^+_1	$p_{3/2}$	118.79	0.110	13.07		
			$f_{7/2}$	9.21	0.731	6.73		
	2.24	4^+_1	$f_{7/2}$	4.47	0.691	3.09		
	3.12	2^+_3	$p_{3/2}$	50.92	0.131	6.67		
	3.35	4^+_2	$p_{3/2}$	44.55	0.153	6.82		
			$f_{7/2}$	1.43	0.698	1.00		
	3.57	3^-_1	$d_{3/2}$	9.43	0.218	2.06		
	3.61	4^-_1	$d_{3/2}$	9.23	0.947	8.74		
	3.70	2^-_1	$d_{3/2}$	8.78	0.121	1.06		
	3.90	6^+_1	$f_{7/2}$	0.75	0.250	0.19		
	3.95	2^-_2	$d_{3/2}$	7.53	0.169	1.27		
	3.95	5^+_1	$f_{7/2}$	0.69	0.406	0.28		
	3.97	1^-_1	$d_{3/2}$	7.43	0.192	1.43		
	4.01	3^+_3	$p_{3/2}$	25.95	0.121	3.14		
	4.08	3^-_2	$d_{3/2}$	6.88	0.220	1.51		
	4.42	5^+_2	$f_{7/2}$	0.17	0.103	0.02		
	4.54	3^-_4	$s_{1/2}$	45.76	0.111	5.08		
	4.69	3^-_5	$d_{3/2}$	3.92	0.187	0.73		
	4.76	4^-_3	$d_{3/2}$	3.59	0.107	0.38		
		Inclusive				87.65	193(45)	2.20(51)
Pb(^{39}Si($7/2^-$),^{38}Si)	0.00	0^+_1	$f_{7/2}$	22.61	0.431	9.74	0(76)	0(8)
S_{1n}(^{39}Si) = 1.58 MeV	1.26	2^+_1	$f_{7/2}$	9.21	0.422	3.89		
	2.24	4^+_1	$f_{7/2}$	4.47	0.351	1.57		
	3.35	4^+_2	$f_{7/2}$	1.43	0.512	0.73		
	3.61	4^-_1	$d_{3/2}$	9.23	0.116	1.07		
	3.74	5^-_1	$d_{3/2}$	8.58	1.004	8.61		
	3.90	6^+_1	$f_{7/2}$	0.75	1.274	0.96		
	3.95	2^-_2	$d_{3/2}$	7.53	0.165	1.24		
	4.16	4^-_2	$d_{3/2}$	6.48	0.212	1.37		
	4.54	3^-_4	$d_{3/2}$	4.62	0.387	1.79		
	4.76	4^-_3	$d_{3/2}$	3.59	0.404	1.45		
	5.46	4^-_7	$s_{1/2}$	26.95	0.303	8.17		
		Inclusive				77.45	193(45)	2.49(58)

Table 6.21: Results for one-neutron removal reactions from ^{39}Si on the Pb target. The ground state of ^{39}Si is assumed as the shell-model excited state with $J^\pi = 5/2^-$ and $7/2^-$. Tabulated are the one-neutron removal cross sections to assumed bound shell-model states below the neutron thresholds in the mass $A-1$ systems, ^{38}Si, of 5.62(11) MeV. The final theoretical cross sections, σ^{th}_{-1n}, include the center-of-mass correction factor $[A/(A-1)]^N$. The errors shown for the ratio of cross sections, $R_s = \sigma^{exp}_{-1n}/\sigma^{th}_{-1n}$, reflect only the errors quoted on the measurements. Configurations with $C^2S \geq 0.1$ are shown.

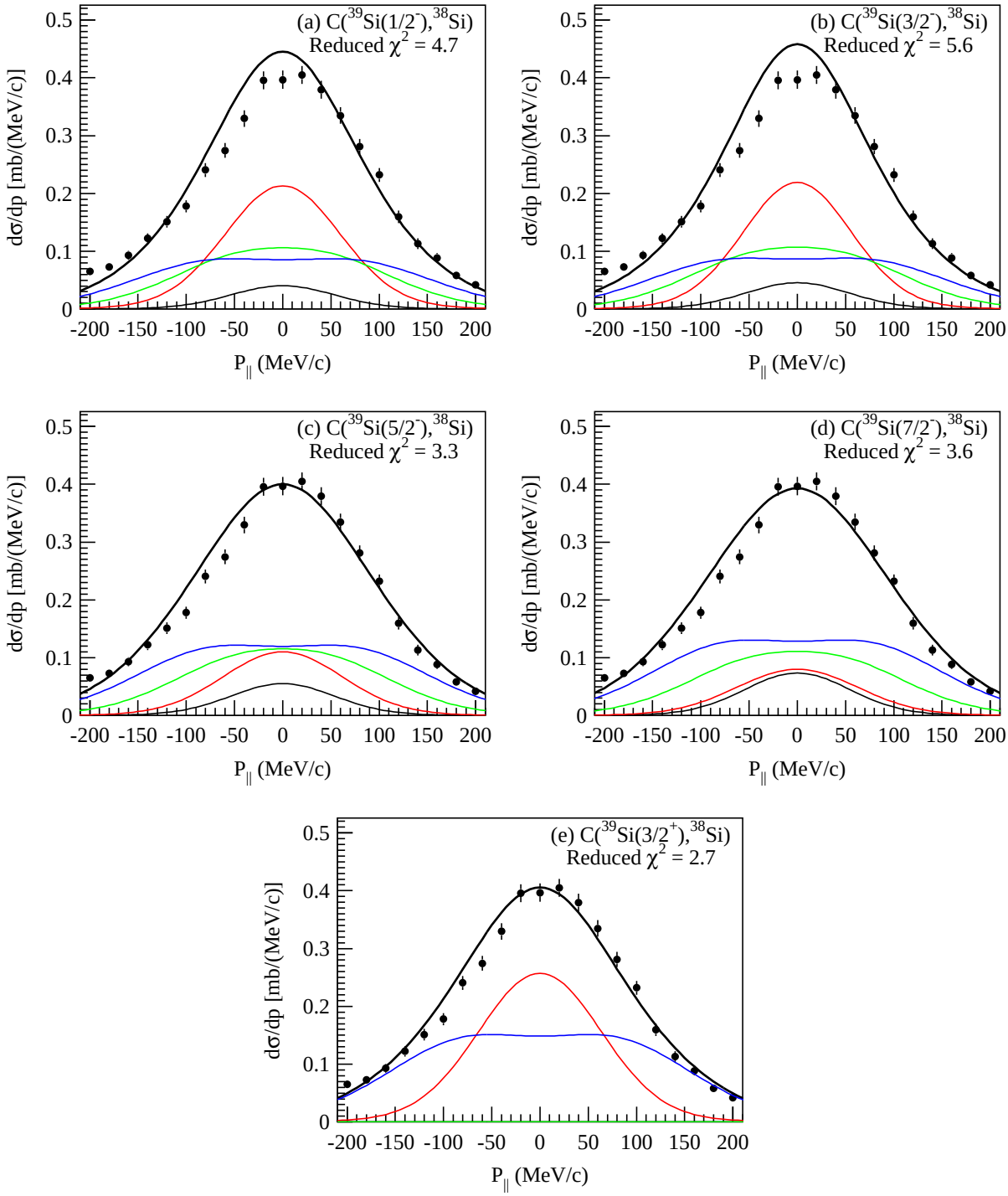

Figure 6.20: Measured parallel momentum distributions of one-neutron removal form ^{39}Si and corresponding theoretical calculations for (a) $1/2^-$, (b) $3/2^-$, (c) $5/2^-$, (d) $7/2^-$, and (e) $3/2^+$ shell model states The red dashed lines show the p-wave components, and blue dotted lines show the f-wave components in total inclusive cross sections. The theoretical momentum distribution curves are normalised to the measured inclusive cross section.

6.10 Results for ^{41}Si

According to the theoretical prediction and systematics of the $N = 27$ nuclei, discussed later in detail, the most probable spin parity of the ground state of ^{37}Mg are $3/2^-$ and $7/2^-$. In the following discussion, we consider only the ground states with $J^\pi = 3/2^-$ and $J^\pi = 7/2^-$, which correspond Figs. 6.7 (b) and (d).

From the combined analysis in Fig. 6.5, the possible configurations is $^{36}\mathrm{Mg}(0^+) \otimes 2p_{3/2}$ with $J^\pi = 3/2^-$. From the same analysis of χ^2 for two parameters as described in Sec. 5.3, the spectroscopic factor $C^2S(0^+, 2s_{1/2})$ is $0.87^{+0.20}_{-0.18}$, and the separation energy S_{1n} is $1.54^{+0.40}_{-0.38}$ MeV.

According to the large-scale Monte Carlo Shell Model (MCSM) calculations employing the SDPF-MU effective interaction [52, 53], the $3/2^-$ shell-model ground state is placed below the first excited $7/2^-_1$ state at $E_x = 0.23$ MeV as listed in Table 6.22 and shown in Fig 6.21, which supports our results.

Table 6.5 shows the comparison between the experimental nuclear breakup cross sections and theoretical calculations for the shell model states with $J^\pi = 3/2^-$ and $7/2^-$. For the shell model states with $J^\pi = 3/2^-$ and $7/2^-$, the experimental inclusive cross section of 110(1) is 30 % and 19 % smaller than the theoretical values of 157.07 mb for $J^\pi = 3/2^-$ and 135.22 mb for $J^\pi = 7/2^-$, respectively. On the other hand, the experimental semi-inclusive cross section of 48(8) is about 3 times and 12 times larger than the theoretical values of 16.84 mb for $J^\pi = 3/2^-$ and 4.18 mb for $J^\pi = 7/2^-$, respectively.

Table 6.5 shows the case for Coulomb breakup. From the comparisons between the experimental and theoretical cross sections for inclusive and semi-inclusive breakup, although the shell model states with $J^\pi = 3/2^-$ is likely to be favored, both cases of $J^\pi = 3/2^-$ and $7/2^-$ can not well explain the experimental result.

At last, Figures. 6.22 (a) and (b) show the measured momentum distributions and theoretical calculations assuming $3/2^-$ and $7/2^-$ ground states. From the results, both assumptions for $3/2^-$ and $7/2^-$ well describe the experimental momentum distribution.

As a result, from the combined analysis, we suggested the $3/2^-$ ground state of ^{41}Si. However, the shell-model calculations can not completely explain the structure of ^{41}Si.

Nucleus	J^π	Energy (MeV)
^{41}Si	$3/2^-$	0.00
	$7/2^-$	0.23
	$5/2^-$	0.52
	$1/2^-$	0.61

Table 6.22: Low-lying shell-model levels for ^{41}Si calculated with the SDPF-M interaction [52,53] are listed. The state of 0.00 MeV corresponds the ground states. Only the yrast states are shown.

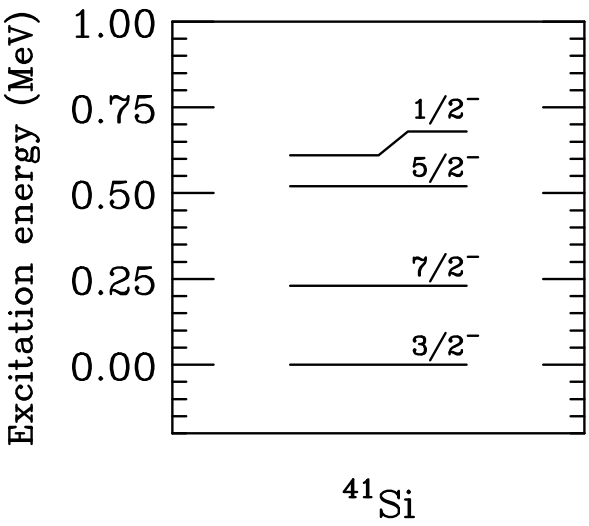

Figure 6.21: Low-lying shell-model level scheme for ^{41}Si with the SDPF-M interaction [52,53] are listed. The state of 0.00 MeV corresponds the ground states. Only the yrast states are shown.

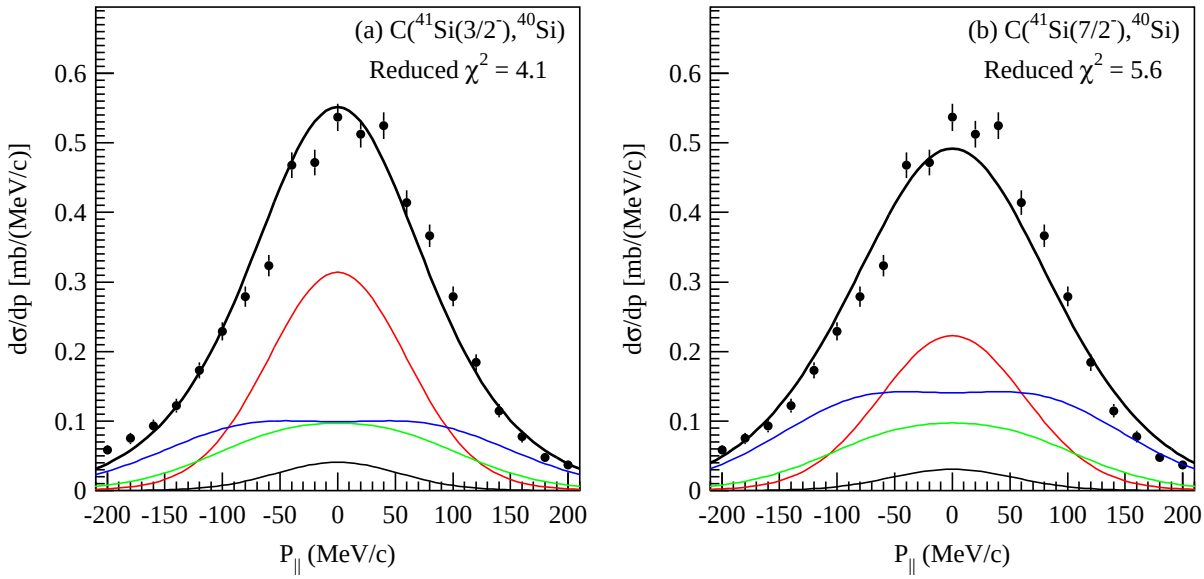

Figure 6.22: Measured parallel momentum distributions of one-neutron removal form ^{41}Si and corresponding theoretical calculations for (a) $3/2^-$ ground state and (b) $7/2^-$ ground state. The red dashed lines show the p-wave components, and blue dotted lines show the f-wave components in total inclusive cross sections. The theoretical momentum distribution curves are normalised to the measured inclusive cross section.

According to the normal shell ordering, the ground state of ^{41}Si is described by 1 neutron hole configuration $(\nu f_{7/2})^{-1}$. However, some experiments suggest that the simple $(\nu f_{7/2})^{-1}$ configuration may not be the ground state of ^{41}Si. Figure 6.23 shows the experimental systematics of the energies of the first $3/2^-$ and $7/2^-$ states in $N = 27$ nuclei. The $7/2^-$ and $3/2^-$ states of ^{47}Ca corresponds to rather pure states of neutron $0p1h$ and $1p2h$ configurations [67,68], $(\nu f_{7/2})^{-1}$ and $(\nu p_{3/2})^1(\nu f_{7/2})^{-2}$, with respect to the doubly magic nucleus ^{48}Ca. Therefore, the shape of these states are considered to be spherical, which is supported by the relatively large energy of the $3/2^-$ state lying at 2.01 MeV. In ^{45}Ar, the $3/2^-$ state comes down to the energy of 537 keV [69], containing about half of the $p_{3/2}$ strength [70]. In ^{43}S, the energy of the $3/2-$ state becomes lower than the $7/2-$ state, lying at 320.5(5) keV below the $7/2-$ state [71–73]. From the life-time measurement by Sarzin *et al.* [71], the "intruder" $7/2^-$ state is known as an isomeric state. Both the low $B(E2)$ value and absence of calculated deformed structure built on the $7/2^-_1$ isomeric state suggest a coexistence of different shapes in the low-lying structure of ^{43}S [73]. Chevrier *et al.* [74] suggest that while the $7/2^-_1$ isomer cannot be regarded as a spherical state, proton–neutron correlations [75] are not developed enough to derive the state towards deformation. Therefore, they conclude that the properties of the isomeric state are understood as a remnant effect of the eroding $N = 28$ shell closure. For ^{41}Si, Sohler *et al.* [75] performed the γ-spectroscopy by in-beam gamma method, finding a γ transition of 672(14) keV. From the result and comparison with the structure of ^{43}S, they suggest isomeric $7/2^-$ lies above the $3/2^-$ ground state. This result is consistent with our data, which is shown in Fig. 6.23.

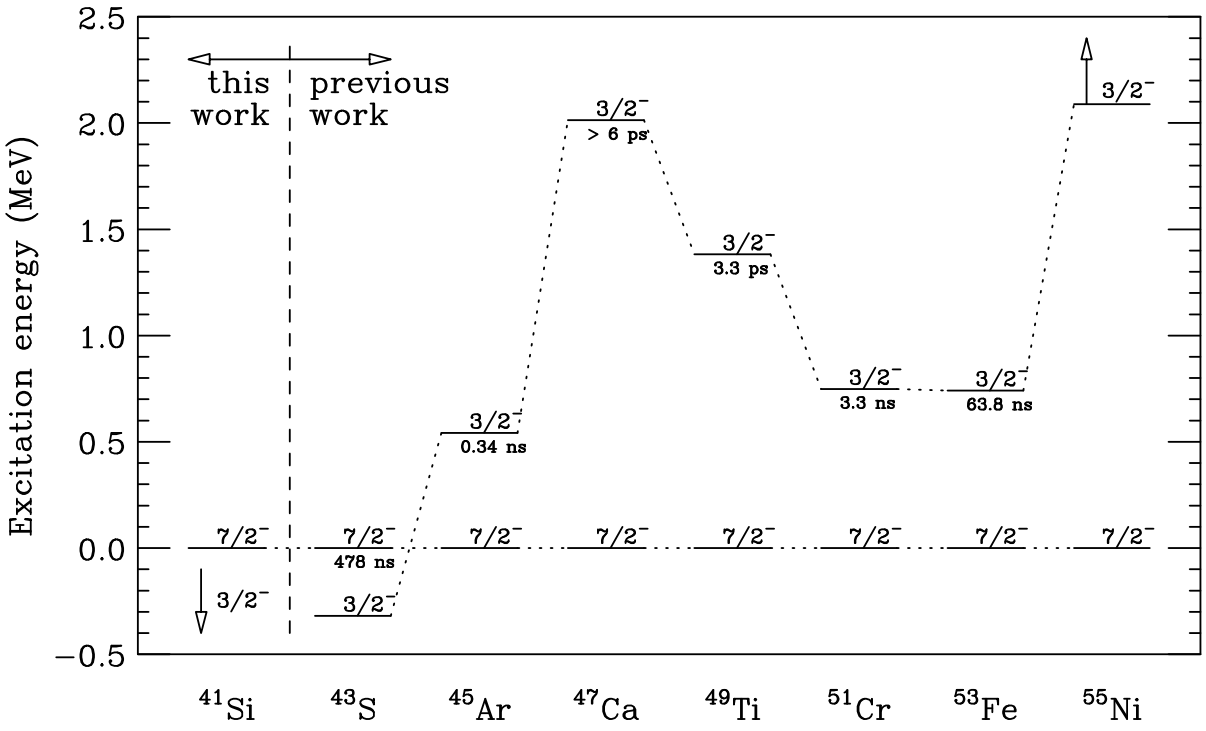

Figure 6.23: Experimental systematics of the energies of the first $3/2^-$ and $7/2^-$ states in $N = 27$ nuclei. From ^{43}S to ^{53}Fe, the energies of these levels are known. For ^{55}Ni, spin-parity of the first excited state of 2.089 MeV is not known. The half-lives of the first excited state of each nucleus are also shown. From our result, the ground state of ^{41}Si is found to be $3/2^-$, which is shown in the figure.

Reaction	E_x (MeV)	J^π	ℓ_j	σ_{sp} (mb)	C^2S	σ^{th}_{-1n}(C) (mb)	σ^{exp}_{-1n}(C) (mb)	R_s
C(^{41}Si($3/2^-$),^{40}Si)	0.00	0^+_1	$p_{3/2}$	50.94	0.307	16.84	48(8)	2.85(48)
S_{1n}(^{41}Si) = 1.38 MeV	1.12	2^+_1	$p_{3/2}$	38.35	0.381	15.73		
	1.74	2^+_2	$f_{7/2}$	15.38	0.207	3.43		
	2.36	3^+_1	$f_{7/2}$	14.52	0.133	2.08		
	2.97	3^-_1	$d_{3/2}$	13.14	0.965	13.32		
	3.28	4^+_3	$f_{5/2}$	11.46	1.134	13.99		
	3.30	2^+_3	$p_{3/2}$	27.14	0.353	10.32		
			$f_{7/2}$	13.44	0.248	3.59		
	3.35	0^-_1	$d_{3/2}$	12.59	0.178	2.35		
	3.38	2^+_4	$p_{3/2}$	26.88	0.440	12.74		
	3.42	1^-_1	$d_{3/2}$	12.49	0.220	2.89		
	3.46	3^+_2	$f_{7/2}$	13.27	0.248	3.54		
	3.49	2^-_1	$d_{3/2}$	12.40	0.454	5.91		
	3.68	2^-_2	$s_{1/2}$	21.88	0.122	2.80		
	3.75	5^+_1	$f_{7/2}$	12.99	0.426	5.96		
	4.08	1^-_2	$d_{3/2}$	11.67	0.135	1.66		
	4.20	5^+_2	$f_{7/2}$	12.58	0.205	2.78		
	4.41	3^+_5	$f_{7/2}$	12.40	0.344	4.59		
	4.83	3^-_5	$d_{3/2}$	10.88	0.122	1.39		
		Inclusive				157.07	110(1)	0.70(1)
C(^{41}Si($7/2^-$),^{40}Si)	0.00	0^+_1	$f_{7/2}$	18.82	0.206	4.18	48(8)	11.5(1.9)
S_{1n}(^{41}Si) = 1.38 MeV	1.12	2^+_1	$f_{7/2}$	16.39	0.533	9.41		
	2.36	3^+_1	$p_{3/2}$	30.87	0.129	4.29		
	2.63	4^+_1	$p_{3/2}$	29.68	0.183	5.85		
	2.79	4^+_2	$f_{7/2}$	14.00	0.684	10.31		
	3.28	4^+_3	$p_{3/2}$	27.21	0.371	10.87		
	3.33	5^-_1	$d_{3/2}$	12.62	0.933	12.37		
	3.46	3^+_2	$p_{3/2}$	26.61	0.162	4.64		
	3.49	2^-_1	$d_{3/2}$	12.40	0.138	1.80		
	3.65	4^-_1	$d_{3/2}$	12.19	0.149	1.91		
	3.68	2^-_2	$d_{3/2}$	12.15	0.117	1.49		
	3.81	4^+_4	$p_{3/2}$	25.54	0.100	2.75		
			$f_{7/2}$	12.93	0.131	1.82		
	3.88	6^+_1	$f_{7/2}$	12.87	1.219	16.89		
	4.20	5^+_2	$f_{7/2}$	12.58	0.168	2.28		
	4.40	4^-_3	$s_{1/2}$	19.85	0.111	2.31		
			$d_{3/2}$	11.32	0.425	5.05		
	4.42	3^-_3	$d_{3/2}$	11.30	0.197	2.34		
	4.60	6^+_2	$f_{7/2}$	12.24	0.117	1.54		
		Inclusive				135.22	110(1)	0.81(1)

Table 6.23: Results for one-neutron removal reactions from ^{41}Si on the C target. Tabulated are the one-neutron removal cross sections to assumed bound shell-model states below the neutron thresholds in the mass $A-1$ systems, ^{40}Si, of 4.96(24) MeV. The final theoretical cross sections, σ^{th}_{-1n}, include the center-of-mass correction factor $[A/(A-1)]^N$. The errors shown for the ratio of cross sections, $R_s = \sigma^{exp}_{-1n}/\sigma^{th}_{-1n}$, reflect only the errors quoted on the measurements. Configurations with $C^2S \geq 0.1$ are shown.

Reaction	E_x (MeV)	J^π	ℓ_j	σ_{sp} (mb)	C^2S	$\sigma^{th}_{-1n}(E1)$ (mb)	$\sigma^{exp}_{-1n}(E1)$ (mb)	R_s
Pb(^{41}Si(3/2$^-$),^{40}Si)	0.00	0^+_1	$p_{3/2}$	240.43	0.307	73.81	115(80)	1.56(1.08)
S_{1n}(^{41}Si) = 1.38 MeV	1.12	2^+_1	$p_{3/2}$	117.81	0.381	44.89		
	1.74	2^+_2	$f_{7/2}$	4.78	0.207	0.99		
	2.36	3^+_1	$f_{7/2}$	2.58	0.133	0.34		
	2.97	3^-_1	$d_{3/2}$	9.94	0.965	9.59		
	3.28	4^+_3	$f_{5/2}$	1.07	1.134	1.21		
	3.30	2^+_3	$p_{3/2}$	25.34	0.353	8.95		
			$f_{7/2}$	0.66	0.248	0.16		
	3.35	0^-_1	$d_{3/2}$	8.13	0.178	1.45		
	3.38	2^+_4	$p_{3/2}$	23.10	0.440	10.16		
	3.42	1^-_1	$d_{3/2}$	7.82	0.220	1.72		
	3.46	3^+_2	$f_{7/2}$	0.49	0.248	0.12		
	3.49	2^-_1	$d_{3/2}$	7.51	0.454	3.41		
	3.68	2^-_2	$s_{1/2}$	48.12	0.122	5.87		
	3.75	5^+_1	$f_{7/2}$	0.28	0.426	0.12		
	4.08	1^-_2	$d_{3/2}$	4.02	0.135	0.54		
	4.20	5^+_2	$f_{7/2}$	0.13	0.205	0.03		
	4.41	3^+_5	$f_{7/2}$	0.07	0.344	0.02		
	4.83	3^-_5	$d_{3/2}$	0.48	0.122	0.06		
		Inclusive				188.82	284(54)	1.50(29)
Pb(^{41}Si(7/2$^-$),^{40}Si)	0.00	0^+_1	$f_{7/2}$	19.51	0.206	4.02	115(80)	28.6(19.9)
S_{1n}(^{41}Si) = 1.38 MeV	1.12	2^+_1	$f_{7/2}$	8.04	0.533	4.29		
	2.36	3^+_1	$p_{3/2}$	57.36	0.129	7.40		
	2.63	4^+_1	$p_{3/2}$	47.06	0.183	8.61		
	2.79	4^+_2	$f_{7/2}$	1.50	0.684	1.03		
	3.28	4^+_3	$p_{3/2}$	25.90	0.371	9.61		
	3.33	5^-_1	$d_{3/2}$	8.21	0.933	7.66		
	3.46	3^+_2	$p_{3/2}$	20.85	0.162	3.38		
	3.49	2^-_1	$d_{3/2}$	7.51	0.138	1.04		
	3.65	4^-_1	$d_{3/2}$	6.75	0.149	1.01		
	3.68	2^-_2	$d_{3/2}$	6.56	0.117	0.77		
	3.81	4^+_4	$p_{3/2}$	13.83	0.100	1.38		
			$f_{7/2}$	0.26	0.131	0.03		
	3.88	6^+_1	$f_{7/2}$	0.23	1.219	0.28		
	4.20	5^+_2	$f_{7/2}$	0.13	0.168	0.02		
	4.40	4^-_3	$s_{1/2}$	24.96	0.111	2.77		
			$d_{3/2}$	1.99	0.425	0.85		
	4.42	3^-_3	$d_{3/2}$	1.87	0.197	0.37		
	4.60	6^+_2	$f_{7/2}$	0.01	0.117	0.00		
		Inclusive				77.79	284(54)	3.65(69)

Table 6.24: Results for one-neutron removal reactions from ^{41}Si on the Pb target. Tabulated are the one-neutron removal cross sections to assumed bound shell-model states below the neutron thresholds in the mass $A-1$ systems, ^{40}Si, of 4.96(24) MeV. The final theoretical cross sections, σ^{th}_{-1n}, include the center-of-mass correction factor $[A/(A-1)]^N$. The errors shown for the ratio of cross sections, $R_s = \sigma^{exp}_{-1n}/\sigma^{th}_{-1n}$, reflect only the errors quoted on the measurements. Configurations with $C^2S \geq 0.1$ are shown.

Chapter 7

Experimental Results and Discussions for Carbon Isotopes

7.1 Experimental Results

The one- and two-neutron removal cross sections extracted here are summarized in Table 7.1 together with the corresponding mid-target energy of the projectile. The cross section for C(^{19}C, ^{18}C) is smaller than that measured at lower energies. For instance, at 64 MeV/nucleon, the cross section σ_{-1n} is 226(65) mb [76], about 40 % larger than the current value. In part, this reflects the smaller intrinsic nucleon-nucleon cross sections at the energy of the current experiment (being closer to the minimum near 300 MeV) as well as changes in the real parts of the optical potentials and a reduced diffractive breakup contribution for energies in excess of 100 MeV/nucleon [77]. For ^{20}C, the yield of ^{19}C residues is much smaller, by a factor of about three, than that of ^{18}C. We note that the recent measurement of one- and two-neutron removal from ^{20}C on a proton target at 40 MeV/nucleon [78] showed a similar trend, where the cross section for one-neutron removal (22(8) mb) is about 1/5 of that for two-neutron removal (107(15) mb). As will be shown later (Section 7.2.1) the final states play a significant role in the cross sections. For ^{22}C, we note an enhanced cross section compared to ^{20}C which, as we will show, reflects the two-neutron halo character of ^{22}C.

The measured momentum distributions in the rest frame of the projectile are shown in Fig. 7.1. We note that that for (^{22}C, ^{20}C) was obtained here for the first time. The width parameters for the momentum distributions are listed in Table 7.1, where they were deduced by fitting the data with a Lorentzian and Gaussian. The momentum distributions for (^{19}C, ^{18}C), (^{20}C, ^{19}C), and (^{22}C, ^{20}C) were fitted over the ranges of $-75 \leq P_{||} \leq 75$ MeV/c, and that for (^{20}C, ^{18}C) was fitted over the range of $-150 \leq P_{||} \leq 150$ MeV/c. The broadening arising from the target effects and detector resolution was found to follow the Gaussian distribution with a sigma width of 23, 23, 28, and 27 MeV/c for (^{19}C, ^{18}C), (^{20}C, ^{19}C), (^{20}C, ^{18}C), and (^{22}C, ^{20}C), respectively. It should be noted that the widths quoted here are only meant to serve as a comparative guide, especially given that they are somewhat dependent on the assumed functional form of the lineshape – in particular when the statistics are limited.

The data show good agreement with the eikonal-model calculations in Figs. 7.2-7.5 after folding with the experimental effects. Based on this comparison the measured widths for (^{19}C, ^{18}C), (^{20}C, ^{19}C), (^{20}C, ^{18}C), and (^{22}C, ^{20}C) are shown to be consistent with the FWHMs listed in Table 7.1, which are obtained from the calculated distributions. We note that in order to derive any structural information comparison should be made with the results of such realistic reaction theory as discussed in Section 7.2.

It is clear that the momentum distributions for (^{19}C, ^{18}C), (^{20}C, ^{19}C), and (^{22}C, ^{20}C) are much narrower, at least by a factor of two, than those expected on the basis of the Goldhaber

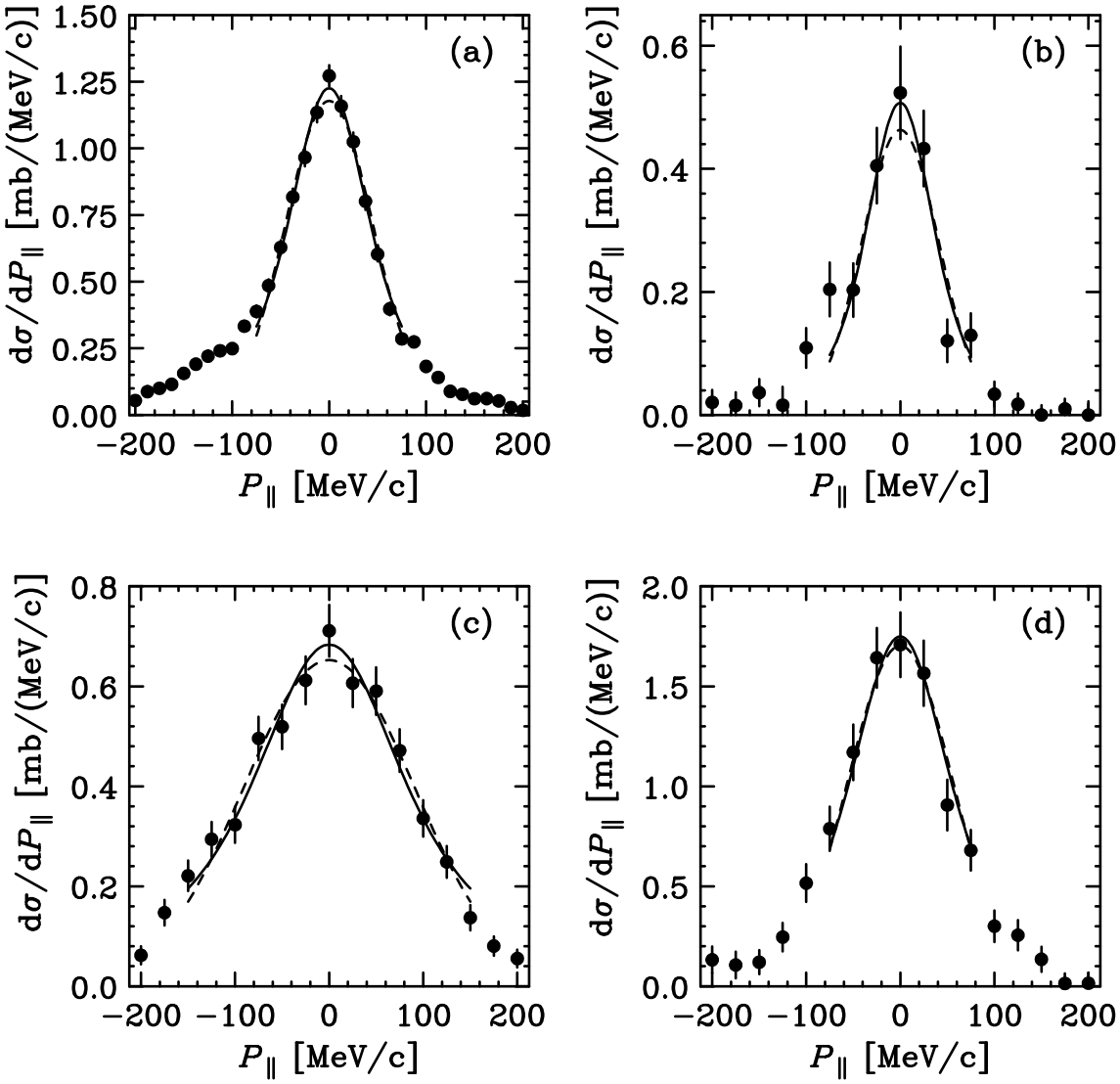

Figure 7.1: The momentum distributions for (a) C(^{19}C, ^{18}C), (b) C(^{20}C, ^{19}C), (c) C(^{20}C, ^{18}C), and (d) C(^{22}C, ^{20}C). These distributions are fitted with Lorentzian distributions (solid line) and Gaussian distributions (dashed line) convoluted with the experimental resolution. The distributions for (a), (b), and (d) were fitted over the range of $-75 \leq P_{||} \leq 75$ MeV/c, and that for (c) was fitted over the range of $-150 \leq P_{||} \leq 150$ MeV/c.

Table 7.1: The one- and two-neutron removal cross sections for each reaction channel at the mid-target energies ($\bar{E}/A$) are shown.

			FWHM (MeV/c)		
Reaction	$\bar{E}/A$ (MeV)	$\sigma_{-xn}^{\rm exp}$ (mb)	Lorentzian fit	Gaussian fit	Calculation
C(^{19}C, ^{18}C)	243	163(12)	70(6)	92(14)	56
C(^{20}C, ^{19}C)	241	58(5)	51(13)	81(18)	77
C(^{20}C, ^{18}C)	241	155(25)	172(16)	204(10)	211
C(^{22}C, ^{20}C)	240	266(19)	92(14)	114(12)	73

model (210 MeV/c for single-neutron removal, 290 MeV/c for two-neutron removal) [79]. The narrow widths for the reactions on ^{19}C and ^{22}C arise from the weakly bound one- and two-neutron halo-like nature of these nuclei and role of s-wave valence neutron(s) in their ground-state structure. It is interesting that the measured distribution for (^{20}C, ^{19}C) is also narrow. This suggests that the reaction probes the $\nu s_{1/2}^2$ component of the ^{20}C(0^+) ground state wave function, as is required to populate the bound ^{19}C$_{\rm g.s.}$($1/2^+$) halo-state.

The momentum distribution for (^{19}C, ^{18}C) is consistent with a recent measurement on protons at 40 MeV/nucleon (FWHM = 83(12) MeV/c) [78], while that for (^{20}C, ^{19}C) is much narrower than the measurement [78] (FWHM = 168(20) MeV/c). The cause of this difference is not entirely clear. We note, however, that the two measurements were made at very different energies on carbon and proton targets and, as such, are governed by different reaction mechanisms, being dominated by inelastic and elastic breakup mechanisms, respectively. Furthermore, the extraction of momentum distributions from measurements employing a zero-degree telescope [78] rather than a spectrometer to separate the reaction products (as was done here), requires subtraction of a strong component (dominant in the case of (^{20}C, ^{19}C)) from reactions arising in the telescope itself. The quantitative analyses and interpretations of the momentum distributions and cross sections obtained here are detailed in the following sections.

7.2 Theoretical Analysis and Discussion

We discuss the results for the inclusive cross sections for one- and two-neutron removal from the ^{19,20,22}C isotopes. We consider in detail the calculated contributions from both indirect and direct two-nucleon removal. The measured and calculated inclusive parallel momentum distributions are also discussed. In all cases these are shown in the projectile rest frame. In the comparisons with the data the theoretical momentum distributions, calculated using the stripping mechanism, have been convoluted with the Gaussian experimental resolution given in Section 6 and then scaled to the measured inclusive cross sections. Further discussion of the calculations of the parallel momentum distributions in the cases of the transitions to unbound final states is included when discussing these; i.e., for the ^{20,22}C cases.

7.2.1 One-neutron Removal Reactions

We first discuss the individual and the inclusive one-neutron removal cross sections to bound, $\sigma_{-1n}^{\rm th}$, and unbound (neutron emitting), $\sigma_{-1n(e)}^{\rm th}$, states of the mass $A-1$ isotopes. The experimental and theoretical results of the present work are collected in Tables 7.2 and 7.3. Also tabulated are the details of the relevant shell-model states, their energies, spins, parities and spectroscopic factors, C^2S. The overall ratios of the measured to the calculated inclusive one-neutron removal cross sections, $R_s = \sigma_{-1n}^{\rm exp}/\sigma_{-1n}^{\rm th}$, are also shown in the tables for each bound

Reaction	E_x (MeV)	J^π	ℓ_j	σ_{sp} (mb)	C^2S	σ^{th}_{-1n} (mb)	σ^{exp}_{-1n} (mb)	R_s
(^{19}C($1/2^+$),^{18}C(J^π))	0.000	0^+_1	0	104.7	0.580	67.63		
$S_{1n}(^{19}\text{C}) = 0.58$ MeV	2.114	2^+_1	2	29.91	0.470	15.67		
	3.639	2^+_2	2	25.91	0.104	3.00		
	3.988	0^+_2	0	39.35	0.319	13.97		
	4.915[1]	3^+_1	2	23.60	1.523	40.04		
	4.975[1]	2^+_3	2	23.50	0.922	24.15		
		Inclusive				164.5	163(12)	0.99(7)
(^{20}C(0^+),^{19}C(J^π))	0.000[2]	$1/2^+_1$	0	48.37	1.099	58.92		
$S_{1n}(^{20}\text{C}) = 2.90$ MeV		Inclusive				58.92	58(5)	0.98(8)

Table 7.2: Results for one-neutron removal reactions from ^{19,20}C. Tabulated are the one-neutron removal cross sections to assumed bound shell-model states near and below the neutron thresholds in the mass $A-1$ systems, ^{18,19}C, of 4.18 and 0.58 MeV, respectively (see also the footnotes). The final theoretical cross sections, σ^{th}_{-1n}, include the center-of-mass correction factor $[A/(A-1)]^N$. The errors shown for the ratio of cross sections, $R_s = \sigma^{exp}_{-1n}/\sigma^{th}_{-1n}$, reflect only the errors quoted on the measurements.

and unbound final states data set.

Results for ^{19}C

The case of ^{19}C provides a valuable link to the earlier work at lower energies, summarized in Ref. [80], and the related and more exclusive results using neutron knockout from a proton target [81]. From the present work, calculated exclusive and experimental inclusive one-neutron removal yields from the ^{19}C($1/2^+$) ground state, with ground-state separation energy $S_{1n}(^{19}\text{C}) = 0.58$ MeV, are shown in Table 7.2. The theoretical cross sections are shown for the six predicted positive parity ^{18}C final states.

In the case of (^{19}C, ^{18}C) the WBP shell-model calculation places several final states near to or between the one- and two-neutron threshold energies of 4.18 MeV and 4.91 MeV, respectively, for ^{18}C. Specifically, the third 2^+_3 and first 3^+_1 states at 4.915 and 4.975 MeV have significant spectroscopic strengths and associated cross sections. Experimentally, recent work of Kondo *et al.* [81], on neutron knockout from ^{19}C on a proton target, observed gamma-rays from a $(2^+, 3^+)$ excited state (or states) near 4.0 MeV, the associated ^{18}C transverse momentum distribution being characteristic of an $\ell = 2$ neutron removal. The earlier (^{19}C, ^{18}C) inclusive data analyses of Maddalena *et al.* [82] and Simpson and Tostevin [80] also assumed these 2^+_3 and 3^+_1 states near 4.9 MeV were neutron bound, citing the results of shell-model calculations using a modified version of the WBT interaction [83].

We have also calculated the inclusive parallel momentum distributions, to bound final states, as the sum of the distributions to these individual final states weighted by the σ^{th}_{-1n} shown in Table 7.2. As in earlier studies [80, 82], the lowest 1^- state (which the present shell-model calculations place at 4.942 MeV) was assumed to be unbound. Figure 7.2 shows the experimental (^{19}C, ^{18}C) inclusive parallel momentum distribution and also those calculated. In all cases the theoretical momentum distribution curves are normalised to the measured inclusive cross section. We show the results obtained by (a) assuming that the 2^+_3 and 3^+_1 states are unbound (dashed curve), having an inclusive cross section of 100.2 mb, and (b) assuming that the 2^+_3

[1]The ^{18}C 2^+_3 and 3^+_1 states at 4.915 and 4.975 MeV are assumed to be bound (see Section 7.2.1).

[2]There is no evidence from the present work that the $E_x = 0.190$ MeV, $5/2^+_1$ shell-model state in ^{19}C is bound. This state is included in Table 7.3 and is treated as unbound.

Reaction	E_x (MeV)	J^π	ℓ_j	σ_{sp} (mb)	C^2S	$\sigma^{th}_{-1n(e)}$ (mb)	σ^{exp}_{-2n} (mb)	R_s
(^{20}C(0^+),^{19}C(J^π))	0.190[1]	$5/2^+_1$	2	27.50	3.649	111.17		
$S_{1n}(^{20}\text{C}) = 2.90$ MeV	0.624	$3/2^+_1$	2	26.34	0.247	7.20		
	0.927	$1/2^-_1$	1	26.46	1.426	41.79		
	1.541	$5/2^+_2$	2	24.31	0.282	7.59		
	2.417	$3/2^-_1$	1	22.27	0.689	17.00		
	3.284	$3/2^+_2$	2	21.50	0.191	4.56		
	3.717	$1/2^+_2$	0	30.53	0.055	1.86		
		Inclusive				191.2	155(25)	$< 0.81(13)$
(^{22}C(0^+),^{21}C(J^π))	0.000	$1/2^+_1$	0	89.35	1.403	137.55		
$S_{1n}(^{22}\text{C}) = 0.70$ MeV	1.109	$5/2^+_1$	2	29.39	4.212	135.87		
	2.191	$3/2^+_1$	2	25.44	0.342	9.55		
		Inclusive				283.0	266(19)	$< 0.94(7)$

Table 7.3: Results for the *indirect* two-neutron removal reaction cross sections. Tabulated are the one-neutron removal cross sections to all predicted *unbound* $A-1$-body shell-model states with energies below the neutron threshold of the mass $A-2$ systems. That is, the neutron-unbound final states of the intermediate, mass $A-1$ systems ^{19,21}C, below 4.18 and 2.90 MeV, respectively. The final theoretical cross sections, $\sigma^{th}_{-1n(e)}$, include the center of mass correction factor $[A/(A-1)]^N$. The errors shown on the ratio of cross sections, $R_s = \sigma^{exp}_{-2n}/\sigma^{th}_{-1n(e)}$, reflect only the errors quoted on the measurements. The $\sigma^{th}_{-1n(e)}$ values do not include *direct* two-neutron breakup events, and the R_s values represent upper limits.

and 3^+_1 states are bound (solid curve), resulting in an inclusive cross section of 164.4 mb. The experimental cross section, in Table 7.2, is 163(12) mb. The comparison with the present momentum distribution data, in particular, provides us with rather compelling evidence for the hypothesis (b), that the 2^+_3 and 3^+_1 states *are* bound.

Results for ^{20}C

The predicted ^{19}C shell-model final states and the calculated and experimental one-neutron removal cross sections from the ^{20}C(0^+) ground state, with separation energy $S_{1n}(^{20}\text{C}) = 2.90$ MeV are collected in Tables 7.2 and 7.3. There is only very incomplete experimental information on the low-lying excited state spectrum of ^{19}C. Using Coulomb dissociation the ^{19}C ground state has been unambiguously identified as a $1/2^+$ s-wave halo state with weak binding [84]. The evaluated ^{19}C first neutron threshold is at 0.58(9) MeV [32]. An unbound excited $5/2^+$ state with $E_x = 1.46(10)$ MeV has also been clearly identified [85] using inverse-kinematics proton inelastic scattering from ^{19}C. Stanoiu *et al.* [83] reported a 201(15) keV gamma-ray transition in ^{19}C with in-beam γ-ray spectroscopy. Using inverse-kinematics proton inelastic scattering Elekes *et al.* [86] also reported evidence of two gamma-ray transitions, with energies 72(4) and 197(6) keV, from two bound ^{19}C excited states. While in both of these cases the transition energy (near 200 keV) is close to that of a predicted $5/2^+$ shell-model bound excited state, we will show that the present experimental data and analysis do not support such a strong transition to a $5/2^+$ bound ^{19}C excited state.

Table 7.2 shows the cross section for the $1/2^+_1$ shell-model ground state transition. The measured cross section, of 58(5) mb, and parallel momentum distribution to a bound ^{19}C final

[1]There is no evidence from the present work that $5/2^+_1$ shell-model state in ^{19}C is bound. It is assumed to be unbound.

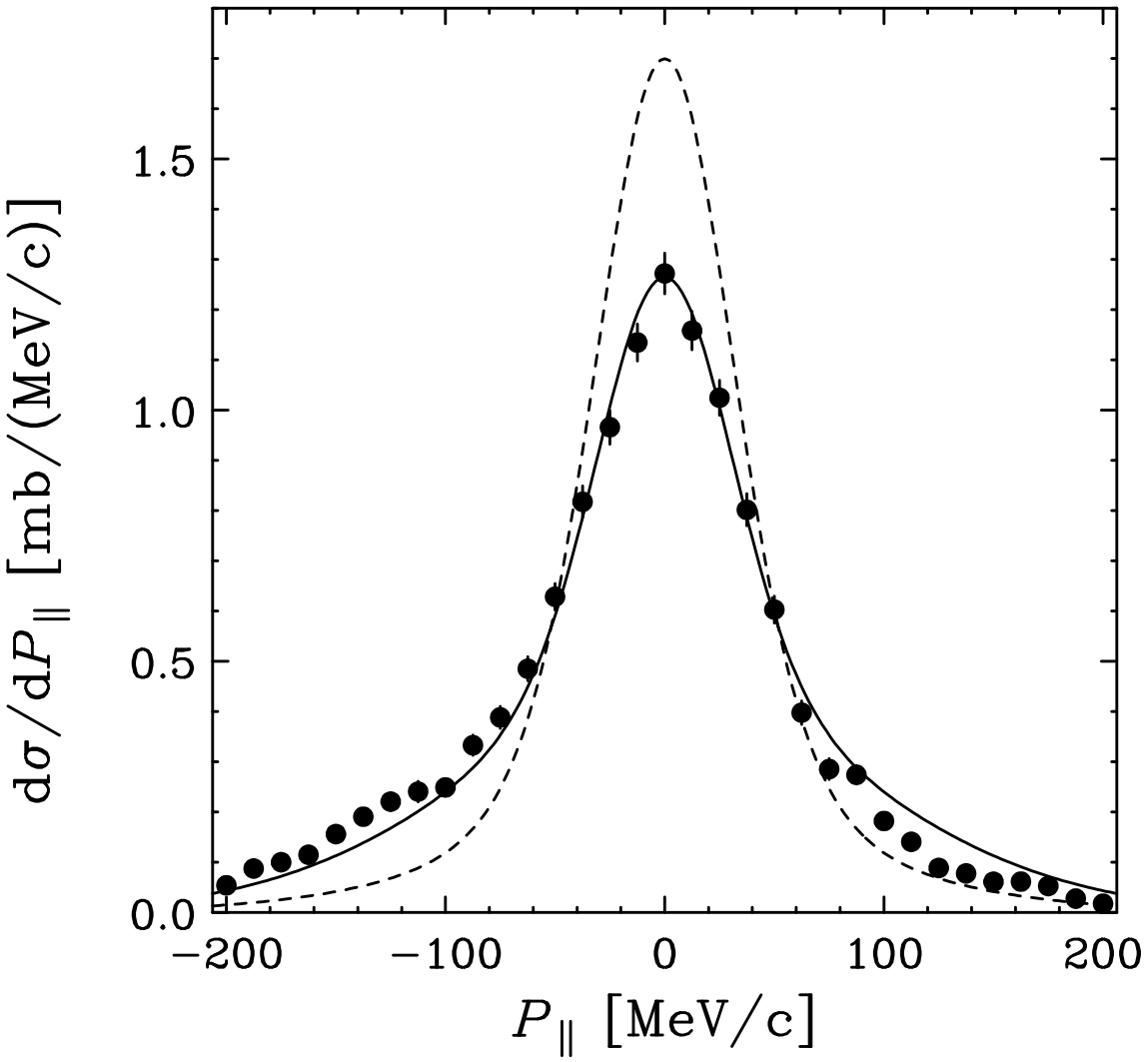

Figure 7.2: Measured inclusive parallel momentum distribution of ^{18}C, following one-neutron removal from ^{19}C on a carbon target at 243 MeV/nucleon compared to the theoretical calculations. The solid line includes contributions from the 2^+_3 and 3^+_1 shell-model states of ^{18}C, assumed bound; see also Table 7.2. The dashed line shows the results when assuming that the 2^+_3 and 3^+_1 states are unbound. Here, and in Fig. 7.3-7.6, the theoretical distributions have been convoluted with the experimental resolution and normalized to the measured inclusive cross section.

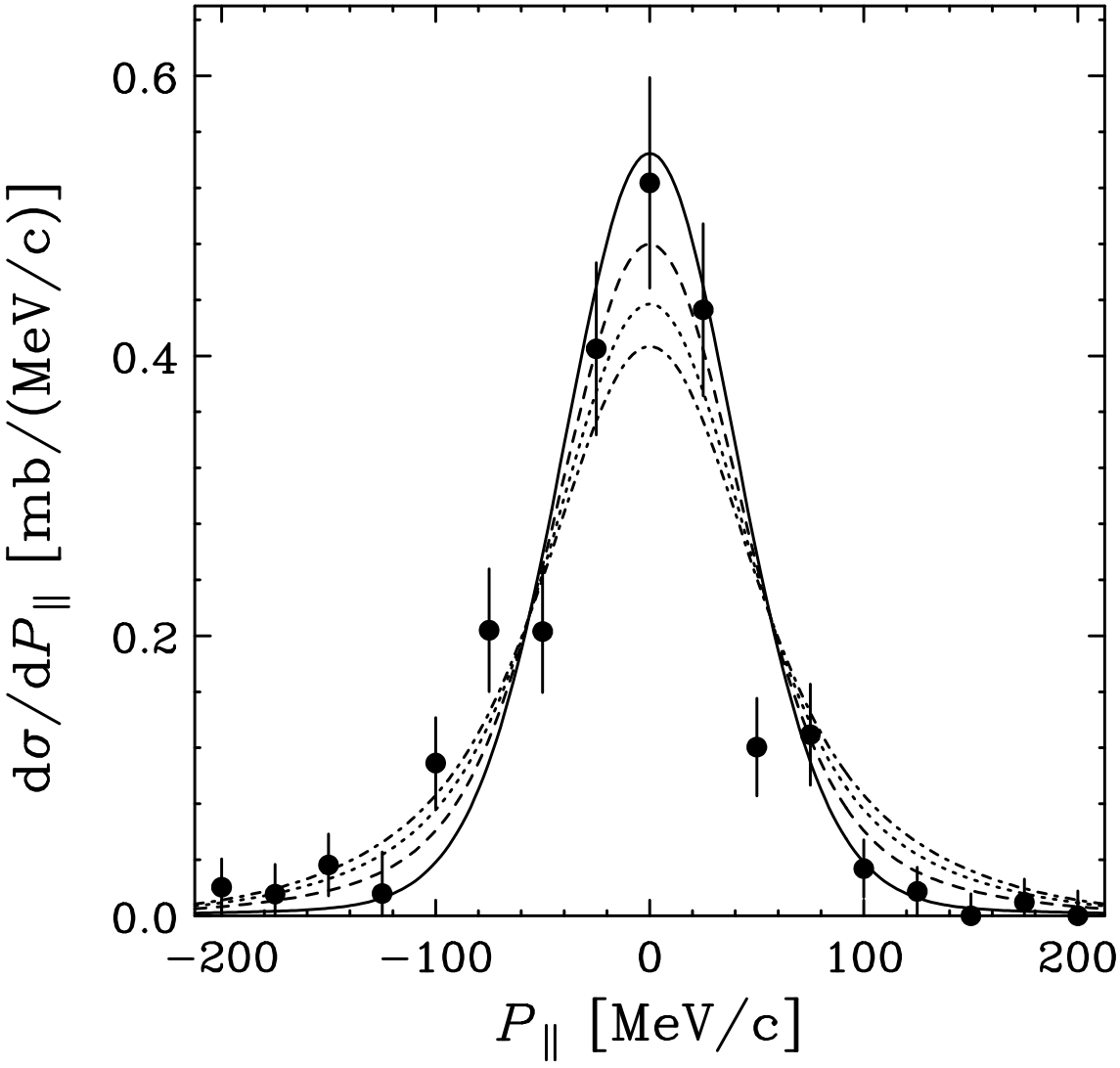

Figure 7.3: Measured inclusive parallel momentum distribution of ^{19}C, following one-neutron removal from ^{20}C on a carbon target at 241 MeV/nucleon compared to the theoretical calculations. The solid curve assumes that only the $1/2^+$ shell-model ground state transition ($2s_{1/2}$ neutron removal) is bound. The long-dashed, short-dashed, and dot-dashed curves result if one assumes that 0.5, 1.0 or 1.5 units of $1d_{5/2}$ spectroscopic strength also leads to bound final states.

state, Fig. 7.3, are consistent with the theoretical expectations for the removal of a $2s_{1/2}$ neutron (solid curve) with the tabulated shell-model spectroscopic factor of near to unity. It is likely that the $1/2^+$ ground state of ^{19}C is the only bound state of this system. The first $5/2^+_1$ state in ^{19}C, with $C^2S = 3.649$, is predicted to be strongly populated with cross section 111.17 mb, far larger than the experimentally observed 58(5) mb. If any bound excited state exists, the only possibility seems to be the first $3/2^+_1$ state predicted at 0.624 MeV, which would add the cross section of only 7.20 mb.

Although the bound $5/2^+$ state is unplausible due to the observed small cross section, we attempt to estimate an upper limit on possible bound d-state strength below. Table 7.3 shows the results for the cross sections leading to the excited ^{19}C shell-model final states. The shell model predicts seven such excited states with significant spectroscopic factors below the ^{18}C neutron threshold of 4.18 MeV. Given these cross sections we note, from Table 7.3, that one unit of the first excited state $1d_{5/2}$ spectroscopic strength makes a contribution of 30.5 mb including the center-of-mass correction factor $[A/(A-1)]^N$ to the theoretical cross section. The calculated $1/2^+_1$ ground state cross section is 58.92 mb. Thus, if there was also $1d_{5/2}$ strength to bound state(s), with a summed spectroscopic strength of 0.5, 1.0, or 1.5 units, the theoretical cross section to bound final states would increase to 74.2, 89.4, or 104.7 mb, respectively, well in excess of the measured value of 58(5) mb. The corresponding effects of such bound $1d_{5/2}$ strength on the shapes of the calculated ^{19}C parallel momentum distributions are shown in Fig. 7.3 by the long-dashed, short-dashed, and dot-dashed curves. Here, each curve is normalized to the experimental cross section of 58(5) mb. We conclude from this comparison that the majority of the strength that the shell-model attributes to the 190 keV $1d_{5/2}$ state is in fact unbound. Based on Fig. 7.3 and the measured cross section to bound ^{19}C, we estimate that 0.5 units or less of bound $1d_{5/2}$ strength might be accommodated by the present data set.

Our assumption, in Table 7.3, is that all of the excited ^{19}C shell-model states are unbound and that these unbound states will decay by neutron emission to ^{18}C. In this and the following case of ^{22}C these unbound mass $A-1$ excited state cross sections are large. For such unbound final state cases our one-neutron removal model calculates the exclusive parallel momentum distributions of the (weakly) unbound ^{19}C and ^{21}C residues in the original projectile rest frame. The subsequent in-flight neutron emission from these excited states will generate additional (recoil) broadening of the momentum distributions of the observed mass $A-2$ residues, i.e., ^{18}C and ^{20}C. The degree of broadening will be dependent on the continuum energy of the unbound, mass $A-1$ intermediate state, denoted ε^*.

We estimate the effect of this recoil. We assume that, in the rest frame of the unbound, mass $A-1$ state, with its given continuum energy ε^*, the mass $A-2$ residue (in its ground state) and the decay neutron separate isotropically. The momentum p of the heavy decay residue in this frame satisfies $p^2 = 2\mu\varepsilon^*$, where μ is the $A-2$ residue-neutron reduced mass. The assumption that this two-body decay is isotropic then requires that the calculated parallel momentum distributions of the unbound mass $A-1$ fragments must be convoluted with a rectangular distribution, of unit integral and total width $2p$, to derive the mass $A-2$ fragment parallel momentum distributions. This is done for the theoretical distributions shown in Figs. 7.4 and 7.5.

Table 7.3 shows that these indirect two-neutron removal cross sections arise predominantly from intermediate states of small ε^*. For the ^{20}C case, a cross section of 160 mb is predicted to arise from the first three shell-model excited states having $E_x < 1$ MeV in ^{19}C. However, as was discussed above, these shell-model energies are not sufficiently accurate. The WBP interaction predicts the first excited $5/2^+_1$ state to be bound with a large spectroscopic factor, whereas the calculated $\sigma^{\rm th}_{-1n}$ to this state and the measured cross section and momentum distribution to the ^{19}C ground state exclude this possibility. Experimentally a ^{19}C excited $5/2^+$ state has been clearly identified at $E_x = 1.46(10)$ MeV by Satou *et al.* [85] in proton inelastic scattering from

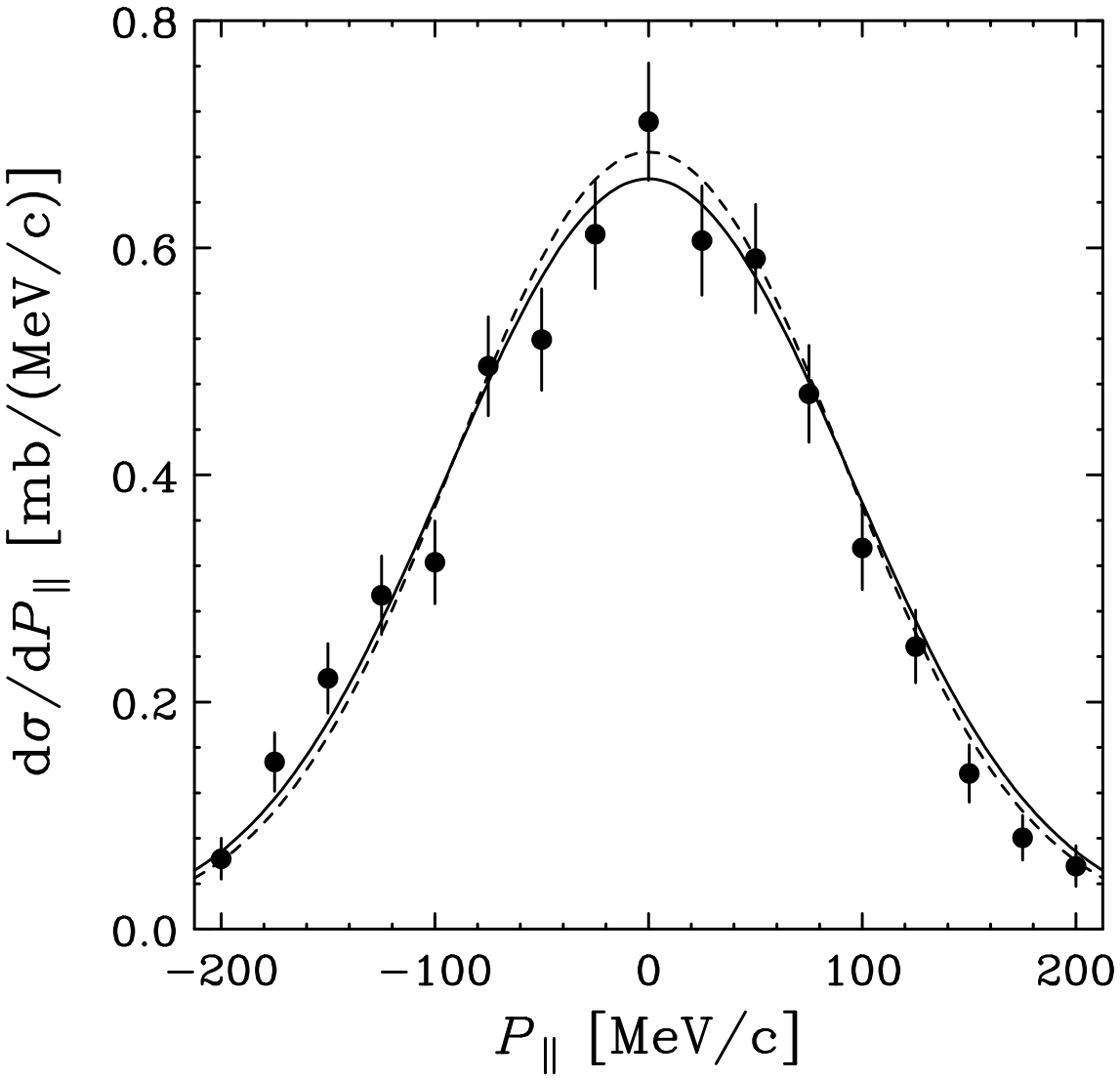

Figure 7.4: Measured inclusive parallel momentum distribution of ^{18}C, following two-neutron removal from ^{20}C on a carbon target at 241 MeV/nucleon compared to the theoretical calculations. The theoretical curves are the weighted sum of the exclusive calculations of the unbound ^{19}C states, see text. Recoil effects associated with the neutron emission are included assuming the most important contributions come from states with ε^* of 1.0 MeV (dashed curve) and 2.0 MeV (solid curve).

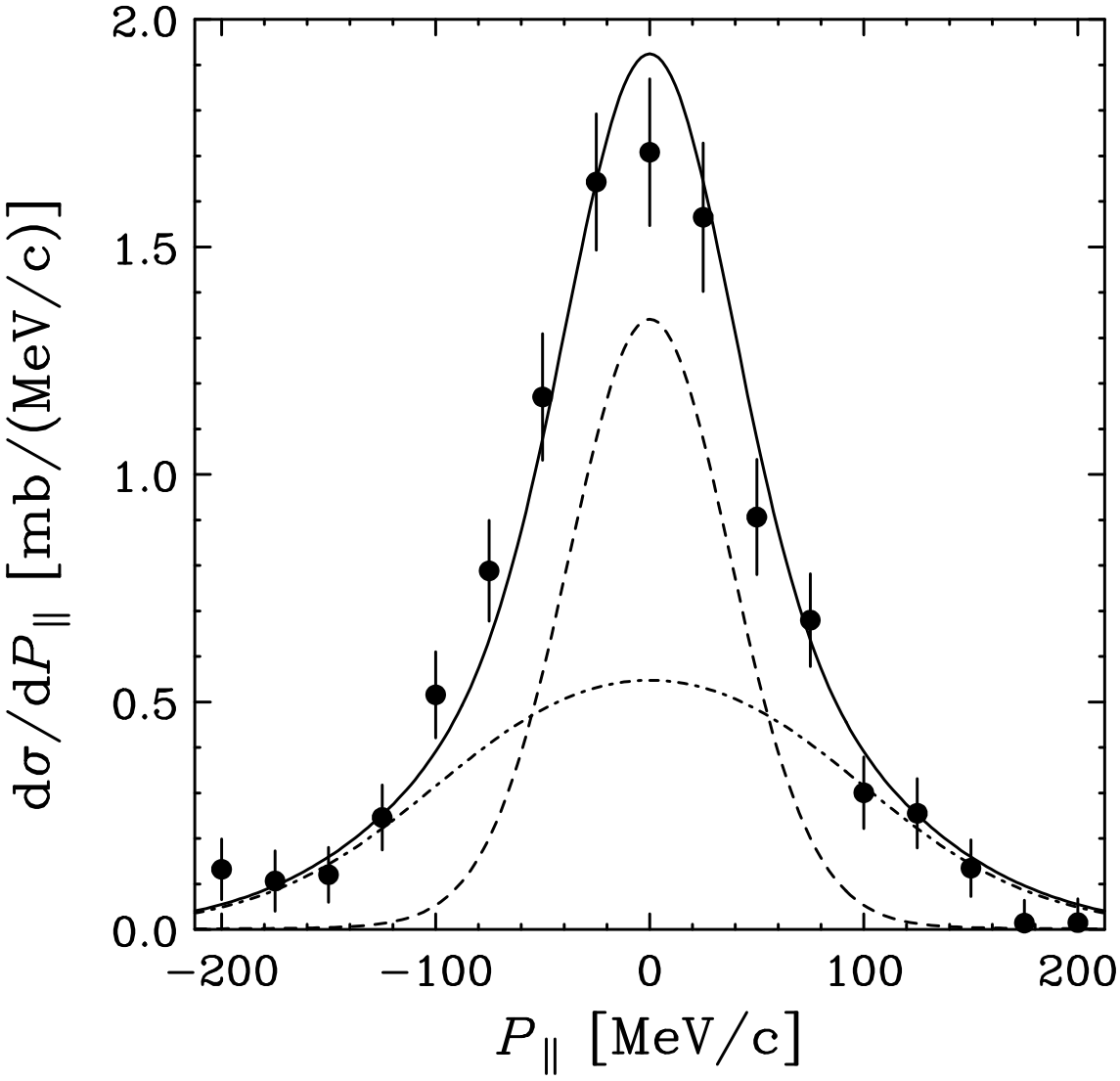

Figure 7.5: Measured inclusive parallel momentum distribution of ^{20}C, following two-neutron removal from ^{22}C on a carbon target at 240 MeV/nucleon compared to the theoretical calculations. The solid curve is the weighted sum of the exclusive calculations for the unbound ^{21}C states, see text. The dashed and dot-dashed curves show the contributions from knockout via the $1/2^+_1$ and $5/2^+_1$ unbound ^{21}C intermediate states, respectively. The recoil broadening arising from neutron emission from these unbound intermediate states is folded in.

^{19}C, i.e., with $\varepsilon^* = 0.88$ MeV. The present inclusive data do not permit a more detailed analysis of this excited state or of the predicted shell-model strength distributions. Our analysis shows, however, that the present data are consistent with an integrated $5/2^+$ strength of about 4 units leading to the ^{19}C continuum, as is given by the shell model.

In the absence of more complete information, and to assess this recoil sensitivity, we calculate the evaporation recoil effects assuming that the most important contributions arise from ^{19}C intermediate states with (i) $\varepsilon^* = 1.0$ MeV and (ii) $\varepsilon^* = 2.0$ MeV. The results are shown in Fig. 7.4 by the dashed line and solid line, respectively. Both outcomes are consistent with the experimental ^{18}C residue momentum distribution. We conclude from this agreement of the inclusive cross section and momentum distribution that the $5/2^+_1$ shell-model excited state is very likely to be unbound. Since, in this case, the shell model appears to systematically produce states with too small an excitation energy, the effective neutron separation energies will also be underestimated and, in turn, the theoretical removal cross sections slightly overestimated. We do not attempt to make any parameter adjustments to compensate for this (small) effect.

Results for ^{22}C

Here all final states of the ^{21}C one-neutron removal residues are particle unbound. The calculated exclusive (and inclusive) and experimental inclusive one-neutron removal yields are collected in the Table 7.3 for the predicted shell-model states of ^{21}C, that decay by neutron emission to ^{20}C.

Very little is known about these isotopes. Both the one- and two-neutron separation energies from ^{22}C are only poorly determined and so we are guided by the 2003 mass evaluation [32]. That is $S_{2n}(^{22}\mathrm{C}) = 0.42(94)$ MeV and $S_{1n}(^{21}\mathrm{C}) = -0.33(56)$ MeV, with large uncertainties. Thus, the ground state of ^{21}C was assumed to be produced at a continuum energy of $\varepsilon^* = 0.30$ MeV after neutron removal with ground state separation energy $S_{1n}(^{22}\mathrm{C}) = 0.70$ MeV. As was discussed for the ^{20}C projectile case, the inclusive (unbound) ^{21}C momentum distribution is calculated as the weighted sum of the momentum distributions to the individual final states with the $\sigma^{\mathrm{th}}_{-1n(e)}$ shown in Table 7.3. The neutron emission recoil broadening is included for each final state according to its ε^* value, i.e., $\varepsilon^* = E_{\mathrm{x}} + 0.30$ MeV, prior to this sum being performed. Three final states are predicted below the ^{20}C first neutron threshold of 2.90 MeV.

Table 7.3 shows that, based on the shell model, the first two final states each contribute almost half of the inclusive one-neutron removal cross section. These states are a $1/2^+_1$ ground state, with spectroscopic factor $C^2S = 1.4$, and a $5/2^+_1$ neutron-hole state at $E_{\mathrm{x}} = 1.11$ MeV, with $C^2S = 4.2$. The associated measured and theoretical inclusive ^{20}C parallel momentum distributions (convoluted with the experimental resolution of 27 MeV/c) are compared in Fig. 7.5. The individual contributions from the two dominant shell-model final states are also shown in the figure. The agreement with the data is very good, providing strong support for the weakly-bound, $\nu s^2_{1/2}$ character for the ^{22}C ground state. This result is consistent with the recent interaction cross section measurement and associated analysis of Ref. [9], that is suggestive of an extended ^{22}C matter density.

Currently, the ^{22}C two-neutron separation energy, $S_{2n}(^{22}\mathrm{C}) = 0.42(94)$ MeV, has a significant uncertainty. Hence, we consider the sensitivity of the theoretical inclusive ^{20}C production cross section and momentum distribution to the value assumed. Figure 7.6 shows the calculated momentum distributions when assuming a ^{22}C two-neutron separation energy of $S_{2n}(^{22}\mathrm{C}) = 0.40$ MeV (solid curve), 0.70 MeV (dashed curve), and 1.20 MeV (dot-dashed curve). In these calculations we continue to assume that the ground state of ^{21}C is at a continuum energy of 0.30 MeV, hence the ground state to ground state one-neutron separation energy of ^{22}C is $S_{1n}(^{22}\mathrm{C}) = 0.70$, 1.00, and 1.50 MeV in these cases. The curves have been convoluted with the experimental resolution of 27 MeV/c and also include the recoil broadening arising from the neutron decay of the unbound ^{21}C states (Table 7.3). The increasing separation energies reduce the corresponding inclusive cross sections: 283, 257, and 227 mb for the $S_{2n}(^{22}\mathrm{C}) =$

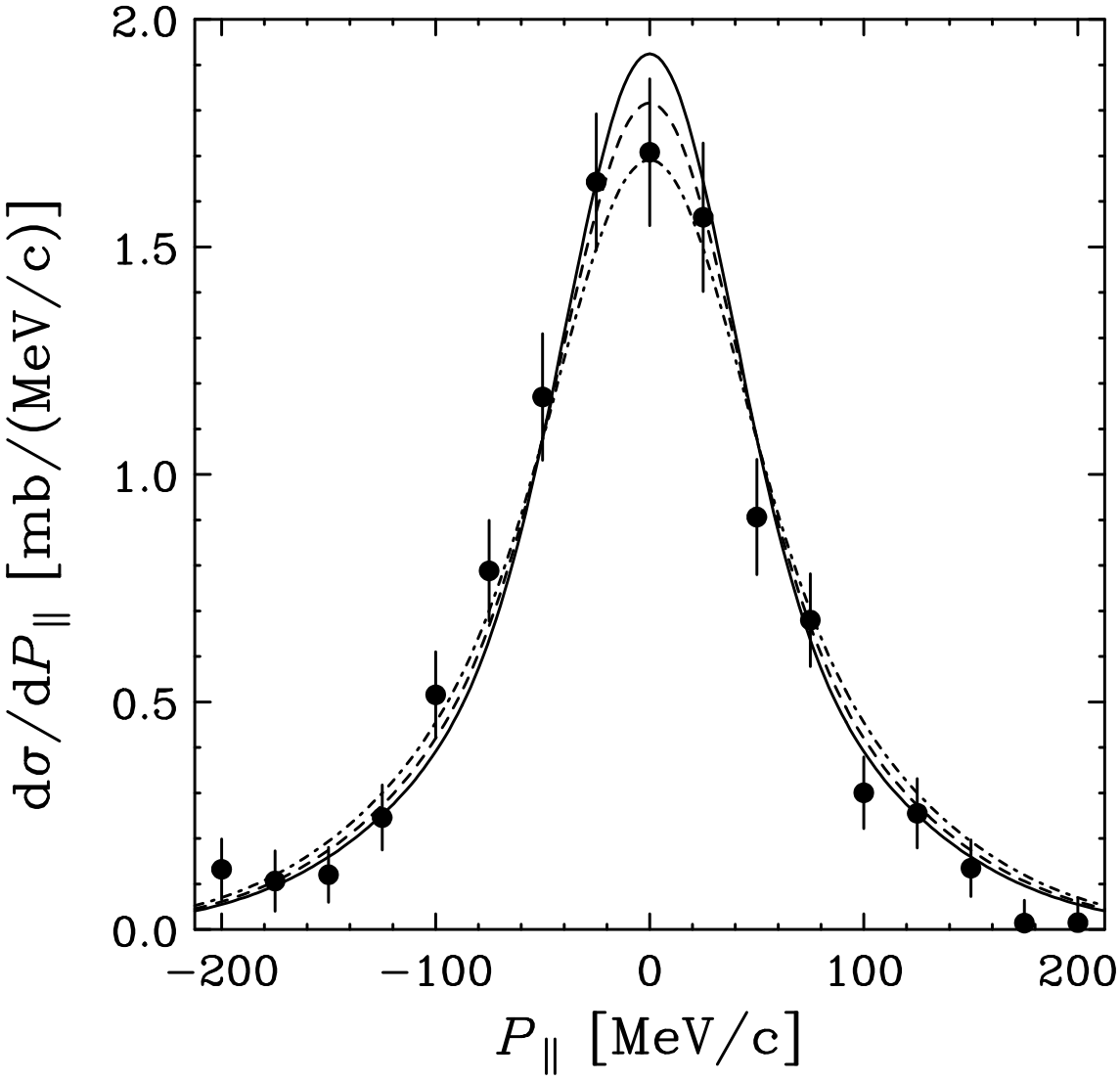

Figure 7.6: Measured inclusive parallel momentum distribution of ^{20}C, following two-neutron removal from ^{22}C on a carbon target at 240 MeV/nucleon compared to the theoretical calculations. The theoretical curves are the inclusive cross sections calculated assuming ^{22}C two-neutron separation energies $S_{2n}(^{22}\mathrm{C})$ = 0.40 MeV (solid curve), 0.70 MeV (dashed curve), and 1.20 MeV (dot-dashed curve). The curves include the recoil broadening arising from the neutron decay of the unbound ^{21}C intermediate states.

Reaction	E_x(MeV)	J^π	$\sigma^{\rm th}_{-2n(d)}$ (mb)
(^{20}C(0^+),^{18}C(J^π))	0.000	0^+_1	5.66
$S_{2n}(^{20}\mathrm{C}) = 3.51$ MeV	2.114	2^+_1	4.00
	3.639	2^+_2	0.53
	3.988	0^+_2	0.36
	4.915[1]	3^+_1	1.98
	4.975[1]	2^+_3	2.10
	Inclusive		14.6
(^{22}C(0^+),^{20}C(J^π))	0.000	0^+_1	5.32
$S_{2n}(^{22}\mathrm{C}) = 0.40$ MeV	2.102	2^+_1	6.81
	Inclusive		12.1

Table 7.4: Theoretical results for the *direct* two-neutron removal reaction cross sections, $\sigma^{\rm th}_{-2n(d)}$. Tabulated are the two-neutron removal cross sections to all predicted shell-model states below the neutron threshold in the mass $A-2$ systems, ^{18,20}C (4.18 and 2.90 MeV, respectively).

0.40, 0.70, and 1.20 MeV, respectively. We note that, owing to the relative insensitivity of our calculated cross sections and momentum distributions to the current experimental uncertainty in $S_{2n}(^{22}\mathrm{C})$, the data of the present work do not determine or place a significant constraint upon this value. We are able to conclude, however, that the sensitivity to the underlying structure of ^{22}C, specifically of the approximately equal contributions of the $1/2^+_1$ and $5/2^+_1$ transitions to the measured inclusive cross section, is robust.

7.2.2 Direct two-neutron Removal Reactions

We summarize only briefly the calculated exclusive and inclusive *direct* two-neutron removal cross sections, $\sigma^{\rm th}_{-2n(d)}$, from ^{20}C and ^{22}C to bound states of the mass $A-2$ isotopes. These results are collected in Table 7.4, computed based on the WBP shell-model two nucleon amplitudes, TNA. As noted earlier, as these calculated cross sections were both expected and found to be small, we will not enter into an extended discussion and details of the calculations. The descriptions of the nucleon overlap functions used and the construction of the residue- and neutron-target S-matrices are the same as for the one-neutron removal analysis. For the full details and the formalism of the exclusive cross sections (and their momentum distributions) the reader is referred to recent references [26, 87, 88].

For ^{20}C projectiles six states below the neutron threshold in ^{18}C have appreciable TNA. These states include the 2^+_3 and 3^+_1 states proposed as being bound from the one-neutron removal analysis (Section 7.2.1). The inclusive direct two-neutron removal cross section is calculated to be 14.6 mb. For ^{22}C projectiles, just two states below the neutron threshold in ^{20}C have appreciable TNA and the direct two-neutron removal cross section is now 12.1 mb. These numbers are to be compared with those for the indirect two-neutron removal paths that predict cross sections of 191.2 and 283.0 mb, respectively. In addition we note that, in the case of the removal of strongly-bound two-neutron pairs, these calculated direct two-nucleon removal cross sections typically overestimate the measured cross sections with $R_s(2N) = \sigma^{\rm exp}_{-2n}/\sigma^{\rm th}_{-2n(d)} \approx 0.5$ [26]. Thus, as was found in the earlier study of the lighter carbon isotopes [80], the direct pathways enter at about an 8% level. Since we are unable to distinguish these direct events with the current experimental setup, they cannot be elucidated or exploited further here.

[1]The ^{18}C 2^+_3 and 3^+_1 states at 4.915 and 4.975 MeV are assumed to be bound (see Section 7.2.1).

Chapter 8

Conclusions

8.1 Conclusions for ^{31}Ne

We have observed a large Coulomb breakup cross section of 529(60) mb for ^{31}Ne, which is indicative of a soft $E1$ excitation. A comparison with calculations based on direct breakup suggests that the ground state of ^{31}Ne involves a valence neutron predominantly in a low-ℓ orbital with very weak binding, which is consistent with the formation of a halo. Furthermore, a dominant $f_{7/2}$ valence-neutron configuration expected from conventional shell ordering is excluded. A comparison with shell-model calculations confirms that ^{31}Ne fragments in the island of inversion and that it is a very loosely bound $p_{3/2}$ valence neutron that drives the soft $E1$ excitation. As such, ^{31}Ne may be the first case of a p-wave $1n$ halo. The present result could hint that, owing to changes in shell structure, halos are more abundant than expected in "heavy" neutron-rich nuclei and are intimately connected with the location of the neutron drip line.

8.2 Conclusions for ^{29}Ne, ^{33,35,37}Mg, and ^{39,41}Si

We have observed a large Coulomb breakup cross section of 491(54) mb for ^{37}Mg, which is indicative of a soft $E1$ excitation. A comparison with calculations for inclusive Coulomb breakup and nuclear breakup suggests that the ground state of ^{37}Mg involves a valence neutron predominantly in a low-ℓ orbital with very weak binding, which is consistent with the formation of a halo.

From combined analysis, γ-ray analysis, and momentum distributions, the ground states of ^{29}Ne, ^{37}Mg, and ^{39,41}Si are deduced. These possible spin-parities of ground states are $1/2^-$ or $3/2^-$ for ^{29}Ne, $1/2^-$ or $3/2^-$ for ^{37}Mg, $1/2^-$ for ^{39}Si, and $3/2^-$ for ^{41}Si. All ground states are considered to have low spin parity. For ^{37}Mg and ^{39,41}Si, a dominant $f_{7/2}$ valence-neutron configuration expected from conventional shell ordering is excluded. For ^{29}Ne , a dominant $d_{3/2}$ configuration expected from conventional shell ordering is excluded. From the results, ^{29}Ne, ^{37}Mg, and ^{39,41}Si are located in or around the island of inversion. This suggests that the melting of $N = 20$ and 28 shell gaps is occur, which cause the deformation of these nuclei.

For ^{33,35}Mg, the possibility that the direct decay from excited states higher than 2^+_1 state to the ground state happens is suggested. Hence, further analysis is needed.

8.3 Conclusions for Carbon Isotopes

The measured cross sections and momentum distributions were interpreted in the light of eikonal reaction model calculations for single-neutron knockout combined with structural input derived from *psd* shell-model calculations employing the WBP interaction. The two-neutron removal

cross sections were calculated by considering (a) the removal of one neutron to unbound states in the $A-1$ daughter, with the assumption that these unbound intermediate states decay by neutron emission to bound states in the mass $A-2$ residue and (b) direct two-neutron removal.

In the case of C(^{22}C, ^{20}C), the cross section and momentum distribution are consistent with the existence of a two-neutron halo with a dominant $\nu s_{1/2}^2$ configuration in ^{22}C. The narrow momentum distribution and relatively low cross section for C(^{20}C, ^{19}C), which arise as the single-neutron removal to the ^{19}C($1/2^+$) ground state, probe specifically the significant $\nu s_{1/2}^2$ component of the ^{20}C ground state. The $\nu d_{5/2}$ component results in the population of unbound states in ^{19}C that neutron decay to ^{18}C. The narrow momentum distribution and enhanced cross section for C(^{19}C, ^{18}C) are consistent with the well developed $\nu s_{1/2}$ halo of ^{19}C.

Overall, the calculated cross sections agreed well with those measured. In particular, in the cases of C(^{19}C, ^{18}C), C(^{20}C, ^{19}C), and C(^{22}C, ^{20}C), $R_s = \sigma_{-1n}^{\rm exp}/\sigma_{-1n}^{\rm th}$ was close to unity and consistent with systematics [21]. Combined with the good agreement for the momentum distributions, it may be seen that the shell model has predictive power in this region and provides a good overall description of level positions and their spectroscopic strengths.

8.4 summary

The Coulomb and nuclear breakup cross sections and fragment momentum distributions reactions for neutron-rich nuclei around $N = 16-28$ were systematically measured. From the measurement, the B($E1$) strength, separation energy and spectroscopic factors were extracted. And then the shell closure for $N = 16, 20, 28$ and deformation of nuclei were discussed based on the shell model and Nilsson diagram.

These results indicate the following story. The conventional shell gap of $N = 20, 28$ is quenched in the neutron-rich Ne, Mg, Si isotopes. The quenching causes the deformation, and the deformation causes the mixing of the many single particle orbitals. As a result, the p-wave components in the ground states of ^{29,31}Ne, ^{37}Mg, and ^{41}Si are considered to become large.

On the other hand, according to Hamamoto [61], the p-component in a deformed nucleus becomes dominant as the separation energy of the nucleus approaches zero. Our results of significance of p-wave components for above nuclei support the loosely-bound effect of deformed nuclei.

We have established a new spectroscopic tools to investigate the neutron-rich nuclei around and heavier than the island of inversion by utilizing the Coulomb and nuclear breakup. This can give the spin parity of the ground state, spectroscopic factors, and separation energy of the nuclei of low-intensity beam (≈ 10 cps).

Appendix A

Neutron removal cross section

A.1 The equation of the x-neutron removal cross section

The x-neutron removal cross section (σ_{-xn}, x = 1, 2, ...) is obtained from the number of the projectiles counted before the secondary target and that of the residues registered after the target. If the target is thick, we have to consider a reaction loss of projectiles and fragments in the target. As a result, the cross section is described as

$$\sigma_{-xn} = \left(\frac{N_i'}{N_i} - \frac{N_o'}{N_o}\right)\left(\frac{\sigma_R - \sigma_R'}{e^{-\sigma_R' N_t} - e^{-\sigma_R N_t}}\right), \tag{A.1}$$

where each value represents the following.

N_i' (N_o'):	the number of the fragments for target-in (target-out) runs
N_i (N_o):	the number of the projectiles for target-in (target-out) runs
N_t:	the number of target nuclei per unit area
σ_R (σ_R'):	the reaction cross section of the projectile (residue)

A.2 The derivation of the equation

The number of projectiles at a "reduced" thickness T is $Ne^{-\sigma_R T}$ (Fig. A.1), where T represents the number of nuclei in a thickness t (g/cm^2) per unit area:

$$T = \frac{N_A t}{A}, \tag{A.2}$$

where N_A (mol^{-1}) represents the Avogadro's number, and A (g/mol) the mass number. The number of fragments produced on a small thickness $[T, T + \Delta T]$ is $Ne^{-\sigma_R T}\sigma_{-xn}\Delta T$, decreasing by the factor of $e^{-\sigma_R'(N_t - T)}$ at the end of the target ($T = N_t$). Therefore the number of fragments, $\Delta N'(T)$, which is produced on ΔT and survive at the end of the target is $Ne^{-\sigma_R T}e^{-\sigma_R'(N_t - T)}\sigma_{-xn}\Delta T$:

$$\Delta N'(T) = Ne^{-\sigma_R T}e^{-\sigma_R'(N_t - T)}\sigma_{-xn}\Delta T. \tag{A.3}$$

By taking the limit $\Delta T \to 0$, we get

$$dN'(T) = Ne^{-\sigma_R T}e^{-\sigma_R'(N_t - T)}\sigma_{-xn}dT \tag{A.4}$$

$$= N\sigma_{-xn}e^{-\sigma_R N_t}e^{-(\sigma_R - \sigma_R')T}dT. \tag{A.5}$$

By integrating the both sides, we get the number of total fragments, $N'(N_t)$, at the end of the target:

$$\int_{T=0}^{T=N_t} dN'(T) = \int_0^{N_t} N\sigma_{-xn} e^{-\sigma_R N_t} e^{-(\sigma_R - \sigma'_R)T} dT \tag{A.6}$$

$$\Leftrightarrow \quad N'(N_t) = N\sigma_{-xn} e^{-\sigma_R N_t} \int_0^{N_t} e^{-(\sigma_R - \sigma'_R)T} dT \tag{A.7}$$

$$= N\sigma_{-xn} e^{-\sigma'_R N_t} \left[\frac{e^{-(\sigma_R - \sigma'_R)T}}{-(\sigma_R - \sigma'_R)} \right]_0^{N_t} \tag{A.8}$$

$$= N\sigma_{-xn} e^{-\sigma'_R N_t} \left(\frac{e^{-(\sigma_R - \sigma'_R)N_t} - 1}{-(\sigma_R - \sigma'_R)} \right) \tag{A.9}$$

$$= N\sigma_{-xn} \left(\frac{e^{-\sigma'_R N_t} - e^{-\sigma_R N_t}}{\sigma_R - \sigma'_R} \right). \tag{A.10}$$

Therefore σ_{-xn} is described as

$$\sigma_{-xn} = \frac{N'(N_t)}{N} \left(\frac{\sigma_R - \sigma'_R}{e^{-\sigma'_R N_t} - e^{-\sigma_R N_t}} \right). \tag{A.11}$$

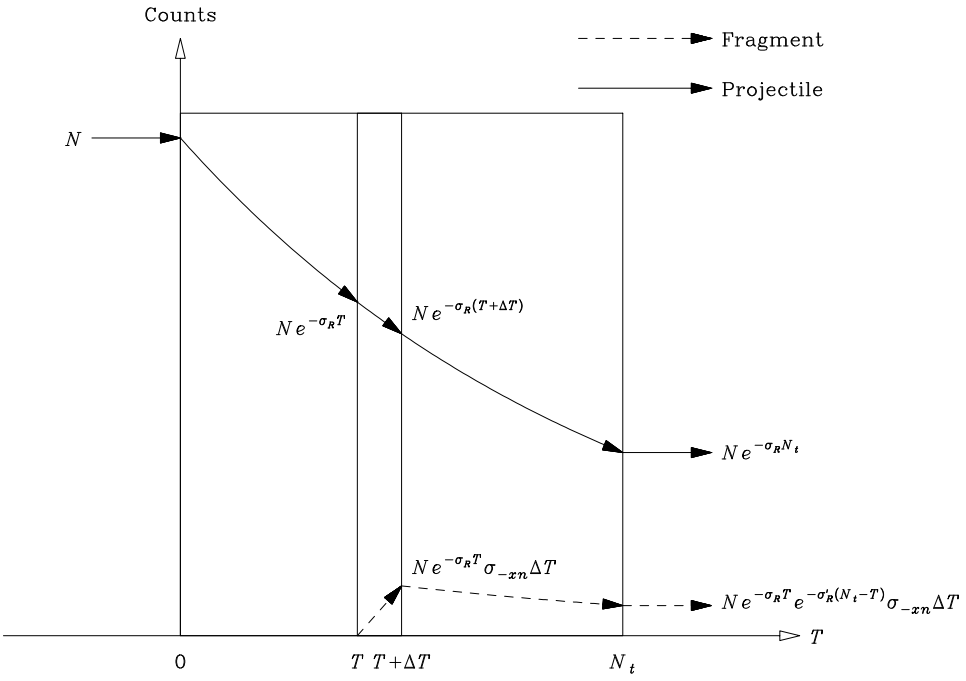

Figure A.1: The number of projectiles and fragments at each position.

A.3 Comparisons of Monte Carlo simulation with some equations

Fig. A.2 shows comparisons of Monte Carlo simulation with some equations. The closed circles are the result of the simulation assuming $\sigma_{-xn} = 0.1$ barn, $\sigma_R = 1.0$ barn, and σ'_R 0.9 barn,

respectively. The solid line is plotted by

$$\frac{N'}{N} = \sigma_{-xn}\left(\frac{e^{-\sigma'_R T} - e^{-\sigma_R T}}{\sigma_R - \sigma'_R}\right). \tag{A.12}$$

, and the dashed line plotted by

$$\frac{N'}{N} = \sigma_{-xn} T, \tag{A.13}$$

where it is assumed that the target is thin enough to ignore the reaction loss of projectiles and fragments in the target. The solid line based on the equation (A.12) agrees with the simulation, so the equation (A.12) is considered to be valid.

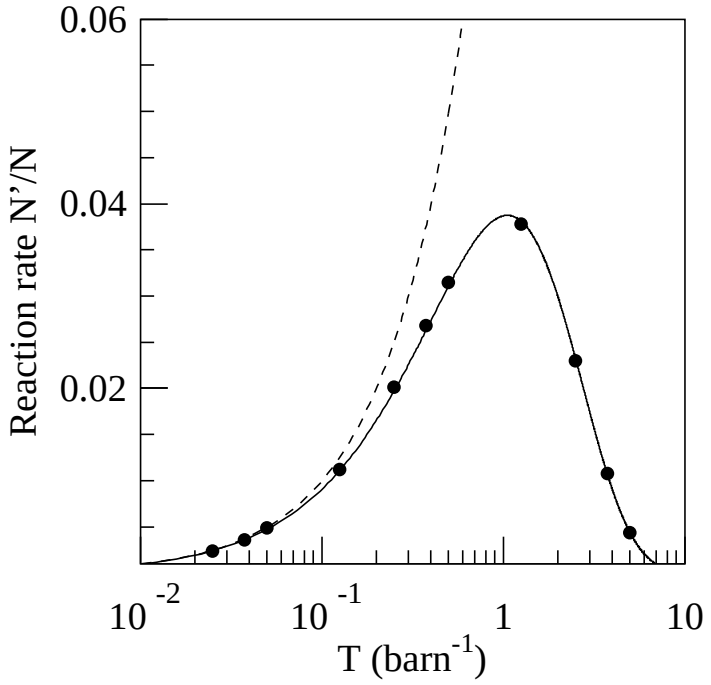

Figure A.2: Comparisons of some equations with Monte Carlo simulation.

Appendix B

Confidence level

In the C^2S vs S_{1n} plane, e.g., Fig. 6.2 (a-3), χ^2 is defined as

$$\chi^2 = \left(\frac{C^2S^{\rm exp}({\rm C}, S_{1n}) - C^2S}{\sigma(C^2S^{\rm exp}({\rm C}, S_{1n}))}\right)^2 + \left(\frac{C^2S^{\rm exp}(E1, S_{1n}) - C^2S}{\sigma(C^2S^{\rm exp}(E1, S_{1n}))}\right)^2 + \left(\frac{S_{1n}^{\rm exp} - S_{1n}}{\sigma(S_{1n}^{\rm exp})}\right)^2, \quad \text{(B.1)}$$

where $C^2S^{\rm exp}({\rm C}, S_{1n})$ and $C^2S^{\rm exp}(E1, S_{1n})$ represent the experimental spectroscopic factors obtained from nuclear and Coulomb breakup, respectively, as a function of S_{1n}. $S_{1n}^{\rm exp}$ represents the separation energy obtained from a mass measurement, which is shown in Sec. 2.3. $\sigma(*)$ represent the error of *. Since χ^2 includes two parameters C^2S and S_{1n}, χ^2 is distributed as a chi-square distribution with 2 degree of freedom. The minimum value of χ^2 in the C^2S vs S_{1n} plane is expressed in $\chi^2_{\rm min}$. At $\chi^2 = \chi^2_{\rm min}$, the values of C^2S and S_{1n} are most probable experimentally. The 68 % confidence level corresponds the position at

$$\chi^2 = \chi^2_{\rm min} + 2.3. \quad \text{(B.2)}$$

If it is suppose that C^2S is held fixed and that S_{1n} is varied so as to minimize χ^2, where the minimum value is expressed in $\chi^2(C^2S)$, $\Delta\chi^2(C^2S) \equiv \chi^2(C^2S) - \chi^2_{\rm min}$ is distributed as a chi-square distribution with 1 degree of freedom. Therefore, the 68 % confidence region of a single parameter C^2S corresponds $\Delta\chi^2(C^2S) < 1$. For example, 68 % confidence region of C^2S for the channel assuming $^{29}{\rm Ne} \rightarrow {}^{28}{\rm Ne}(0^+) + s_{1/2}$ is shown in Fig. B.1. The edges of this region are adopted as the errors of C^2S. Similarly, $\Delta\chi^2(S_{1n}) \equiv \chi^2(S_{1n}) - \chi^2_{\rm min}$ give the 68 % confidence region of S_{1n}.

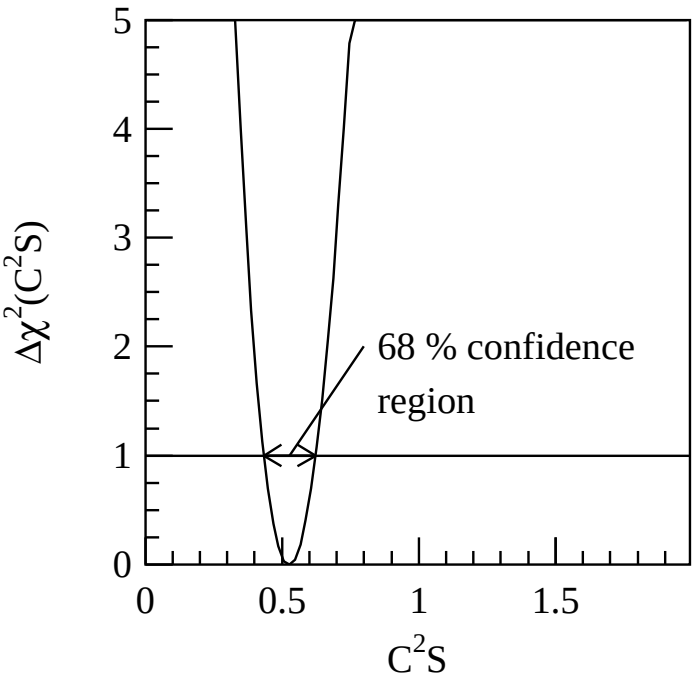

Figure B.1: The arraw represents the 68 % confidence region of C^2S for $^{29}\mathrm{Ne} \rightarrow {}^{28}\mathrm{Ne}(0^+) + s_{1/2}$. The line of $\Delta\chi^2(C^2S) = 1$ is shown. See the text for details of $\Delta\chi^2(C^2S)$.

Acknowledgements

The present experiment was performed by the following collaborators:

- *Tokyo Institute of Technology*
  T. Nakamura, Y. Kondo, S. Deguchi, G. S. Lee, Y. Kawada, K. Takahashi, T. Sako, K. N. Tanaka, N. Tanaka, R. Tanaka, Y. Togano
- *University of Surrey*
  J. A. Tostevin, E. C. Simpson
- *RIKEN Nishina Center for Accelerator-Based Science*
  N. Aoi, H. Baba, N. Fukuda, N. Inabe, M. Ishihara, D. Kameda, T. Kubo, K. Kusaka, T. Motobayashi, T. Ohnishi, H. Otsu, M. Ohtake, H. Sakurai, H. Takeda, S. Takeuchi, E. Takeshita, K. Yoneda, A. Yoshida, K. Yoshida
- *International Atomic Energy Agency (IAEA)*
  A. Mengoni
- *LPC-ENSICAEN, IN2P3-CNRS et Université de Caen*
  N. A. Orr, J. Gibelin
- *Seoul National University*
  Y. Satou, H. S. Lee, S. Kim
- *Saint Mary's University*
  R. Kanungo
- *Western Michigan University*
  M. A. Famiano, R. Barthelemy
- *Center for Nuclear Study (CNS), University of Tokyo*
  T. Otsuka, A. Saito, S. Shimoura, M. Matsushita
- *Japan Atomic Energy Agency*
  Y. Utsuno
- *Tokyo University of Science*
  T. Sumikama
- *ExtreMe Matter Institute (EMMI) and Research Division, GSI*
  M. Takechi

I would like to acknowledge all of the collaborators for their works during the experiments and discussions of the data analysis. I am grateful to RIKEN RI Beam Factory (RIBF) crews for excellent operations to produce a nice beam during experiments. I would like to give special thanks to my thesis adviser, Prof. T. Nakamura, for his valuable suggestions, encouragement,

and teaching me many things on nuclear physics throughout entire period as a undergraduate and graduate student at Tokyo Tech. I deeply thank Prof. Y. Satou and Dr. Y. Kondo for his great contribution to the experiments and analysis. I'm appreciative of the fruitful discussion with Prof. K. Asahi, Prof. I. Hamamoto, Prof. J. A. Tostevin, Prof. Y. Utsuno, Prof. N. A. Orr, and Prof. T. Motobayashi.

The present study was supported by Grant-in-Aid for JSPS Fellows (No. 22·9675) from the Ministry of Education, Culture, Sports, Science and Technology (MEXT) Japan. The support of th Global Center of Excellence Program "Nanoscience and Quantum Physics" at Tokyo Tech is also acknowledged.

Finally, I would like to thank my mother, Mrs. S. Kobayashi, and friends for their contributions, encouragements and supports.

Bibliography

[1] M. G. Mayer. *On Closed Shells in Nuclei. II.* Phys. Rev. **75**, 1969–1970 (1949).

[2] O. Haxel, J. H. D. Jensen, and H. E. Suess. *On the "Magic Numbers" in Nuclear Structure.* Phys. Rev. **75**, 1766–1766 (1949).

[3] I. Tanihata, H. Hamagaki, O. Hashimoto, Y. Shida, N. Yoshikawa, K. Sugimoto, O. Yamakawa, T. Kobayashi, and N. Takahashi. *Measurements of Interaction Cross Sections and Nuclear Radii in the Light p-Shell Region.* Phys. Rev. Lett. **55**, 2676–2679 (1985).

[4] T. Kobayashi, O. Yamakawa, K. Omata, K. Sugimoto, T. Shimoda, N. Takahashi, and I. Tanihata. *Projectile Fragmentation of the Extremely Neutron-Rich Nucleus ^{11}Li at 0.79 GeV/nucleon.* Phys. Rev. Lett. **60**, 2599–2602 (1988).

[5] N. A. Orr, N. Anantaraman, S. M. Austin, C. A. Bertulani, K. Hanold, J. H. Kelley, D. J. Morrissey, B. M. Sherrill, G. A. Souliotis, M. Thoennessen, J. S. Winfield, and J. A. Winger. *Momentum distributions of ^{9}Li fragments following the breakup of ^{11}Li.* Phys. Rev. Lett. **69**, 2050–2053 (1992).

[6] T. Nakamura and Y. Kondo. *Neutron Halo and Breakup Reactions.* Lecture Notes in Physics 848, Clusters in Nuclei, Vol.2, 67 – 119 (2012).

[7] T. Nakamura, N. Fukuda, T. Kobayashi, N. Aoi, H. Iwasaki, T. Kubo, A. Mengoni, M. Notani, H. Otsu, H. Sakurai, S. Shimoura, T. Teranishi, Y. X. Watanabe, K. Yoneda, and M. Ishihara. *Coulomb Dissociation of ^{19}C and its Halo Structure.* Phys. Rev. Lett. **83**, 1112–1115 (1999).

[8] T. Nakamura, N. Kobayashi, Y. Kondo, Y. Satou, N. Aoi, H. Baba, S. Deguchi, N. Fukuda, J. Gibelin, N. Inabe, M. Ishihara, D. Kameda, Y. Kawada, T. Kubo, K. Kusaka, A. Mengoni, T. Motobayashi, T. Ohnishi, M. Ohtake, N. A. Orr, H. Otsu, T. Otsuka, A. Saito, H. Sakurai, S. Shimoura, T. Sumikama, H. Takeda, E. Takeshita, M. Takechi, S. Takeuchi, K. Tanaka, K. N. Tanaka, N. Tanaka, Y. Togano, Y. Utsuno, K. Yoneda, A. Yoshida, and K. Yoshida. *Halo Structure of the Island of Inversion Nucleus ^{31}Ne.* Phys. Rev. Lett. **103**, 262501 (2009).

[9] K. Tanaka, T. Yamaguchi, T. Suzuki, T. Ohtsubo, M. Fukuda, D. Nishimura, M. Takechi, K. Ogata, A. Ozawa, T. Izumikawa, T. Aiba, N. Aoi, H. Baba, Y. Hashizume, K. Inafuku, N. Iwasa, K. Kobayashi, M. Komuro, Y. Kondo, T. Kubo, M. Kurokawa, T. Matsuyama, S. Michimasa, T. Motobayashi, T. Nakabayashi, S. Nakajima, T. Nakamura, H. Sakurai, R. Shinoda, M. Shinohara, H. Suzuki, E. Takeshita, S. Takeuchi, Y. Togano, K. Yamada, T. Yasuno, and M. Yoshitake. *Observation of a Large Reaction Cross Section in the Drip-Line Nucleus ^{22}C.* Phys. Rev. Lett. **104**, 062701 (2010).

[10] E. K. Warburton, J. A. Becker, and B. A. Brown. *Mass systematics for A = 29 - 44 nuclei: The deformed A $\sim$ 32 region.* Phys. Rev. C **41**, 1147–1166 (1990).

[11] B. H. Wildenthal and W. Chung. *Collapse of the conventional shell-model ordering in the very-neutron-rich isotopes of Na and Mg.* Phys. Rev. C **22**, 2260–2262 (1980).

[12] T. Motobayashi, Y. Ikeda, K. Ieki, M. Inoue, N. Iwasa, T. Kikuchi, M. Kurokawa, S. Moriya, S. Ogawa, H. Murakami, S. Shimoura, Y. Yanagisawa, T. Nakamura, Y. Watanabe, M. Ishihara, T. Teranishi, H. Okuno, and R. Casten. *Large deformation of the very neutron-rich nucleus ^{32}Mg from intermediate-energy Coulomb excitation.* Physics Letters B **346**, 9 – 14 (1995).

[13] T. Nakamura, S. Shimoura, T. Kobayashi, T. Teranishi, K. Abe, N. Aoi, Y. Doki, M. Fujimaki, N. Inabe, N. Iwasa, K. Katori, T. Kubo, H. Okuno, T. Suzuki, I. Tanihata, Y. Watanabe, A. Yoshida, and M. Ishihara. *Coulomb dissociation of a halo nucleus ^{11}Be at 72A MeV.* Physics Letters B **331**, 296 – 301 (1994).

[14] N. Fukuda, T. Nakamura, N. Aoi, N. Imai, M. Ishihara, T. Kobayashi, H. Iwasaki, T. Kubo, A. Mengoni, M. Notani, H. Otsu, H. Sakurai, S. Shimoura, T. Teranishi, Y. X. Watanabe, and K. Yoneda. *Coulomb and nuclear breakup of a halo nucleus ^{11}Be.* Phys. Rev. C **70**, 054606 (2004).

[15] R. Palit, P. Adrich, T. Aumann, K. Boretzky, B. V. Carlson, D. Cortina, U. Datta Pramanik, T. W. Elze, H. Emling, H. Geissel, M. Hellström, K. L. Jones, J. V. Kratz, R. Kulessa, Y. Leifels, A. Leistenschneider, G. Münzenberg, C. Nociforo, P. Reiter, H. Simon, K. Sümmerer, and W. Walus. *Exclusive measurement of breakup reactions with the one-neutron halo nucleus ^{11}Be.* Phys. Rev. C **68**, 034318 (2003).

[16] P. G. Hansen. *Momentum Content of Single-Nucleon Halos.* Phys. Rev. Lett. **77**, 1016–1019 (1996).

[17] Y. Ogawa, Y. Suzuki, and K. Yabana. *Momentum distributions of a ^{9}Li fragment arising from the (^{11}Li, ^{9}Li) reaction and neutron correlations.* Nuclear Physics A **571**, 784 – 802 (1994).

[18] F. Barranco and E. Vigezzi. *Break-up of Halo States Induced by Nuclear Interactions.* World Scientific, Singapore 217 (1998).

[19] P. Hansen and J. Tostevin. *DIRECT REACTIONS WITH EXOTIC NUCLEI.* Annual Review of Nuclear and Particle Science **53**, 219–261 (2003).

[20] C. A. Bertulani and P. G. Hansen. *Momentum distributions in stripping reactions of radioactive projectiles at intermediate energies.* Phys. Rev. C **70**, 034609 (2004).

[21] A. Gade, P. Adrich, D. Bazin, M. D. Bowen, B. A. Brown, C. M. Campbell, J. M. Cook, T. Glasmacher, P. G. Hansen, K. Hosier, S. McDaniel, D. McGlinchery, A. Obertelli, K. Siwek, L. A. Riley, J. A. Tostevin, and D. Weisshaar. *Reduction of spectroscopic strength: Weakly-bound and strongly-bound single-particle states studied using one-nucleon knockout reactions.* Phys. Rev. C **77**, 044306 (2008).

[22] H. Esbensen and G. F. Bertsch. *Eikonal approximation in heavy-ion fragmentation reactions.* Phys. Rev. C **64**, 014608 (2001).

[23] G. F. Bertsch and H. Esbensen. *Dynamic Effects in Fragmentation Reactions.* Progress of Theoretical Physics Supplement **146**, 319–328 (2002).

[24] J. Tostevin. *Single-nucleon knockout reactions at fragmentation beam energies.* Nuclear Physics A **682**, 320 – 331 (2001).

[25] J. A. Tostevin, G. Podolyák, B. A. Brown, and P. G. Hansen. *Correlated two-nucleon stripping reactions.* Phys. Rev. C **70**, 064602 (2004).

[26] J. A. Tostevin and B. A. Brown. *Diffraction dissociation contributions to two-nucleon knockout reactions and the suppression of shell-model strength.* Phys. Rev. C **74**, 064604 (2006).

[27] J. S. Al-Khalili, J. A. Tostevin, and I. J. Thompson. *Radii of halo nuclei from cross section measurements.* Phys. Rev. C **54**, 1843–1852 (1996).

[28] B. Alex Brown. *New Skyrme interaction for normal and exotic nuclei.* Phys. Rev. C **58**, 220–231 (1998).

[29] L. Ray. *Proton-nucleus total cross sections in the intermediate energy range.* Phys. Rev. C **20**, 1857–1872 (1979).

[30] D. Bazin, R. J. Charity, R. T. d. Souza, M. A. Famiano, A. Gade, V. Henzl, D. Henzlova, S. Hudan, J. Lee, S. Lukyanov, W. G. Lynch, S. McDaniel, M. Mocko, A. Obertelli, A. M. Rogers, L. G. Sobotka, J. R. Terry, J. A. Tostevin, M. B. Tsang, and M. S. Wallace. *Mechanisms in Knockout Reactions.* Phys. Rev. Lett. **102**, 232501 (2009).

[31] C. A. Bertulani and C. De Conti. *Pauli blocking and medium effects in nucleon knockout reactions.* Phys. Rev. C **81**, 064603 (2010).

[32] G. Audi, A. Wapstra, and C. Thibault. *The Ame2003 atomic mass evaluation: (II). Tables, graphs and references.* Nuclear Physics A **729**, 337 – 676 (2003).

[33] B. Jurado, H. Savajols, W. Mittig, N. Orr, P. Roussel-Chomaz, D. Baiborodin, W. Catford, M. Chartier, C. Demonchy, Z. Dlouhý, A. Gillibert, L. Giot, A. Khouaja, A. Lépine-Szily, S. Lukyanov, J. Mrazek, Y. Penionzhkevich, S. Pita, M. Rousseau, and A. Villari. *Mass measurements of neutron-rich nuclei near the and 28 shell closures.* Physics Letters B **649**, 43 – 48 (2007).

[34] L. Gaudefroy, W. Mittig, N. A. Orr, S. Varet, M. Chartier, P. Roussel-Chomaz, J. P. Ebran, B. Fernández-Domínguez, G. Frémont, P. Gangnant, A. Gillibert, S. Grévy, J. F. Libin, V. A. Maslov, S. Paschalis, B. Pietras, Y.-E. Penionzhkevich, C. Spitaels, and A. C. C. Villari. *Direct Mass Measurements of ^{19}B, ^{22}C, ^{29}F, ^{31}Ne, ^{34}Na and Other Light Exotic Nuclei.* Phys. Rev. Lett. **109**, 202503 (2012).

[35] Y. Yano. *The RIKEN RI Beam Factory Project: A status report.* Nucl. Instrum. Methods Phys. Res., Sect. B **261**, 1009 – 1013 (2007).

[36] T. Kubo. *In-flight RI beam separator BigRIPS at RIKEN and elsewhere in Japan.* Nucl. Instrum. Methods Phys. Res., Sect. B **204**, 97 – 113 (2003).

[37] T. Kubo, K. Kusaka, K. Yoshida, A. Yoshida, T. Ohnishi, M. Ohtake, Y. Yanagisawa, N. Fukuda, T. Haseyama, Y. Yano, N. Kakutani, T. Tsuchihashi, and K. Sato. *Status and Overview of Superconducting Radioactive Isotope Beam Separator BigRIPS at RIKEN.* IEEE Trans. Appl. Supercond. **17**, 1069 – 1077 (2007).

[38] T. Ohnishi, T. Kubo, K. Kusaka, A. Yoshida, K. Yoshida, N. Fukuda, M. Ohtake, Y. Yanagisawa, H. Takeda, D. Kameda, Y. Yamaguchi, N. Aoi, K. i. Yoneda, H. Otsu, S. Takeuchi, T. Sugimoto, Y. Kondo, H. Scheit, Y. Gono, H. Sakurai, T. Motobayashi, H. Suzuki, T. Nakao, H. Kimura, Y. Mizoi, M. Matsushita, K. Ieki, T. Kuboki, T. Yamaguchi,

T. Suzuki, A. Ozawa, T. Moriguchi, Y. Yasuda, T. Nakamura, T. Nannichi, T. Shimamura, Y. Nakayama, H. Geissel, H. Weick, J. A. Nolen, O. B. Tarasov, A. S. Nettleton, D. P. Bazin, B. M. Sherrill, D. J. Morrissey, and W. Mittig. *Identification of New Isotopes ^{125}Pd and ^{126}Pd Produced by In-Flight Fission of 345 MeV/nucleon ^{238}U: First Results from the RIKEN RI Beam Factory.* J. Phys. Soc. Jpn. **77**, 083201 (2008).

[39] K. Kimura, T. Izumikawa, R. Koyama, T. Ohnishi, T. Ohtsubo, A. Ozawa, W. Shinozaki, T. Suzuki, M. Takahashi, I. Tanihata, T. Yamaguchi, and Y. Yamaguchi. *High-rate particle identification of high-energy heavy ions using a tilted electrode gas ionization chamber.* Nuclear Instruments and Methods in Physics Research Section A: Accelerators, Spectrometers, Detectors and Associated Equipment **538**, 608 – 614 (2005).

[40] H. Otsu, M. Takechi, Y. Kondo, T. Onishi, N. Fukuda, M. Lantz, K. Ozeki, S. Deguchi, Y. Kawada, T. Kuboki, I. Hachiuma, and K. Namihira. *Manipulation and performance of ionization chambers for BigRIPS experiments.* RIKEN Accel. Prg. Rep. **42**, 163 – 164 (2009).

[41] M. Takechi, T. Ohtsubo, M. Fukuda, D. Nishimura, T. Kuboki, T. Suzuki, T. Yamaguchi, A. Ozawa, T. Moriguchi, H. Ooishi, D. Nagae, H. Suzuki, S. Suzuki, T. Izumikawa, T. Sumikama, M. Ishihara, H. Geissel, N. Aoi, R.-J. Chen, D.-Q. Fang, N. Fukuda, I. Hachiuma, N. Inabe, Y. Ishibashi, Y. Ito, D. Kameda, T. Kubo, K. Kusaka, M. Lantz, Y.-G. Ma, K. Matsuta, M. Mihara, Y. Miyashita, S. Momota, K. Namihira, M. Nagashima, Y. Ohkuma, T. Ohnishi, M. Ohtake, K. Ogawa, H. Sakurai, Y. Shimbara, T. Suda, H. Takeda, S. Takeuchi, K. Tanaka, R. Watanabe, M. Winkler, Y. Yanagisawa, Y. Yasuda, K. Yoshinaga, A. Yoshida, and K. Yoshida. *Interaction cross sections for Ne isotopes towards the island of inversion and halo structures of ^{29}Ne and ^{31}Ne.* Physics Letters B **707**, 357 – 361 (2012).

[42] R. Kanungo, C. Nociforo, A. Prochazka, Y. Utsuno, T. Aumann, D. Boutin, D. Cortina-Gil, B. Davids, M. Diakaki, F. Farinon, H. Geissel, R. Gernhäuser, J. Gerl, R. Janik, B. Jonson, B. Kindler, R. Knöbel, R. Krücken, M. Lantz, H. Lenske, Y. Litvinov, K. Mahata, P. Maierbeck, A. Musumarra, T. Nilsson, T. Otsuka, C. Perro, C. Scheidenberger, B. Sitar, P. Strmen, B. Sun, I. Szarka, I. Tanihata, H. Weick, and M. Winkler. *Structure of ^{33}Mg sheds new light on the island of inversion.* Physics Letters B **685**, 253 – 257 (2010).

[43] S. Agostinelli, J. Allison, K. Amako, J. Apostolakis, H. Araujo, P. Arce, M. Asai, D. Axen, S. Banerjee, G. Barrand, F. Behner, L. Bellagamba, J. Boudreau, L. Broglia, A. Brunengo, H. Burkhardt, S. Chauvie, J. Chuma, R. Chytracek, G. Cooperman, G. Cosmo, P. Degtyarenko, A. Dell'Acqua, G. Depaola, D. Dietrich, R. Enami, A. Feliciello, C. Ferguson, H. Fesefeldt, G. Folger, F. Foppiano, A. Forti, S. Garelli, S. Giani, R. Giannitrapani, D. Gibin, J. G. Cadenas, I. González, G. G. Abril, G. Greeniaus, W. Greiner, V. Grichine, A. Grossheim, S. Guatelli, P. Gumplinger, R. Hamatsu, K. Hashimoto, H. Hasui, A. Heikkinen, A. Howard, V. Ivanchenko, A. Johnson, F. Jones, J. Kallenbach, N. Kanaya, M. Kawabata, Y. Kawabata, M. Kawaguti, S. Kelner, P. Kent, A. Kimura, T. Kodama, R. Kokoulin, M. Kossov, H. Kurashige, E. Lamanna, T. Lampén, V. Lara, V. Lefebure, F. Lei, M. Liendl, W. Lockman, F. Longo, S. Magni, M. Maire, E. Medernach, K. Minamimoto, P. M. d. Freitas, Y. Morita, K. Murakami, M. Nagamatu, R. Nartallo, P. Nieminen, T. Nishimura, K. Ohtsubo, M. Okamura, S. O'Neale, Y. Oohata, K. Paech, J. Perl, A. Pfeiffer, M. Pia, F. Ranjard, A. Rybin, S. Sadilov, E. D. Salvo, G. Santin, T. Sasaki, N. Savvas, Y. Sawada, S. Scherer, S. Sei, V. Sirotenko, D. Smith, N. Starkov, H. Stoecker, J. Sulkimo, M. Takahata, S. Tanaka, E. Tcherniaev, E. S. Tehrani, M. Tropeano, P. Truscott, H. Uno, L. Urban, P. Urban, M. Verderi, A. Walkden, W. Wander, H. Weber, J. Wellisch, T. Wenaus, D. Williams, D. Wright, T. Yamada, H. Yoshida, and D. Zschiesche. *Geant4 – a*

simulation toolkit. Nuclear Instruments and Methods in Physics Research Section A: Accelerators, Spectrometers, Detectors and Associated Equipment **506**, 250 – 303 (2003).

[44] M. Belleguic, F. Azaiez, Z. Dombrádi, D. Sohler, M. J. Lopez-Jimenez, T. Otsuka, M. G. Saint-Laurent, O. Sorlin, M. Stanoiu, Y. Utsuno, Y.-E. Penionzhkevich, N. L. Achouri, J. C. Angelique, C. Borcea, C. Bourgeois, J. M. Daugas, F. D. Oliveira-Santos, Z. Dlouhy, C. Donzaud, J. Duprat, Z. Elekes, S. Grévy, D. Guillemaud-Mueller, S. Leenhardt, M. Lewitowicz, S. M. Lukyanov, W. Mittig, M. G. Porquet, F. Pougheon, P. Roussel-Chomaz, H. Savajols, Y. Sobolev, C. Stodel, and J. Timár. *Search for neutron excitations across the $N = 20$ shell gap in $^{25-29}Ne$.* Phys. Rev. C **72**, 054316 (2005).

[45] Y. Yanagisawa, M. Notani, H. Sakurai, M. Kunibu, H. Akiyoshi, N. Aoi, H. Baba, K. Demichi, N. Fukuda, H. Hasegawa, Y. Higurashi, M. Ishihara, N. Iwasa, H. Iwasaki, T. Gomi, S. Kanno, M. Kurokawa, Y. Matsuyama, S. Michimasa, T. Minemura, T. Mizoi, T. Nakamura, A. Saito, M. Serata, S. Shimoura, T. Sugimoto, E. Takeshita, S. Takeuchi, K. Ue, K. Yamada, K. Yoneda, and T. Motobayashi. *The first excited state of ^{30}Ne studied by proton inelastic scattering in reversed kinematics.* Physics Letters B **566**, 84 – 89 (2003).

[46] V. Tripathi, S. L. Tabor, P. Bender, C. R. Hoffman, S. Lee, K. Pepper, M. Perry, P. F. Mantica, J. M. Cook, J. Pereira, J. S. Pinter, J. B. Stoker, D. Weisshaar, Y. Utsuno, and T. Otsuka. *Excited intruder states in ^{32}Mg.* Phys. Rev. C **77**, 034310 (2008).

[47] K. Yoneda, H. Sakurai, T. Gomi, T. Motobayashi, N. Aoi, N. Fukuda, U. Futakami, Z. Gacsi, Y. Higurashi, N. Imai, N. Iwasa, H. Iwasaki, T. Kubo, M. Kunibu, M. Kurokawa, Z. Liu, T. Minemura, A. Saito, M. Serata, S. Shimoura, S. Takeuchi, Y. Watanabe, K. Yamada, Y. Yanagisawa, K. Yogo, A. Yoshida, and M. Ishihara. *Deformation of ^{34}Mg studied via in-beam γ-ray spectroscopy using radioactive-ion projectile fragmentation.* Physics Letters B **499**, 233 – 237 (2001).

[48] A. Gade, P. Adrich, D. Bazin, M. D. Bowen, B. A. Brown, C. M. Campbell, J. M. Cook, S. Ettenauer, T. Glasmacher, K. W. Kemper, S. McDaniel, A. Obertelli, T. Otsuka, A. Ratkiewicz, K. Siwek, J. R. Terry, J. A. Tostevin, Y. Utsuno, and D. Weisshaar. *Spectroscopy of ^{36}Mg: Interplay of Normal and Intruder Configurations at the Neutron-Rich Boundary of the "Island of Inversion".* Phys. Rev. Lett. **99**, 072502 (2007).

[49] S. Takeuchi, M. Matsushita, N. Aoi, P. Doornenbal, K. Li, T. Motobayashi, H. Scheit, D. Steppenbeck, H. Wang, H. Baba, D. Bazin, L. Càceres, H. Crawford, P. Fallon, R. Gernhäuser, J. Gibelin, S. Go, S. Grévy, C. Hinke, C. R. Hoffman, R. Hughes, E. Ideguchi, D. Jenkins, N. Kobayashi, Y. Kondo, R. Krücken, T. Le Bleis, J. Lee, G. Lee, A. Matta, S. Michimasa, T. Nakamura, S. Ota, M. Petri, T. Sako, H. Sakurai, S. Shimoura, K. Steiger, K. Takahashi, M. Takechi, Y. Togano, R. Winkler, and K. Yoneda. *Well Developed Deformation in ^{42}Si.* Phys. Rev. Lett. **109**, 182501 (2012).

[50] C. Campbell, N. Aoi, D. Bazin, M. Bowen, B. Brown, J. Cook, D.-C. Dinca, A. Gade, T. Glasmacher, M. Horoi, S. Kanno, T. Motobayashi, L. Riley, H. Sagawa, H. Sakurai, K. Starosta, H. Suzuki, S. Takeuchi, J. Terry, K. Yoneda, and H. Zwahlen. *Quadrupole collectivity in silicon isotopes approaching neutron number.* Physics Letters B **652**, 169 – 173 (2007).

[51] C. M. Campbell, N. Aoi, D. Bazin, M. D. Bowen, B. A. Brown, J. M. Cook, D.-C. Dinca, A. Gade, T. Glasmacher, M. Horoi, S. Kanno, T. Motobayashi, W. F. Mueller, H. Sakurai, K. Starosta, H. Suzuki, S. Takeuchi, J. R. Terry, K. Yoneda, and H. Zwahlen. *Measurement of Excited States in ^{40}Si and Evidence for Weakening of the $N = 28$ Shell Gap.* Phys. Rev. Lett. **97**, 112501 (2006).

[52] Y. Utsuno, T. Otsuka, T. Mizusaki, and M. Honma. *Varying shell gap and deformation in $N \sim 20$ unstable nuclei studied by the Monte Carlo shell model.* Phys. Rev. C **60**, 054315 (1999).

[53] Y. Utsuno, T. Otsuka, B. A. Brown, M. Honma, T. Mizusaki, and N. Shimizu. *Tensor-force-driven Jahn-Teller effect and shape transitions in exotic Si isotopes.* arXiv:1201.4077 (2012).

[54] T. Kobayashi, S. Shimoura, I. Tanihata, K. Katori, K. Matsuta, T. Minamisono, K. Sugimoto, W. Müller, D. Olson, T. Symons, and H. Wieman. *Electromagnetic dissociation and soft giant dipole resonance of the neutron-dripline nucleus ^{11}Li.* Physics Letters B **232**, 51 – 55 (1989).

[55] R. Serber. *The Production of High Energy Neutrons by Stripping.* Phys. Rev. **72**, 1008–1016 (1947).

[56] P. Doornenbal, H. Scheit, N. Aoi, S. Takeuchi, K. Li, E. Takeshita, H. Wang, H. Baba, S. Deguchi, N. Fukuda, H. Geissel, R. Gernhäuser, J. Gibelin, I. Hachiuma, Y. Hara, C. Hinke, N. Inabe, K. Itahashi, S. Itoh, D. Kameda, S. Kanno, Y. Kawada, N. Kobayashi, Y. Kondo, R. Krücken, T. Kubo, T. Kuboki, K. Kusaka, M. Lantz, S. Michimasa, T. Motobayashi, T. Nakamura, T. Nakao, K. Namihira, S. Nishimura, T. Ohnishi, M. Ohtake, N. A. Orr, H. Otsu, K. Ozeki, Y. Satou, S. Shimoura, T. Sumikama, M. Takechi, H. Takeda, K. N. Tanaka, K. Tanaka, Y. Togano, M. Winkler, Y. Yanagisawa, K. Yoneda, A. Yoshida, K. Yoshida, and H. Sakurai. *Spectroscopy of ^{32}Ne and the "Island of Inversion".* Phys. Rev. Lett. **103**, 032501 (2009).

[57] K. Bear and P. E. Hodgson. *The systematics of nuclear bound states.* Journal of Physics G: Nuclear Physics **4**, L287 (1978).

[58] A. Mengoni, T. Otsuka, and M. Ishihara. *Direct radiative capture of p-wave neutrons.* Phys. Rev. C **52**, R2334–R2338 (1995).

[59] M. H. Macfarlane and J. B. French. *Stripping Reactions and the Structure of Light and Intermediate Nuclei.* Rev. Mod. Phys. **32**, 567–691 (1960).

[60] T. Misu, W. Nazarewicz, and S. Åberg. *Deformed nuclear halos.* Nuclear Physics A **614**, 44 – 70 (1997).

[61] I. Hamamoto. *Dominance of low-ℓ component in weakly bound deformed single-neutron orbits.* Phys. Rev. C **69**, 041306 (2004).

[62] I. Hamamoto. *Nilsson diagrams for light neutron-rich nuclei with weakly-bound neutrons.* Phys. Rev. C **76**, 054319 (2007).

[63] H. Iwasaki, T. Motobayashi, H. Sakurai, K. Yoneda, T. Gomi, N. Aoi, N. Fukuda, Z. Fülöp, U. Futakami, Z. Gacsi, Y. Higurashi, N. Imai, N. Iwasa, T. Kubo, M. Kunibu, M. Kurokawa, Z. Liu, T. Minemura, A. Saito, M. Serata, S. Shimoura, S. Takeuchi, Y. Watanabe, K. Yamada, Y. Yanagisawa, and M. Ishihara. *Large collectivity of ^{34}Mg.* Physics Letters B **522**, 227 – 232 (2001).

[64] K. Yoneda, H. Sakurai, T. Gomi, T. Motobayashi, N. Aoi, N. Fukuda, U. Futakami, Z. Gacsi, Y. Higurashi, N. Imai, N. Iwasa, H. Iwasaki, T. Kubo, M. Kunibu, M. Kurokawa, Z. Liu, T. Minemura, A. Saito, M. Serata, S. Shimoura, S. Takeuchi, Y. Watanabe, K. Yamada, Y. Yanagisawa, K. Yogo, A. Yoshida, and M. Ishihara. *Gamma-ray spectroscopy of ^{34}Mg via RI beam fragmentation.* Nuclear Physics A **701**, 437 – 440 (2002).

[65] D. T. Yordanov, M. Kowalska, K. Blaum, M. De Rydt, K. T. Flanagan, P. Lievens, R. Neugart, G. Neyens, and H. H. Stroke. *Spin and Magnetic Moment of ^{33}Mg: Evidence for a Negative-Parity Intruder Ground State.* Phys. Rev. Lett. **99**, 212501 (2007).

[66] *Intruder Configurations in the $A = 33$ Isobars: ^{33}Mg.*

[67] T. A. Belote, H. Y. Chen, O. Hansen, and J. Rapaport. *$Ca^{46}(d,p)Ca^{47}$ Reaction at 7-MeV Bombarding Energy.* Phys. Rev. **142**, 624–632 (1966).

[68] M. Williams-Norton and R. Abegg. *Study of low-lying levels in ^{47}Ca with the ^{48}Ca(d, t)^{47}Ca reaction.* Nuclear Physics A **291**, 429 – 442 (1977).

[69] Z. Dombrádi, D. Sohler, O. Sorlin, F. Azaiez, F. Nowacki, M. Stanoiu, Y.-E. Penionzhkevich, J. Timár, F. Amorini, D. Baiborodin, A. Bauchet, F. Becker, M. Belleguic, C. Borcea, C. Bourgeois, Z. Dlouhy, C. Donzaud, J. Duprat, Z. Elekes, D. Guillemaud-Mueller, F. Ibrahim, M. Lewitowicz, M. Lopez, R. Lucas, S. Lukyanov, V. Maslov, C. Moore, J. Mrazek, M. Saint-Laurent, F. Sarazin, J. Scarpaci, G. Sletten, C. Stodel, M. Taylor, C. Theisen, and G. Voltolini. *Search for particle–hole excitations across the N=28 shell gap in $^{45,46}Ar$ nuclei.* Nuclear Physics A **727**, 195 – 206 (2003).

[70] L. Gaudefroy, O. Sorlin, F. Nowacki, D. Beaumel, Y. Blumenfeld, Z. Dombrádi, S. Fortier, S. Franchoo, S. Grévy, F. Hammache, K. W. Kemper, K. L. Kratz, M. G. St. Laurent, S. M. Lukyanov, L. Nalpas, A. N. Ostrowski, Y.-E. Penionzhkevich, E. C. Pollacco, P. Roussel, P. Roussel-Chomaz, D. Sohler, M. Stanoiu, and E. Tryggestad. *Structure of the $N = 27$ isotones derived from the $^{44}Ar(d,p)^{45}Ar$ reaction.* Phys. Rev. C **78**, 034307 (2008).

[71] F. Sarazin, H. Savajols, W. Mittig, F. Nowacki, N. A. Orr, Z. Ren, P. Roussel-Chomaz, G. Auger, D. Baiborodin, A. V. Belozyorov, C. Borcea, E. Caurier, Z. Dlouhý, A. Gillibert, A. S. Lalleman, M. Lewitowicz, S. M. Lukyanov, F. d. Oliveira, Y. E. Penionzhkevich, D. Ridikas, H. Sakuraï, O. Tarasov, and A. d. Vismes. *Shape Coexistence and the $N = 28$ Shell Closure Far from Stability.* Phys. Rev. Lett. **84**, 5062–5065 (2000).

[72] L. A. Riley, P. Adrich, T. R. Baugher, D. Bazin, B. A. Brown, J. M. Cook, P. D. Cottle, C. A. Diget, A. Gade, D. A. Garland, T. Glasmacher, K. E. Hosier, K. W. Kemper, A. Ratkiewicz, K. P. Siwek, J. A. Tostevin, and D. Weisshaar. *Rotational and neutron-hole states in ^{43}S via the neutron knockout and fragmentation reactions.* Phys. Rev. C **80**, 037305 (2009).

[73] L. Gaudefroy, J. M. Daugas, M. Hass, S. Grévy, C. Stodel, J. C. Thomas, L. Perrot, M. Girod, B. Rossé, J. C. Angélique, D. L. Balabanski, E. Fiori, C. Force, G. Georgiev, D. Kameda, V. Kumar, R. L. Lozeva, I. Matea, V. Méot, P. Morel, B. S. N. Singh, F. Nowacki, and G. Simpson. *Shell Erosion and Shape Coexistence in $^{43}_{16}S_{27}$.* Phys. Rev. Lett. **102**, 092501 (2009).

[74] R. Chevrier, J. M. Daugas, L. Gaudefroy, Y. Ichikawa, H. Ueno, M. Hass, H. Haas, S. Cottenier, N. Aoi, K. Asahi, D. L. Balabanski, N. Fukuda, T. Furukawa, G. Georgiev, H. Hayashi, H. Iijima, N. Inabe, T. Inoue, M. Ishihara, Y. Ishii, D. Kameda, T. Kubo, T. Nanao, G. Neyens, T. Ohnishi, M. M. Rajabali, K. Suzuki, H. Takeda, M. Tsuchiya, N. Vermeulen, H. Watanabe, and A. Yoshimi. *Is the $7/2^-_1$ Isomer State of ^{43}S Spherical?* Phys. Rev. Lett. **108**, 162501 (2012).

[75] D. Sohler, S. Grévy, Z. Dombrádi, O. Sorlin, L. Gaudefroy, B. Bastin, N. Achouri, J. Angélique, F. Azaiez, D. Baiborodin, R. Borcea, C. Bourgeois, A. Buta, A. Burger, L. Caceres, R. Chapman, J. Dalouzy, Z. Dlouhy, A. Drouard, Z. Elekes, S. Franchoo, S. Iacob, I. Kuti, B. Laurent, M. Lazar, X. Liang, E. Liénard, S. Lukyanov, J. Mrazek, L. Nalpas,

F. Negoita, F. Nowacki, N. Orr, Y. Penionzkhevitch, Z. Podolyḱ, F. Pougheon, A. Poves, P. Roussel-Chomaz, M. Stanoiu, I. Stefan, and M. St-Laurent. *Spectroscopy of* ^{39,41}*Si and the border of the island of inversion.* Physics Letters B **703**, 417 – 421 (2011).

[76] M. Chiba, R. Kanungo, B. Abu-Ibrahim, S. Adhikari, D. Fang, N. Iwasa, K. Kimura, K. Maeda, S. Nishimura, T. Ohnishi, A. Ozawa, C. Samanta, T. Suda, T. Suzuki, I. Tanihata, Q. Wang, C. Wu, Y. Yamaguchi, K. Yamada, A. Yoshida, and T. Zheng. *Neutron removal studies on* ^{19}*C.* Nuclear Physics A **741**, 29 – 41 (2004).

[77] K. Hencken, G. Bertsch, and H. Esbensen. *Breakup reactions of the halo nuclei* ^{11}*Be and* ^{8}*B.* Phys. Rev. C **54**, 3043–3050 (1996).

[78] A. Ozawa, Y. Hashizume, Y. Aoki, K. Tanaka, T. Aiba, N. Aoi, H. Baba, B. A. Brown, M. Fukuda, K. Inafuku, N. Iwasa, T. Izumikawa, K. Kobayashi, M. Komuro, Y. Kondo, T. Kubo, M. Kurokawa, T. Matsuyama, S. Michimasa, T. Motobayashi, T. Nakabayashi, S. Nakajima, T. Nakamura, T. Ohtsubo, H. Sakurai, R. Shinoda, M. Shinohara, H. Suzuki, T. Suzuki, M. Takechi, E. Takeshita, S. Takeuchi, Y. Togano, K. Yamada, T. Yamaguchi, T. Yasuno, and M. Yoshitake. *One- and two-neutron removal reactions from* ^{19,20}*C with a proton target.* Phys. Rev. C **84**, 064315 (2011).

[79] A. Goldhaber. *Statistical models of fragmentation processes.* Physics Letters B **53**, 306 – 308 (1974).

[80] E. C. Simpson and J. A. Tostevin. *One- and two-neutron removal from the neutron-rich carbon isotopes.* Phys. Rev. C **79**, 024616 (2009).

[81] Y. Kondo, T. Nakamura, Y. Satou, T. Matsumoto, N. Aoi, N. Endo, N. Fukuda, T. Gomi, Y. Hashimoto, M. Ishihara, S. Kawai, M. Kitayama, T. Kobayashi, Y. Matsuda, N. Matsui, T. Motobayashi, T. Nakabayashi, K. Ogata, T. Okumura, H. J. Ong, T. K. Onishi, H. Otsu, H. Sakurai, S. Shimoura, M. Shinohara, T. Sugimoto, S. Takeuchi, M. Tamaki, Y. Togano, and Y. Yanagisawa. *One-neutron removal reactions of* ^{18}*C and* ^{19}*C on a proton target.* Phys. Rev. C **79**, 014602 (2009).

[82] V. Maddalena, T. Aumann, D. Bazin, B. A. Brown, J. A. Caggiano, B. Davids, T. Glasmacher, P. G. Hansen, R. W. Ibbotson, A. Navin, B. V. Pritychenko, H. Scheit, B. M. Sherrill, M. Steiner, J. A. Tostevin, and J. Yurkon. *Single-neutron knockout reactions: Application to the spectroscopy of* ^{16,17,19}*C.* Phys. Rev. C **63**, 024613 (2001).

[83] M. Stanoiu, D. Sohler, O. Sorlin, F. Azaiez, Z. Dombrádi, B. A. Brown, M. Belleguic, C. Borcea, C. Bourgeois, Z. Dlouhy, Z. Elekes, Z. Fülöp, S. Grévy, D. Guillemaud-Mueller, F. Ibrahim, A. Kerek, A. Krasznahorkay, M. Lewitowicz, S. M. Lukyanov, S. Mandal, J. Mrázek, F. Negoita, Y.-E. Penionzhkevich, Z. Podolyák, P. Roussel-Chomaz, M. G. Saint-Laurent, H. Savajols, G. Sletten, J. Timár, C. Timis, and A. Yamamoto. *Disappearance of the* $N = 14$ *shell gap in the carbon isotopic chain.* Phys. Rev. C **78**, 034315 (2008).

[84] T. Nakamura, N. Fukuda, T. Kobayashi, N. Aoi, H. Iwasaki, T. Kubo, A. Mengoni, M. Notani, H. Otsu, H. Sakurai, S. Shimoura, T. Teranishi, Y. X. Watanabe, K. Yoneda, and M. Ishihara. *Coulomb Dissociation of* ^{19}*C and its Halo Structure.* Phys. Rev. Lett. **83**, 1112–1115 (1999).

[85] Y. Satou, T. Nakamura, N. Fukuda, T. Sugimoto, Y. Kondo, N. Matsui, Y. Hashimoto, T. Nakabayashi, T. Okumura, M. Shinohara, T. Motobayashi, Y. Yanagisawa, N. Aoi, S. Takeuchi, T. Gomi, Y. Togano, S. Kawai, H. Sakurai, H. Ong, T. Onishi, S. Shimoura, M. Tamaki, T. Kobayashi, H. Otsu, Y. Matsuda, N. Endo, M. Kitayama, and M. Ishihara. *Unbound excited states in* ^{19,17}*C.* Physics Letters B **660**, 320 – 325 (2008).

[86] Z. Elekes, Z. Dombrádi, R. Kanungo, H. Baba, Z. FÏöp, J. Gibelin, A. Horváth, E. Ideguchi, Y. Ichikawa, N. Iwasa, H. Iwasaki, S. Kanno, S. Kawai, Y. Kondo, T. Motobayashi, M. Notani, T. Ohnishi, A. Ozawa, H. Sakurai, S. Shimoura, E. Takeshita, S. Takeuchi, I. Tanihata, Y. Togano, C. Wu, Y. Yamaguchi, Y. Yanagisawa, A. Yoshida, and K. Yoshida. *Low-lying excited states in* $^{17,19}C$. Physics Letters B **614**, 174 – 180 (2005).

[87] E. C. Simpson, J. A. Tostevin, D. Bazin, B. A. Brown, and A. Gade. *Two-Nucleon Knockout Spectroscopy at the Limits of Nuclear Stability.* Phys. Rev. Lett. **102**, 132502 (2009).

[88] E. C. Simpson, J. A. Tostevin, D. Bazin, and A. Gade. *Longitudinal momentum distributions of the reaction residues following fast two-nucleon knockout reactions.* Phys. Rev. C **79**, 064621 (2009).